Photochemical Dynamics of Molecular Switches

A thesis submitted in partial fulfilment of the requirements for the degree of Master of Science by Research at the University of East Anglia

Eleanor K. Ashworth

School of Chemistry
University of East Anglia

June 2022

This copy of the thesis has been supplied on condition that anyone who consults it is understood to recognise that its copyright rests with the author and that use of any information derived there-from must be in accordance with current UK Copyright Law. In addition, any quotation or extract must include full attribution.

Acknowledgements

I would like to express my thanks to my supervisor, Dr James Bull, for his ongoing support and encouragement.

I am grateful to my second supervisor Prof. Steve Meech and his research group for their help. I would especially like to thank Dr Giovanni Bressan and Dr Palas Roy for their help in using the fluorescence up-conversion experiment. I also thank Robert Hindmarsh for showing me the ropes on the FS5 spectrofluorometer.

Contributions

Substituted *p*HBDI anions

Photodissociation action spectroscopy performed by Dr James Bull, Dr Mark Stockett, and Dr Christina Kjaer using the Sep1 accelerator mass spectrometer at Aarhus University, Denmark.
Contents from this chapter have been published: Complexation of Green and Red Kaede Fluorescent Protein Chromophores by a Zwitterion to Probe Electrostatic and Induction Field Effects, E. K. Ashworth, M. H. Stockett, C. Kjær, P. C. Bulman Page, S. R. Meech, S. Brøndsted Nielsen, and J. N. Bull, *J. Phys. Chem. A.*, 2022, **126**, 1158-1167

Photophysics of *p*CK$^-$

Photodetachment and photoisomerisation action spectroscopy performed by Dr James Bull using a custom-built tandem ion-mobility mass spectrometer at the University of Melbourne, Australia.
Photodissociation action spectroscopy performed by Dr Neville Coughlan using an instrument at the University of Waterloo, Canada.

Characterisation of DTEs

DTE molecules synthesised by Dr George Vamvounis at James Cook University, Australia.

Abstract

Photoswitches form a general and versatile family of compounds whose properties change in response to the absorption of light. They range from naturally-occurring chromophores that facilitate protein and enzyme activity, to synthetic compounds that are routinely deployed in technological applications, including optogenetics, biological fluorescent tags, sunscreens, and optoelectronics. The photochemical dynamics of photoswitches are driven by a combination of the intrinsic dynamics and environmental influences, for example, solvent and temperature. This thesis explores the photophysics of three families of photoswitch molecules: (i) a selection of deprotonated chromophore derivatives of green fluorescent protein, (ii) an anionic model chromophore for photoactive yellow protein, and (iii) a series of synthetic dithienylethene compounds targeted for development into optoelectronics. The intrinsic photophysics and environmental impacts are probed using a range of experimental methods, including photodissociation action spectroscopy, ultrafast fluorescence up-conversion ($\approx$50 fs time resolution), and time-resolved fluorescence ($<$700 ps time resolution). The experimental data are interpreted with the aid of electronic structure calculations.

Access Condition and Agreement

Each deposit in UEA Digital Repository is protected by copyright and other intellectual property rights, and duplication or sale of all or part of any of the Data Collections is not permitted, except that material may be duplicated by you for your research use or for educational purposes in electronic or print form. You must obtain permission from the copyright holder, usually the author, for any other use. Exceptions only apply where a deposit may be explicitly provided under a stated licence, such as a Creative Commons licence or Open Government licence.

Electronic or print copies may not be offered, whether for sale or otherwise to anyone, unless explicitly stated under a Creative Commons or Open Government license. Unauthorised reproduction, editing or reformatting for resale purposes is explicitly prohibited (except where approved by the copyright holder themselves) and UEA reserves the right to take immediate ‘take down’ action on behalf of the copyright and/or rights holder if this Access condition of the UEA Digital Repository is breached. Any material in this database has been supplied on the understanding that it is copyright material and that no quotation from the material may be published without proper acknowledgement.

Contents

Contents iv

List of Figures vii

List of Tables xix

1 Introduction 1

1.1 Biochromophores . . . 1

1.1.1 Protein environments . . . 2

1.2 Synthetic photoswitches . . . 4

1.3 General photoswitch properties . . . 6

1.4 Photoswitches of interest in this thesis . . . 7

2 Background to theory and computational methods 13

2.1 Computational methods . . . 13

2.1.1 The Hartree-Fock wavefunction and friends . . . 13

2.1.2 Coupled-cluster methods . . . 18

2.1.3 CASSCF theory . . . 19

2.1.4 Density functional theory . . . 21

2.1.5 Semi-empirical methods . . . 23

2.1.6 Comparison of common computational methods . . . 23

2.2 Potential energy surfaces and reaction dynamics . . . 24

2.2.1 Photochemistry . . . 25

3 Methods and analysis 38

3.1 Ultrafast fluorescence up-conversion . . . 38

3.1.1 Modelocking . . . 41

3.1.2 Dispersion . . . 43

3.1.3 Cross-correlation . . . 45

3.2 Fluorescence decay analysis . . . 46

3.3 Computational methods . . . 47

4 Substituted *p*HBDI anions **52**
4.1 Introduction . . . 52
4.2 Experimental methods . . . 59
4.3 Theoretical methods . . . 60
4.3.1 Vertical excitation wavelengths . . . 62
4.3.2 Symmetry-adapted perturbation theory (SAPT) . . . 63
4.4 Results and discussion . . . 65
4.4.1 Photodissociation action spectra . . . 65
4.4.2 Anion-betaine binding . . . 69
4.4.3 SAPT analysis . . . 72
4.4.4 Anion-betaine spectral shifts . . . 75
4.5 Conclusion and future work . . . 77

5 Photophysics of *p*CK$^-$ **85**
5.1 Introduction . . . 85
5.2 Computational methods . . . 90
5.3 Experimental methods . . . 91
5.3.1 Absorption and fluorescence . . . 91
5.3.2 Ultrafast fluorescence up-conversion . . . 91
5.4 Results and discussion . . . 92
5.4.1 Merits of computational methods: TD-DFT, CC2, and STEOM 92
5.4.2 Modelling solvation . . . 94
5.4.3 Absorption and fluorescence spectra . . . 95
5.4.4 Time-resolved fluorescence . . . 102
5.4.5 Temperature-dependent fluorescence . . . 113
5.5 Gas-phase photophysics . . . 115
5.5.1 Experimental methods . . . 116
5.5.2 Computational methods . . . 120
5.5.3 Results and discussion . . . 121
5.6 Conclusion and future work . . . 128

6 Characterisation of DTEs **139**
6.1 Introduction . . . 139
6.2 Computational methods . . . 145
6.3 Experimental methods . . . 145
6.4 Results and discussion . . . 146
6.4.1 Comparison of computational methods . . . 146

6.4.2 Modelling solvation 148
6.4.3 Absorption and fluorescence spectra 151
6.4.4 Time-resolved fluorescence 160
6.4.5 Change in absorption spectra over time 165
6.4.6 The strange case of the yellow CG1-94 solution 165
6.4.7 Fatigue 170
6.5 Conclusion and future work 173

7 Summary **179**

Appendix **181**
A1 Photophysics of pCK$^-$ 181
A2 Characterisation of DTEs 192

Abbreviations **209**

List of Figures

Figure **Page**

1.1 **(a)** PYP chromophore binding pocket, showing the hydrogen bonding interactions (dashed lines) between the thioester pCT$^-$ (centre) and PYP amino acid residues (*e.g.* Glu46). Adapted from Anderson *et al.*[34] **(b)** GFP chromophore binding pocket, showing the hydrogen bonding interactions (dashed lines) between pHBDI$^-$ (centre), GFP amino acid residues (*e.g.* S205), and water molecules (*e.g.* w22). Adapted from Nielsen *et al.*[7] 4

1.2 Chemical structures of **(a)** stilbene, **(b)** azobenzene, **(c)** a general diarylethene, and **(d)** a general heterocyclic fulgide. 5

2.1 The ground-state, singly-, and doubly-excited determinants, with respective configurations, for H_2 in a minimal basis with two 1s orbitals (φ_1 and φ_2). α and β represent the two electron spins. 16

2.2 Schematic representation of a CASSCF(4,4) active space. Doubly-occupied orbitals make up the inactive space. The active space contains the orbitals of interest, and the virtual space is omitted from the calculation. All possible electron configurations over the active space orbitals are included in the CASSCF wavefunction. CASSCF calculations essentially treat the active space with a FCI wavefunction. 20

2.3 Jacob's Ladder with examples of DFT methods on each rung. LDA = local density approximation, GGA = generalised gradient approximation, MGGA = meta-GGA, HGGA = hybrid-GGA, HMGGA = hybrid meta-GGA, RS = range-separated, DH = double hybrid. 22

2.4 Graphical representation of the approximate computational cost and accuracy of a selection of common quantum chemical methods. 24

2.5 Potential energy diagrams of **(a)** an avoided crossing, and **(b)** a conical intersection. The red arrow indicates excitation of the reactants, resulting in promotion to the excited state. The blue arrows indicate the respective relaxation pathways. 26

2.6 The two main forms conical intersections can take: **(a)** Peaked and **(b)** sloped. For a peaked CI, relaxation from the excited (R*) to the ground state results in various potential products (P_n) and the original reactant (R). Relaxation to the ground state *via* a sloped CI only returns the original reactant. Adapted from Boggio-Pasqua.[56] 27

2.7 Diagrams of **(a)** a generic seam conical intersection between states A and B, adapted from Asturiol *et al.*[59] and **(b)** the S_0/S_1 minimum energy conical intersections (MECIs) of benzene, adapted from Harabuchi *et al.*[60] Panel **(a)** shows sloped and peaked intersection segments (red and green, respectively), and indicates two potential trajectories (white arrows) of an excited reactant. 28

2.8 Generic potential energy surfaces depicting photochemical processes to overcome a ground-state (S_0) barrier to thermal isomerisation, where the sum of $h\nu$ and the initial internal vibrational energy exceeds the excited-state barrier height. Panel **(a)** describes motion along a barrierless excited state (S_1) to a conical intersection, while **(b)** and **(c)** represent potential motion along an excited state with a barrier. A molecule with vibrational energy distributed in **(b)** favourable modes will reach a conical intersection faster than when **(c)** the rate of IVR is fast and redistributes vibrational energy into modes less favourable for crossing the excited state barrier and reaching the conical intersection. 32

3.1 Schematic diagram of the basic principles of fluorescence up-conversion. The green and red lines correspond to the sample fluorescence (ω_f) and the gate pulse (ω_p), respectively. The angle (θ) of the non-linear optical (NLO) crystal is adjusted to maximise overlap between ω_f and ω_p, thus maximising the up-converted signal, ω_s. Adapted from Chosrowjan *et al.*[5] 39

3.2 Schematic of the fluorescence up-conversion experimental setup at UEA. A neodymium yttrium vanadate ($Nd:YVO_4$) laser drives the titanium:sapphire (Ti:S) oscillator at 532 nm, producing 800 nm radiation. λ_1 is the fundamental wavelength (800 nm), acting as the gate pulse. λ_2 is the second harmonic wavelength (400 nm), which is used to excite the sample. λ_3 is the up-converted signal, determined by summing the energies of the gate pulse and the sample fluorescence. 40

3.3 Representation of the oscillations within a laser cavity producing **(a)** continuous wave and **(b)** pulsed laser beams. On the left is a fully-reflecting (FR) mirror, while on the right there is a partially-transmitting (PT) mirror, through which some of the oscillations are conducted, forming the output laser beam. Gain is increased in the laser cavity by adding **(c)** additional optics, which filter out returning low-intensity pulses, only permitting high-intensity pulses to return to the Ti:S crystal. 42

3.4 To correct for pulse broadening and positive chirp, **(a)** pulse compressors and **(b)** chirped mirrors are included in the fluorescence up-conversion setup. The pulse compressor contains four prisms which retard the faster-travelling red wavelengths, allowing the slower blue wavelengths to "catch up". Chirped mirrors are made of many dielectric layers, allowing for wavelength-dependent penetration depths, achieving a similar pulse outcome as the pulse compressor. 43

3.5 Cross-correlation of two laser pulses, λ_1 and λ_2. The resulting wavelength, λ_3 is created by sum frequency generation (SFG). The full-width half-maximum (FWHM) represents the experimental time-resolution. 44

3.6 Cross-correlation of heptane Raman scattering, fitted with a Gaussian function. The full-width half-maximum (blue arrows), yields an ≈50 fs time resolution of the fluorescence up-conversion setup. Data extracted from Addison PhD thesis.[12] 45

4.1 Structure of green fluorescent protein (GFP) and its chromophore (insert), located inside the protein β-barrel (pdb 2WUR). Adapted from the Protein Data Bank[5] and visualised in Mol* Viewer.[6–8] 53

4.2 Structures of the six target chromophores and the betaine zwitterion (Z). Compounds 26Me$^-$, 35Me$^-$, 35Bu$^-$, and Phe$^-$ are alkylated and phenylated derivatives of *p*HBDI$^-$. Molecule rKFP$^-$ is a more complex derivative of *p*HBDI and is also a model chromophore of red Kaede fluorescent protein (rKFP). 57

4.3 Schematic representation of **(a)** the Sep1 accelerator mass spectrometer used to study the photodissociation of the *p*HBDI$^-$ series. Insert **(b)** shows the apparatus for ion-packet formation. The ions, produced by electrospray ionisation, pass through a heated capillary before being collected in an octupole ion trap. At 25 ms intervals, ion packets are ejected and accelerated to a kinetic energy of ≈50 keV. The ions of interest are mass separated by the bending magnet and then traverse the linear flight region, where every second ion bunch is excited by a laser pulse, causing dissociation. The electrostatic analyser separates the fragment ions, which are counted by the channeltron detector. Adapted from Støchkel *et al.*[28] 60

4.4 Anion-betaine complexes with **(a)** the major binding sites (**1**-**3**) for betaine, shown on *p*HBDI$^-$. O(1) and O(2) indicate the phenoxide and imidazolinone oxygen atoms, the former being the deprotonation site. **(b)** The side-on interaction between an HBDI anion and betaine, shown for the 35Bu$^-$·Z(**3**) cluster. 61

4.5 Photodissociation action spectra for various anion-betaine complexes and their bare ion counterparts: **(a)** *p*HBDI$^-$, **(b)** 26Me$^-$, **(c)** 35Me$^-$, **(d)** 35Bu$^-$, **(e)** Phe$^-$, and **(f)** rKFP$^-$. The black traces correspond to the bare ions, obtained by monitoring the loss of a methyl group (m/z = 15, >95% photodissociation yield), and the red traces correspond to data for the anion-betaine complexes, obtained by monitoring the formation of the bare anion, *i.e.* loss of the betaine molecule. The grey data in **(a)** are photoneutralisation measurements obtained using the ELISA ion storage ring at Aarhus University, taken from Langeland *et al.*[22] 66

4.6 Illustrations of (a) 26Me$^-$ and (b) 26Me$^-$·Z(**3**) complex involving side-on binding, showing the internal twist about the core *p*HBDI bridge due to steric interactions from the methyl groups. 69

5.1 **(a)** Structure of photoactive yellow protein (PYP), with the *E*-4-hydroxycinnamate unit and cysteine residue shown (PDB 1UWN). Adapted from the Protein Data Bank[8] and visualised in Mol* Viewer.[9–11] **(b)** The potential energy surface of excited and ground states of the deprotonated chromophore in the protein, for $E \rightarrow Z$ isomerisation, adapted from Groenhof *et al.*[12] Torsion b coordinate corresponds to the $E \rightarrow Z$ isomerisation reaction and the yellow line indicates a typical trajectory along the PES. Structures **(c)** and **(d)** show the chromophore with the thioester bond to the protein, *via* the cysteine residue, and deprotonated *para*-coumaric ketone (pCK$^-$), commonly used as a model for the PYP chromophore, respectively. 86

5.2 Structures of **(a)** *para*-coumaric acid (pCA$^-$), as both its phenoxide (top) and carboxylate (bottom) deprotomers, and its derivatives **(b)** pCEs$^-$ and **(c)** pCEt$^-$. 87

5.3 Schematic representation of the solvent rearrangement process following excitation of a sample. Note that the change in dipole moment of the chromophore leads to solvent rearrangement, particularly for a polar solvent. 88

5.4 Panel **(a)** illustrates the single-bond twisted S_1 structure of pCK$^-$ and the orbitals of the S_0 and S_1 states, illustrating the charge-transfer nature of the $S_1 \leftarrow S_0$ transition. Bond twisting can induce charge-transfer character. Adapted from Boggio-Pasqua *et al.*[31] Also illustrated are the pCK$^-$ **(b)** HOMO and **(c)** LUMO, computed in the Firefly 8.2.0[47] software package at the CASSCF(12,11)/aug-cc-pVDZ level of theory. 92

5.5 Computed vertical excitation wavelengths (λ_{VEE}) of pCK$^-$ obtained at various levels of theory using different implicit and explicit solvation models. Panel **(a)** shows the oscillating behaviour of the vertical excitation wavelengths obtained at the TD-ωB97X-D/aug-cc-pVDZ level of theory, with PCM, for pCK$^-$ surrounded by an increasing number of explicit water molecule (0–5). The data is fitted to a polynomial function (red curve). Panel **(b)** depicts calculated vertical excitation wavelengths for pCK$^-$ surrounded by five explicit water molecules, using different computational methods. 95

5.6 Absorption spectra of neutral (red) and anionic (blue) pCK in water. . . . 96

5.7 Absorption (dotted) and emission (solid) spectra of pCK$^-$ in various mixture of ethylene glycol and water: 0%, 20%, 40%, 60%, 80%, and 100% water. 98

5.8 Excitation (ex) and emission (em) spectra of **(a)** concentrated and **(b)** dilute solutions of $p\mathrm{CK}^-$ in water (at arbitrary concentrations). Panel **(a)** shows emission spectra from exciting the concentrated sample at 400 nm and 440 nm. The emission spectrum in **(b)** was excited at 400 nm. 100

5.9 Measured and simulated spectra of dilute (40 µM) and concentrated (5 mM) aqueous $p\mathrm{CK}^-$ solution. Panel **(a)** depicts the overlap (region marked by the star) of the dilute excitation spectrum (red) with the simulated absorption spectrum of the concentrated solution (blue). Panel **(b)** shows the close agreement of the simulated (line) and measured (dotted) excitation spectra of the 5 mM solution. 101

5.10 Panel **(a)** shows the absorption (grey), excitation (red), and emission (blue) spectra of $p\mathrm{CK}^-$ in water, overlaid with the measured profile of the ≈400 nm pump laser pulse (dotted). Panel **(b)** shows the emission wavelengths monitored during fluorescence up-conversion experiments on $p\mathrm{CK}^-$ in water (crosses) shown on an emission spectrum of the same system. The fluorescence decays with the corresponding detection wavelength and fluorescence lifetime (without uncertainties) are also depicted (see insert). 102

5.11 Fluorescence decays and fitting residuals for $p\mathrm{CK}^-$ in methanol (**(a)** and **(c)**) and octanol (**(b)** and **(d)**. Panels **(a)** and **(b)** show single-exponential fitting, while **(c)** and **(d)** are double-exponential fits. 105

5.12 Fluorescence lifetimes of $p\mathrm{CK}^-$ (from double-exponential fitting) in various solvents/solvent mixtures measured in a static (red) and flow (blue) cell setup – **(a)** τ_1, the fast component (corresponding to solvent rearrangement), and **(b)** τ_2, the slower component (species fluorescence lifetime). Percentages indicate vol% of ethylene glycol in the water–ethylene-glycol solutions. 107

5.13 Single-exponential fluorescence decay fits for $p\mathrm{CK}^-$ in water–ethylene-glycol mixtures, from which fluorescence lifetimes were obtained. The fluorescence decay curves are each normalised to the peak intensity. Percentages indicate vol% of water in the water–ethylene-glycol solutions. 108

5.14 Fluorescence lifetimes (τ_2) for $p\mathrm{CK}^-$ in (**(a)** and **(b)**) a selection of alcohols and (**(c)** and **(d)**) water–ethylene-glycol mixtures, obtained from double-exponential fitting of decay curves from static (blue) and flow (red) fluorescence up-conversion experiments. 110

5.15 Experimental (curves) emission spectra of pCK$^-$ at **(a)** $T = 77\,\mathrm{K}$ (in ethanol) and **(b)** $T = 300\,\mathrm{K}$ (in water). The FCHT simulated line spectra (lines) were computed, at the ωB97X-D/aug-cc-pVDZ level of theory, for isolated pCK$^-$. * indicates the 0-0 transition. Vibronic features to shorter wavelengths of the 0-0 transition are hot bands. The simulated emission spectrum does not account for the solvent interactions. 113

5.16 The temperature dependence of fluorescence excitation and emission of pCK$^-$: **(a)** excitation (dotted) and emission spectra (solid) at $T \approx 77\,\mathrm{K}$ (blue) and $T \approx 300\,\mathrm{K}$ (red), and **(b)** & **(c)** excitation-emission maps at $T \approx 300\,\mathrm{K}$ and $T \approx 77\,\mathrm{K}$, respectively. Asterisk indicates an artefact from excitation light. 114

5.17 Schematic representation of the tandem ion-mobility mass spectrometer used to obtain action spectra of gas-phase pCK$^-$. Ions produced by electrospray ionisation are collected in the first ion funnel (IF1) and are injected as packets into the first IMS stage (IMS1) by the ion gate (IG1). Ion-mobility selected ion packets are transmitted into the second IMS stage (IMS2) by the second ion gate (IG2). Every second isomer-selected ion packet is irradiated with light from an OPO laser system. Daughter ions are collected in the second ion funnel (IF2) and are then guided into a quadrupole mass filter (QMF) by an octupole ion guide. The QMF mass-selects ions, which are counted by the channeltron detector. Adapted from Scholz *et al.*[85] 117

5.18 Schematic representation of the photodissociation action spectroscopy setup used to obtain action spectra of gas-phase pCK$^-$. Ions, produced by electrospray ionisation (ESI) are carried by the buffer gas between the DMS electrodes. The mobility-selected ions traverse through quadrupole elements Q1–2 until reaching Q3 where they are excited by an optical parametric oscillator (OPO) laser system. The detector monitors and records the intensities of the parent and daughter ions at each OPO output wavelength. Supplied from the Hopkins research group (University of Waterloo). 118

5.19 Boggio-Pasqua and Groenhof used thio-pCT$^-$ (thioester of pCK$^-$ to investigate the effect of reducing active space size on molecular orbital descriptions by visualising the orbitals from CASSCF calculations with active spaces of differing sizes. Adapted from Boggio-Pasqua and Groenhof.[95] 120

5.20 Action spectra of (*E*)-*p*CK$^-$. Panels **(a)** and **(b)** show "light-off" (black) and "light-on"/photoaction (blue) arrival time distributions at 420 nm excitation in pure N_2 buffer gas and N_2 buffer gas seeded with ≈1% SF_6 and ≈1% propan-2-ol, respectively. The plots in panel **(c)** are the photodetachment (red) and $E \rightarrow Z$ photoisomerisation (blue) spectra, recorded using the Melbourne ion-mobility experiment. Overlaid over the photoisomerisation and photodetachment spectra in panel **(d)** is the photodissociation spectrum (black), recorded over the $S_1 \leftarrow S_0$ absorption band, using the Waterloo experiment. The dashed line shows the maximum photodissociation response (corresponding to vertical excitation wavelength) and the dotted line indicates the electron affinity of *p*CK, computed by Anstöter *et al.*[51] (see text regarding scaling of spectra in **(d)**.) 122

5.21 Bonding and anti-bonding π-orbitals of *p*CK$^-$, computed in the Firefly 8.2.0[47] software package at the CASSCF(12,11)/aug-cc-pVDZ level of theory. . 126

5.22 Bonding and anti-bonding π-orbitals of *p*CEs$^-$, computed in the Firefly 8.2.0[47] software package at the CASSCF(12,11)/aug-cc-pVDZ level of theory. 127

5.23 S_0 and S_1 potential energy surfaces for double-bond twisting in *p*CK$^-$, calculated at the XMCQDPT2/aug-cc-pVDZ level of theory. The vertical excitation energy is shown in red (≈2.66 eV) and the S_1 barrier height in orange (≈0.4 eV). The purple bonds in the *p*CK$^-$ structure indicate the double-bond twist dihedral angle. 128

6.1 Dis- and conrotatory motion of the antiparallel and parallel forms of the mechanistically important DAE hexatriene unit. The favoured state, motion, and conformer for cyclisation is highlighted in green. Adapted from Staykov *et al.*[12] 140

6.2 Reaction pathway of a generic DTE. The parallel and antiparallel conformers thermally interconvert, but only the antiparallel conformer can cyclise on UV irradiation. The open isomer is recovered on irradiation at visible wavelengths. Further UV irradiation of the closed isomer forms a by-product, from which other forms cannot be recovered. 141

6.3 Chemical structures and abbreviations of eight dithienylethenes investigated in this thesis. Naming convention follows organic synthesis reaction scheme by the synthetic group at James Cook University, Australia. 143

6.4 Absorption spectra of the antiparallel (black) and closed (red) isomers of NS2-22, adapted from Irie *et al.*[8] 147

6.5 The calculated vertical excitation wavelengths of closed NS2-22 are shown by **(a)** coloured lines on the absorption spectrum of closed NS2-22 in methanol (region expanded in insert). The explicit solvated excitation wavelengths are **(b)** plotted as a function solvated structure, fitted to an asymptotic exponential function ($y = a - bc^x$) to demonstrate the tendency towards a plateau. TD-DFT indicates a calculation at the TD-ωB97X-D level of theory, while '+ PCM' includes implicit solvation. The abbreviations sol1.0, sol2.1, and sol3.5 are the lowest energy structures for the singly, doubly, and triply explicitly solvated NS2-22, respectively, computed at the TD-ωB97X-D level of theory with PCM. 149

6.6 Lowest energy doubly- (**(a)** and **(b)**) and triply-solvated (**c** and **d**) structures of antiparallel (left) and closed (right) NS2-22. The first methanol hydrogen bonds to a fluorine atom, while subsequent methanol molecules hydrogen-bond with the preceding methanol. 150

6.7 Absorption spectra of the open (black) and closed (coloured) forms of **(a)** B2287, **(b)** NS2-22, **(c)** NS2-24, **(d)** CG1-79, **(e)** CG1-91, **(f)** CG1-94, **(g)** CG1-107, and **(h)** CG1-108, recorded in methanol. The colours of the spectra indicate the colour of the irradiated DTE solutions (at arbitrary concentrations). Bands in the range of 380–400 nm **(c)**–**(h)** likely arise due to by-product formation. 152

6.8 Excitation-emission (XM) maps of the closed-isomer forms of **(a)** NS2-22, **(c)** NS2-24, **(e)** B2287, and **(f)** CG1-79, recorded at $T \approx 300\,\mathrm{K}$ in methanol. Panels **(b)** and **(d)** show the XM maps, recorded at $T \approx 77\,\mathrm{K}$ in methanol, of NS2-22 and NS2-24, respectively. Inserts are XM maps of areas of weak fluorescence signal. Diagonal lines are an artefact from scattering of the excitation light. 155

6.9 Excitation-emission (XM) maps of the closed-isomer forms of **(a)** CG1-91, **(b)** CG1-94, **(c)** CG1-107, and **(e)** CG1-108, recorded at $T \approx 300\,\mathrm{K}$ in methanol. Panels **(d)** and **(f)** show the XM maps, recorded at $T \approx 77\,\mathrm{K}$ in methanol, of CG1-107 and CG1-108, respectively. The insert is an excitation-emission map of an area of weak fluorescence signal. Diagonal lines are an artefact from scattering of the excitation light. 156

6.10 Excitation (red) and emission (blue) spectra of **(a)** B2287, **(b)** NS2-22, **(c)** NS2-24, and **(d)** CG1-79, recorded at $T \approx 300\,\mathrm{K}$ (solid lines) and $T \approx 77\,\mathrm{K}$ (dotted lines) in methanol. Gaps in the $T \approx 77\,\mathrm{K}$ excitation spectra are present due to removal of signal that arose from internal reflections in the spectrofluorometer setup. These are the disregarded diagonal lines in the XM maps. 157

6.11 Excitation (red) and emission (blue) spectra of **(a)** CG1-91, **(b)** CG1-94, **(c)** CG1-107, and **(d)** CG1-108, recorded at $T \approx 300\,\mathrm{K}$ (solid lines) and $T \approx 77\,\mathrm{K}$ (dotted lines) in methanol. Gaps in the $T \approx 77\,\mathrm{K}$ excitation spectra are present due to removal of signal that arose from internal reflections in the spectrofluorometer setup. 158

6.12 Time-resolved emission for DTEs **(a)** NS2-22 and **(b)** CG1-79 in methanol at **(a)**–**(b)** $T \approx 300\,\mathrm{K}$ and **(c)**–**(e)** at $T \approx 77\,\mathrm{K}$. A double-exponential fit is shown to be more suited for **(e)** CG1-79 at $T \approx 77\,\mathrm{K}$. The other decay curves are suited to single-component fits. 159

6.13 Diarylethene cycloreversion reaction scheme. 1A and 2A are the ground- and excited-states, respectively. $2A_C$ is a local closed-isomer minimum and $2A_O$ is the geometry at the 2A/1A conical intersection. Adapted from Sotome *et al.*[27] 160

6.14 Panel **(a)** is a schematic of multiple possible relaxation pathways for a closed-isomer thiophenylethene (a type of DTE) upon excitation. Adapted from Matis *et al.*[49] Panel **(b)** shows a representation of a thiophenylethene's potential energy surfaces (S_0, orange; S_1, green) for the initial fatigue coordinate. CHD and HT represent the closed and open isomers, respectively. SeamGeom is an S_1/S_0 conical intersection, ultimately leading to by-product formation (not shown). Adapted from Mendive-Tapia *et al.*[50] 161

6.15 Time-series absorption spectra of irradiated **(a)** B2287, **(c)** NS2-22, **(e)** NS2-24, and **(g)** CG1-79, in methanol. The peak absorbance of the 500–600 nm band from each spectrum are plotted on the right, **(b, d, f, h)**. Absorbance is normalised to the maximum signal. 163

6.16 Time-series absorption spectra of irradiated **(a)** CG1-91, **(c)** CG1-94, **(e)** CG1-107, and **(g)** CG1-108, in methanol. The peak absorbance of the 500–600 nm band of each spectrum are plotted on the right, **(b, d, f, h)**. On plots **(c)** and **(d)**, blue represents the disappearing band, arising from the closed isomer, while orange represents the new band, attributed to the by-product. CG1-94 decomposes rapidly. Absorbance is normalised to the maximum signal. 164

6.17 Absorption spectra in methanol of **(a)** the open (black) and closed (blue) isomers of CG1-94, and **(b)** the initial yellow solution of CG1-94, followed by irradiation at 590 nm for 15 and 55 minutes. **(c)** Fluorescence emission spectra of the initial yellow solution, followed by irradiation at 275 nm for 145 minutes, show that the fluorescence intensity increased while the absorption spectrum **(d)** did not change. Absorbance is normalised to the maximum signal. 166

6.18 A methanol solution of open-antiparallel CG1-94 (initial) was irradiated at 275 nm for 10 minutes and **(a)** absorption spectra recorded at 10 minute intervals. **(b)** The change in absorbance of the 380 nm (yellow) and 575 nm (blue) bands were plotted as a function of time, fitted to exponential growth ($y = A_1 e^{(x/t_1)} + y_0$) and decay ($y = A_1 e^{(-x/t_1)} + y_0$) curves, respectively. Also shown are the structures of the **(c)** closed isomer ($\lambda_{\text{max}} = 575\,\text{nm}$) and **(d)** by-product ($\lambda_{\text{max}} = 380\,\text{nm}$). 167

6.19 Excitation-emission (XM) maps of CG1-94 in methanol irradiated at 275 nm and recorded at regular time intervals. Panels **(a)**–**(c)** correspond to time after irradiation: **(a)** 5 minutes, **(b)** 30 minutes, and **(c)** 55 minutes. Panels **(d)** and **(e)** show the XM maps of the CG1-94 by-product at $T \approx 300\,\text{K}$ and $T \approx 77\,\text{K}$, respectively. As a comparison, **(f)** gives the excitation (red) and emission (blue) spectra of the CG1-94 by-product at $T \approx 300\,\text{K}$ (solid lines) and $T \approx 77\,\text{K}$ (dotted lines). The emission spectra were excited at 575 nm (dark blue) and 478 nm (light blue), respectively. Gaps in the $T \approx 77\,\text{K}$ excitation spectra are present due to removal of signal that arose from internal reflections in the spectrofluorometer setup. 169

6.20 A solution of open-antiparallel CG1-107 (initial) was alternately irradiated at **(b)** 275 nm (5 mins) and **(a)** 590 nm (35 mins), and absorption spectra recorded after each irradiation. 171

6.21 A solution of open-antiparallel CG1-94 (initial) was alternately irradiated at **(b)** 275 nm (5 mins) and **(a)** 590 nm (35 mins) and absorption spectra recorded after each irradiation. The change in absorbance of **(c)** the 380 nm (yellow) band from the 590 nm spectrum, plotted as a function of switching cycle, showed an increasing linear trend. The change in absorbance of **(d)** the 380 nm (yellow) and 575 nm (blue) bands from the 275 nm spectrum, plotted as a function of switching cycle, also follow linear trends (increasing and decreasing, respectively). 172

A1.1 Lowest energy structures of anionic *para*-coumaric ketone (pCK$^-$) solvated with **(a)**–**(e)** 1–5 water molecules, at the ωB97X-D/aug-cc-pVDZ level of theory, in Gaussian 16B.01. 181
A1.2 Computational process by which the effect of explicit solvation of pCK$^-$ was explored. All calculations were performed in Gaussian 16B.01. 182
A2.1 All the forms of four out of the eight dithienylethenes under investigation. Reactants (open-antiparallel, open-parallel) and products (closed, and by-product). 192
A2.2 All the forms of four out of the eight dithienylethenes under investigation. Reactants (open-antiparallel, open-parallel) and products (closed, and by-product). 193
A2.3 Computational process by which the effect of explicit solvation of dithienylethene NS2-22 was explored. All calculations were performed in Gaussian 16B.01. 194
A2.4 Open NS2-22 structures, optimised under explicit solvation, with **(a)** one, **(b)** two, and **(c)** three methanol molecules, at the ωB97X-D/cc-pVDZ level of theory, in Gaussian 16B.01. 197
A2.5 Closed NS2-22 structures, optimised under explicit solvation, with **(a)** one, **(b)** two, and **(c)** three methanol molecules, at the ωB97X-D/cc-pVDZ level of theory, in Gaussian 16B.01. 198

List of Tables

Table **Page**

2.1 The average absolute errors in bond lengths (AH and AB) and angles (HAH), over 184 small molecules, obtained by different methods using the aug-cc-pVTZ basis set.[2] 14

2.2 Photoisomerisation lifetimes of two related retinoids, *trans* retinal protonated Schiff base (*trans*-RPSB) and deprotonated *trans*-retinoic acid (*trans*-RA^-), in isolation (τ_g) and in methanol (τ_{MeOH}). Lifetimes (note the different units) were obtained by QM/MM simulations and femtosecond experiments for *trans*-RPSB and *trans*-retinoic acid, respectively.[64–66] . 30

4.1 Summary of the terms into which the SAPT0 interaction energy, E_{SAPT0} can be decomposed, accompanied by their definitions and physical interpretations.[69] 64

4.2 Action spectra wavelengths of the maximum responses for bare anion photodissociation (λ_{anion}) and anion-betaine complex photodissociation ($\lambda_{complex}$) (see spectra in Figure 4.5). The betaine-induced spectral shift is Δ. VDE_{calc} is the vertical detachment energy calculated at the DLPNO-CCSD(T)/aug-cc-pVDZ level of theory for the bare anion. Uncertainty in Δ is approximately ± 0.01 eV. 68

4.3 Photon energies at absorption maxima for the bare anions in aqueous (E_{aq}) and ethanol (E_{eth}) solution. Values in parentheses are spectral shifts relative to the anion gas-phase photodissociation action spectra. [a]Ref. 37. [b]Ref. 43. 68

4.4 Relative anion-betaine complex energy (E) for binding site **1**/**2**/**3**. CBE is the dissociation energy for the complex, i.e. anion-betaine $\rightarrow$ anion + betaine, for betaine binding site **1**/**2**/**3**. VDE is the vertical detachment energy of the complex for betaine binding site **1**/**2**/**3**. All values are at the DLPNO-CCSD(T)/aug-cc-pVDZ level of theory and include BSSE correction. 70

4.5 Relative anion-betaine complex energy, ΔE in kJ mol^{-1} and relative Boltzmann population, $\frac{N_c}{N_t}$, relative to the lowest energy binding site complex for each anion-betaine species. (Assumes DLPNO-CCSD(T)/aug-cc-pVDZ + BSSE energies). 71

4.6 Symmetry adapted perturbation theory (SAPT) analysis of the anion-betaine complexes. Contributions with superscript (1) are a first-order perturbation terms, and those with superscript (2) are second-order perturbation terms. Negative and positive terms indicate binding and repulsive interactions, respectively. Energies are in kJ mol^{-1} except for the complex binding energy (CBE), which is in eV. SAPT analysis was performed using the jun-cc-pVDZ basis set, except in the cases of: [a]aug-cc-pVDZ basis set and [b]jun-cc-pVTZ basis set. * indicates the lowest energy structure. 74

4.7 Calculated $S_1 \leftarrow S_0$ transition wavelengths for the bare anions, anion-betaine complexes, MBS (PC-M), NBO (PC-N), and CM5 (PC-C) point charge models of betaine. Wavelengths were computed at the DLPNO-STEOM-CCSD/aug-cc-pVDZ level of theory. Values in parentheses are deviations (in eV) from the experimental data (action spectra, Table 4.2). For S_1 Z(**1**/**2**/**3**), deviations (relative to experiment) are included for the lowest energy anion-betaine complexes. 76

5.1 Comparison of vertical excitation energies (VEEs) for *p*CK$^-$ and *p*CA$^-$ from computations, at different levels of theory, and from gas-phase experiments. Δ is the relative difference in VEE between the experimental and computed values. [a] indicates calculations were performed using the aug-cc-pVDZ basis set. 93

5.2 Absorption (λ^{A}_{max})and emission (λ^{E}_{max}) maxima with corresponding Stokes shift $\Delta\nu$ and solvent polarity (ε, obtained from Ref. 57). Percentages indicate vol% of water in the water–ethylene-glycol solutions. *Likely an outlier due to water in the sample. 97

5.3 Fluorescence lifetimes of *p*CK$^-$ in various solvents and solvent mixtures measured using static (s) and flow (f) fluorescence up-conversion cells, and obtained from single- (τ_0) and double-exponential fitting (τ_1 and τ_2). τ_1 is limited by experiment cross-correlation (55 fs). Percentages indicate vol% of water in the water–ethylene-glycol solutions. $\pm$ indicates the fitted uncertainty. EtGly is ethylene glycol. 104

5.4 Fluorescence lifetimes of $p\mathrm{CK}^-$ (single-component fit) measured in a range of polar protic solvents using static (τ_0^{s}) and flow (τ_0^{f}) cells. $\pm$ indicates the fitted uncertainty. 106

5.5 Fluorescence lifetimes of $p\mathrm{CK}^-$ in water–ethylene glycol mixtures (obtained from single- (τ_0) and double-exponential fitting (τ_1 and τ_2)). τ_1 is limited by experiment cross-correlation (55 fs). Percentages indicate the relative volume of water to ethylene glycol in the solutions. 109

5.6 Parameter α (from power law $k_{\mathrm{i}} \propto \eta^{-\alpha}$) obtained from fitting τ_2 values for a series of alcohols (**A**) and water–ethylene-glycol mixtures (**B**) (See Figure 5.14). Regression coefficient (R^2) in parentheses. 111

5.7 Fluorescence lifetimes of $p\mathrm{CK}^-$ in different solvents measured at $T \approx 300\,\mathrm{K}$, by fluorescence up-conversion ($\lambda_{\mathrm{ex}} \approx 400\,\mathrm{nm}$), and $T \approx 77\,\mathrm{K}$, by time-resolved emission ($\lambda_{\mathrm{ex}} \approx 365\,\mathrm{nm}$). λ_{m} is the emission monitoring wavelength. 115

6.1 Bright excited states from df-CC2/cc-pVDZ and TD-ωB97X-D/cc-pVDZ calculations on the antiparallel (AP) and closed (CL) isomers of NS2-22. Oscillator strengths are given in parentheses. 147

6.2 Summary of the vertical excitation wavelengths of the unsolvated, and lowest energy singly- (sol1.x) and doubly-solvated (sol2.x) geometries of the antiparallel (AP) and closed (CL) isomers of NS2-22. The wavelengths correspond to those of the first and third excited states of the CL and AP isomers, respectively. Data were obtained from df-CC2 and TD-ωB97X-D calculations with the cc-pVDZ basis set. '+ PCM' indicates the addition of PCM implicit solvation to the calculation. 148

6.3 Absorption maxima (λ_{max}) of DTE compounds of the same and comparable structures to NS2-22, B2287, and NS2-24 from this work (expt.) and literature. 153

6.4 Fluorescence lifetimes of DTEs in methanol measured at $T \approx 300\,\mathrm{K}$ and $T \approx 77\,\mathrm{K}$, by time-resolved emission ($\lambda_{\mathrm{ex}} = 575\,\mathrm{nm}$). Emission was monitored at 620 nm at $T \approx 300\,\mathrm{K}$ and 630 nm at $T \approx 77\,\mathrm{K}$. Lifetimes denoted by * are limited by the pump pulse duration ($\approx$400 ps). 162

A1.1 Energies of the various geometries of pCK$^-$ solvated with 1–5 water molecules, obtained from calculations at the PM6/aug-cc-pVDZ and ωB97X-D/aug-cc-pVDZ levels of theory, in Gaussian 16B.01. ΔE(DFT) is the difference in energy of the solvated forms relative to the most stable form. The darker shading indicates the most stable geometries for the respective solvations. 183

A1.2 Excitation energies of the first eight excited states of pCK$^-$ obtained from MRCC calculations, at the df-CC2/aug-cc-pVDZ and df-CC2/aug-cc-pVTZ levels of theory, and TD-DFT calculations (in Gaussian 16B.01), at the ωB97X-D/aug-cc-pVDZ and ωB97X-D/aug-cc-pVTZ levels of theory. The oscillator strengths (f) are highlighted by their relative magnitudes, where green indicates a large value. 184

A1.3 Excitation energies of the first eight excited states of pCK$^-$, with PCM (water), obtained from MRCC calculations, at the df-CC2/aug-cc-pVDZ and df-CC2/aug-cc-pVTZ levels of theory, and TD-DFT calculations (in Gaussian 16B.01), at the ωB97X-D/aug-cc-pVDZ and ωB97X-D/aug-cc-pVTZ levels of theory. The oscillator strengths (f) are highlighted by their relative magnitudes, where green indicates a large value. 185

A1.4 Excitation energies of the first eight excited states of the three lowest energy structures of pCK$^-$ solvated by one explicit water molecule. Of the three, sol1.0 is the most stable. Along with the explicit solvation, PCM was included for the second row results. Obtained from TD-DFT calculations at the ωB97X-D/aug-cc-pVDZ level of theory, in Gaussian 16B.01. The oscillator strengths (f) are highlighted by their relative magnitudes, where green indicates a large value. 186

A1.5 Excitation energies of the first eight excited states of the three lowest energy structures of pCK$^-$ solvated by two explicit water molecules. Of the three, sol2.3 is the most stable. Along with the explicit solvation, PCM was included for the second row results. Obtained from TD-DFT calculations at the ωB97X-D/aug-cc-pVDZ level of theory, in Gaussian 16B.01. The oscillator strengths (f) are highlighted by their relative magnitudes, where green indicates a large value. 187

A1.6 Excitation energies of the first eight excited states of the three lowest energy structures of pCK$^-$ solvated by three explicit water molecules. Of the three, sol3.3 is the most stable. Along with the explicit solvation, PCM was included for the second row results. Obtained from TD-DFT calculations at the ωB97X-D/aug-cc-pVDZ level of theory, in Gaussian 16B.01. The oscillator strengths (f) are highlighted by their relative magnitudes, where green indicates a large value. 188

A1.7 Excitation energies of the first eight excited states of the three lowest energy structures of pCK$^-$ solvated by four explicit water molecules. Of the three, sol4.0 is the most stable. Along with the explicit solvation, PCM was included for the second row results. Obtained from TD-DFT calculations at the ωB97X-D/aug-cc-pVDZ level of theory, in Gaussian 16B.01. The oscillator strengths (f) are highlighted by their relative magnitudes, where green indicates a large value. 189

A1.8 Excitation energies of the first eight excited states of the three lowest energy structures of pCK$^-$ solvated by five explicit water molecules. Of the three, sol5.0 is the most stable. Along with the explicit solvation, PCM was included for the second row results. Obtained from TD-DFT calculations at the ωB97X-D/aug-cc-pVDZ level of theory, in Gaussian 16B.01. The oscillator strengths (f) are highlighted by their relative magnitudes, where green indicates a large value. 190

A1.9 Excitation energies of the first eight excited states of the lowest energy solvated geometries (1,3, and 5 water molecules) of pCK$^-$. Obtained from MRCC calculations at the df-CC2/aug-cc-pVDZ level of theory, with PCM (water). The oscillator strengths (f) are highlighted by their relative magnitudes, where green indicates a large value. 191

A2.1 Energies of the various geometries of the singly-, doubly-, and triply-solvated antiparallel NS2-22, obtained from calculations at the PM6/cc-pVDZ and ωB97X-D/cc-pVDZ levels of theory, in Gaussian 16B.01. ΔE(DFT) is the difference in energy of the solvated forms relative to the most stable form. The darker shading indicates the most stable geometries for the respective solvations. 195

A2.2 Energies of the various geometries of the singly-, doubly-, and triply-solvated closed NS2-22, obtained from calculations at the PM6/cc-pVDZ and ωB97X-D/cc-pVDZ levels of theory, in Gaussian 16B.01. ΔE(DFT) is the difference in energy of the solvated forms relative to the most stable form. The darker shading indicates the most stable geometries for the respective solvations. 196

A2.3 Excitation energies of the first eight excited states of antiparallel (AP), parallel (PA), closed (CL), and by-product (BP) NS2-22 obtained from TD-DFT calculations at the ωB97X-D/cc-pVDZ and ωB97X-D/cc-pVTZ levels of theory, in Gaussian 16B.01. The oscillator strengths (f) are highlighted by their relative magnitudes, where green indicates a large value. 199

A2.4 Excitation energies of the first eight excited states of antiparallel (AP), parallel (PA), closed (CL), and by-product (BP) NS2-22 obtained from MRCC calculations at the df-CC2/cc-pVDZ and df-CC2/cc-pVTZ levels of theory. The oscillator strengths (f) are highlighted by their relative magnitudes, where green indicates a large value. 200

A2.5 Excitation energies of the first eight excited states of antiparallel (AP) and closed (CL) NS2-22, with added PCM to include solvation effects of methanol. Obtained from TD-DFT calculations at the ωB97X-D/cc-pVDZ and ωB97X-D/cc-pVTZ levels of theory, in Gaussian 16B.01. The oscillator strengths (f) are highlighted by their relative magnitudes, where green indicates a large value. 201

A2.6 Excitation energies of the first eight excited states of antiparallel (AP) and closed (CL) NS2-22, with added PCM to include solvation effects of methanol. Obtained from MRCC calculations at the df-CC2/cc-pVDZ and df-CC2/cc-pVTZ levels of theory. The oscillator strengths (f) are highlighted by their relative magnitudes, where green indicates a large value. 202

A2.7 Excitation energies of the first eight excited states of the three lowest energy singly-solvated geometries of antiparallel NS2-22. Of the three, o-sol1.0 is the most stable. Along with the explicit solvation (addition of one methanol molecule), PCM was included for those on the second row. Obtained from TD-DFT calculations at the ωB97X-D/cc-pVDZ level of theory, in Gaussian 16B.01. The oscillator strengths (f) are highlighted by their relative magnitudes, where green indicates a large value. 203

A2.8 Excitation energies of the first eight excited states of the three lowest energy doubly-solvated geometries of antiparallel NS2-22. Of the three, o-sol2.2 is the most stable. Along with the explicit solvation (addition of two methanol molecules), PCM was included for the second row results. Obtained from TD-DFT calculations at the ωB97X-D/cc-pVDZ level of theory, in Gaussian 16B.01. The oscillator strengths (f) are highlighted by their relative magnitudes, where green indicates a large value. 204

A2.9 Excitation energies of the first eight excited states of the three lowest energy singly-solvated geometries of closed NS2-22. Of the three, c-sol1.0 is the most stable. Along with the explicit solvation (addition of one methanol molecule), PCM was included for the second row results. Obtained from TD-DFT calculations at the ωB97X-D/cc-pVDZ level of theory, in Gaussian 16B.01. The oscillator strengths (f) are highlighted by their relative magnitudes, where green indicates a large value. 205

A2.10 Excitation energies of the first eight excited states of the three lowest energy doubly-solvated geometries of closed NS2-22. Of the three, c-sol2.1 is the most stable. Along with the explicit solvation (addition of two methanol molecules), PCM was included for the second row results. Obtained from TD-DFT calculations at the ωB97X-D/cc-pVDZ level of theory, in Gaussian 16B.01. The oscillator strengths (f) are highlighted by their relative magnitudes, where green indicates a large value. 206

A2.11 Excitation energies of the first eight excited states of the lowest energy doubly-solvated geometries of antiparallel and closed NS2-22. Obtained from MRCC calculations at the df-CC2/cc-pVDZ level of theory with PCM. The oscillator strengths (f) are highlighted by their relative magnitudes, where green indicates a large value. 207

A2.12 Excitation energies of the first eight excited states of the lowest energy triply-solvated geometries of antiparallel and closed NS2-22. Along with the explicit solvation (addition of three methanol molecules), PCM was included for the second column results. Obtained from TD-DFT calculations at the ωB97X-D/cc-pVDZ level of theory, in Gaussian 16B.01. The oscillator strengths (f) are highlighted by their relative magnitudes, where green indicates a large value. 208

Chapter 1

Introduction

This thesis explores the photophysics of some selected natural and synthetic photoswitches using spectroscopic and computational techniques, aiming to develop a greater understanding of the effect of an environment and functionalisation on photoswitch dynamics. Photoswitches are molecules which, upon irradiation with light of particular wavelengths, undergo reversible structural changes (photoisomerisation), effecting a change in their chemical and/or physical properties, such as solubility or conductivity.[1] Photoswitches cover a plethora of compounds – from naturally-occurring chromophores to synthetic species – for which a range of applications have been found, such as in optogenetics and optoelectronics. Fluorescent protein chromophores are commonly used in *in vivo* fluorescent tagging, but also find applications elsewhere. For example, cinnamate-based molecules (related to a protein chromophore) are used as UV-B filters in sunscreens.

1.1 Biochromophores

Photoswitch molecules embedded in protein structures are ubiquitous in nature, including visual and sensory rhodopsins (retinal chromophore),[2,3] green fluorescent and Dronpa proteins (*p*-hydroxybenzylideneimidazolidinone, *p*-HBDI chromophore),[4] and photoactive yellow protein, PYP (*E*-4-hydroxycinnamic acid/*p*-hydroxycinnamate chromophores).[5] Green fluorescent protein (GFP) was discovered in the early 1960s by Shimomura and co-workers, but it was only after the 1994 work of Chalfie *et al.*[6] that GFP found widespread use in bioimaging and tagging. The *p*HBDI chromophore of GFP is formed by autocatalytic intramolecular cyclisation involving three amino acid residues (Ser65-Tyr66-Gly67).[7] As a result, *p*HBDI-based chromophores are found in many natural systems and can be synthesised fairly easily for fluorescent tagging applications.[8–11] The basic photoswitching chromophore unit in PYP is also found throughout the Plantae kingdom where it serves as a UV-filter in the leaves of plants[12] and in protective mucus secretions on the skin of some South American amphibians. PYP itself is a

blue-light sensing protein found in *Halorhodospira halophila* bacterium[13,14] where it is the primary photoreceptor. On absorption of blue light (harmful to the bacterium), the chromophore (a thioester, $p\mathrm{CT}^-$) undergoes $E \rightarrow Z$ isomerisation which triggers a complex photocycle that drives a negative phototactic response of the bacterium.

In these examples, the photoswitches are a comparatively small chromophore unit (*cf.* 15–30 atoms) embedded within a protein binding pocket. It is well established that protein-chromophore interactions in part define a system's photophysics (Section 1.1.1). The chromophore is bound to the protein by covalent bonds to amino acid residues which, in GFP, ensures very stable fluorescence. The binding pocket is optimised to provide protection to the chromophore from the outside environment. Furthermore, the environment around the chromophore (*e.g.* protein-chromophore interactions) is tuned specifically to maximise the efficiency of the chromophore's photochemistry.[15,16] Previous studies have shown that perturbing the environment around the chromophore changes its photophysical properties.[17–20] However, it is difficult to disentangle the relative effects and importance of each interaction within the protein binding pocket. Systematic exploration of the individual interactions/effects allows for the construction of a more accurate picture of the protein-chromophore interactions.

Aside from their biological importance, photoswitching molecules have become increasingly important in technological applications over the last two decades, with applications ranging from optoelectronics and optical storage to photopharmacology and nanotechnology.[21–25] Due to the topical nature of these systems and the fact that much of their photodynamical behaviour is not fully understood, there is a need for fundamental characterisations of pre-existing and proposed photoswitches. One of the ultimate goals from this knowledge is to direct the rational design of new photoswitches with improved characteristics.

1.1.1 Protein environments

Proteins are necessary for all life. A large variety of proteins have chromophores embedded in their structure which effectively act as photoswitches for complex biological processes – so-called photoactive proteins.[2–5] These chromophores sit in a binding pocket within the protein and interact with the protein *via* non-covalent (electrostatic, inductive, and dispersive) interactions, whose importance are, in part, determined by steric constraints on the chromophore due to the protein environment.[26] However, the com-

plex protein environment makes it difficult to disentangle the importance of individual electrostatic or steric effects.[26,27] Rather than attempting to treat all of the protein-chromophore interactions simultaneously, it is beneficial to consider them individually. From the individual contributions, the relative importance and influence of each interaction can be used to establish a picture of the overall protein-chromophore binding.

As the chromophores of PYP and GFP (pCT$^-$ and pHBDI$^-$, respectively) are comparatively small molecules, they can readily be studied experimentally and computationally. Both compounds interact with pCT$^-$ and pHBDI$^-$ are interact with the protein by covalent bonds and are stabilised within their respective binding pockets, predominantly by hydrogen bonding interactions with neighbouring amino acid residues.[7,28–31] GFP (more specifically a derivative, Dronpa) and PYP are light-sensitive proteins which undergo physical and chemical changes on irradiation with particular wavelengths of light. The two absorption maxima of GFP (395 nm and 475 nm) correspond to the neutral and anionic forms of pHBDI$^-$, respectively. An equilibrium is believed to exist between these two forms, mediated by the hydrogen-bonding network which allows proton transfer between pHBDI$^-$ and amino acid residues.[29] In contrast, no such equilibrium exists for pCT$^-$. However, hydrogen bonds remain important in PYP, because steps of the PYP photocycle, initiated by the absorption of blue light by pCT$^-$, involve proton transfer.[19,32,33]

The protein cavity in which the pCT$^-$ is bound is hydrophobic due to the positioning of particular amino acid side chains that block the pathway for water penetration into the cavity.[35] Thus, the hydrogen bonding network forms primarily between the phenoxide deprotonation site on the chromophore and the PYP amino acid residues (Figure 1.1(a)). Proton transfer is key in the recovery step of the PYP photocycle (recovery step). A number of studies have explored the functional importance of the hydrogen bonding network in the proximity of pCT$^-$.[35–38] Brudler *et al.*[36] demonstrated the effect of disrupting the normal hydrogen-bond network through site-directed mutagenesis of PYP. This caused changes to both the absorption spectrum of the chromophore and to the kinetics of several photocycle steps, confirming the importance of the hydrogen-bonding network in directing PYP dynamics. This intricate hydrogen-bonding network is important for proton transfer – a step in the PYP photocycle. In contrast to PYP, the chromophore in GFP is covalently embedded inside the protein β-barrel, which is a hydrophilic environment. The system is stabilised by, amongst other things, a complex network of hydrogen bonds arising between pHBDI$^-$, GFP amino acid residues, and a few water molecules (Figure 1.1(b)). As in PYP, the GFP photocycle also involves

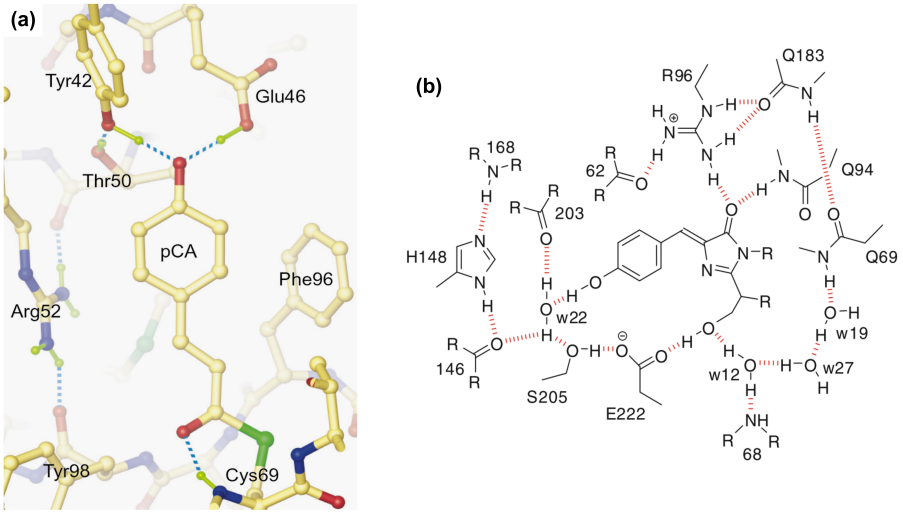


Figure 1.1: **(a)** PYP chromophore binding pocket, showing the hydrogen bonding interactions (dashed lines) between the thioester pCT$^-$ (centre) and PYP amino acid residues (*e.g.* Glu46). Adapted from Anderson *et al.*[34] **(b)** GFP chromophore binding pocket, showing the hydrogen bonding interactions (dashed lines) between pHBDI$^-$ (centre), GFP amino acid residues (*e.g.* S205), and water molecules (*e.g.* w22). Adapted from Nielsen *et al.*[7]

proton transfer although, in this case, it is mediated both by amino acid residues and a water molecule.[39,40]

As stated previously, it is difficult to disentangle both the importance of specific interactions and the impact of these interactions on the photophysics. In this thesis, the dynamics of the ketone derivative of pCA$^-$ and several derivative pHBDI$^-$ molecules are explored in gas-phase and solution environments, using computational and experimental approaches, in an attempt to understand the importance/effects of specific interactions, particularly electrostatics.

1.2 Synthetic photoswitches

The ability to manipulate the isomeric form of biological or technological molecules with light is appealing, because it offers the potential for precise control in optoelectronic applications, such as photoswitching peptide/protein conformation control or direct site-selective photoactivation of drugs in specific tissue regions, switches, memory

devices, actuators,[41] optically-controlled thin-film electronics,[42] and colorimetric detection.[43] Many common photoswitches employed in technology are relatives of stilbene (*e.g.* azobenzene), the majority of which are thermally reversible (T-type), a property not suited to photoswitches. Diarylethenes (DAEs) are one of the few families of thermally irreversible photoswitches.[1] Unlike stilbene, which undergoes $E \rightarrow Z$ photoisomerisation, DAEs undergo 6π-photocyclisation and ring opening. Both the ring-open and ring-closed forms are thermally stable; thus, they are classed as P-type (photochemically reversible) photoswitches. In addition, DAE compounds are photochromic – undergoing reversible changes in absorption spectra (and colour) upon irradiation.[41] Because photoisomerisation of DAEs causes both substantial geometric and electronic structural changes, Irie *et al.*[41] suggested these changes could be harnessed for use in various applications. For example, changes in molecular/geometrical structure are useful in photonic devices or photo-controlled actuators, while changes in electronic structure can be applied to optical memory and molecular photoswitching devices. The technological promise of these versatile compounds is an incentive to understand their photochemical properties and dynamics.

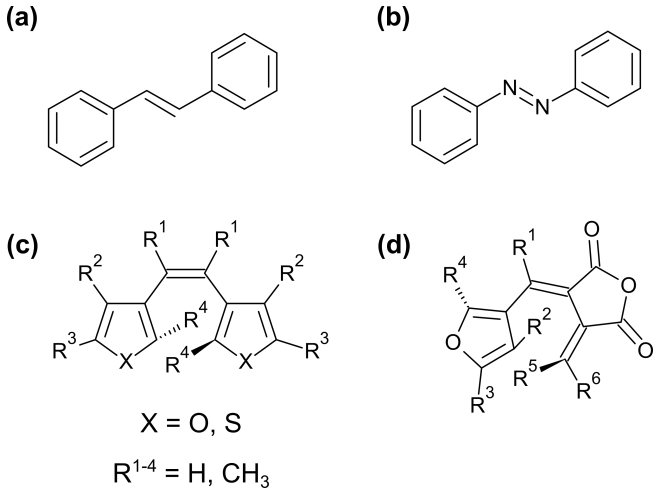


Figure 1.2: Chemical structures of **(a)** stilbene, **(b)** azobenzene, **(c)** a general diarylethene, and **(d)** a general heterocyclic fulgide.

Quantum chemical calculations are important for supporting the interpretations of experiment, although there are still many challenges (*e.g.* cost *versus* accuracy) when tackling larger molecules, such as biochromophores and synthetic photoswitches. For example, high-level electronic structure theory methods become prohibitively expensive

and it is often difficult to achieve a reliable description of electronic transitions, particularly those with charge-transfer character. Theoretical modelling of solvation provides a means of visualising the immediate solvation sphere around a molecule. Unfortunately, the accurate treatment of solvation is difficult for two main reasons: (1) the inclusion of explicit solvent molecules greatly increases computational cost, often becoming prohibitive, and (2) the computationally less demanding implicit solvation methods (which consider an average field according to a solvent's properties) are known to yield unsatisfactory results. In this thesis, explicit solvation of $p\mathrm{CK}^-$ and a simple DAE by water and methanol, respectively, is considered (Chapters 5 and 6).

1.3 General photoswitch properties

From a fundamental perspective, ideal photoswitches have several key properties:

1. Possess at least two forms with distinct absorption spectra enabling independent addressability with different colours of light
2. Fast response to a specific stimulus, *i.e.* light but not heat
3. High photoisomerisation quantum yield
4. Low fatigue on repetitive photoswitching cycles, *i.e.* fatigue resistant
5. Ease of synthesis and grafting into application
6. Thermally stable isomers (depending on end application, see below)

For the first property, photoswitches possessing at least two isomers with distinct absorption spectra allow each form to be addressed individually, thus enabling 'on-off' optical control in a given application. While molecules such as stilbenes and azobenzenes are common photoswitches that undergo $E \rightarrow Z$ photoisomerisation, strong overlap of the absorption profiles for each isomer can greatly restrict any end applications since they do not allow for clean 'on-off' switching. In other key properties, the photoisomerisation is ideally fast – *i.e.* driven by excited state dynamics occurring over the femtosecond to nanosecond timescale – and ideally occurs with a high quantum yield, meaning that the process is efficient. In this context, quantum yield is the probability that photoswitching occurs after absorption of one photon. On the latter point, while $E \rightarrow Z$ photoisomerisations (and the reverse) for simple azobenzenes and stilbenes often have quantum yields of 10–30 %, ring-closing photoswitch reactions can have very low

quantum yields of >1 % due to conformational flexibility, *e.g.* spiropyran-merocyanine photoswitch molecules. In another case, DAEs and related photoswitch families actually have high ring-closing quantum yields but very low quantum yield for cycloreversion, due to competitive internal conversion pathways via conical intersections that do not involve ring opening.[44] For photoswitching systems in which repeat photoswitching cycles are required, it is desirable to have minimal by-product formation (*i.e.* low fatigue). For example, heterocyclic fulgide derivatives have a fatigue resistance two orders of magnitude lower than that of DAEs. The DAE fatigue coordinate involves formation of a condensed ring by-product which is non-photoactive (one of the subjects in this work). The next key property is the capacity to incorporate the photoswitch molecules in applications with synthetic ease, where incorporation does not negatively impact the other photoswitching properties, *e.g.* efficiency. One of the overarching goals of the work described in this thesis is to compare and contrast the excited state dynamics and switching behaviour of photoswitch molecules in isolation (gas phase) and in solution in order to characterise how solvation affects the inherent dynamics.

The importance of thermal stability for each photoswitch isomer depends on the end application. For example, photoactivated enzymes or enzyme inhibitors, which often use an azobenzene-based photoswitch (common in biotechnology), ideally have thermally stable 'on' and 'off' forms, thus requiring each isomer to be stable with respect to thermal reversion over the timescale of the end application.[45,46] On the other hand, photopharmacology research, involving the development of photoactive drugs, desire active forms only when exposed to red light (most transmissible through mammalian tissue), and rapid reversion to an inactive form when the drug molecules move out of an irradiation zone. Such a photopharmacology strategy is useful for localised medical treatments, such as delivering a toxic drug only to the site of a tumour, or to areas of tissue where medical operation is difficult.[47,48]

1.4 Photoswitches of interest in this thesis

This thesis details the experimental and computational investigation of some photophysics of three families of photoswitches:

- The chromophore of GFP (pHBDI$^-$) and relatives

As HBDI chromophores have biological applications, such as cell tagging and tracking, many studies have been performed, aiming to understand chromophore dynamics. A recently-proposed strategy of informing on the effect of environment on a biochromophore (betaine tagging)[49,50] has been previously applied to pHBDI$^-$,[26] although an accompanying quantum chemical analysis of binding interactions or benchmarking of spectral shift has been omitted. This work provides a computational comparison to gas-phase experiments, whereby important binding interactions will be determined and methods of modelling spectral shift evaluated.

- A model chromophore of PYP – pCK$^-$

  The excited state dynamics of the model PYP chromophore derivative pCK$^-$ have been explored in various solvents.[17,18,51] This thesis aims to inform on the properties/dynamics of pCK$^-$ in a wider range of polar solvents. Moreover, this work provides fluorescence lifetimes obtained from time-resolved fluorescence up-conversion experiments (offering ≈50 fs resolution). To complement experiment, a computational study of pCK$^-$ solvation by water is performed. The data are compared with gas-phase experiments and calculations.

- A selection of thiophene-containing DAEs

  Much of the literature on DAEs focuses on understanding the detailed dynamics in non-polar or slightly-polar solvents, such as (cyclo)hexane and chloroform.[44,52–55] This thesis will provide a comparison of the properties of variously functionalised DAEs, of which three have been the subject of previous studies,[44,53,56–60] in a highly polar solvent (methanol). These photoswitches are being actively developed by synthetic groups for incorporation into technological applications.

References

[1] M. Irie and M. Morimoto, in *Photochemistry*, Royal Society of Chemistry, 2019, pp. 457–497.

[2] B. O'Leary, B. Duke, J. E. Eilers and E. W. Abrahamson, *Nature*, 1973, **246**, 166–167.

[3] J. L. Spudich and H. Luecke, *Curr. Opin. Struct. Biol.*, 2002, **12**, 540–546.

[4] R. Y. Tsien, *Annu. Rev. Biochem.*, 1998, **67**, 509–544.

[5] W. W. Sprenger, W. D. Hoff, J. P. Armitage and K. J. Hellingwerf, *J. Bacteriol.*, 1993, **175**, 3096–3104.

[6] M. Chalfie, Y. Tu, G. Euskirchen, W. W. Ward and D. C. Prasher, *Science*, 1994, **263**, 802–805.

[7] M. B. Nielsen, L. H. Andersen and T. Rocha-Rinza, *Monatsh. Chem.*, 2010, **142**, 709–715.

[8] D. A. Shagin, E. V. Barsova, Y. G. Yanushevich, A. F. Fradkov, K. A. Lukyanov, Y. A. Labas, T. N. Semenova, J. A. Ugalde, A. Meyers, J. M. Nunez, E. A. Widder, S. A. Lukyanov and M. V. Matz, *Mol. Biol. Evol.*, 2004, **21**, 841–850.

[9] S. J. Remington, *Curr. Opin. Struct. Biol.*, 2006, **16**, 714–721.

[10] J. S. Paige, K. Y. Wu and S. R. Jaffrey, *Science*, 2011, **333**, 642–646.

[11] S. Bose, S. Chakrabarty and D. Ghosh, *J. Phys. Chem. B*, 2017, **121**, 4790–4798.

[12] L. A. Baker, M. D. Horbury, S. E. Greenough, F. Allais, P. S. Walsh, S. Habershon and V. G. Stavros, *J. Phys. Chem. Lett.*, 2015, **7**, 56–61.

[13] T. Meyer, *Biochim. Biophys. Acta*, 1985, **806**, 175–183.

[14] T. E. Meyer, E. Yakali, M. A. Cusanovich and G. Tollin, *Biochemistry*, 1987, **26**, 418–423.

[15] P. Changenet-Barret, A. Espagne, S. Charier, J.-B. Baudin, L. Jullien, P. Plaza, K. J. Hellingwerf and M. M. Martin, *Photochem. Photobiol. Sci.*, 2004, **3**, 823–829.

[16] M. Vengris, M. A. van der Horst, G. Zgrablić, I. H. van Stokkum, S. Haacke, M. Chergui, K. J. Hellingwerf, R. van Grondelle and D. S. Larsen, *Biophys. J.*, 2004, **87**, 1848–1857.

[17] A. Espagne, P. Changenet-Barret, P. Plaza and M. M. Martin, *J. Phys. Chem. A*, 2006, **110**, 3393–3404.

[18] A. Espagne, D. H. Paik, P. Changenet-Barret, M. M. Martin and A. H. Zewail, *ChemPhysChem*, 2006, **7**, 1717–1726.

[19] E. C. Carroll, S.-H. Song, M. Kumauchi, I. H. M. van Stokkum, A. Jailaubekov, W. D. Hoff and D. S. Larsen, *J. Phys. Chem. Lett.*, 2010, **1**, 2793–2799.

[20] H. Chosrowjan, S. Taniguchi and F. Tanaka, *FEBS J.*, 2015, **282**, 3003–3015.

[21] M. Sauer, *Proc. Natl. Acad. Sci.*, 2005, **102**, 9433–9434.

[22] J. Boelke and S. Hecht, *Adv. Opt. Mater.*, 2019, **7**, 1900404.

[23] M. J. Fuchter, *J. Med. Chem.*, 2020, **63**, 11436–11447.

[24] A. Goulet-Hanssens, F. Eisenreich and S. Hecht, *Adv. Mater.*, 2020, **32**, 1905966.

[25] M. Mansø, A. U. Petersen, Z. Wang, P. Erhart, M. B. Nielsen and K. Moth-Poulsen, *Nat. Commun.*, 2018, **9**, 1945.

[26] J. Langeland, C. Kjær, L. H. Andersen and S. Brøndsted Nielsen, *ChemPhysChem*, 2018, **19**, 1686–1690.

[27] J. W. Park and Y. M. Rhee, *J. Am. Chem. Soc.*, 2016, **138**, 13619–13629.

[28] G. E. O. Borgstahl, D. R. Williams and E. D. Getzoff, *Biochemistry*, 1995, **34**, 6278–6287.

[29] K. Brejc, T. K. Sixma, P. A. Kitts, S. R. Kain, R. Y. Tsien, M. Ormo and S. J. Remington, *Proc. Natl. Acad. Sci.*, 1997, **94**, 2306–2311.

[30] S. Yamaguchi, H. Kamikubo, K. Kurihara, R. Kuroki, N. Niimura, N. Shimizu, Y. Yamazaki and M. Kataoka, *Proc. Natl. Acad. Sci.*, 2009, **106**, 440–444.

[31] P. J. Taenzler, K. Sadeghian and C. Ochsenfeld, *J. Chem. Theory Comput.*, 2016, **12**, 5170–5178.

[32] A. Xie, W. D. Hoff, A. R. Kroon and K. J. Hellingwerf, *Biochemistry*, 1996, **35**, 14671–14678.

[33] E. J. M. Leenders, L. Guidoni, U. Röthlisberger, J. Vreede, P. G. Bolhuis and E. J. Meijer, *J. Phys. Chem. B*, 2007, **111**, 3765–3773.

[34] S. Anderson, S. Crosson and K. Moffat, *Acta Crystallogr. D*, 2004, **60**, 1008–1016.

[35] P. Campomanes and S. Vanni, *Molecules*, 2021, **26**, 2025.

[36] R. Brudler, T. E. Meyer, U. K. Genick, S. Devanathan, T. T. Woo, D. P. Millar, K. Gerwert, M. A. Cusanovich, G. Tollin and E. D. Getzoff, *Biochemistry*, 2000, **39**, 13478–13486.

[37] A. F. Philip, K. T. Eisenman, G. A. Papadantonakis and W. D. Hoff, *Biochemistry*, 2008, **47**, 13800–13810.

[38] P. A. Sigala, M. A. Tsuchida and D. Herschlag, *Proc. Natl. Acad. Sci.*, 2009, **106**, 9232–9237.

[39] J. J. van Thor, G. Y. Georgiev, M. Towrie and J. T. Sage, *J. Biol. Chem.*, 2005, **280**, 33652–33659.

[40] S. J. Remington, *Protein Sci.*, 2011, **20**, 1509–1519.

[41] M. Irie, T. Fukaminato, K. Matsuda and S. Kobatake, *Chem. Rev.*, 2014, **114**, 12174–12277.

[42] C. Ritchie, G. Vamvounis, H. Soleimaninejad, T. A. Smith, E. J. Bieske and V. Dryza, *Phys. Chem. Chem. Phys.*, 2017, **19**, 19984–19991.

[43] W. Woodland, R. Lim, C. Motti, P. Irving, J. Wang, M. Payne, P. C. Junk and G. Vamvounis, *Aust. J. Chem.*, 2019, **72**, 874–880.

[44] K. Seo, I. Eom, S. Shim, C. H. Kim and T. Joo, *Bull. Korean Chem. Soc.*, 2019, **40**, 352–358.

[45] Y. Kim, J. A. Phillips, H. Liu, H. Kang and W. Tan, *Proc. Natl. Acad. Sci.*, 2009, **106**, 6489–6494.

[46] M. Reynders, A. Chaikuad, B.-T. Berger, K. Bauer, P. Koch, S. Laufer, S. Knapp and D. Trauner, *Angew. Chem. Int. Ed.*, 2021, **60**, 20178–20183.

[47] W. A. Velema, W. Szymanski and B. L. Feringa, *J. Am. Chem. Soc.*, 2014, **136**, 2178–2191.

[48] C. Matera, A. M. J. Gomila, N. Camarero, M. Libergoli, C. Soler and P. Gorostiza, *J. Am. Chem. Soc.*, 2018, **140**, 15764–15773.

[49] M. H. Stockett, M. Boesen, J. Houmøller and S. Brøndsted Nielsen, *Angew. Chem. Int. Ed.*, 2017, **56**, 3490–3495.

[50] J. N. Bull, E. Carrascosa, L. Giacomozzi, E. J. Bieske and M. H. Stockett, *Phys. Chem. Chem. Phys.*, 2018, **20**, 19672–19681.

[51] A. Espagne, D. H. Paik, P. Changenet-Barret, P. Plaza, M. M. Martin and A. H. Zewail, *Photochem. Photobiol. Sci.*, 2007, **6**, 780–787.

[52] P. R. Hania, R. Telesca, L. N. Lucas, A. Pugzlys, J. van Esch, B. L. Feringa, J. G. Snijders and K. Duppen, *J. Phys. Chem. A*, 2002, **106**, 8498–8507.

[53] S. Shim, T. Joo, S. C. Bae, K. S. Kim and E. Kim, *J. Phys. Chem. A*, 2003, **107**, 8106–8110.

[54] C. Yun, J. You, J. Kim, J. Huh and E. Kim, *J. Photochem. Photobiol. C Photochem. Rev.*, 2009, **10**, 111–129.

[55] Y. Ishibashi, T. Umesato, S. Kobatake, M. Irie and H. Miyasaka, *J. Phys. Chem. C*, 2012, **116**, 4862–4869.

[56] M. Murakami, H. Miyasaka, T. Okada, S. Kobatake and M. Irie, *J. Am. Chem. Soc.*, 2004, **126**, 14764–14772.

[57] K. Higashiguchi, K. Matsuda, Y. Asano, A. Murakami, S. Nakamura and M. Irie, *Eur. J. Org. Chem.*, 2005, **2005**, 91–97.

[58] T. Yamaguchi and M. Irie, *J. Mater. Chem*, 2006, **16**, 4690–4694.

[59] T. Sumi, Y. Takagi, A. Yagi, M. Morimoto and M. Irie, *Chem. Commun.*, 2014, **50**, 3928–3930.

[60] H. Sotome, K. Une, T. Nagasaka, S. Kobatake, M. Irie and H. Miyasaka, *J. Chem. Phys.*, 2020, **152**, 034301.

Chapter 2

Background to theory and computational methods

This chapter introduces background material on computational methods, potential energy surfaces, and reaction dynamics. These concepts are important for understanding this thesis because it explores molecular photochemistry using experimental and computational methods. The computational material covers selected background to, and basic principles of, various computational methods relevant to this thesis.
Separately, the topology of, and dynamics on, potential energy surfaces is introduced. Instead of describing reactions in one or two dimensions, as in transition state theory, photochemical reactions are typically described in three (Cartesian) dimensions, using potential energy surfaces. These can be determined from computations and are useful to corroborate or explain experimentally measured molecular dynamics.

2.1 Computational methods

2.1.1 The Hartree-Fock wavefunction and friends

Hartree-Fock (HF) theory forms the basis of most *ab initio* computational methods for treating multi-electron systems using wavefunction theory. HF theory makes use of an overarching approximation which assumes independent electron motion and averages individual electron-electron repulsions, where each electron interacts with a mean field created by the other electrons.[1,2] The framework expresses all electrons as a single configuration of spin orbitals (a single Slater determinant), thus creating a simpler one-electron problem. HF theory uses the Slater determinant as the wavefunction ansatz (trial wavefunction) and seeks to minimise the expectation value of the Hamiltonian operator by varying coefficients for the spin orbitals in the Slater determinant. The expectation value of the HF Hamiltonian is labelled as an approximate energy, E_{HF}.

The HF wavefunction can readily provide a wide range of properties, including dipole moments and electronic excitation energies, and reproduces the equilibrium molecular geometry *reasonably* well, for main-group chemical compounds.[3] For example, Güllüoğlu and co-workers[4] compared the structural parameters, obtained from geometry optimisations of piperidine using HF and the "bulk standard" density functional theory (DFT) method B3LYP, to electron diffraction data.[5] In general, B3LYP was shown to perform better than HF, although there were a few parameters, such as internal H-C-H bond angle, where both HF and B3LYP were within 3% of the experimental value (110.0°). Overall, however, HF is systematically less accurate than higher-level methods, such as Møller-Plesset perturbation theory or coupled-cluster, which have much smaller standard deviations (relative to experiment) in calculated bond distance (≈0.7–0.8 pm), compared with HF (≈2.2 pm).[6] As another example, over a series of 184 small molecules, Feller and Peterson[7] showed HF to exhibit the largest average absolute errors in bond lengths and angles over a series of methods (Table 2.1).[2,7]

Table 2.1: The average absolute errors in bond lengths (AH and AB) and angles (HAH), over 184 small molecules, obtained by different methods using the aug-cc-pVTZ basis set.[2]

	HF	**MP2**	**MP4**	**CCSD**	**CCSD(T)**
ΔAH / Å	0.014	0.011	0.007	0.009	0.009
ΔAB / Å	0.028	0.022	0.030	0.011	0.016
ΔHAH	1.6°	0.3°	0.3°	0.3°	0.4°

Another shortfall of HF theory is that it tends to overestimate the exact energy (E_{exact}). This is because both electron-electron correlation interactions and relativistic contributions are neglected, although the relativistic term only tends to be important for systems containing heavy atoms (those on the fourth row or heavier). For main-group compounds, the relation between the energy terms values is

$$E_{\text{corr}} = E_{\text{exact}} - E_{\text{HF}} \tag{2.1}$$

where E_{HF} and E_{exact} are the Hartree-Fock and exact energies of a given system, respectively, and the difference, E_{corr}, is the correlation energy. Although E_{corr} is typically only a few percent of E_{HF}, its absence can have a significant effect on the computed molecular properties. In modern computational chemistry methods, the correlation energy term

can conceptually be divided into two contributors: static and dynamical correlation – $E_{\text{corr}} = E_{\text{stat}} + E_{\text{dyn}}$. However, the distinction between these two terms is not as well defined for highly-correlated multi-reference methods, such as near full configuration interaction (FCI) wavefunctions. Single-reference methods, including configuration interaction (CI) and coupled-cluster (CC), use a single Slater determinant, in the form of a HF self-consistent field (SCF) wavefunction, as the starting reference state.[8] Conversely, multi-reference (MR) methods start with a multiconfigurational self-consistent field (MCSCF) determinant, which is used as the reference from which excitations are generated. Examples of such methods include the multi-reference configuration interaction (MRCI) and coupled-cluster (MRCC) methods.[9] MR methods are designed to treat systems that are poorly described by a single Slater determinant, such as open-shell molecules or excited states.[10,11]

Consider the HF wavefunction, which can be represented by a single Slater determinant. Numerous types of many-electron systems are poorly represented by this single determinant due to (near-)degenerate orbitals. Near-degenerate orbitals will contribute to determinants of similar weighting, in which case there is no one dominant determinant. More generally, HF theory is not sufficiently flexible for systems containing degeneracies, as one determinant does not provide a satisfactory description of the system.[12] This is the first source of E_{corr}, termed the static correlation. This situation becomes particularly important for excited states, where electrons are excited to anti-bonding states, leading to singly-occupied orbitals. Furthermore, the HF wavefunction approximates an average field due to electron-electron interaction where all electrons move independently. In a multi-electron system, electron motion is correlated, where the motion of one electron influences the motion of other electrons. The net result is the HF procedure overestimates electron repulsion energies. The absence of correlated electron motion is the second source of E_{corr}, termed the dynamic correlation, because it relates to electron dynamics.[12,13] Correlation energies are important for any wavefunction method.

2.1.1.1 Post-Hartree-Fock methods

The configuration interaction (CI) wavefunction is a step towards accounting for the correlation energy (E_{corr}). The CI wavefunction is constructed from a linear combination of Slater determinants and improves on the HF wavefunction by mixing different excited configurations, essentially replacing one (or more) occupied orbitals with virtual

orbitals.[1,3] For most closed-shell molecules, the CI wavefunction has one dominant configuration and smaller contributions from other configurations.[14] In a simple example, consider H_2 in a minimal basis with two 1s orbitals (φ_1 and φ_2). As shown in Figure 2.1, along with the ground-state wavefunction, two singly- and one doubly-excited determinant can also form part of the CI wavefunction. Depending on which determinants are included in the CI calculation, the wavefunction is either described as *full* or *truncated*.

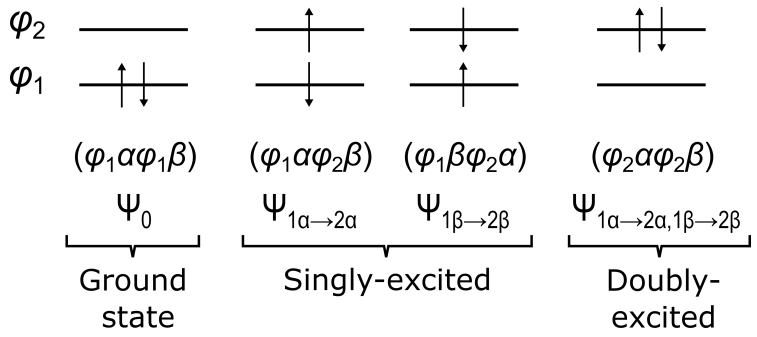


Figure 2.1: The ground-state, singly-, and doubly-excited determinants, with respective configurations, for H_2 in a minimal basis with two 1s orbitals (φ_1 and φ_2). α and β represent the two electron spins.

Using the determinants from Figure 2.1, a singlet (*i.e.* singlet spin state) full-CI (FCI) wavefunction can be constructed. All singlet determinants are included, *i.e.* all possible singlet distributions of the electrons over the available orbitals.

$$\Psi_{\mathrm{CI}} = C_0\Psi_0 + C_{1\to 2}\left(\frac{1}{\sqrt{2}}(\Psi_{1\beta\to 2\beta} - \Psi_{1\alpha\to 2\alpha}) + (\Psi_{1\beta\to 2\beta,1\alpha\to 2\alpha})\right) \tag{2.2}$$

This can be written in the general form

$$\Psi_{\mathrm{CI}} = C_0\Psi_0 + \sum_{I=1}^{L} C_I\Psi_I \tag{2.3}$$

where Ψ is a wavefunction, C is an expansion coefficient for a particular state wavefunction, and L is the number of excited configurations.

In principle, solving the FCI wavefunction for a molecular system provides energies nearing those obtained from solving the Schrödinger equation, particularly with a near-complete basis set. However, in practice, constructing the FCI wavefunction is not feasible for larger molecules (*e.g.* those with five atoms or more), as the number of

Slater determinants has a factorial dependence on the number of orbitals and electrons in a particular system.[3,12] By using a truncated-CI wavefunction, which only includes determinants for a particular family of excited configurations, the computational expense is decreased. A common CI truncation method is CI singles and doubles (CISD). Continuing the example of H_2, the singlet *singly-excited* CI (known as configuration interaction singles, CIS) wavefunction takes the form

$$\Psi_{\mathrm{CIS}} = C_0\Psi_0 + C_{1\to 2}\left(\frac{1}{\sqrt{2}}(\Psi_{1\beta\to 2\beta} - \Psi_{1\alpha\to 2\alpha})\right) \tag{2.4}$$

CIS is the simplest CI wavefunction that can be constructed for a given molecule. This is commonly used as the initial guess wavefunction for more sophisticated excited state theories. For the vast majority of systems, only the valence orbitals and the low energy virtual orbitals (the orbitals around the highest-occupied and lowest-unoccupied molecular orbitals, respectively) are important. In a FCI calculation, all configurations are considered important, including higher energy virtual orbitals that have no chemical significance. As a result, excluding these has little effect on the level of electron correlation, allowing truncated-CI wavefunctions to maintain the level of electron correlation accounted for in FCI.[14] However, truncated-CI calculations have some important limitations. To outline these limitations, two terms must be defined which, unfortunately, are often used interchangeably in the literature – *size-consistency* and *size-extensivity*.

Size-consistency requires that the sum of the energies of two subsystems (A and B) at infinite separation is the same as the energy of the overall system – $E_{\mathrm{AB}} = E_{\mathrm{A}} + E_{\mathrm{B}}$. This requires correct description of the dissociation curve for the AB system.
Size-extensivity applies at any geometry and requires that the calculated energy scales linearly with the number of particles in a system.[15]

The main limitations of truncated-CI wavefunctions are that they are neither size-consistent nor size-extensive. The extent to which this is important depends on the degree of truncation and neglect of orbitals involved in the molecular property/reaction. The full-CI wavefunction, on the other hand, is both size-extensive and size-consistent, as are some other excited state theories, such as EOM-CC, which are generally preferred over CI analogues. Since FCI is computationally too expensive for most systems, and truncated-CI wavefunctions suffer from a lack of size-consistency and -extensivity, other methods are needed that provide a balance between these two cases.

2.1.2 Coupled-cluster methods

Coupled-cluster methods go some way to achieving a desirable cost *versus* accuracy balance. Unlike CI, CC methods are size consistent and use an HF self-consistent field (SCF) wavefunction as the reference state. CC theory is considered to provide a highly accurate approach to electronic-structure calculations,[16] primarily for smaller molecules (see Table 2.1).[17] Moreover, CC rigorously describes dynamic correlation.[18] It is important to note that CC methods are most effectively used on ground state systems near their equilibrium geometry, as the corresponding electronic states are dominated by a single determinant.[11,18] CC methods are typically seen in the truncated forms, for example CCSD (coupled-cluster singles and doubles) and CCSD(T) (CCSD with perturbative triples). CCSD includes predominantly single and double excitations (singles and doubles, respectively), as well as some special non-connected triples. CCSD and CCSD(T) scale by N^6 and N^7, respectively, where N is the number of basis functions.[8] The more excitation terms included, the greater the computation cost, but the closer the result is to the FCI limit.[16]

A limitation of CC methods is the difficulty in describing excited states and geometries close to bond dissociation limits, since the electronics states are no longer dominated by a single determinant. Fortunately, instead of having to turn to the more cumbersome multi-reference methods, excited state calculations can be performed using the equation-of-motion coupled-cluster (EOM-CC) methods. EOM-CC generates an excited state wavefunction from a CC reference state (typically a closed shell state, such as the ground state).[10,11] An advantage of EOM-CC is that it is able to describe both static and dynamic correlation. This method is also favourable over multi-reference methods, because it is able to describe the excited states using a simpler single-reference approach. Furthermore, the EOM-CCSD (singles and doubles CC truncation) method has an N^6 computational scaling, equivalent to that of CISD and CCSD methods.[10]

The CC2 formalism was developed as a more efficient single-reference approach to excited state calculations than EOM-CCSD and works on the basis of approximating EOM-CCSD.[19] Unfortunately, CC2 retains a high computational cost (N^5 scaling),[20] limiting this method to systems containing fewer than ≈500 basis functions in C_1 symmetry.[21] A computationally cheaper alternative to CC2 is its density-fitted cousin (density-fitted second-order approximate coupled cluster singles and doubles, df-CC2), sometimes called resolution of identity (RI) CC2. This method has N^2 scaling,[21,22] enabling more efficient computation of excitation energies for molecules containing up to 100 atoms.[23]

However, given that the perturbative approximation to EOM-CCSD in CC2 is not deemed particularly robust, alternative methods have been developed to further improve on the EOM-CC approach.[24] One example is similarity transformed (ST)EOM which, unlike EOM-CC, includes triple excitation (triples) effects. As a result, STEOM is charge-transfer separable and is thus able to treat charge transfer states more accurately than EOM-CC.[25,26] Moreover, this enables STEOM to outperform CC2 consistently, especially in single-point energy calculations of closed-shell molecules.[27]

A useful addition to STEOM is the domain-based local pair natural orbital (DLPNO) formalism.[19,28] The result is an approach to excited state calculations that have a similar computational cost and scaling to time-dependent DFT (TD-DFT) but, unlike TD-DFT, retains the ability to describe charge transfer states well.[24] A particular triumph of the DLPNO-STEOM approach is its ability to compute excitation energies of molecules containing up to 100 atoms, or as many as 2500 basis functions, while other excited state methods, such as CC2, applied to such large systems are prohibitively expensive.[19] Both DLPNO-STEOM and df-CC2 methods are used in this thesis.

2.1.3 CASSCF theory

CASSCF is a class of multi-configurational self-consistent field (MCSCF) method. In some literature, CASSCF is called FORS (fully-optimised reaction space). These are not "black-box" methods, since some *a priori* knowledge of the system is necessary to create the calculation input and to interpret the output meaningfully. Instead of solving for all possible Slater determinants in the wavefunction for a particular system, as in a full-CI calculation, only those for a limited set of orbitals and electrons are included.[12] This constitutes the 'complete active space', where m electrons are distributed over n orbitals, denoted as an (m,n) active space (Figure 2.2).

The 'active space' usually contains the orbitals most relevant to a particular chemical process. For example, orbitals involved in bond making/breaking, or the π-orbitals important to an electronic excitation. The relevant orbitals can often be inferred from a series of CIS calculations along the reaction coordinate. The complete set of Slater determinants, representing all the possible distributions of active electrons over active orbitals, are treated with a full-CI wavefunction approach. The remaining doubly-occupied orbitals are defined as the 'inactive space' (or the frozen core) and are treated

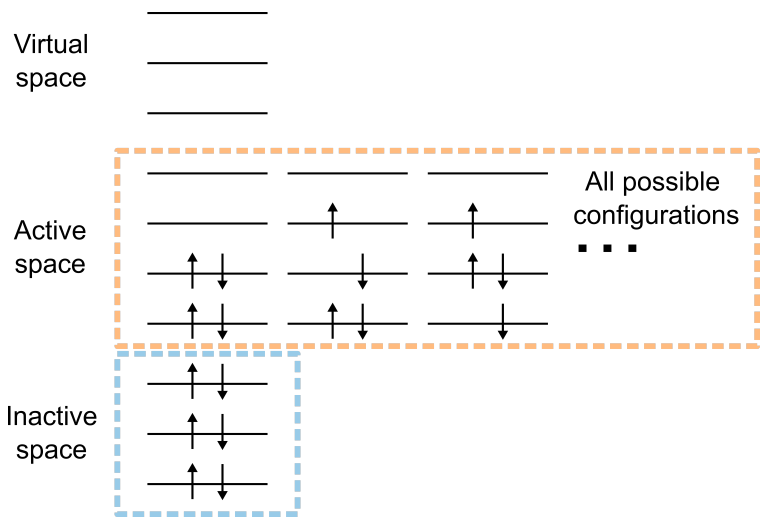


Figure 2.2: Schematic representation of a CASSCF(4,4) active space. Doubly-occupied orbitals make up the inactive space. The active space contains the orbitals of interest, and the virtual space is omitted from the calculation. All possible electron configurations over the active space orbitals are included in the CASSCF wavefunction. CASSCF calculations essentially treat the active space with a FCI wavefunction.

by mean-field methods. The remaining unoccupied orbitals are defined as the 'virtual space' and are omitted from the calculation. An appropriate choice of active space is needed to describe important excitations, for example, orbitals contributing the single- and double-bond rotations must be included for an $E \rightarrow Z$ photoisomerisation process.[3,12] In general, orbitals involved in the chemical process under study should be included in the active space. An (18,18) active space is nearing the upper limit of the capabilities of modern computing systems.[29]

By only applying the FCI treatment to the limited active space and applying a simple treatment to the frozen core, the computational cost of the CASSCF calculation is significantly lower compared to that of a FCI calculation. The framework also ensures a full set of excitations is treated within the active space, thus achieving a size-consistent and size-extensive method, but where FCI is applied only to the most important orbitals for a particular chemical process.[12,30]

As with every computational method, CASSCF involves approximations. Computational cost increases significantly with increasing size of active space, since there is a factorial scaling with respect to the number of orbitals in the active space.[12,13] Moreover, while static electron correlation is included,[14] much of the dynamic electron correlation

is not (static and dynamic correlation defined in Section 2.1.1). Incorporation of additional perturbations, such as complete active space second-order perturbation theory (CASPT2) or the closely-related variant XMCQDPT2, is necessary to account for the latter correlation.[12]

CASSCF offers several advantages over single-reference methods, such as HF or CI. Firstly, CASSCF is suited to describe bond dissociation/breaking and making processes, and is often used to compute the potential energy surface (PES) of a chemical reaction, although this does rely on a judicious choice of active space.[30,31] Secondly, it is a flexible method and allows for a single framework to be applied to the study of both ground and excited states.[3,30] Finally, CASSCF can achieve good results even when only accounting for static correlation, arising because of (near-)degenerate configurations in the active space.[3,12]

2.1.4 Density functional theory

Density functional theory (DFT) is based on the Hohenberg-Kohn and Kohn-Sham theorems. The Hohenberg-Kohn theorem states that the electronic energy of a ground state is determined by the molecular electron probability density ($\rho(\mathbf{r})$) of said ground state, *i.e.* instead of calculating molecular energy from the molecular wavefunction, as in HF theory, the molecular energy is calculated from ρ.[2] From this, the Kohn-Sham equations introduce orbitals to DFT, for which a Slater determinant represents the wavefunction of the optimised orbitals. Total DFT energy is expressed as

$$E_{\mathrm{DFT}}[\rho] = T_{\mathrm{S}}[\rho] + E_{\mathrm{en}}[\rho] + J[\rho] + E_{\mathrm{xc}}[\rho] \tag{2.5}$$

where $T_{\mathrm{S}}[\rho]$ is the kinetic energy calculated from a Slater determinant, $E_{\mathrm{en}}[\rho]$ is the attractive potential energy (between electrons and nuclei), $J[\rho]$ is the repulsive potential energy (between electrons), and $E_{\mathrm{xc}}[\rho]$ is the exchange-correlation term. The latter term compensates for differences between the exact and theoretical kinetic and interaction energies

$$E_{\mathrm{xc}}[\rho] = (T[\rho] - T_{\mathrm{S}}[\rho]) + (E_{\mathrm{ee}}[\rho] - J[\rho]) \tag{2.6}$$

where $T[\rho]$ is the exact kinetic energy and $E_{\mathrm{ee}}[\rho]$ is the exact (classical) electron-electron interaction energy.[32] By avoiding calculation of the molecular wavefunction, overall computational expense is decreased, compared with HF. This is because the HF wavefunction

contains $3N$ coordinates (where N is the number of interacting electrons), thus causing a rapid increase in computational cost with increasing N. Conversely, DFT is feasibly applicable to larger systems as it only requires three spatial coordinates to define ρ, making DFT independent of system size.[33,34] It should be noted that most DFT calculations start with a HF calculation to provide the initial orbital guess from which ρ is obtained. DFT accuracy and efficiency is highly dependent on the quality of the basis set and functionals, particularly the E_{xc} term.[34] The various generations of DFT, which contain various approximations to the exchange-correlation functional, are categorised into a hierarchy – a Jacob's ladder (Figure 2.3).[35]

A commonly used DFT method, particularly popular in the late-20th and early-21st centuries, is the B3LYP hybrid functional;[36–40] however, more sophisticated methods now supersede B3LYP, such as ωB97X-D – able to account for long-range dispersion

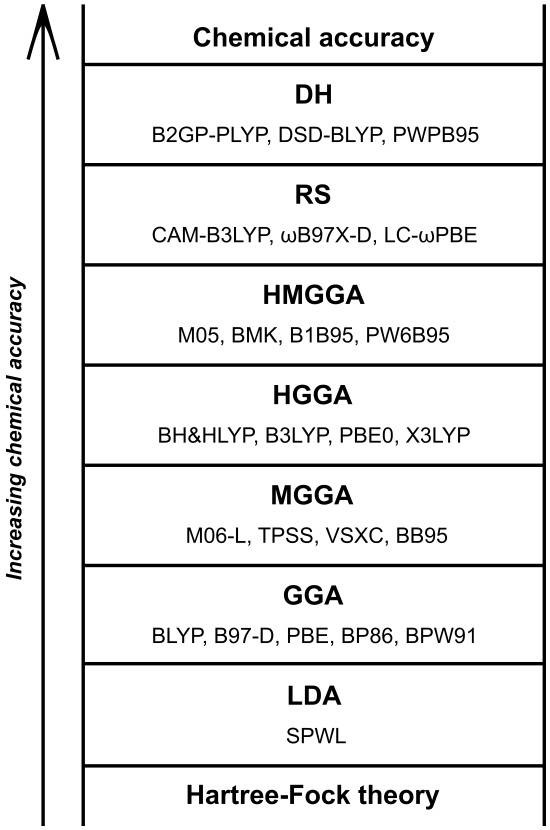


Figure 2.3: Jacob's Ladder with examples of DFT methods on each rung. LDA = local density approximation, GGA = generalised gradient approximation, MGGA = meta-GGA, HGGA = hybrid-GGA, HMGGA = hybrid meta-GGA, RS = range-separated, DH = double hybrid.

corrections for excited state properties. ωB97X-D is discussed here as it has been used for the work discussed in this thesis. Long-range interactions are particularly important when investigating systems containing significant non-covalent interactions, such as hydrogen bonds.[41] This is demonstrated in a recent study by Kozłowska *et al.*[42] on hydrogen-bonded complexes, where ωB97X-D consistently outperformed B3LYP, and other DFT methods. Furthermore, benchmarking studies have shown that, although B3LYP does provide comparatively accurate structural parameters, ωB97X-D performs significantly better for computing chemical properties.[43]

2.1.5 Semi-empirical methods

While *ab initio* HF-based methods are powerful, they do have a limit on the size of molecule they can practically address. One solution is through the use of the comparatively cheap semi-empirical methods. Such methods are based on HF equations, but contain additional approximations, which reduce the computational expense. The approximations involve neglecting some integrals and treating the remainder in one of two ways – either computed exactly or computed from experimental parameters (empirical data). As a result, the predictive accuracy of the method is often reasonable (particularly for geometries).

There are a variety of semi-empirical methods, each offering slightly different approximations.[12] One such family are the parameterised models, in which the parameterisation is geared more towards correctly treating the geometry of hydrogen-bonded complexes, compared with other semi-empirical methods.[44] A commonly used method is the parameterised model 6 (PM6), which contains 70 parameterised elements and is able to predict geometries more accurately than its forerunners.[45] However, PM6, like other semi-empirical methods, fails to describe non-covalent interactions (including hydrogen-bonding) accurately, substantially underestimating the true interaction strength.[44] Semi-empirical methods are useful for exploratory calculations (*e.g.* exploring conformations) before performing accurate calculations, as they require only approximately 5% of the time a HF calculation would take.

2.1.6 Comparison of common computational methods

When considering any computational method, there is a balance between the accuracy of the results and the expense of the computation (Figure 2.4). The scope of some methods,

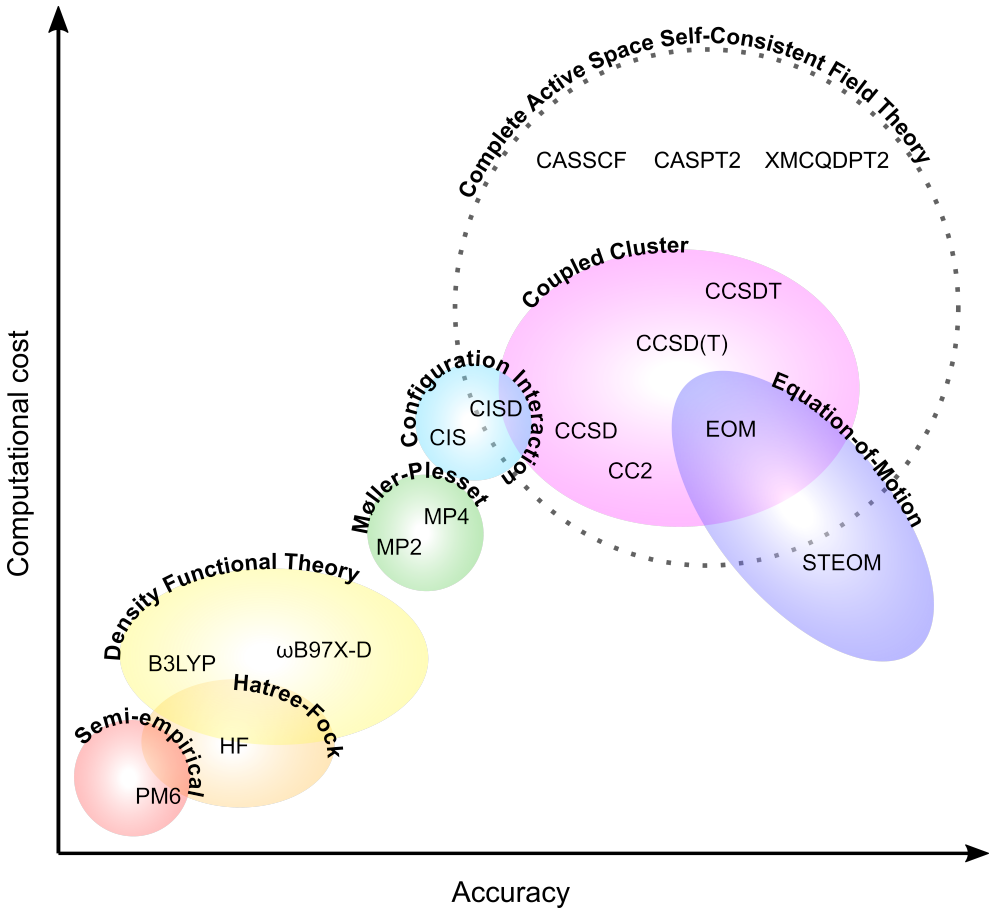


Figure 2.4: Graphical representation of the approximate computational cost and accuracy of a selection of common quantum chemical methods.

such as the use of active space in CASSCF, creates a plethora of method subsets with varying accuracies and costs. For example, for thio-*para*-coumaric acid, CASSCF(6,6) is inadequate to describe orbital ordering and shape, while CASSCF(12,11) more accurately describes orbital shapes, but is computationally significantly more expensive.[31] The choice of method depends on the specific requirements of a particular investigation.

2.2 Potential energy surfaces and reaction dynamics

A potential energy surface is essentially a multidimensional map of the inter-atomic forces that govern a chemical reaction and atomic motion. All reactions (unimolecular, bimolecular, *etc.*) can be represented by a potential energy surface (PES); however, the topology depends on the reaction type. The concept of potential energy surfaces arises

from the Born-Oppenheimer approximation, which assumes that nuclear and electronic motion can be treated separately.[46] This assumption stems from the relative masses of nuclei and electrons – the heavy nuclei are effectively stationary in relation to electron motion. PESs are an important concept for explaining reaction dynamics, in both thermo- and photochemical reactions. While thermochemical reactions occur on the ground state, relying on transition states, photochemical reactions are excited state processes, involving both conical intersections and transition states. It is important to note that it is extremely complex to compute robust potential energy surfaces, in part due to their multidimensionality. The following sub-sections describe some important topologies of potential energy surfaces.

2.2.1 Photochemistry

Thermochemical processes can be often described by transition state theory (TST), which describes reactions in terms of a ground-state potential energy surface (PES) containing wells and saddle points (transition states, $TS^{\ddagger}$). Transition states are effectively unstable intermediates along a ground-state reaction coordinate. Conversely, photochemical processes occur over both ground- and excited-state potential energy surfaces. As a result, both transition states and conical intersections dictate the reaction outcome. For example, in $E \rightarrow Z$ photoisomerisation of *para*-coumaric acid and $p\mathrm{CK}^{-}$, there is a barrier on the excited state between the Franck-Condon geometry and a twisted minimum, which is close to a conical intersection.[47] Just as transition states connect reactants and products over multiple possible pathways on the ground-state PES, conical intersections connect reactants and products *via* multiple pathways from the excited to the ground state.

2.2.1.1 Crossing potential energy surfaces

First described as 'crossing points',[48] then as 'funnels'[49] and 'allowed crossings',[50] conical intersections (CIs) are a key mechanistic component of photochemical reactions.
In 1937, Teller[48] demonstrated a key feature of these crossing points on potential energy surfaces – that they facilitate rapid, radiationless decay, and are thus important for non-adiabatic processes.[51] Teller also suggested a special type of "conical crossing" would exist for polyatomic molecules (molecules containing more than two atoms), which would have a high transition probability.[48] Although such conical intersections had been suggested, the prevailing opinion up to the early 1990s was that they were

rare and, if they did occur, that the crossing would be 'avoided'.[49] Confirmation of the presence of conical intersections in a vast number of photochemical processes was made possible through the advent of ultrafast (femtosecond) spectroscopic techniques, pioneered in significant part by Zewail.[52,53] Experiments on isolated systems have broadly shown sub-picosecond excited-state lifetimes, significantly faster than predicted from an avoided crossing and consistent with the intersection of two electronic states – a conical intersection.[46]

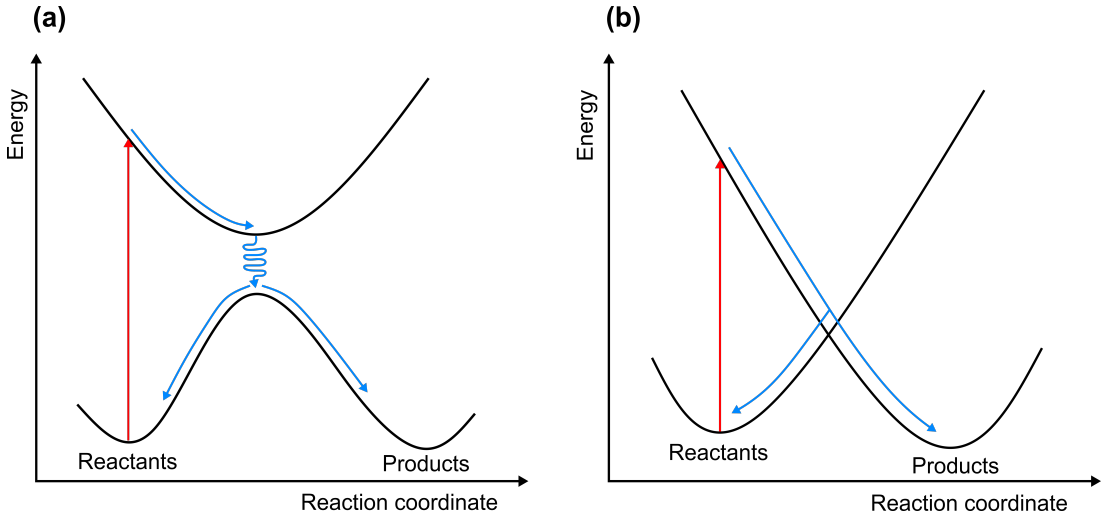


Figure 2.5: Potential energy diagrams of **(a)** an avoided crossing, and **(b)** a conical intersection. The red arrow indicates excitation of the reactants, resulting in promotion to the excited state. The blue arrows indicate the respective relaxation pathways.

As suggested by the name, avoided crossings describe potential energy surfaces of near-degenerate electronic states that do not intersect. These arise due to the non-crossing rule, as described by Winger and von Neumann.[54] This rule states that the surfaces of two electronic states with the same symmetry cannot and will not cross, but that this principle does not apply on ultrafast timescales.[54,55] Thus, the non-crossing rule applies particularly to steady states[55] and diatomics,[56] whose single degree of freedom is insufficient to allow an intersection. On the other hand, polyatomics have significantly more internal degrees of freedom. In these cases, the non-crossing rule breaks down, allowing the intersection of electronic states of the same symmetry. Furthermore, large systems tend to have low (C_1 or C_s) symmetry, which reduces the possible symmetries available for the electronic states to one (A) and two (A′ or A″), respectively. This is important for *same-symmetry* CIs, as these describe the intersections of electronic states with the same, rather than different (*symmetry-allowed* CI), symmetry.[57] Moreover, a large

molecule of C_s point group can easily reach a C_1 geometry through vibrations causing slight changes in bonds.

In electronic structure theory, a conical intersection search involves finding the lowest energy on the intersection "seam" of two electronic potential energy surfaces of the same spin and space symmetry. In contrast, optimisation to a minimum energy crossing point (MECP) involves searching for the lowest energy geometry on the intersection "seam" of two different electronic potential energy surfaces, where the two surfaces differ by either space or spin symmetry. MECPs are important for processes such as spin-orbit coupling and intersystem crossing.

2.2.1.2 Conical intersection topologies

Conical intersections, formed by the intersections of electronic states, are typically interpreted as having two limiting topologies – *peaked* or *sloped* (Figure 2.6). Peaked CIs

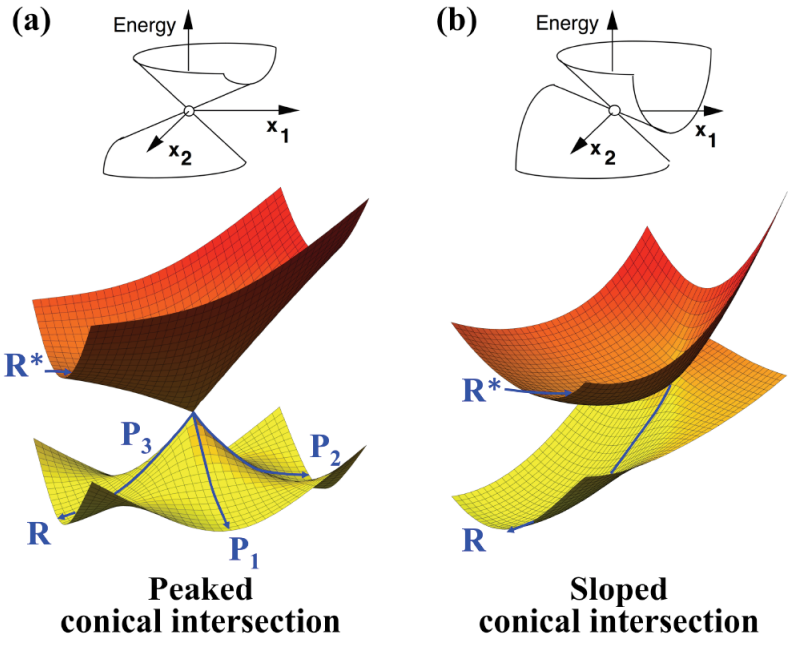


Figure 2.6: The two main forms conical intersections can take: **(a)** Peaked and **(b)** sloped. For a peaked CI, relaxation from the excited (R*) to the ground state results in various potential products (P_n) and the original reactant (R). Relaxation to the ground state *via* a sloped CI only returns the original reactant. Adapted from Boggio-Pasqua.[56]

can be described as two opposing cones sharing a common tip, where there is more than one relaxation pathway to the ground state, resulting in a variety of potential products (*e.g.* products P_1, P_2, P_3 in Figure 2.6). On the other hand, sloped CIs occur when the intersecting surfaces have the same gradient direction, conducive to single product formation. The PES topology in the intersection area dictates the possible relaxation pathways to the ground state. For example, the PES in Figure 2.6(b) would facilitate fast and efficient reactant recovery, but would be unlikely to yield product formation.[56] The situation depicted in Figure 2.6 represents a simplified picture of the PES for a molecule or reaction. Potential energy surfaces are complex constructs with high dimensionality ($3N - 6$ coordinates, where N is the number of atoms in a molecule). Where electronic states cross, the PES displays intersection *seams* (Figure 2.7(a)), which have $N_i - 2$ dimensionality (where N_i is the number of internal degrees of freedom).

In the context of photochemistry/excited state dynamics, conical intersections on a PES act as funnels, directing the excited reactants through the crossing point or seam to the ground state.[56,58] Due to the high dimensionality of PESs, it is possible to travel along and through that funnel following a large variety of paths, *i.e.* a seam of geometries. These different trajectories determine both the relaxation pathway an excited reactant follows and where along the seam the molecule will return to the ground state. This,

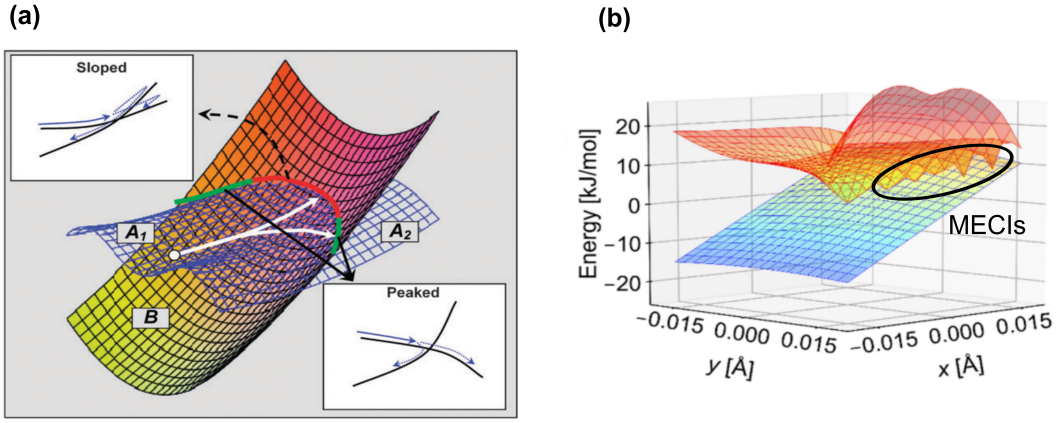


Figure 2.7: Diagrams of **(a)** a generic seam conical intersection between states A and B, adapted from Asturiol *et al.*[59] and **(b)** the S_0/S_1 minimum energy conical intersections (MECIs) of benzene, adapted from Harabuchi *et al.*[60] Panel **(a)** shows sloped and peaked intersection segments (red and green, respectively), and indicates two potential trajectories (white arrows) of an excited reactant.

in turn, dictates the branching ratio of, for example, two photoisomers. Quantitatively, this branching ratio for isomerisation corresponds to the quantum yield of the photochemical process.

The intersection seams are a continuum of conical intersection points; it is not realistic to describe every geometry potentially important to the photochemical reaction mechanism.[46] Instead, minimum energy points along the seam are characterised (Figure 2.7(b)), leading to the minimum energy conical intersections (MECIs), which are described as analogous to ground-state transition states. In the same way transition state geometries define a thermal reaction mechanism, the geometries of MECIs aid the description of a photochemical reaction mechanism.[46,58]

2.2.1.3 Dynamics in isolation and in solution

Photochemical processes occurring in the gas phase (in isolation) and in solution often have distinct dynamics. In the gas phase, the molecule of interest is studied in a vacuum, where it may exist under spatial or temporal isolation conditions (no interactions before detection or probing). In solution, the compound of interest is surrounded by, and constantly interacts with, many solvent molecules. Energy transfer to solvent usually occurs on the picosecond timescale, altering the internal energy distribution during the course of a reaction.

At room temperature ($T \approx 300\,\mathrm{K}$), a typical molecular ensemble will have a Boltzmann distribution of thermal energies, $k_\mathrm{B}T$, where k_B is the Boltzmann constant and T is temperature. A Boltzmann distribution describes the equilibrium probability distribution of molecular energies in a system at a given temperature. At $T \approx 300\,\mathrm{K}$, molecules will have some degree of vibrational excitation. Upon photoexcitation, the vibrational excitation will be retained in the nascent electronic excited state, as photoexcitation is very fast compared with intramolecular vibrational redistribution (IVR). However, usually only the lowest vibrational level ($v = 0$) of each electronic energy level will be populated because, for most molecules, the energy different between vibrational energy levels is greater than $k_\mathrm{B}T$.

In a vertical excitation, vibrational modes are populated according to the Franck-Condon principle,[61] but this may also include some Herzberg-Teller vibrational modes when vibronic coupling is important,[62] *e.g.* in many aromatic molecules. Forces on the excited-

state PES now direct the reaction trajectory. In many instances, the trajectory can be influenced through vibrational energy, which may come about from the vibrational modes accessed in the excitation, or because of initial thermal vibrational energy of the molecule. If the combination of the trajectory due to potential energy surface forces and vibrational energy are conducive to access the conical intersection (CI) seam geometry, the excited state lifetime will be short. On the other hand, if the intersection is inaccessible (*e.g.* because of a barrier on the excited-state PES) the excited state will survive longer.

In the gas phase, the main competing pathway to internal conversion is intramolecular vibrational redistribution (IVR). This relates to the picosecond-timescale redistribution of energy between vibrational modes of a particular electronic state, due to coupling of vibrational modes, occurring independently of collisions.[63] If the initial photoexcitation energy input does not result in a favourable trajectory towards the CI, IVR can cause redistribution of the input energy into the correct modes, shortening excited state lifetime. On the other hand, IVR can also result in longer-lived excited states, when the energy from the CI trajectory is redistributed to other (less favourable) modes. Thus, the time taken to reach the CI is protracted, particularly if there is a barrier to reach the intersection. Whereas in gases IVR is the main competing process to motion towards a CI, in solution, this competition is further complicated by the presence of the solvent. Not only is there IVR, but energy is also transferred from the excited species to solvent molecules by intermolecular vibrational energy redistribution/relaxation (IVER). This loss of vibrational energy can result in significantly longer excited state lifetimes, compared with the gas phase (Table 2.2). To further complicate matters, solvation can change the topology of the reaction PES, for example, due to stabilising interactions between the solvent and the species of interest.

Table 2.2: Photoisomerisation lifetimes of two related retinoids, *trans* retinal protonated Schiff base (*trans*-RPSB) and deprotonated *trans*-retinoic acid (*trans*-RA^-), in isolation (τ_g) and in methanol (τ_{MeOH}). Lifetimes (note the different units) were obtained by QM/MM simulations and femtosecond experiments for *trans*-RPSB and *trans*-retinoic acid, respectively.[64–66]

Species	τ_g / **fs**	τ_{MeOH} / **ps**	**Ref.**
trans-RPSB	257 ± 25	2.78 ± 0.36	64
trans-RA^-	180 ± 10	1.3 ± 0.2	65,66

As an example of the impact of solvation, literature data for $E \rightarrow Z$ photoisomerising retinoids is examined. The difference in excited state (photoisomerisation) lifetime in gas phase and solution environments is clearly identifiable (Table 2.2). Punwong *et al.*[64] performed large-scale quantum mechanics/molecular mechanics (QM/MM) simulations to ascertain the non-adiabatic dynamics of a truncated analogue of *trans*-retinal protonated Schiff base (*trans*-RPSB), revealing a significant difference between the photoisomerisation lifetimes of *trans*-RPSB in isolation and in methanol. A related species, deprotonated *trans*-retinoic acid (*trans*-RA^-), has been studied in the gas phase[65] and in solution,[66] using femtosecond methods, to elucidate on the excited state dynamics. The resulting experimental data confirm the accuracy of the simulation, as the photoisomerisation lifetimes from the *trans*-RPSB simulation are of the same order of magnitude and timescale as the corresponding experimental values for *trans*-RA^-. In solution, the isomerisation lifetime could be varied by over an order of magnitude by changing the solvent.

2.2.1.4 Surface topology and dynamics

While solvation can modify the PES topology, it is important to consider the inherent topological features of a surface. Any potential energy surface will exhibit peaks and troughs, since the energy of a molecule changes along a reaction coordinate, due to changes in geometry. Such features play a significant role in determining a reaction mechanism, since, for example, barriers on the ground and/or excited states will effect the pathway by which a particular photochemical reaction may proceed.

Consider, for instance, a molecule with a C=C double bond about which it can isomerise. If there is a large barrier to isomerisation on the ground state, the molecule will not thermally isomerise. On excitation to a barrierless excited state, the ground-state barrier to isomerisation can be overcome (Figure 2.8(a)). In this case, motion towards a conical intersection is not heavily reliant on having sufficient vibrational energy in the right vibrational modes (*e.g.* $Z \rightarrow E$ isomerisation of stilbene). However, if there is a barrier along the required reaction coordinate on the excited state, two requirements must be fulfilled to overcome it: (1) internal energy after excitation must exceed the barrier height and (2) vibrational motion must be in the correct modes to allow motion over the barrier (Figure 2.8(b)). These conditions are affected by (1) the total internal energy before and after excitation and (2) the rate of IVR, respectively. Should the molecule's total internal energy be less than the height of the barrier, the barrier cannot be crossed

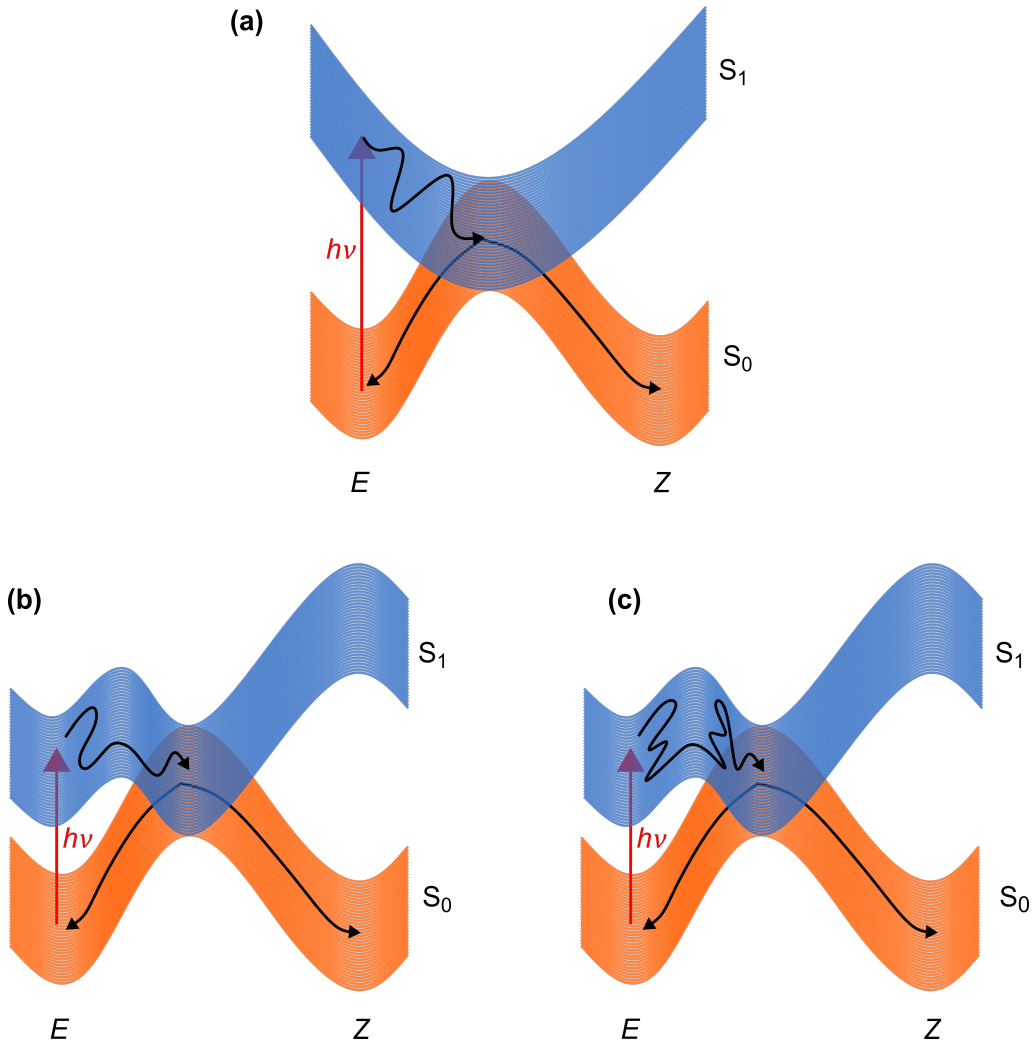


Figure 2.8: Generic potential energy surfaces depicting photochemical processes to overcome a ground-state (S_0) barrier to thermal isomerisation, where the sum of $h\nu$ and the initial internal vibrational energy exceeds the excited-state barrier height. Panel **(a)** describes motion along a barrierless excited state (S_1) to a conical intersection, while **(b)** and **(c)** represent potential motion along an excited state with a barrier. A molecule with vibrational energy distributed in **(b)** favourable modes will reach a conical intersection faster than when **(c)** the rate of IVR is fast and redistributes vibrational energy into modes less favourable for crossing the excited state barrier and reaching the conical intersection.

(except through tunnelling), regardless of whether the necessary vibrational modes are in motion. Once the energy of the incoming photon is sufficiently high, the molecule's internal energy will surpass the barrier height, thus allowing barrier crossing. If the rate of

IVR is particularly fast, then vibrational motion will be redistributed amongst the many molecular vibrational modes, potentially taking energy away from the modes possessing the correct coordinates to allow barrier crossing (Figure 2.8(c)). Generally, intramolecular redistribution/relaxation processes occur over the 1–10 ps timescale, which is slow compared with vibrational periods (typically a few hundreds of femtoseconds).[63,67] The example in this work is $E \rightarrow Z$ isomerisation of $p\mathrm{CK}^-$.

References

[1] A. S. Neil S. Ostlund, *Modern Quantum Chemistry: Introduction to Advanced Electronic Structure Theory*, Dover Publications Inc., 1996.

[2] I. N. Levine, *Quantum Chemistry*, Prentice Hall, 2000.

[3] T. Helgaker, P. Jørgensen and J. Olsen, *Molecular Electronic-Structure Theory*, Wiley, 2000.

[4] M. T. Güllüoğlu, Y. Erdoğdu and Ş. Yurdakul, *J. Mol. Struct.*, 2007, **834-836**, 540–547.

[5] G. Gundersen and D. W. H. Rankin, *Acta Chem. Scand.*, 1983, **37a**, 865–874.

[6] T. Helgaker, J. Gauss, P. Jørgensen and J. Olsen, *J. Chem. Phys.*, 1997, **106**, 6430–6440.

[7] D. Feller and K. A. Peterson, *J. Chem. Phys.*, 1998, **108**, 154–176.

[8] K. L. Bak, P. Jørgensen, J. Olsen, T. Helgaker and J. Gauss, *Chem. Phys. Lett.*, 2000, **317**, 116–122.

[9] J. Lowe and K. A. Peterson, *Quantum Chemistry*, Elsevier Academic Press, 2006.

[10] A. I. Krylov, *Annu. Rev. Phys. Chem.*, 2008, **59**, 433–462.

[11] I. Shavitt and R. J. Bartlett, *Many-Body Methods in Chemistry and Physics: MBPT and Coupled-Cluster Theory*, Cambridge University Press, Cambridge New York, 2009.

[12] C. Cramer, *Essentials of Computational Chemistry: Theories and Models*, Wiley, 2002.

[13] A. J. Wallace, *Ph.D. thesis*, University of Canterbury, 2016.

[14] E. Ramos-Cordoba, P. Salvador and E. Matito, *Phys. Chem. Chem. Phys.*, 2016, **18**, 24015–24023.

[15] W. Duch and G. H. F. Diercksen, *J. Chem. Phys.*, 1994, **101**, 3018–3030.

[16] J. Liu and L. Cheng, *WIREs Comput. Mol. Sci.*, 2021, **11**, e1536.

[17] R. J. Bartlett and M. Musiał, *Rev. Modern Phys.*, 2007, **79**, 291–352.

[18] M. Kállay and J. Gauss, *J. Chem. Phys.*, 2004, **121**, 9257–9269.

[19] R. Izsák, *Int. J. Quantum Chem.*, 2020, **121**, e26327.

[20] O. Christiansen, H. Koch and P. Jørgensen, *Chem. Phys. Lett.*, 1995, **243**, 409–418.

[21] C. Hättig and F. Weigend, *J. Chem. Phys.*, 2000, **113**, 5154–5161.

[22] D. Kats, T. Korona and M. Schütz, *J. Chem. Phys.*, 2006, **125**, 104106.

[23] D. Mester, P. R. Nagy and M. Kállay, *J. Chem. Phys.*, 2017, **146**, 194102.

[24] A. Sirohiwal, F. Neese and D. A. Pantazis, *J. Chem. Theory Comput.*, 2021, **17**, 1858–1873.

[25] M. Nooijen and R. J. Bartlett, *J. Chem. Phys.*, 1997, **107**, 6812–6830.

[26] B. Kozma, A. Tajti, B. Demoulin, R. Izsák, M. Nooijen and P. G. Szalay, *J. Chem. Theory Comput.*, 2020, **16**, 4213–4225.

[27] R. Izsák, *WIREs Comput. Mol. Sci.*, 2019, **10**, e1445.

[28] C. Riplinger and F. Neese, *J. Chem. Phys.*, 2013, **138**, 034106.

[29] D. S. Levine, D. Hait, N. M. Tubman, S. Lehtola, K. B. Whaley and M. Head-Gordon, *J. Chem. Theory Comput.*, 2020, **16**, 2340–2354.

[30] H. Nakano, K. Sorakubo, K. Nakayama and K. Hirao, in *Theoretical and Computational Chemistry*, Elsevier, 2002, pp. 55–77.

[31] M. Boggio-Pasqua and G. Groenhof, *Comput. Theor. Chem.*, 2014, **1040-1041**, 6–13.

[32] J. M. Seminario, in *Modern Density Functional Theory: A Tool for Chemistry*, ed. J. Seminario and P. Politzer, Elsevier, 1995, pp. 1–27.

[33] S. Kurth, M. Marques and E. Gross, in *Encyclopedia of Condensed Matter Physics*, Elsevier, 2005, pp. 395–402.

[34] J. R. Gomes, J. L. Fajín, M. N. D. Cordeiro, C. Teixeira, P. Gomes, R. S. Pillai, G. Novell-Leruth, J. Toda and M. Jorge, in *Density Functional Theory: Principles, Applications and Analysis*, ed. J. Morin and J. M. Pelletier, Nova Science Publishers, Inc, New York, 2013, ch. Density Functional Treatment of Interactions and Chemical Reactions at Interfaces, pp. 1–57.

[35] A. Karton, *J. Comput. Chem.*, 2016, **38**, 370–382.

[36] M. Boggio-Pasqua, M. Ravaglia, M. J. Bearpark, M. Garavelli and M. A. Robb, *J. Phys. Chem. A*, 2003, **107**, 11139–11152.

[37] D. Guillaumont, T. Kobayashi, K. Kanda, H. Miyasaka, K. Uchida, S. Kobatake, K. Shibata, S. Nakamura and M. Irie, *J. Phys. Chem. A*, 2002, **106**, 7222–7227.

[38] A. Staykov and K. Yoshizawa, *J. Phys. Chem. C*, 2009, **113**, 3826–3834.

[39] Y. Ishibashi, T. Umesato, M. Fujiwara, K. Une, Y. Yoneda, H. Sotome, T. Katayama, S. Kobatake, T. Asahi, M. Irie and H. Miyasaka, *J. Phys. Chem. C*, 2016, **120**, 1170–1177.

[40] K. Seo, I. Eom, S. Shim, C. H. Kim and T. Joo, *Bull. Korean Chem. Soc.*, 2019, **40**, 352–358.

[41] J.-D. Chai and M. Head-Gordon, *Phys. Chem. Chem. Phys.*, 2008, **10**, 6615–6620.

[42] J. Kozłowska, P. Lipkowski, A. Roztoczyńska and W. Bartkowiak, *Phys. Chem. Chem. Phys.*, 2019, **21**, 17253–17273.

[43] Y. Minenkov, Å. Singstad, G. Occhipinti and V. R. Jensen, *Dalton Trans.*, 2012, **41**, 5526–5541.

[44] J. Řezáč, J. Fanfrlík, D. Salahub and P. Hobza, *J. Chem. Theory Comput.*, 2009, **5**, 1749–1760.

[45] J. J. P. Stewart, *J. Mol. Model.*, 2007, **13**, 1173–1213.

[46] B. G. Levine and T. J. Martínez, *Annu. Rev. Phys. Chem.*, 2007, **58**, 613–634.

[47] G. Groenhof, M. Bouxin-Cademartory, B. Hess, S. P. de Visser, H. J. C. Berendsen, M. Olivucci, A. E. Mark and M. A. Robb, *J. Am. Chem. Soc.*, 2004, **126**, 4228–4233.

[48] E. Teller, *J. Phys. Chem.*, 1937, **41**, 109–116.

[49] J. Michl, *Pure Appl. Chem.*, 1975, **41**, 507–534.

[50] A. Devaquet, *Pure Appl. Chem.*, 1975, **41**, 455–473.

[51] D. R. Yarkony, *Chem. Rev.*, 2011, **112**, 481–498.

[52] M. Dantus, M. J. Rosker and A. H. Zewail, *J. Chem. Phys.*, 1987, **87**, 2395–2397.

[53] A. H. Zewail, *Faraday Discuss. Chem. Soc.*, 1991, **91**, 207–237.

[54] J. von Neumann and E. P. Wigner, in *The Collected Works of Eugene Paul Wigner*, Springer Berlin Heidelberg, 1993, pp. 294–297.

[55] H. Nohira and T. Nohira, *J. Theor. Comput. Chem.*, 2019, **18**, 1950013.

[56] M. Boggio-Pasqua, *Habilitation à diriger des recherches*, Université Toulouse III, 2015.

[57] D. R. Yarkony, *Acc. Chem. Res.*, 1998, **31**, 511–518.

[58] M. Ben-Nun, F. Molnar, K. Schulten and T. J. Martínez, *Proc. Natl. Acad. Sci.*, 2002, **99**, 1769–1773.

[59] D. Asturiol, B. Lasorne, G. A. Worth, M. A. Robb and L. Blancafort, *Phys. Chem. Chem. Phys.*, 2010, **12**, 4949–4958.

[60] Y. Harabuchi, M. Hatanaka and S. Maeda, *Chem. Phys. Lett. X*, 2019, **2**, 100007.

[61] A. Ellis, M. Fehér and T. G. Wright, *Electronic and Photoelectron Spectroscopy: Fundamentals and Case Studies*, Cambridge University Press, Cambridge, UK New York, 2005.

[62] F. Santoro, A. Lami, R. Improta, J. Bloino and V. Barone, *J. Chem. Phys.*, 2008, **128**, 224311.

[63] T. Uzer and W. Miller, *Phys. Rep.*, 1991, **199**, 73–146.

[64] C. Punwong, J. Owens and T. J. Martínez, *J. Phys. Chem. B*, 2014, **119**, 704–714.

[65] J. N. Bull, C. W. West, C. S. Anstöter, G. da Silva, E. J. Bieske and J. R. R. Verlet, *Phys. Chem. Chem. Phys.*, 2019, **21**, 10567–10579.

[66] I. Presiado, S. Shomer, Y. Erez, R. Gepshtein, N. Amdursky and D. Huppert, *J. Photochem. Photobiol. A*, 2013, **258**, 30–40.

[67] M. Quack, in *Energy Storage and Redistribution in Molecules*, ed. J. Hinze, Springer, 1983, pp. 493–511.

Chapter 3

Methods and analysis

This chapter covers the principles and data analysis behind the time-resolved fluorescence up-conversion experiment, used to explore fluorescence lifetimes of pCK$^-$ and dithienylethenes (Chapters 5 and 6), along with a short description of the Boltzmann factor and its relevance to non-covalent interactions. Various computational methods for solvation used in this thesis are also discussed.

3.1 Ultrafast fluorescence up-conversion

Ultrafast fluorescence up-conversion is a time-resolved spectroscopy method for the study of the ultrafast dynamics in fluorophores.[1–3] In application, the sample is excited by a laser pulse (ω_{exc}) and emission from the excited state (ω_{f}), as an up-converted signal, measured as a function of time, where temporal evolution is obtained by changing the delay time (τ) between the pump pulse and gate laser pulse (Figure 3.1). The up-converted signal is obtained by sum frequency generation (SFG), which acts as a light gate and permits time resolution comparable to the temporal bandwidth of the laser (on the order of tens of femtoseconds).[4]

The experimental setup at UEA is summarised in Figure 3.2. The system has previously been used to investigate many fluorophore systems, including the green fluorescent protein chromophore (pHBDI) and analogues,[6] dyes and stains,[7,8] and molecular motors.[9] The seed laser system is a Coherent Micra 10, in which a continuous wave (CW) Nd:YVO_4 laser drives a Kerr lens mode-locked Ti:Sapphire (Ti:S) oscillator (Section 3.1.1). Nd:YVO_4 lasing generates a fundamental wavelength of 1064 nm, which is frequency doubled to 532 nm (green) to pump the Ti:S crystal. The Ti:S output is centred around 800 nm. This laser offers ≈20 fs temporal width and 80 MHz repetition rate. A pulse compressor situated after the Ti:S compensates for pulse dispersion, due to the different relative speeds at which different wavelengths propagate through different

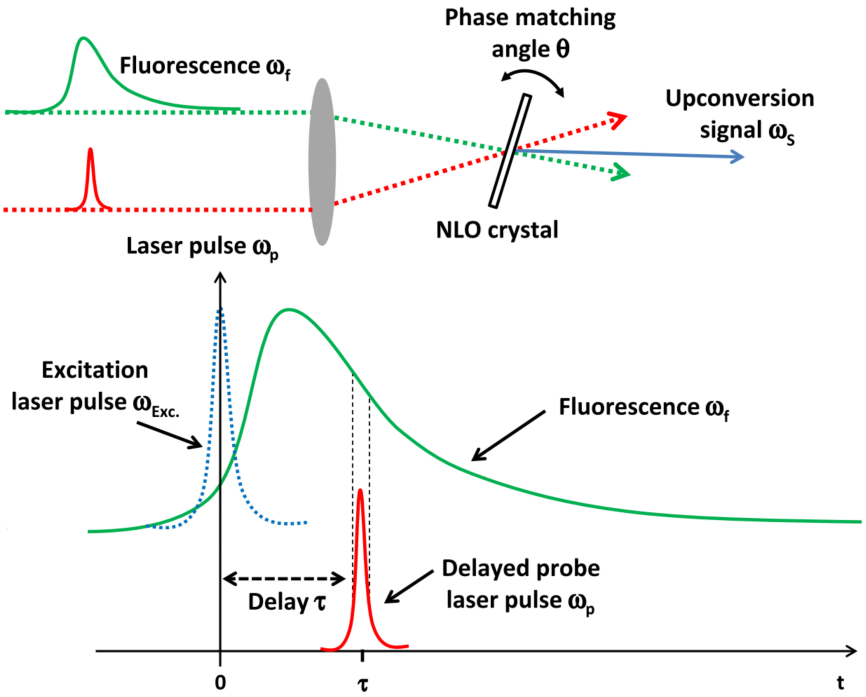


Figure 3.1: Schematic diagram of the basic principles of fluorescence up-conversion. The green and red lines correspond to the sample fluorescence (ω_f) and the gate pulse (ω_p), respectively. The angle (θ) of the non-linear optical (NLO) crystal is adjusted to maximise overlap between ω_f and ω_p, thus maximising the up-converted signal, ω_s. Adapted from Chosrowjan *et al.*[5]

media (Section 3.1.2). The second harmonic (400 nm, pump, ≈5–12 mW) is generated by focussing the fundamental (800 nm, gate, ≈840 mW) pulse onto a barium borate crystal (BBO, type I, 50 µm thickness) with a 150 mm focal length concave mirror. The fundamental and second harmonic wavelengths are separated by a dichroic mirror. A dichroic mirror preferentially reflects certain wavelengths, allowing the 400 nm and 800 nm pulses to be separated on different paths. The pathlength difference between the two pulses is determined by a computer-controlled motorised delay stage (0.1 µm resolution). Further pulse broadening of both the pump and gate pulses is minimised by chirped mirrors. The 400 nm pump pulse is then focussed onto the sample in a 2 mm quartz cell using a 150 mm focal length concave mirror. The resulting fluorescence is magnified and focussed by a reflective microscope objective (15x magnification). The sample fluorescence and the gate pulse are focussed onto a BBO crystal (type I, 100 µm thickness). To achieve frequency mixing and sum frequency generation, the two spots

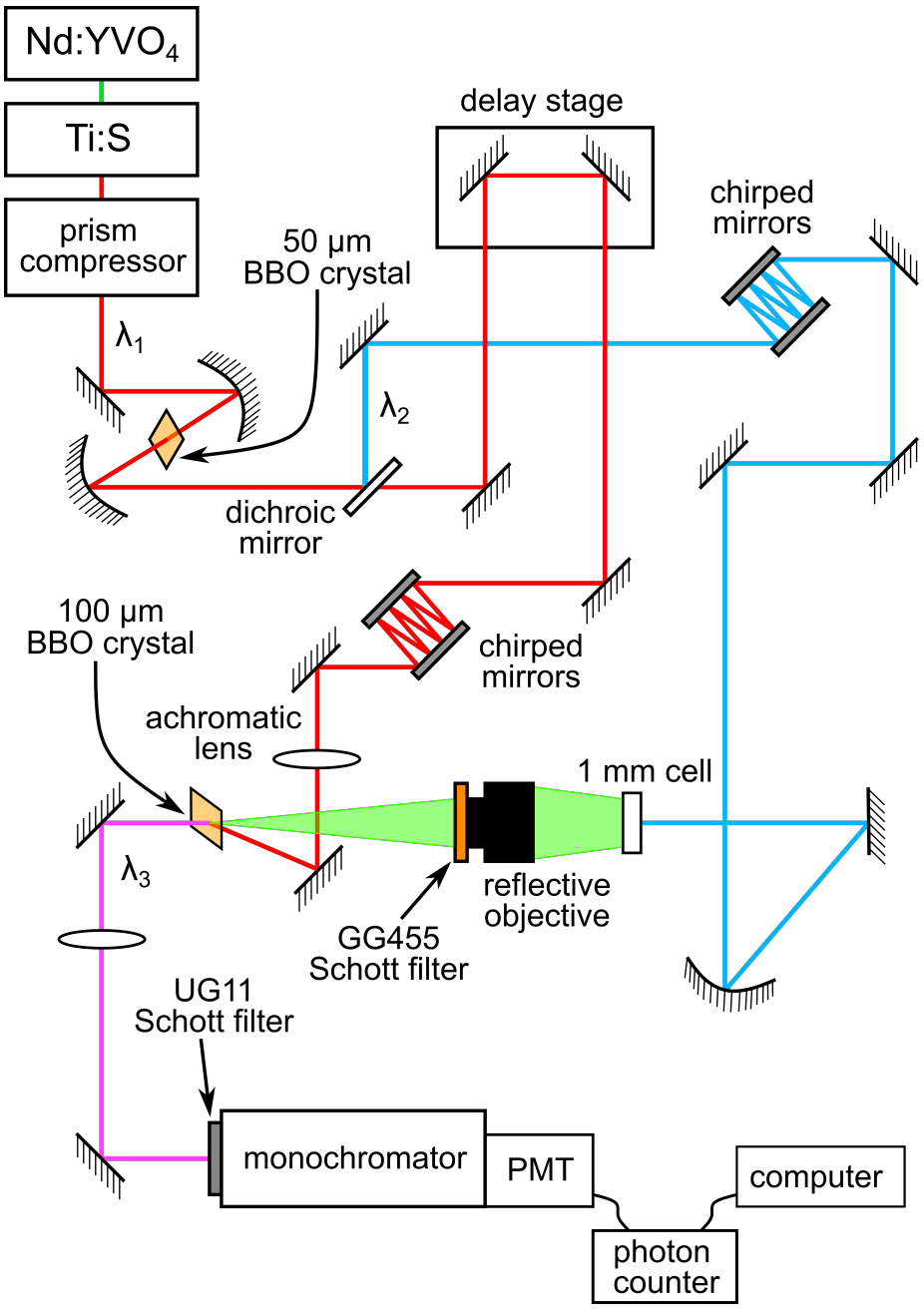


Figure 3.2: Schematic of the fluorescence up-conversion experimental setup at UEA. A neodymium yttrium vanadate (Nd:YVO_4) laser drives the titanium:sapphire (Ti:S) oscillator at 532 nm, producing 800 nm radiation. λ_1 is the fundamental wavelength (800 nm), acting as the gate pulse. λ_2 is the second harmonic wavelength (400 nm), which is used to excite the sample. λ_3 is the up-converted signal, determined by summing the energies of the gate pulse and the sample fluorescence.

must overlap, spatially and temporally. To minimise the background or scattered light detected by the low-noise photomultiplier tube (PMT, Hamamatsu R585) and photon counter (Stanford Research Systems SR400), the up-converted signal travels through a monochromator (Photon Technology International Model 101, resolution 2 nm/mm, spectral range 0–500 nm) and Schott filters. Schott filters are glass lenses that selectively block particular wavelengths. The first Schott filter (GG455) minimises scattering from the pump beam, while the second (UG11) prevents non-upconverted light from being detected by the PMT. The monochromator wavelength is manually tuned to match that of the up-converted signal.

Photomultiplier tubes, consisting of a photocathode, a series of dynodes, and a collection anode, are highly photosensitive and operate through utilising the photoelectric effect. The incoming photons strike a photocathode, causing ejection of electrons. The electrons are accelerated towards the dynodes, which multiply the incoming electrons. The anode terminating the dynode chain collects the multiplied electrons, which forms the amplified output signal.

3.1.1 Modelocking

The location of the gain medium in a laser, in this case Ti:S, is within a space described as the laser cavity. A simple laser cavity consists of two mirrors, a high reflector (fully-reflecting mirror) and an output coupler (partially transmitting mirror), either side of the Ti:S crystal (Figure 3.3(a)).[10] As the light travels between the mirrors, constructive interference forms standing waves of particular frequencies, termed longitudinal modes. These modes must be exactly an integral number of half wavelengths of the distance between the mirrors,

$$\frac{2L}{\lambda} = N \tag{3.1}$$

where L is the optical length of the cavity, λ is the mode wavelength, and N is an integer. If a wavelength, λ produces an integer, N, the mode is longitudinal and can be amplified by the gain medium.[11] Gain is increased by the addition of optics that remove low intensity pulses, while the high intensity pulses are returned to the Ti:S crystal (Figure 3.3(c)).[12]

There are two main families of laser – continuous wave (CW) and pulsed. In a CW

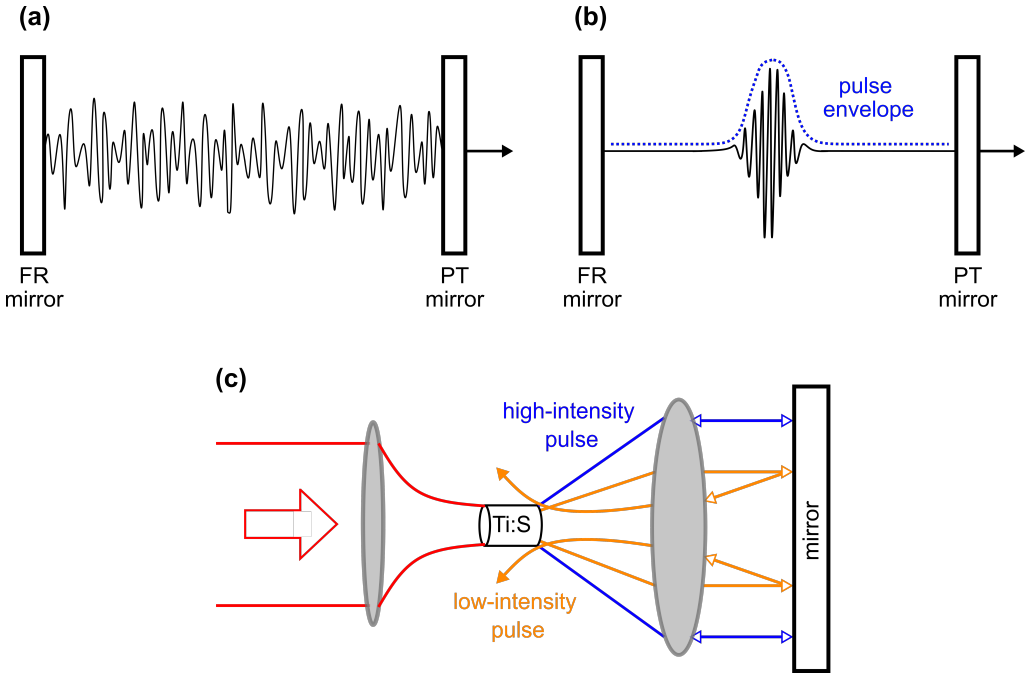


Figure 3.3: Representation of the oscillations within a laser cavity producing **(a)** continuous wave and **(b)** pulsed laser beams. On the left is a fully-reflecting (FR) mirror, while on the right there is a partially-transmitting (PT) mirror, through which some of the oscillations are conducted, forming the output laser beam. Gain is increased in the laser cavity by adding **(c)** additional optics, which filter out returning low-intensity pulses, only permitting high-intensity pulses to return to the Ti:S crystal.

laser, there are many longitudinal modes oscillating with no fixed relationship between their respective phases. This results in a constant laser output, hence continuous wave (Figure 3.3(a)). To access ultrashort pulses, the phase difference between these modes should be non-random and constant. At a given time, the frequencies will interact constructively, producing a short, intense light pulse (Figure 3.3(b)). The peak powers will be much larger compared to those of a CW output. At this point, the modes are said to be locked together. The larger the number of modes, the greater the intensity of the pulse and the narrower the temporal pulsewidth.[10,13] The time between pulses is dictated by the time it takes for the beam to travel from the output coupler (*i.e.* the PT mirror) to the reflector (FR mirror) and back. In the Coherent Micra 10, this results in a standard repetition rate of 80 MHz.

The Ti:S laser makes use of the Kerr-lens passive mode-locking technique, which functions using the optical Kerr effect, where there is a non-linear change in refractive index

with greater optical intensity, by virtue of the inherent electric field of the light beam.[14] The non-linear effect of self-focussing is important for Kerr lens mode-locking, as the refractive index of a material is changed by changing beam intensity. Consider a beam travelling through a material, such as a Ti:S crystal. The closer to the centre of the beam, the more intense the light, thereby producing a higher refractive index at the centre rather than at the periphery of the beam. This results in the medium acting as an intensity-dependent lens, slightly focussing the beam while it traverses through the Ti:S crystal. The extent of focussing is determined by the intensity of the beam and the pathlength through the crystal.[10]

3.1.2 Dispersion

Laser pulses contain different component frequencies. The combined waves are described by an envelope that travels with a particular velocity, termed the *group velocity*. The frequency-dependent change in group velocity is defined as the *group velocity disper-*

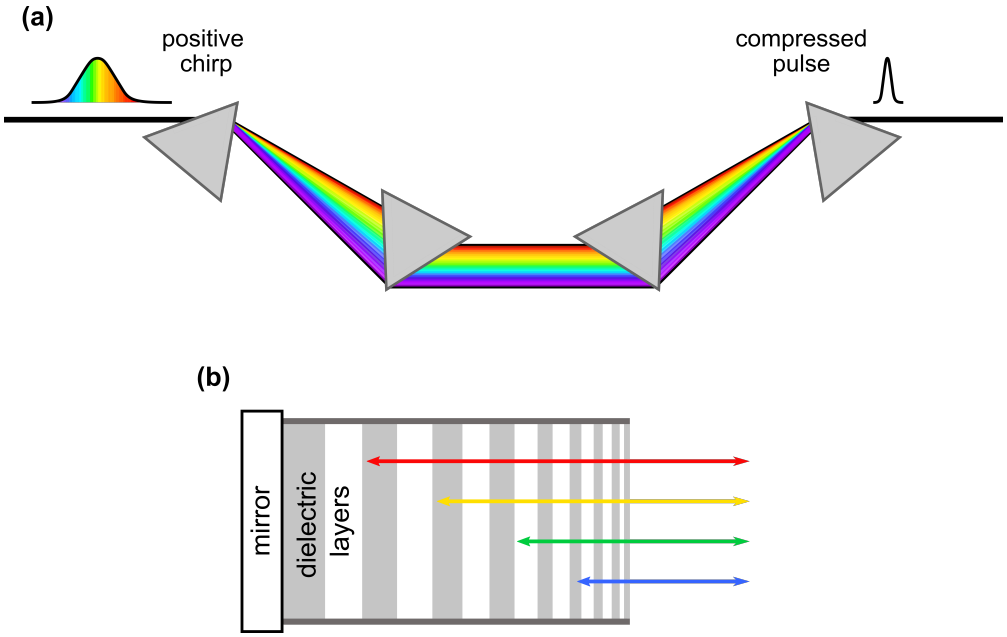


Figure 3.4: To correct for pulse broadening and positive chirp, **(a)** pulse compressors and **(b)** chirped mirrors are included in the fluorescence up-conversion setup. The pulse compressor contains four prisms which retard the faster-travelling red wavelengths, allowing the slower blue wavelengths to "catch up". Chirped mirrors are made of many dielectric layers, allowing for wavelength-dependent penetration depths, achieving a similar pulse outcome as the pulse compressor.

sion (GVD), while the product of GVD and the length of the medium traversed by the beam is the *group delay dispersion* (GDD). As a laser pulse propagates through different media, it begins to broaden and its peak power reduces. This is because shorter wavelengths tend to travel through media slower than longer wavelengths, forming a positive temporal chirp, or positive GDD. A temporally broad pulse is inconvenient when performing experiments where very short (fs) pulses are required. To compensate for the positive chirp, prism compressors and chirped mirrors are used to introduce a negative GDD.[5,12,13]

A prism compressor typically consists of four prisms, arranged in such a way that the longer wavelengths experience a longer optical pathlength, compared to the slower (shorter wavelength) components (Figure 3.4). The negative GDD introduced allows the slower wavelengths to "catch up" with the faster, lower frequencies.[10] Chirped mirrors perform a similar role; they account for both the constant GDD and higher-order disper-

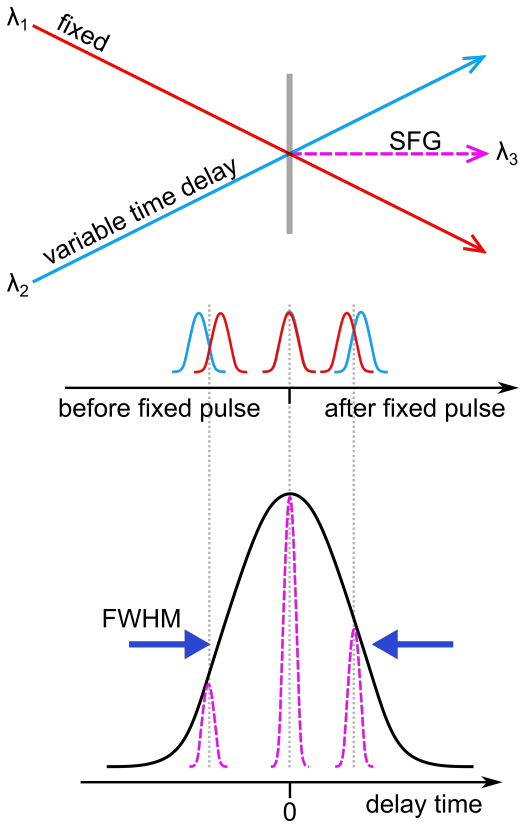


Figure 3.5: Cross-correlation of two laser pulses, λ_1 and λ_2. The resulting wavelength, λ_3 is created by sum frequency generation (SFG). The full-width half-maximum (FWHM) represents the experimental time-resolution.

sion. These mirrors are coated with many dielectric layers. Negative GDD is introduced because red wavelengths travel further into the material, delaying them with respect to the shorter wavelengths. The net effect is pulse compression.[12]

3.1.3 Cross-correlation

The cross-correlation, also termed the instrument response function (IRF), of a laser experiment is determined by a very similar principle to sum-frequency generation (SFG) used in fluorescence up-conversion (Figure 3.5). Briefly, one laser pulse (λ_2) is pumped at a time delay relative to a fixed pulse (λ_1) and the sum-frequency generated pulse (λ_3) monitored as a function of the delay time of λ_2. The full-width half-maximum (FWHM) of the resulting Gaussian-type curve indicates the time resolution of the experiment.

A previous measurement of the fluorescence up-conversion IRF[12] gave an ≈50 fs time resolution (Figure 3.6). In this thesis, a value of 55 fs is used.

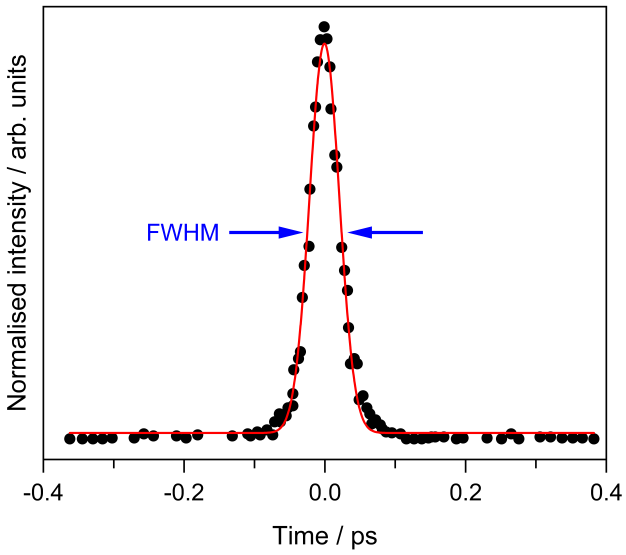


Figure 3.6: Cross-correlation of heptane Raman scattering, fitted with a Gaussian function. The full-width half-maximum (blue arrows), yields an ≈50 fs time resolution of the fluorescence up-conversion setup. Data extracted from Addison PhD thesis.[12]

3.2 Fluorescence decay analysis

A time-resolved fluorescence experiment involves recording fluorescence signal as a function of delay time (between the pump and probe pulses). These decay curves can be fitted with an exponential function convoluted with a Gaussian function (the experimental time resolution/cross-correlation), yielding the fluorescence lifetime. Both single and double exponential convolution functions are used for fitting of fluorescence decay data in this thesis. Although the fluorescence up-conversion data fits well to a single exponential in most cases, the double exponential can account for the rapid effect of solvent rearrangement. It is important to account for solvent motion because, when the solute is exited, its charge distribution changes effectively instantaneously. The solvent has to react to this change; however, this does not occur immediately. The duration of the delay between excitation and solvent rearrangement depends on the solvent properties. Water is generally considered one of the 'fastest' solvents and it has been shown that, in aqueous solution, the solvent response timescale can be faster than 50 fs.[15]

As discussed by Jimenez *et al.*,[15] there is a bimodal response in the solvent as a result of a change in solute charge distribution. The initial ultrafast component (τ_1), arising mainly due to librational solvent motion, is followed by a slow component (τ_2), resulting from diffusive motions of the solvent. Jiminez and co-workers demonstrated this by a global fitting procedure on fluorescence decay data for coumarin 343 in water (obtained by fluorescence up-conversion):

$$S(t) = a_{\mathrm{g}}\, e^{(-\frac{1}{2}\omega_{\mathrm{g}}^2 t^2)} + a_1\, e^{(-t/\tau_1)} + a_2\, e^{(-t/\tau_2)} \tag{3.2}$$

which is a convolution of a Gaussian function, $a_{\mathrm{g}}\, e^{(-\frac{1}{2}\omega_{\mathrm{g}}^2 t^2)}$, and two exponential functions, $a_1\, e^{(-t/\tau_1)}$ and $a_2\, e^{(-t/\tau_2)}$. The parameters are a_x, the pre-exponential factor of each function, ω_{g}, the full-width half-maximum of the Gaussian curve, and τ_x, the time constant (fluorescence lifetime) of the respective exponential components. The time constants of coumarin 343 are quoted as 120 fs (τ_1) and 880 fs (τ_2),[15] which agrees with the time constants of other coumarin dyes.[16]

To achieve a more accurate quantification of the fluorescence lifetimes, more complex Gaussian-exponential convolution equations are used in this thesis, in the form of single- and double-exponential convolutions (Equations 3.3 and 3.4, respectively):

$$y = y_0 + \left[\frac{A}{\tau_0} e^{\left\{\frac{1}{2}\left(\frac{\omega_0}{\tau_0}\right)^2 - \left(\frac{x-x_{\mathrm{c}}}{\tau_0}\right)\right\}}\right] \left[\frac{1}{2}\left\{\mathrm{erf}\left(\frac{z}{\sqrt{2}}\right) + 1\right\}\right] \tag{3.3}$$

and

$$y = y_0 + \left[\frac{A_1}{\tau_1} e^{\left\{\frac{1}{2}\left(\frac{\omega_1}{\tau_1}\right)^2 - \left(\frac{x - x_{c_1}}{\tau_1}\right)\right\}}\right]\left[\frac{1}{2}\left\{\text{erf}\left(\frac{z_1}{\sqrt{2}}\right) + 1\right\}\right] + \left[\frac{A_2}{\tau_2} e^{\left\{\frac{1}{2}\left(\frac{\omega_2}{\tau_2}\right)^2 - \left(\frac{x - x_{c_2}}{\tau_2}\right)\right\}}\right]\left[\frac{1}{2}\left\{\text{erf}\left(\frac{z_2}{\sqrt{2}}\right) + 1\right\}\right] \tag{3.4}$$

where

$$\text{erf} = \frac{1}{\sqrt{2\pi}} \int_{-\infty}^{z} e^{-\frac{y^2}{2}}\, \text{dy} \tag{3.5}$$

and

$$z_x = \frac{(x - x_{c_x})}{\omega_x} - \frac{\omega_x}{\tau_0} \tag{3.6}$$

The terms A, x_c, and ω define the amplitude, centre, and width of the Gaussian curve, and y_0 represents the y-offset. The fluorescence lifetime obtained from the single-exponential fit is defined as τ_0 and the lifetimes from the double-exponential fit defined as τ_1 and τ_2. In this thesis, $\omega_{0,1,2}$ are equal (55 fs), defined as the time resolution/cross-correlation of the experiment.

The small experimental time resolution (≈50 fs) enables the short timescale fluorescence lifetime components (τ_1) to be accessed, which informs on the solvent dynamics (rearrangement) on excitation. If desired, parameter A_2 can be restrained so that the growth of A_2 is proportional to the decay of A_1 with time. The same single- and double-exponential fitting procedures were used to analyse the time-resolved fluorescence measurements of room temperature (≈ 300 K) and cryogenically cooled (≈ 77 K) DTE solutions, and cryogenically cooled pCK$^-$ solutions. The pulsed laser/LED units used in the Edinburgh FS5 experiments had longer pulse widths than the up-conversion experiment (several hundred picoseconds), so the values of ω were adjusted accordingly.

3.3 Computational methods

Choice of theoretical method and basis set are important in computations and depends on the specific requirements of a particular investigation. Solvation calculations of pCK$^-$ and a DTE (NS2-22) were performed to explore the solvation sphere around the two compounds (procedures shown in Figures A1.2 and A2.3).

In both cases, preliminary time-dependent DFT (TD-DFT) and multireference coupled-cluster (MRCC) calculations, using double- and triple-ζ basis sets, were performed.

For pCK$^-$, aug-cc-pVDZ contains 158 spherical harmonic basis functions, while aug-cc-pVTZ contains 258 basis functions. For NS2-22, the cc-pVDZ basis set contains almost half the number of basis functions compared with its triple-ζ sibling, significantly decreasing computational expense. Advantageously, there was little change in computed excitation energies between the two basis sets for either compound, thus showing the double-ζ basis set to be appropriate.

Excited state calculations to obtain vertical excitation energies of unsolvated and solvated pCK$^-$ and NS2-22 were performed using TD-ωB97X-D, df-CC2, and STEOM-DLPNO-CCSD (Section 2.1.2). While TD-ωB97X-D is computationally cheaper than df-CC2, the latter provides more accurate excitation energies.[17] This is particularly true when considering charge transfer (CT) states, as TD-DFT is well-known for failing to correctly describe transitions containing significant CT character, although df-CC2 still relies on large approximations.[18] It must be noted that both TD-DFT and CC2 approaches are classed as linear response (LR) methods, which endows them with limitations when it comes to excited state calculations.[19] These limitations stem from the fact that LR approaches use the ground state charge density to compute excited state charge density, instead of explicitly computing the charge densities for both the ground and excited states, as in state specific (SS) methods (*e.g* XMCQDPT2).[20]

Incorporation of solvation was achieved through the use of explicit and implicit solvation methods. Explicit solvation is the addition of individual solvent molecules around the compound of interest, whereas implicit solvation models (also known as continuum solvation models) approximate the dielectric properties or electrostatic contribution of a solvent, disregarding the solvent's molecular structure. The oldest implicit model is the polarisable continuum model (PCM).[21] PCM simply represents the solvent as a dielectric polarisable continuum, where the dielectric constant is characteristic to a given solvent, thus mimicking the overall electrostatic potential effect of the solvent.[22] The continuum contains a cavity, in which the solute is placed, which is defined by interlocking of the solute's atomic van der Waals radii.[19] In this thesis, the PCM method is used with the TD-ωB97X-D and df-CC2 methods. Over the years, PCM has been built on, resulting in a variety of approaches, such as the conductor-like polarisation continuum model (CPCM). CPCM is based on the conductor-like solvation model COSMO, which uses a distribution of polarisation charges over the cavity surface to represent the solvent reaction field (a form of continuum).[23] Unlike continuum-based models, the SMD model (a solvation model based on the full solute electron density)[24] separates contributions to solvation into two components. These are the electrostatic contribution from the bulk

solvent and the short-range dispersion interactions between the first solvation shell and the solute. Thereby, SMD provides a more accurate model of solvation compared with PCM-type methods. CPCM and SMD were both used with STEOM-DLPNO-CCSD to compare their relative performances. Implicit methods are useful in order to gain a general appreciation for the effect of the solvent; however, explicit solvation provides a more accurate representation of solvation properties. Once the excitation energies from solvation calculations are sufficiently unchanging with addition of solvent, it can be said that the inner solvation sphere has been recreated. At this point, the computed energies should match well with the absorption spectra (within the limit of the excited state method).

References

[1] M. Murakami, H. Miyasaka, T. Okada, S. Kobatake and M. Irie, *J. Am. Chem. Soc.*, 2004, **126**, 14764–14772.

[2] K. Seo, I. Eom, S. Shim, C. H. Kim and T. Joo, *Bull. Korean Chem. Soc.*, 2019, **40**, 352–358.

[3] V. Maffeis, R. Brisse, V. Labet, B. Jousselme and T. Gustavsson, *J. Phys. Chem. A*, 2018, **122**, 5533–5544.

[4] J. Shah, *IEEE J. of Quantum Electron.*, 1988, **24**, 276–288.

[5] H. Chosrowjan, S. Taniguchi and F. Tanaka, *FEBS J.*, 2015, **282**, 3003–3015.

[6] K. Addison, I. A. Heisler, J. Conyard, T. Dixon, P. C. B. Page and S. R. Meech, *Faraday Discussions*, 2013, **163**, 277–296.

[7] S. P. Laptenok, K. Addison, I. A. Heisler and S. R. Meech, *Chem. Phys. Lett.*, 2014, **607**, 43–46.

[8] I. A. Heisler, M. Kondo and S. R. Meech, *J. Phys. Chem. B*, 2009, **113**, 1623–1631.

[9] A. S. Sardjan, P. Roy, W. Danowski, G. Bressan, L. N. dos Santos Comprido, W. R. Browne, B. L. Feringa and S. R. Meech, *ChemPhysChem*, 2020, **21**, 594–599.

[10] W. T. Silfvast, *Laser fundamentals*, Cambridge University Press, Cambridge, 1996.

[11] N. Tkachenko, *Optical Spectroscopy: Methods and Instrumentations*, Elsevier, Amsterdam, 2006.

[12] K. Addison, *Ph.D. thesis*, University of East Anglia, 2015.

[13] J.-C. Diels and W. Rudolph, *Ultrashort Laser Pulse Phenomena: Fundamentals, Techniques, and Applications on a Femtosecond Time Scale*, Academic Press, San Diego, 1996.

[14] A. E. Siegman, *Lasers*, University Science Books, Sausalito, 1986.

[15] R. Jimenez, G. R. Fleming, P. V. Kumar and M. Maroncelli, *Nature*, 1994, **369**, 471–473.

[16] W. Jarzeba, G. C. Walker, A. E. Johnson, M. A. Kahlow and P. F. Barbara, *J. Phys. Chem.*, 1988, **92**, 7039–7041.

[17] M. Kállay, P. R. Nagy, D. Mester, Z. Rolik, G. Samu, J. Csontos, J. Csóka, P. B. Szabó, L. Gyevi-Nagy, B. Hégely, I. Ladjánszki, L. Szegedy, B. Ladóczki, K. Petrov, M. Farkas, P. D. Mezei and Á. Ganyecz, *J. Chem. Phys.*, 2020, **152**, 074107.

[18] D. Mester, P. R. Nagy and M. Kállay, *J. Chem. Phys.*, 2017, **146**, 194102.

[19] G. Scalmani, M. J. Frisch, B. Mennucci, J. Tomasi, R. Cammi and V. Barone, *J. Chem. Phys.*, 2006, **124**, 094107.

[20] S. Corni, R. Cammi, B. Mennucci and J. Tomasi, *J. Chem. Phys.*, 2005, **123**, 134512.

[21] J. Tomasi, B. Mennucci and R. Cammi, *Chem. Rev.*, 2005, **105**, 2999–3094.

[22] S. Miertuš, E. Scrocco and J. Tomasi, *Chem. Phys.*, 1981, **55**, 117–129.

[23] V. Barone and M. Cossi, *J. Phys. Chem. A*, 1998, **102**, 1995–2001.

[24] A. V. Marenich, C. J. Cramer and D. G. Truhlar, *J. Phys. Chem. B*, 2009, **113**, 6378–6396.

Chapter 4

Substituted *p*HBDI anions

This chapter discusses the photophysics of green fluorescent protein (GFP) chromophore derivatives in the gas phase, probed using photodissociation action spectroscopy and electronic structure calculations. While I was unable to be part of the experimental data collections at Aarhus University, Denmark, due to the COVID-19 pandemic, I am responsible for the computational work. There are many uses for GFP and its chromophore derivatives, for example as fluorescent tags and in optogenetics, necessitating the need to understand the intrinsic chromophore properties, which can guide design of synthetic derivatives with improved characteristics. In this work, bare and complexed chromophore anions are investigated to inform on microenvironmental perturbations to the absorption properties (action spectra). The study deploys complexation of the betaine zwitterion to provide a model for dipole microsolvation, the effect of which is explored through electronic structure calculations and energy decomposition analysis. Betaine binding is found to occur mainly *via* the phenoxide deprotonation site, with complex cohesion dominated by electrostatic interactions. The betaine-induced spectral shift is well-reproduced through STEOM-DLPNO-CCSD calculations, while point-charge models, in which betaine is represented by electrostatic and point-charge induction interactions, are shown to be inadequate.

4.1 Introduction

Green fluorescent protein (GFP) is a widely-studied biomolecule which has found extensive use as a biomarker for *in vivo* labelling.[1,2] GFP was first isolated from the *Aequorea victoria* jellyfish by Shimomura and co-workers in the early 1960s.[3] The GFP chromophore is based on deprotonated *para*-hydroxybenzylidene-2,3-dimethylimidazolinone (pHBDI$^-$) and interacts through covalent and hydrogen bonds with the protein β-barrel structure (Figure 4.1). The HBDI chromophore is common to other photoactive proteins, such as Dronpa. In Dronpa, $E \rightarrow Z$ photoisomersiation takes place; however, this process

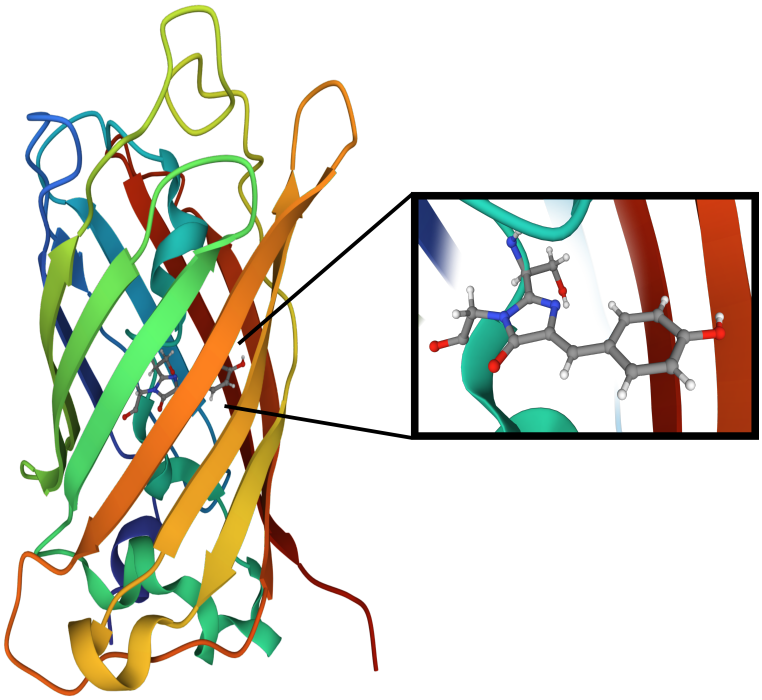


Figure 4.1: Structure of green fluorescent protein (GFP) and its chromophore (insert), located inside the protein β-barrel (pdb 2WUR). Adapted from the Protein Data Bank[5] and visualised in Mol* Viewer.[6–8]

is inhibited in GFP (due to unfavourable protein scaffold).[4] For Dronpa, photoisomerisation triggers changes in the interactions between the chromophore and amino acid residues, ultimately resulting in conformational changes within the protein.[2]

The *p*HBDI chromophore, as the deprotonated anion (*p*HBDI$^-$), interacts with the protein binding pocket through a complex network of hydrogen bonds, involving neighbouring amino acid side-chains and water molecules.[9] The amalgamation of these interactions leads to the so-called electrochromatic shift. Different electrostatic environments in the binding pocket for mutant proteins can tune the optical transition wavelength up to 65 nm.[3,10] The importance of electrostatic interactions in defining both the electrochromatic shift and detailed photophysics of GFP and derivatives have been inferred through numerous experiments,[11–14] and large-scale calculations.[11,15–20] Yet, it is important to note that the inherent (gas phase) $S_1 \leftarrow S_0$ absorption spectrum for *p*HBDI$^-$ is only

sightly shifted compared with the GFP absorption spectrum.[4,21,22] It has therefore been argued that, although the protein environment may have a determinative effect on the photophysics (e.g. hindering isomerisation and maximizing fluorescence quantum yield), there is no net perturbation to the Franck-Condon electronic structure (for the $S_1 \leftarrow S_0$ transition) that would lead to an electrochromatic shift.

Computational protocols for investigating the effect of protein environment on the excitation energies of chromophore(s), using conventional electronic structure packages have been established for a range of photoactive proteins.[23–25] These studies usually show that electrostatic effects of the protein matrix influence the chromophore properties and play a key role in defining electrochromatic shifts in excitation energies. To demonstrate this, quantum mechanics/molecular mechanics (QM/MM) approaches are often deployed, partitioning the chromophore and its immediate environment (treated quantum mechanically) from the rest of the protein (described by a force field). However, the central challenge lies in modelling these shifts correctly, which requires incorporation of the protein's electrostatic effects in order to produce accurate excited states.[26] In this work, an alternative strategy is described, involving consideration of the microperturbations caused by chromophore-zwitterion binding, using the betaine molecule (Z, Figure 4.2). While the betaine tagging strategy certainly does not model all aspects of protein binding pockets, it provides an avenue for assessing microsolvation and perturbations by charged side chains to chromophore electronic structure.

Experimentally, it is difficult to disentangle the various contributions to the interactions between the protein β-barrel and *p*HBDI$^-$ in GFP. Solution-phase experiments enable the influence of solvent properties, such as viscosity, polarity, and pH to be routinely studied. Whereas solution-based strategies ultimately rely on trends and indirect observations to imply intrinsic photophysical behaviour, gas-phase investigations enable the intrinsic dynamics to be probed directly. However, practically, it is difficult to generate a known number density of gas-phase molecules in a localised volume and record any change in light absorption, as per conventional absorption spectroscopy. To overcome this challenge, photodissociation action spectroscopy is used. The crux of action spectroscopy techniques, such as photodissociation action spectroscopy, is to infer the inherent absorption profile and obtain some information on the photophysical dynamics leading to the "action".[27,28] For example, if single-photon absorption is capable of producing a photodissociation response over a timescale that is rapid compared with the time taken for detection, then the action spectrum should parallel the absorption spectrum. This correspondence assumes that alternative deactivation pathways, such

as fluorescence or electron detachment (in anions), is either small or constant over the spectrum. Such gas-phase methods can provide a means of assessing the effect of solvation or a microenvironment (*e.g.* a protein binding pocket) on the photodynamics of the chromophore.[29,30] A further convenience of gas-phase methods is that results can be compared directly with computational data. It is becoming common practise for robust gas-phase studies to consider several data sets recorded on different instruments offering characterisation of several "actions" (e.g. dissociation, isomerisation, electron detachment, and fluorescence) in order to confirm this correspondence. For the present *p*HBDIs, time-resolved photoelectron spectroscopy and frequency-dependent photodetachment measurements have been performed on the target *p*HBDI$^-$ chromophores (see Section 4.5) to demonstrate that: (1) excited state lifetimes are sub-picosecond, and (2) internal conversion followed by statistical dissociation is the predominant deactivation pathway. Gas-phase fluorescence measurements were performed using the LUNA apparatus at Aarhus University, but were unable to detect any fluorescence response, consistent with fluorescence not being important at $T \approx 300\,\mathrm{K}$. In summary, the present photodissociation action spectra are expected to parallel the gas-phase absorption spectra.

The simplest strategy for quantifying solvation involves comparing action spectra of isolated molecules with the absorption spectra of the target molecule in solution. Alternatively, cluster microsolvation approaches provide a more systematic way to explore microsolvation. In such approaches, ions, complexed with a specific number of solvent molecules, are selected on the basis of the complex's mass-to-charge ratio or shape, using mass spectrometry or ion-mobility spectrometry, respectively.[31] A particular difficulty is that the complexed solvent molecules are typically weakly bound (*e.g.* 0.1–0.5 eV), which is likely less than the average cluster energy at room temperature, leading to the solvent "boiling off" during the experiment. As a result, cluster microsolvation experiments often require cryocooling conditions, especially when they involve several solvent molecules, since the strength of the solvent-solute interaction decreases with increasing solvation.[32]

A novel approach to explore the effect of an environment (*e.g.* an electric field) of a biochromophore was proposed by Brøndsted Nielsen and co-workers, which involves studying ion-zwitterion complexes.[22,31,33] This strategy can inform on the locally excited (LE) and charge transfer (CT) character of electronic transitions by comparing the gas-phase action spectra of bare ions with those for ion-zwitterion complexes. In an LE transition, the charge density remains localised, while in a CT transition, the charge

density distribution in the excited state is different to that in the ground state. For a given ion in a microenvironment, there is an associated Coulomb interaction energy between the ion and the nearby dipoles, which changes on excitation. The higher the degree of CT character in an electronic transition, the greater the effect nearby dipoles will have on the excitation.[33]

Betaine (*N*,*N*,*N*-trimethylglycine, Figure 4.2) is a zwitterionic molecule that possesses a large dipole moment ($|\mu| = 11.5 - 11.9\,\mathrm{D}$).[34,35] Ions with binding sites possessing a high affinity for betaine, such as the phenoxide deprotonation site in *p*HBDI$^-$,[22] experience significant perturbations in the potential energy surfaces associated with the lowest energy electronic transition.[33] The large dipole moment on betaine means that it coordinates preferentially with the charge site on a gas-phase ion. Coordination of betaine to the chromophore's charge site leads to polarisation and stabilisation (lowering in energy) of the molecular orbitals on and around the charge site. The most significant perturbation is observed in ions whose charge distribution is localised (asymmetric) and highly polarisable. These changes to the charge site molecular orbitals are reflected as electrochromatic shifts in the photodissociation action spectra. Electronic transitions with significant CT character are blue-shifted in the action spectra for the ion-betaine complex. This blue-shift arises because the occupied molecular orbitals are stabilised relative to the unoccupied orbital(s) associated with the transition, as the CT transition moves charge density away from the deprotonation site and the coordinated betaine molecule. In contrast, molecules with low polarisability and/or delocalised (symmetric) charge distributions exhibit high LE character and thus show little betaine-induced spectral shift (the red-shift originating from symmetry breaking often cancelling the blue-shift due to induction forces).[33]

The large dipole moment in betaine provides a further benefit to the investigation of chromophore dynamics, since betaine exerts a dipolar field of 50–70 $\mathrm{MV\,cm^{-1}}$ at bonding separations in conventional intermolecular complexes (several Angstroms).[20] This field is close to the 100 $\mathrm{MV\,cm^{-1}}$ electric field experienced by the phenoxide site when in the protein, thus providing an easier means of replicating some of the electrostatic effect of the protein matrix. For *p*HBDI$^-$, this shift has been characterised by Langeland *et al.*,[22] who showed a 0.05 eV difference between the absorption spectra of the *p*HBDI$^-$-betaine complex and *p*HBDI$^-$ in GFP, which is comparable with a previous theoretical study quantifying the absorption shift due to the protein matrix as 0.08 eV.[36] Although this earlier study predicted electrostatic effects to dominate the GFP electrochromatic shift, it is hard to disentangle the relative importance of different interactions within the

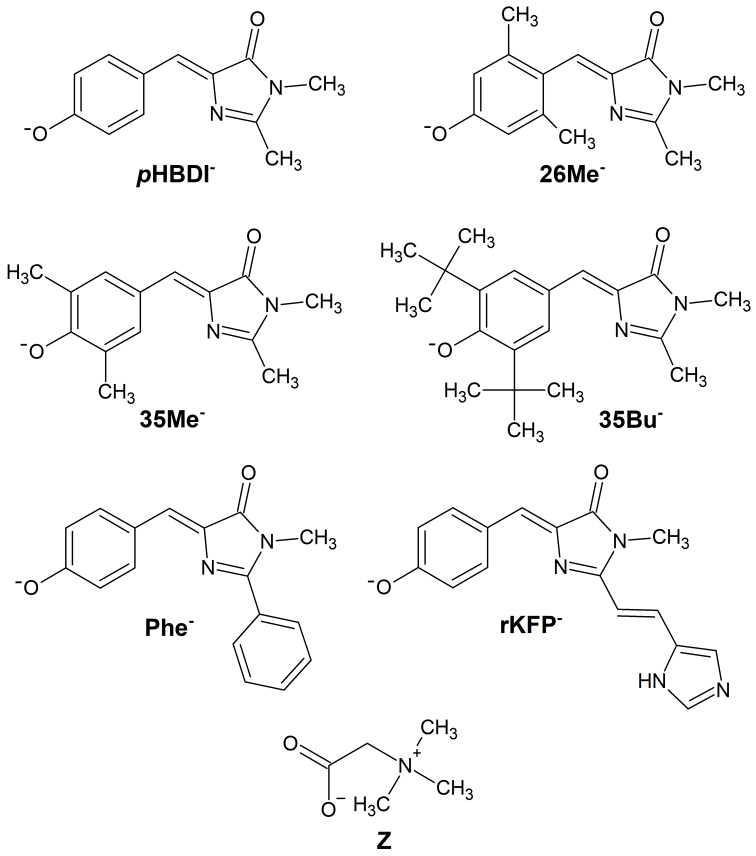


Figure 4.2: Structures of the six target chromophores and the betaine zwitterion (Z). Compounds $26Me^-$, $35Me^-$, $35Bu^-$, and Phe^- are alkylated and phenylated derivatives of pHBDI$^-$. Molecule $rKFP^-$ is a more complex derivative of pHBDI and is also a model chromophore of red Kaede fluorescent protein (rKFP).

protein binding pocket. Systematically exploring the contribution of individual interactions/effects, *e.g* using anion-betaine complexes, allows establishment of a more accurate picture of ion-complex interactions and, ultimately, of the chromophore-protein interactions.

While spectral changes across a range of anionic and cationic molecules,[31,33] including pHBDI$^-$,[22] have been quantified using betaine-tagging, a detailed theoretical analysis of betaine-anion binding interactions, and comparison to the bare ion's electronic structure, is lacking (*e.g.* contributions of polarisation, dispersion, and ionic character to the interactions). Here, photodissociation action spectroscopy has been used on a series of six pHBDI-based anions (Figure 4.2) complexed with betaine to characterise spectral shifts, compared with the bare ions, and to explore how alkylation affects the absorption

properties by providing steric bulk around the deprotonation site. The choice of this alkylated series of pHBDI$^-$ species is in part because solution absorption spectroscopy measurements in water and alcoholic solvents have revealed significantly red-shifted absorption spectra for the deprotonated anions (e.g. by 0.16 eV and 0.40 eV for 35Me$^-$ and 35Bu$^-$), relative to pHBDI$^-$.[37] The origin for this substantial red shift with alkylation is unclear and assumed inductive (*i.e.* interactions between permanent and induced dipole moments),[38] although this does raise questions regarding the degree of CT character associated with the $S_1 \leftarrow S_0$ transition in isolated pHBDI molecules.[39]

Computationally, it is challenging to obtain a reliable description of the CT character of electronic transition, especially for larger molecules, including fluorescent protein chromophores. The molecular size of biochromophores often prohibits high-level electronic structure theory methods, including multireference configuration interaction (MRCI) and coupled cluster (CC). Time-dependent density functional theory (TD-DFT) is often favoured as an alternative, due to its lower computational cost. TD-DFT methods are widely used to calculate electronic excitation energies and spectra of larger molecules (up to a few hundred second-row atoms), as such methods can reach accuracies comparable to those of more sophisticated quantum chemical methods. However, this accuracy is only achieved for LE transitions in systems with little CT character. Due to the approximations implemented in TD-DFT, the calculated potential energy curves often fail to exhibit the correct asymptotic behaviour. This results in substantial errors in calculated excitation energies (up to several electron volts, eV).[40,41] While improvements have been made to density functional (and other) procedures to more accurately account for CT character,[42] it is often unclear whether a method is suitable for a given system if benchmarks are not available. Moreover, new electronic structure methods can take years to be incorporated into standard computational software packages.

In this chapter, photodissociation action spectra of the six deprotonated pHBDI anions (Figure 4.2) complexed with betaine are compared with results from the bare anions. The physiochemical impact of pHBDI$^-$ complexation with betaine is explored using electronic structure theory methods, including semi-empirical modelling of geometries and fluxionality (at $T \approx 300$ K), full quantum mechanical coupled-cluster calculations with energy decomposition analysis schemes, symmetry adapted perturbation theory, point-charge models within several frameworks, and excited state calculations of transition energies.

Four key questions relating to the GFP chromophore's inherent photophysics are ad-

dressed:

(i) How strongly do the *p*HBDI$^-$ series bind with betaine and what is the nature of the binding forces?

(ii) What is the influence of betaine binding on the action spectra?

(iii) Can betaine-induced spectral shifts be reproduced by electronic structure calculations of anion-betaine complexes and/or treatment of betaine with point charges (*i.e.* electrostatics only)?

(iv) Can a simple protocol using standard electronic structure methods for analysing anion-betaine complexes be developed?

4.2 Experimental methods

Photodissociation action spectroscopy of the HBDI anion-betaine complexes were performed using the Sep1 accelerator mass spectrometer (Figure 4.3) at Aarhus University.[27,28] Anions were produced by electrospray ionisation and passed through a heated capillary followed by a tube lens/skimmer region. The anions were accumulated in an octupole ion trap (Figure 4.3(b)). The trap was emptied at 25 ms intervals (40 Hz repetition rate) and the ion bunches accelerated to a kinetic energy of ≈50 keV. The anions of interest were selected, according to their mass-to-charge (m/z) ratio, using a bending magnet (electromagnet). The selected ions then traversed a 2.5 m linear flight region (10^{-6} Torr background pressure). Midway along this region, a nanosecond-pulsed laser system (EKSPLA NT342A, 20 Hz, unfocussed) excited every second ion packet, causing dissociation. The EKSPLA laser system consists of a nanosecond Nd:YAG laser that pumps an optical parametric oscillator (OPO) with a 20 Hz repetition rate. An electrostatic analyser, situated after the laser-ion interaction region, separated the fragment ions, which were then detected with a channeltron (Figure 4.3(a)). In a recent gas-phase study on rKFP$^-$ using isomer-specific photodissociation action spectroscopy,[43] it was shown that three gas-phase forms may be generated using electrospray ionisation (two deprotomers and one tautomer). On the basis of that study, judicious choice of solvent and electrospray conditions allowed generation of a pure gas-phase ensemble of the phenoxide deprotomer (structures shown in Figure 4.2).

For the bare anions, loss of a methyl group accounted for more than 95% of the total photofragmentation yield.[21,43–45] For the anion-betaine complexes, loss of the betaine 'tag' molecule is the only photodissociation channel under low laser fluence conditions

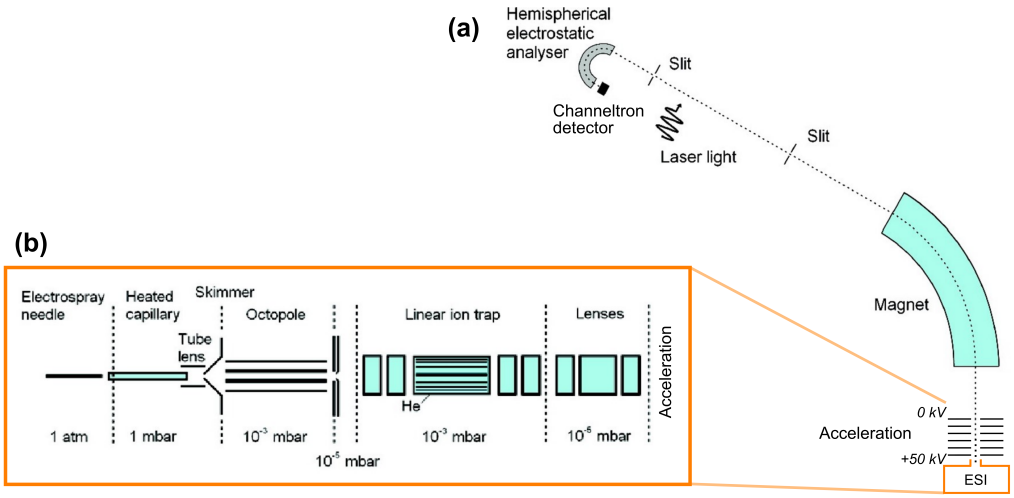


Figure 4.3: Schematic representation of **(a)** the Sep1 accelerator mass spectrometer used to study the photodissociation of the *p*HBDI$^-$ series. Insert **(b)** shows the apparatus for ion-packet formation. The ions, produced by electrospray ionisation, pass through a heated capillary before being collected in an octupole ion trap. At 25 ms intervals, ion packets are ejected and accelerated to a kinetic energy of ≈50 keV. The ions of interest are mass separated by the bending magnet and then traverse the linear flight region, where every second ion bunch is excited by a laser pulse, causing dissociation. The electrostatic analyser separates the fragment ions, which are counted by the channeltron detector. Adapted from Støchkel *et al.*[28]

(1–2 mJ pulse^{-1}). The photoinduced signal was measured, as a function of wavelength, as the difference in the number of counts between the 'laser-on' and 'laser-off' injections of ion bunches.

4.3 Theoretical methods

Electronic structure calculations were performed using Gaussian 16.B01,[46] ORCA 5.0.1,[47,48] and PSI4 1.3.2.[49] Anion-betaine cluster geometries were first computed using the PM6 semi-empirical Hamiltonian from a large number of starting conformations, and involved placing the betaine molecule at various positions around the HBDI unit. The lowest energy complexed structures were reoptimised, and structures of the bare anions optimised, at the ωB97X-D/aug-cc-pVDZ level of theory.[50,51] Note that diffuse basis functions are important for the correct treatments of both the anionic chromophore and the anionic

portion of betaine, and also to describe the dipole moment of betaine. Vibrational frequency calculations provided zero-point energy (ZPE) corrections. These calculations revealed three betaine binding positions (Figure 4.4(a)): **(1)** coordination to the phenoxide O(1) atom, **(2)** coordination to the imidazolinone O(2) atom, and **(3)** side-one coordination over the π-bonding system (Figure 4.4(b)).

Using the optimised clusters for each binding site and the geometries of each bare anion, the relative energies and adiabatic bond dissociation energies were computed at the DLPNO-CCSD(T)/aug-cc-pVDZ level of theory (TightPNO setting) in ORCA 5.0.1.[47,48] DLPNO (domain-based local pair-natural orbital coupled-cluster, with singles and doubles excitations) approaches are an efficient way to work on large molecules with coupled-cluster (CC) methods. The computational cost of CC methods on large systems is often prohibitive. For example, full CCSD(T) calculations on the present complexes are extremely expensive and would be prohibitively so on larger complexes. How-

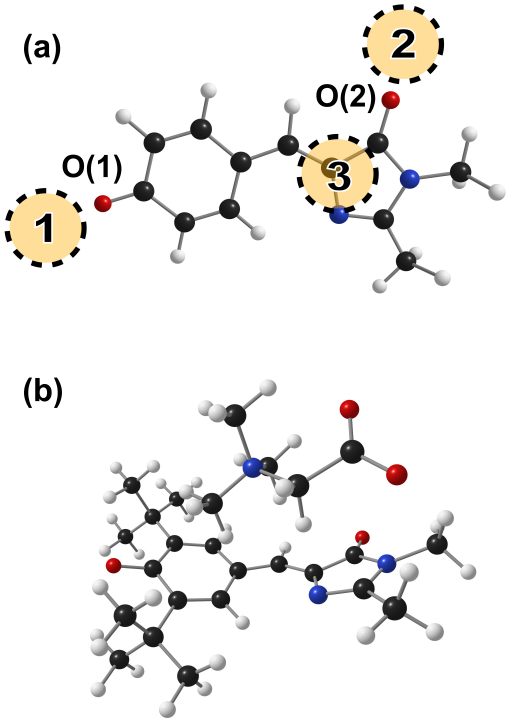


Figure 4.4: Anion-betaine complexes with **(a)** the major binding sites (**1**-**3**) for betaine, shown on *p*HBDI$^-$. O(1) and O(2) indicate the phenoxide and imidazolinone oxygen atoms, the former being the deprotonation site. **(b)** The side-on interaction between an HBDI anion and betaine, shown for the 35Bu$^-$·Z(**3**) cluster.

ever, DLPNO-CCSD methods exhibit near-linear scaling with system size, allowing large molecules to be tackled at a reasonable computational expense.[52] Furthermore, benchmarking studies have consistently demonstrated that the DLPNO-CCSD(T) method is able to compute energies to within $2\,\mathrm{kJ\,mol^{-1}}$ of the corresponding CCSD(T) value.[53–55] The "TightPNO" setting refers to a specific, tighter, set of threshold parameters for convergence that can be applied to DLPNO calculations.

Basis set superposition error (BSSE) corrections were performed using the Counterpoise method.[56] The BSSE is an important consideration in complexed systems where the constituent fragments bind through non-covalent interactions.[57] Consider a dimer complex AB. The interaction energy between the constituent monomers A and B is described as:

$$\Delta E_{\mathrm{IE}} = E_{\mathrm{AB}}^{\mathrm{AB}} - E_{\mathrm{A}}^{\mathrm{AB}} - E_{\mathrm{B}}^{\mathrm{AB}} \tag{4.1}$$

where the subscripts indicate the species and superscripts represent the basis set with which the energy is calculated. In the dimer, the monomers share their atomic basis functions; the extent to which depends on intermolecular distance.[58] This results in a more flexible wavefunction, since atomic basis functions on one monomer can influence the *intra*molecular bonding on the other monomer, lowering the dimer energy (*i.e.* yielding an overstabilised dimer complex).[59–61] The Counterpoise (CP) correction method, as introduced by Boys and Bernardi,[56] provides an approximation of the BSSE size. It is calculated as the sum of the stabilisation of monomer A in the dimer by monomer B and *vice versa*:

$$\Delta E_{\mathrm{BSSE}} = \left(E_{\mathrm{A}}^{\mathrm{AB}} - E_{\mathrm{A}}^{\mathrm{A}}\right) + \left(E_{\mathrm{B}}^{\mathrm{AB}} - E_{\mathrm{B}}^{\mathrm{B}}\right) \tag{4.2}$$

where the subscripts indicate the species and superscripts represent the calculation basis set. While BSSE is important for all non-covalently bound complexes, its inclusion is particularly necessary when using smaller basis sets.[57] Benchmarking studies have shown that double- and triple-ζ basis sets are affected by some BSSE (typically 5–10%); however, BSSE becomes irrelevant when basis set size reaches the complete basis set limit.[62] Note that, in general, BSSE can be ignored when using basis sets of equal or greater quality to the augmented triple-ζ size, or when the complex binding energy is large (*e.g.* $> 2\,\mathrm{eV}$).[57]

4.3.1 Vertical excitation wavelengths

Vertical excitation energies (VEEs) for the $S_1\,(\pi\pi^*) \leftarrow S_0$ transition of the bare anions and the anion-betaine complexes were computed at the DLPNO-STEOM-CCSD/aug-

cc-pVDZ level of theory.[63] DLPNO-STEOM-CCSD was favoured over other "efficient" wavefunction theories, such as CC2 or ADC, because of good performance in several recent benchmarking studies focussing on quantum chemical approaches to explore the effect of protein environment on electrochemical shifts.[23,26]

The contribution from electrostatic interactions to the betaine-induced spectral shift was explored by computing vertical excitation energies in a point-charge model framework for the anion-betaine complexes. In the point-charge model, betaine atoms in the geometry-optimised complexes were replaced with point charges computed from one of three population schemes: (i) minimum basis set Mulliken populations (MBS),[64] (ii) natural bond order populations (NBO),[65] and (iii) Hirshfeld-CM5 populations (CM5).[66] MBS Mulliken populations are preferred over Mulliken populations computed with the aug-cc-pVDZ basis set because those obtained from 'large' or extended basis sets are known to produce non-physical results due to incomplete orbital localisation.[64] The NBO method is based on a traditional Lewis structure view of bonding and has proven to be a highly successful formulation. In NBO, the wavefunction is localised either on one (lone pair) or two centres (bonds), rather than being delocalised over the whole structure.[67] The final method, CM5, can be advantageous over other models, such as Mulliken or NBO analyses, because the predicted dipole moments are, on average, more accurate.[66] Furthermore, CM5 is effectively basis set independent, so does not exhibit large changes in atomic charges with small variations in basis set, unlike Mulliken population analyses.[66,68] These population schemes were considered in order to explore variation in computed atomic charges and because of ongoing discussion regarding which method provides the most robust set of point charges.

4.3.2 Symmetry-adapted perturbation theory (SAPT)

For small complexes (*e.g.* up to 15–20 atoms), accurate interaction energies between the fragments of the complex can be obtained by CCSD(T) calculations. If sufficiently converged to the complete basis set limit, CCSD(T) interaction energy calculations are the "*gold standard*".[70] For larger systems, symmetry-adapted perturbation theory (SAPT) is able to attain interaction energies of similar accuracy to CCSD(T) but, unlike CCSD(T), can decompose the interaction energy into physically meaningful terms.[71–73] These components are electrostatic, exchange, induction (polarisation), and dispersion terms.[70,71] Here, SAPT (as implemented in PSI4 version 1.3.2)[49] was used to analyse the bonding interactions in the anion-betaine complexes.

Table 4.1: Summary of the terms into which the SAPT0 interaction energy, E_{SAPT0} can be decomposed, accompanied by their definitions and physical interpretations.[69]

Term	**Definition**	**Physical Interpretation**
$E_{\mathrm{ES}}^{(1)}$	Electrostatic	Electrostatic (Coulomb) interactions between the charge densities of the fragments in the complex. Includes ionic, hydrogen-, and halogen-bonding.
$E_{\mathrm{EX}}^{(1)}$	Exchange repulsion	A consequence of the Pauli exclusion principle. Pauli repulsion effectively limits how close two electron densities approach to each other. Includes 'steric' interactions.
$E_{\mathrm{I,R}}^{(2)}$	Induction	Interactions between permanent and induced dipole moments. Alternatively described as the polarisation of the molecular orbitals of one species by the electric field of the other interacting fragment.
$E_{\mathrm{EX-I,R}}^{(2)}$	Exchange-induction	Exchange contribution to electrostatic induction. Arises due to coupling of the induction interaction and the exchange energy.
$E_{\mathrm{D}}^{(2)}$	Dispersion	Interactions between instantaneous dipole moments of the fragments in the complex, *i.e.* London dispersion forces. The weakest intermolecular forces that arise through temporary attractive forces due to instantaneous dipoles (*i.e.* induced-dipole induced-dipole attractions).
$E_{\mathrm{EX-D}}^{(2)}$	Exchange-dispersion	Exchange contribution to dispersion. Arises due to coupling of the dispersion interaction and the exchange energy.

The SAPT framework uses perturbation theory to express the interaction energy between fragments and requires many terms, although many are close to zero. A computationally cheaper, truncated form is often used, termed SAPT0. The truncated form is able to approximately account for both the intermolecular terms of Hartree-Fock (HF) theory and the dispersion terms of second-order Møller-Plesset perturbation theory (MP2).[71] The interaction energy, E_{SAPT0}, can be expressed as a series of summed terms:

$$E_{\mathrm{SAPT0}} = E_{\mathrm{ES}}^{(1)} + E_{\mathrm{EX}}^{(1)} + E_{\mathrm{I,R}}^{(2)} + E_{\mathrm{EX-I,R}}^{(2)} + E_{\mathrm{D}}^{(2)} + E_{\mathrm{EX-D}}^{(2)} \tag{4.3}$$

The superscripts (1) and (2) denote first- and second-order interactions, respectively. The terms are defined, with a brief explanation of their physical interpretation, in Table 4.1. Note that the *electrostatic*, *inductive*, and *dispersive* terms are long-range effects, while the inclusion of *exchange* terms is necessary for short-range effects.

4.4 Results and discussion

4.4.1 Photodissociation action spectra

Photodissociation action spectra for the bare anions and anion-betaine complexes were recorded by monitoring loss of a methyl group (the predominant photodissociation process) and loss of the betaine molecule, respectively (Figure 4.5). Wavelengths of maximum response for each spectrum are tabulated in Table 4.2. For *p*HBDI$^-$, the grey ELISA spectrum in Figure 4.5(a) is a total photoneutralisation spectrum for *p*HBDI$^-$ recorded in a high vacuum ion storage ring.[22] Neutral fragments include those formed through electron detachment and photodissociation processes and are recorded over a long acquisition window after photoexcitation (milliseconds). As a result, the ELISA action spectrum should closely parallel the actual gas-phase absorption spectrum. The close agreement of the ELISA *p*HBDI$^-$ spectrum and the present *p*HBDI$^-$ photodissociation action spectrum supports that the spectra in Figure 4.5 should be good proxies for the $S_1 \leftarrow S_0$ absorption profiles.

The photodissociation action spectra for the bare anions show a small red-shift in maximum wavelength with methylation (either 26Me$^-$ or 35Me$^-$) or tert-butylation (35Bu$^-$) of the core chromophore. This mirrors, to a lesser extent, trends seen in solution,[37] and is presumed to result from stabilising inductive effects from the alkyl functional groups.

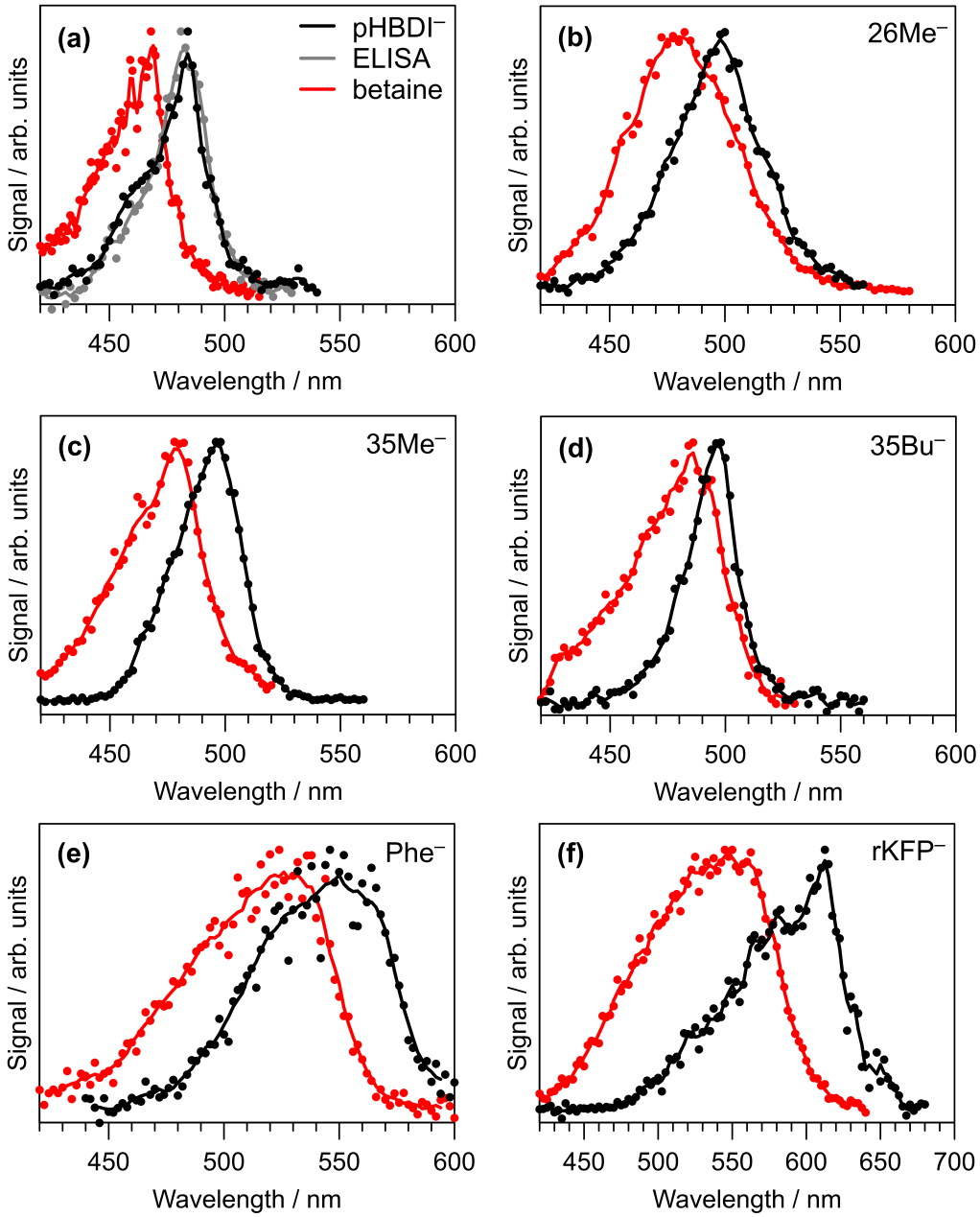


Figure 4.5: Photodissociation action spectra for various anion-betaine complexes and their bare ion counterparts: **(a)** *p*HBDI$^-$, **(b)** 26Me$^-$, **(c)** 35Me$^-$, **(d)** 35Bu$^-$, **(e)** Phe$^-$, and **(f)** rKFP$^-$. The black traces correspond to the bare ions, obtained by monitoring the loss of a methyl group (m/z = 15, >95% photodissociation yield), and the red traces correspond to data for the anion-betaine complexes, obtained by monitoring the formation of the bare anion, *i.e.* loss of the betaine molecule. The grey data in **(a)** are photoneutralisation measurements obtained using the ELISA ion storage ring at Aarhus University, taken from Langeland *et al.*[22]

On the other hand, there is a noticeable red-shift in the maximum response wavelengths for Phe^- and $rKPF^-$, compared with pHBDI$^-$, attributable to the extended conjugation. As shown in Table 4.2, there is a concomitant increase in the computed vertical detachment energy (VDE) for Phe^- and $rKFP^-$ because greater charge delocalisation results in increased electron binding forces. The ≈0.1 eV difference in the $35Bu^-$ VDE, relative to its alkylated-HBDI relatives, arises from a slight stabilisation effect due to the butyl groups.

Each of the target chromophore anions may exist as Z- and E- geometric isomers about the allyl bond connecting the two rings in the core pHBDI unit. However, the action spectra have been interpreted in terms of the Z-isomers only, for two reasons: (i) the synthesis and crystallisation procedure exclusively yields the Z-isomer, and (ii) it has been shown, by ion mobility experiments,[4] that pHBDI$^-$ electrosprayed at $T \approx 300$ K is produced in a single isomeric form (Z), with collisional activation of the electrosprayed ions required to generate and kinetically trap the E-isomer (calculated to lie 0.11 eV higher in energy than the Z-isomer).[74] The $Z \rightarrow E$ barrier was calculated at 1.26 eV, which is sufficiently large to prevent thermal isomerisation at room temperature.[74] In the present experiments, gentle ion source conditions were used to transfer nascent electrosprayed ions into high vacuum (i.e. minimal collisional activation), thus only the Z-isomers should be important. Gentle ion source conditions are also required to generate the anion-betaine complexes; anion-betaine complex binding energies (CBEs) are likely lower than the $Z \rightarrow E$ isomerisation barrier based on the value for pHBDI$^-$.

The betaine-induced spectral shifts (Δ) are summarised in Table 4.2. Note that, due to the high fluxionality of these complexes (arising from 'shallow' potential energy surfaces, characteristic of intermolecular complexes), these experimental betaine-induced spectral shifts correspond to average values for the complexes at $T \approx 300$ K. Compared with pHBDI$^-$·Z, the shifts are smaller for $26Me^-$·Z, $35Bu^-$·Z, and Phe^-·Z, but are larger for $35Me^-$·Z and $rKFP^-$·Z. The spectral shift measured for $rKFP^-$·Z ($\Delta = 0.24$ eV) is substantial and similar to those previously reported for the oxyluciferin (≈0.2 eV) and m-nitrophenolate (≈0.3 eV) anions,[33] but less than half of that for protonated Schiff base retinal (≈0.6 eV).[75] Both the m-nitrophenolate and the protonated Schiff base retinal in the gas phase are systems that undergo CT transitions; these trends suggest that the $S_1 \leftarrow S_0$ transition in $rKFP^-$ has significant CT character.

The photodissociation action spectra can be compared with earlier aqueous and ethanol absorption spectra (Table 4.3). In aqueous solution, all six chromophores show blue spec-

Table 4.2: Action spectra wavelengths of the maximum responses for bare anion photodissociation (λ_{anion}) and anion-betaine complex photodissociation (λ_{complex}) (see spectra in Figure 4.5). The betaine-induced spectral shift is Δ. VDE_{calc} is the vertical detachment energy calculated at the DLPNO-CCSD(T)/aug-cc-pVDZ level of theory for the bare anion. Uncertainty in Δ is approximately ± 0.01 eV.

Species	λ_{anion} / nm	λ_{complex} / nm	Δ / eV	VDE_{calc} / eV
*p*HBDI$^-$	484±2	468±2	0.09	2.62
26Me$^-$	498±2	483±2	0.08	2.69
35Me$^-$	498±2	476±2	0.13	2.60
35Bu$^-$	498±2	486±2	0.06	2.75
Phe$^-$	552±5	539±5	0.05	2.82
rKFP$^-$	615±2	550±5	0.24	2.96

Table 4.3: Photon energies at absorption maxima for the bare anions in aqueous (E_{aq}) and ethanol (E_{eth}) solution. Values in parentheses are spectral shifts relative to the anion gas-phase photodissociation action spectra. [a]Ref. 37. [b]Ref. 43.

Species	E_{aq} / eV	E_{eth} / eV
*p*HBDI$^-$	2.92[a] (0.36)	2.81[a] (0.24)
26Me$^-$	3.02[a] (0.53)	2.81[a] (0.32)
35Me$^-$	2.76[a] (0.27)	2.60[a] (0.12)
35Bu$^-$	2.52[a] (0.03)	2.44[a] (−0.05)
Phe$^-$	2.74 (0.50)	2.59 (0.34)
rKFP$^-$	2.52[b] (0.50)	2.34 (0.32)

tral shifts (particularly 26Me$^-$), although the 35Bu$^-$ spectral shift is small. In ethanol, five of the six chromophores show blue spectral shifts, although to a lesser extent than in aqueous solution. The red spectral shift for 35Bu$^-$ in ethanol, compared to the gas phase and the small blue shift in aqueous solution, is consistent with the tert-butyl groups sterically encumbering solvation, thus limiting stabilisation of the deprotonation site.

Comparing the betaine-induced spectral shifts (Table 4.2) with the solution absorption spectra, it is observed that the aqueous-solvation-induced shifts for *p*HBDI$^-$ and 35Me$^-$ are approximately four-fold and two-fold larger than the betaine-induced spectral shift,

while the 26Me$^-$ aqueous shift is around seven-fold larger. In contrast, for 35Bu$^-$ the betaine-induced spectral shift is nearly double the aqueous shift. The solvent-induced shifts in water for the Phe$^-$ and rKFP$^-$ species are larger than for *p*HBDI$^-$, but similar to that for 26Me$^-$. Overall, these trends indicate that the betaine binding pattern is important in determining the magnitude of the solvation-induced shift.

4.4.2 Anion-betaine binding

The optimised geometries for the anion-betaine complexes reveal three low energy coordination patterns, shown in Figure 4.4. Betaine binding site **1** has the positive end of the betaine molecule coordinated to the phenoxide oxygen atom O(1). Betaine binding site **2** has the positive end of the betaine molecule coordinated to the imidazolinone oxygen atom, O(2). In these geometries, the anion and betaine molecule are roughly in the same plane. For betaine binding site **3**, the betaine molecule is positioned side-on over the π-bonding system (the core HBDI unit), with the positive end of the betaine molecule directed toward the phenoxide oxygen atom – see example in Figure 4.4(b). The relative anion-betaine complex energies calculated at the DLPNO-CCSD(T)/aug-cc-pVDZ level of theory are given in Table 4.4. Aside for 26Me$^-$·Z and 35Bu$^-$·Z, betaine binding site **1** (coordination to the phenoxide deprotonation site) corresponds to the lowest energy complex. For 26Me$^-$·Z, the preference for betaine binding site **3** is linked to torsion of the allyl backbone due to intramolecular steric interactions by the methyl groups (Figure 4.6). For 35Bu$^-$·Z the preference for betaine binding site **3** is related to the steric interactions from the tert-butyl groups flanking the phenoxide. The conclusion drawn from this is that the tert-butylation provides sufficient steric bulk around the

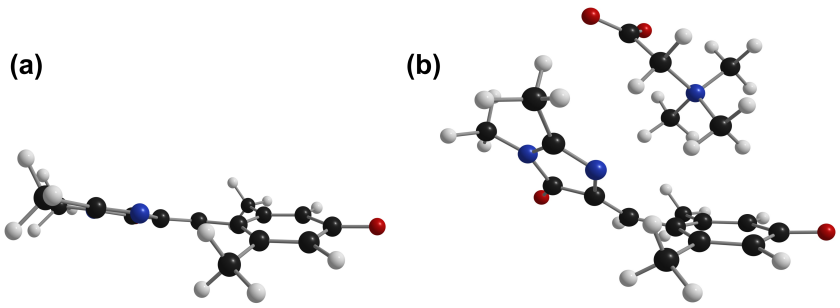


Figure 4.6: Illustrations of (a) 26Me$^-$ and (b) 26Me$^-$·Z(**3**) complex involving side-on binding, showing the internal twist about the core *p*HBDI bridge due to steric interactions from the methyl groups.

deprotonation site to inhibit coordination of betaine at site **3**.

The relative energies of the complexes (Table 4.4) were sensitive to the incorporation of basis set superposition error (BSSE) corrections. As discussed in Section 4.3, BSSE is an important consideration in non-covalently bound systems, such as these HBDI-betaine complexes. Furthermore, BSSE is larger for smaller basis sets, such as double-ζ. When the BSSE corrections were neglected, betaine binding site **3** was calculated as the lowest energy structure for each chromophore (true both at the ωB97X-D/aug-cc-pVDZ and MP2/aug-cc-pVDZ levels of theory). This is presumably because of the increased variational freedom in wavefunction description due to betaine atomic orbital functions describing the π-system on the *p*HBDI unit, since BSSE corrections are ≈10% for betaine binding sites **1** and **2**, and ≈30% for site **3**.

Table 4.4: Relative anion-betaine complex energy (E) for binding site **1**/**2**/**3**. CBE is the dissociation energy for the complex, i.e. anion-betaine → anion + betaine, for betaine binding site **1**/**2**/**3**. VDE is the vertical detachment energy of the complex for betaine binding site **1**/**2**/**3**. All values are at the DLPNO-CCSD(T)/aug-cc-pVDZ level of theory and include BSSE correction.

Species	E / meV	CBE / eV	VDE / eV
*p*HBDI$^-$·Z	0 / 145 / 52	1.09 / 0.95 / 1.04	3.66 / 3.61 / 3.64
26Me$^-$·Z	73 / 228 / 0	1.03 / 0.86 / 1.09	3.69 / 3.67 / 3.71
35Me$^-$·Z	0 / 145 / 62	1.02 / 0.87 / 0.96	3.61 / 3.50 / 3.57
35Bu$^-$·Z	83 / 104 / 0	0.88 / 0.85 / 0.96	3.81 / 3.60 / 3.77
Phe$^-$·Z	0 / 166 / 10	0.95 / 0.78 / 0.94	3.71 / 3.64 / 3.71
rKFP$^-$·Z	0 / 83 / 31	0.88 / 0.80 / 0.85	3.85 / 3.69 / 3.83

As a check of relative complex stability with improved basis set description, the energies for the *p*HBDI$^-$·Z complex were computed at the DLPNO-CCSD(T)/def2-TZVP level of theory with and without inclusion of BSSE corrections. At this level of theory, the BSSE corrections are much smaller and betaine binding site **1** is predicted to be 31 meV more stable than binding site **3**. The conclusion is that binding site **1** is the preferential site in the gas-phase for *p*HBDI$^-$, 35Me$^-$, Phe$^-$ and rKFP$^-$, although the electrosprayed ion beam at $T \approx 300$ K may have a minor contribution from binding site **3** complexes. The relative propensity of various cluster binding sites can be informed by Boltzmann population (Table 4.5):

$$\frac{N_c}{N_t} = e^{\left(-\frac{\varepsilon_c}{k_B T}\right)} \tag{4.4}$$

where ε_c is the relative energy of a cluster, and the fraction of $^{N_c}/_{N_t}$ shows the relative population of a given cluster form (N_c is the cluster population and N_t is the total population), k_B is the Boltzmann constant, and T is temperature. The $^{N_c}/_{N_t}$ ratio is a useful measure of the stability/favourability of particular cluster binding site.

Adiabatic anion-betaine complex binding energies (CBEs) and vertical detachment energies (VDEs) including BSSE corrections are given in Table 4.4. CBE values for sites **1** and **3** are 0.9–1.1 eV, which is roughly twice that for *p*HBDI$^-$·H_2O complexes.[76,77] However, since absorption of a single visible photon imparts sufficient energy to dissociate each complex, the anion-betaine photodissociation action spectra should parallel the absorption spectra. The computed VDE values are all roughly 1 eV higher for the complexes relative to the bare anions. Interestingly, each anion-betaine cluster $S_1 \leftarrow S_0$ absorption band (Figure 4.5) lies below the respective detachment threshold (Table 4.4), which will have important implications for the gas-phase excited state dynamics. In particular, it is known that excitation of *p*HBDI$^-$ at $T \approx 300$ K in the gas phase, at a photon energy near the maximum response in the $S_1 \leftarrow S_0$ band, results in a competition between vibrational autodetachment, internal conversion, and isomerisation on a sub-picosecond timescale.[4,78,79] Autodetachment occurs when the total internal energy exceeds the electron binding energy. The betaine complexes have higher VDEs (electron

Table 4.5: Relative anion-betaine complex energy, ΔE in kJ mol^{-1} and relative Boltzmann population, $\frac{N_c}{N_t}$, relative to the lowest energy binding site complex for each anion-betaine species. (Assumes DLPNO-CCSD(T)/aug-cc-pVDZ + BSSE energies).

Species	**ΔE**	$\mathbf{N_c/N_t}$	**Species**	**ΔE**	$\mathbf{N_c/N_t}$
*p*HBDI$^-$·Z(**1**)	0.0	1.0	35Bu$^-$·Z(**1**)	8.2	3.7×10^{-2}
*p*HBDI$^-$·Z(**2**)	14.0	3.6×10^{-3}	35Bu$^-$·Z(**2**)	10.4	1.5×10^{-2}
*p*HBDI$^-$·Z(**3**)	5.0	1.3×10^{-1}	35Bu$^-$·Z(**3**)	0.0	1.0
26Me$^-$·Z(**1**)	6.6	7.2×10^{-2}	Phe$^-$·Z(**1**)	0.0	1.0
26Me$^-$·Z(**2**)	22.2	1.4×10^{-4}	Phe$^-$·Z(**2**)	16.4	1.4×10^{-3}
26Me$^-$·Z(**3**)	0.0	1.0	Phe$^-$·Z(**3**)	0.8	7.4×10^{-1}
35Me$^-$·Z(**1**)	0.0	1.0	rKFP$^-$·Z(**1**)	0.0	1.0
35Me$^-$·Z(**2**)	14.1	3.5×10^{-3}	rKFP$^-$·Z(**2**)	8.1	3.9×10^{-2}
35Me$^-$·Z(**3**)	5.8	9.9×10^{-2}	rKFP$^-$·Z(**3**)	2.7	3.4×10^{-1}

affinities) than the isolated anion; as a result, the autodetachment channel of the complexes is closed, since the solution absorption spectra do not shift much, relative to the gas-phase action spectra (see VDE values in Table 4.3). This is a similar situation to that in the protein environment. Time-resolved spectroscopy on the betaine complexes may prove insightful for exploring microperturbations to the chromophore photophysics.

4.4.3 SAPT analysis

The anion-betaine intermolecular binding interactions were analysed using SAPT theory to obtain the total SAPT0 energy and decomposed terms for each complex (Table 4.6). The total SAPT0 energies (E_{SAPT0}), when expressed as CBE values, indicate an overestimation of the intermolecular complexion energy by ≈10% compared with the (adiabatic) DLPNO-CCSD(T) values in Table 4.4. A substantial source of this overestimation is the failure of the SAPT framework to include geometry relaxation for separated fragments when calculating diabatic energies, the absence of which is not remedied within the SAPT framework. Inspection of SAPT term pairs in Table 4.6 (binding interaction with the corresponding exchange contribution) reveal several general trends:

- The electrostatic term dominates complex cohesion for betaine binding sites **1** and **2** for each of the six chromophores. While O(1) is the deprotonation site, electron delocalisation through conjugation to O(2) likely means that the electrostatic term is dominated by charge-dipole interactions in both complex geometries (**1** and **2**). Taking into account Pauli repulsion, the electrostatic term accounts for 40–50% of the interaction energy (30% for $35Bu^{-}\cdot Z(\mathbf{1})$), while induction and dispersion account for ≈30% and ≈20%, respectively.

- The predominant interaction for betaine binding site **3** are dispersion forces, accounting for 50–60% of the complex binding energy. Although the electrostatic and induction terms are substantial for these complexes, they are largely countered by Pauli exchange due to the extensive overlap of the occupied molecular orbitals of the two fragments (large volume interaction between betaine and the HBDI species *via* the HBDI species' π-system).

- For betaine binding sites **1** and **3**, increase of the basis set to jun-cc-pVTZ yielded only small changes in each term, indicating that the jun-cc-pVDZ basis set should provide a satisfactory description (provided fortuitous BSSE cancellation).

As shown in Table 4.4, the relative anion-betaine complex energy (E) is less for binding

site **1** than site **2**. The greater stability of position **1**, relative to **2**, is likely related to properties of the deprotonation site. Since O(1) is deprotonated, there are strong electrostatic interactions between the anion and betaine at position **1**. Although conjugation in the anions allows the O(1) negative charge to be delocalised to O(2), the electrostatic interactions will nevertheless be weaker at site **2**. This stability trend is also observed in the relative Boltzmann populations (Table 4.5), where the value for binding site **1** is up to four orders of magnitude larger than for site **2**, and sites **1** and **3** are separated by approximately two orders of magnitude.

One of the original motivations to study this series of chromophore was because alkylation around the phenoxide deprotonation site (O(1)) may sterically hinder betaine binding. This appears to be the case for the 35Bu$^-$·Z complex. In this case, betaine binding site **3** corresponds to the lowest energy complex, in contrast to *p*HBDI$^-$·Z and 35Me$^-$·Z, which favour binding site **1** in terms of stability (Table 4.4). The SAPT0 terms for the *p*HBDI$^-$·Z $\rightarrow$ 35Me$^-$·Z $\rightarrow$ 35Bu$^-$·Z alkylation series only shows a small decrease in the electrostatic term ($E_{ES}^{(1)}$) for 35Me$^-$·Z(**1**) compared with *p*HBDI$^-$·Z(**1**), but a significant decrease for 35Bu$^-$·Z(**1**) when considering the Pauli repulsion term ($E_{EX}^{(1)}$). This is unsurprising given that the Pauli repulsion term accounts for steric effects, which is a significant consideration for 35Bu$^-$, as the phenoxide (O(1)) is sterically crowded. On the other hand, there is an increase in the dispersion forces for 35Bu$^-$ complexes to $\approx$40% such that they dominate complex cohesion. As for 35Bu$^-$ and 26Me$^-$, binding site 3 is the most favourable complex and dispersion forces dominate the interactions, although the change in electrostatic and dispersion interactions between Z(1) and Z(3) are smaller for 35Bu$^-$ than for 26Me$^-$.

In summary, betaine molecules coordinated to the phenoxide sites of *p*HBDI-based chromophores are predominately bound through electrostatic forces. In general, these geometries correspond to the lowest energy complexes. However, introduction of steric hindrance from tert-butyl groups around the deprotonation site leads to alternative complex binding in which dispersion forces become dominant.

Table 4.6: Symmetry adapted perturbation theory (SAPT) analysis of the anion-betaine complexes. Contributions with superscript (1) are a first-order perturbation terms, and those with superscript (2) are second-order perturbation terms. Negative and positive terms indicate binding and repulsive interactions, respectively. Energies are in kJ mol^{-1} except for the complex binding energy (CBE), which is in eV. SAPT analysis was performed using the jun-cc-pVDZ basis set, except in the cases of: [a]aug-cc-pVDZ basis set and [b]jun-cc-pVTZ basis set. * indicates the lowest energy structure.

Species	$\mathbf{E_{ES}^{(1)}}$	$\mathbf{E_{EX}^{(1)}}$	$\mathbf{E_{I,R}^{(2)}}$	$\mathbf{E_{EX-I,R}^{(2)}}$	$\mathbf{E_{D}^{(2)}}$	$\mathbf{E_{EX-D}^{(2)}}$	$\mathbf{E_{SAPT0}}$	**CBE**
* *p*HBDI$^-$·Z(**1**)	-131.6	72.3	-57.0	14.7	-28.6	5.3	-124.9	1.29
*p*HBDI$^-$·Z(**1**)^a	-128.5	72.9	-57.7	14.7	-36.2	6.3	-128.5	1.33
*p*HBDI$^-$·Z(**1**)^b	-128.3	72.8	-59.1	15.8	-37.8	6.6	-129.9	1.35
*p*HBDI$^-$·Z(**2**)	-106.3	58.3	-40.2	10.9	-27.5	4.2	-100.4	1.04
*p*HBDI$^-$·Z(**3**)	-114.4	92.8	-61.3	23.2	-71.4	8.9	-122.2	1.27
*p*HBDI$^-$·Z(**3**)^b	-111.9	92.7	-61.3	24.2	-87.0	10.6	-135.0	1.40
26Me$^-$·Z(**1**)	-130.1	72.3	-57.5	18.7	-34.4	6.0	-125.9	1.30
26Me$^-$·Z(**2**)	-107.7	63.1	-41.1	11.5	-32.8	4.7	-102.3	1.06
* 26Me$^-$·Z(**3**)	-133.2	102.7	-66.0	24.6	-80.4	10.0	-142.3	1.48
* 35Me$^-$·Z(**1**)	-131.2	78.0	-58.6	15.4	-34.5	5.9	-125.1	1.30
35Me$^-$·Z(**1**)^b	-127.9	78.4	-60.7	16.6	-44.6	7.2	-130.6	1.36
35Me$^-$·Z(**2**)	-107.9	59.2	-41.1	11.1	-27.8	4.3	-102.3	1.06
35Me$^-$·Z(**3**)	-116.4	95.4	-63.2	24.2	-73.9	9.2	-124.8	1.29
35Me$^-$·Z(**3**)^b	-113.7	95.3	-65.5	12.3	-89.8	10.9	-137.6	1.43
35Bu$^-$·Z(**1**)	-114.6	81.0	-50.4	13.8	-49.3	6.3	-113.1	1.17
35Bu$^-$·Z(**2**)	-104.3	57.2	-39.4	10.7	-27.9	4.2	-99.5	1.03
* 35Bu$^-$·Z(**3**)	-124.2	110.3	-72.9	26.5	-89.0	10.7	-138.7	1.44
* Phe$^-$·Z(**1**)	-126.2	69.1	-54.4	13.5	-22.8	5.1	-120.7	1.25
Phe$^-$·Z(**2**)	-90.9	52.2	-37.5	11.7	-26.9	3.9	-87.4	0.91
Phe$^-$·Z(**3**)	-110.2	91.4	-59.1	22.6	-73.9	9.1	-120.1	1.25
* rKFP$^-$·Z(**1**)	-117.9	66.5	-52.1	16.5	-31.1	5.3	-112.7	1.17
rKFP$^-$·Z(**2**)	-100.4	55.9	-38.4	10.4	-27.1	4.1	-95.6	0.99
rKFP$^-$·Z(**3**)	-112.1	97.2	-64.8	24.0	-79.3	9.6	-125.4	1.30

4.4.4 Anion-betaine spectral shifts

Vertical excitation wavelengths for the $S_1(\pi\pi^*) \leftarrow S_0$ transition in the bare anions, anion-betaine complexes, and anion–point-charge complexes were computed at the STEOM-DLPNO-CCSD/aug-cc-pVDZ level of theory (Table 4.7). The full quantum mechanical (QM) treatment of the anion-betaine complexes includes betaine in the *ab initio* calculation, while point-charge models only treat the electrostatic terms of betaine (represented by a point charge). Three point-charge models (MBS, NBO, and CM5) are assessed, as they have different strategies for distributing charge density over the betaine atom (Section 4.3.1).

As mentioned in Section 4.4.1, the experimental betaine-induced shifts correspond to averaged values for the complexes at $T \approx 300\,\mathrm{K}$. For example, the calculated average thermal energy, from a harmonic partition function, for pHBDI$^-$·Z(1) at $T = 300\,\mathrm{K}$ is 0.67 eV, which is nearly two thirds of the cluster binding energy. Comparisons between calculations (which assume only equilibrium geometries) and experiments focus on trends (*e.g.* mean deviations across the series) rather than quantitative agreement.

In general, the computed bare anion transition wavelengths (Table 4.7) are in good accord with the experimental data as, over the chromophore series, the mean deviation between the computed and experimental wavelength in terms of photon energy is 0.04 eV. Of the anions, 35Me$^-$ presents the largest deviation (0.06 eV) while, of the lowest energy anion-betaine complexes, the largest deviation (0.07 eV) is in rKFP$^-$·Z(1). Overall, however, the mean deviation in the lowest energy anion-betaine complexes matches that of the bare anion (0.04 eV), indicating that the betaine-induced spectral shift is accounted for satisfactorily at the STEOM-DLPNO-CCSD/aug-cc-pVDZ level of theory. Although computational expense can be decreased using point-charge models, this comes at a detriment to computational accuracy. The point-charge treatment of the anion-betaine complexes correctly predict blue-shifted absorption (relative to the bare anion), but the overall agreement with experiment is substantially worse (particularly for CM5). To illustrate this, the mean deviations of the point charge models, relative to experiment, were 0.04 eV, 0.07 eV, and 0.10 eV, for MBS, NBO, and CM5, respectively. Therefore, more than just electrostatic and point-charge induction forces are necessary to account for experimental anion-betaine spectral shifts. Fortunately, the favourable computational scaling of the STEOM-DLPNO-CCSD method allows the present methodology (full description of betaine) to be applied to substantially larger betaine complexes, on conventional laboratory computing resources. To illustrate this,

Table 4.7: Calculated $S_1 \leftarrow S_0$ transition wavelengths for the bare anions, anion-betaine complexes, MBS (PC-M), NBO (PC-N), and CM5 (PC-C) point charge models of betaine. Wavelengths were computed at the DLPNO-STEOM-CCSD/aug-cc-pVDZ level of theory. Values in parentheses are deviations (in eV) from the experimental data (action spectra, Table 4.2). For S_1 Z(**1**/**2**/**3**), deviations (relative to experiment) are included for the lowest energy anion-betaine complexes.

Species	S_1 anion	S_1 Z(**1**/**2**/**3**)	S_1 PC-M[Z(**1**/**2**/**3**)]	S_1 PC-N[Z(**1**/**2**/**3**)]	S_1 PC-C[Z(**1**/**2**/**3**)]
*p*HBDI$^-$	494 (0.05)	463 (0.03) / 479 / 485	432 / 387 / 477	441 / 389 / 475	447 / 390 / 479
26Me$^-$	499 (0.00)	479 / 444 / 490 (0.04)	480 / 477 / 476	487 / 449 / 468	481 / 458 / 448
35Me$^-$	510 (0.06)	469 (0.04) / 490 / 492	460 / 483 / 470	460 / 499 / 486	470 / 460 / 474
35Bu$^-$	507 (0.04)	485 / 498 / 480 (0.03)	464 / 505 / 487	469 / 499 / 490	476 / 507 / 475
Phe$^-$	564 (0.05)	551 (0.05) / 567 / 533	538 / 506 / 531	542 / 548 / 527	548 / 544 / 536
rKFP$^-$	608 (0.02)	568 (0.07) / 568 / 541	573 / 576 / 551	568 / 575 / 549	585 / 582 / 554

it took ≈12 hours to compute the first three excited states of the 35Bu$^-$·Z(3) complex (69 atoms), while the point-charge model calculations for the 35Bu$^-$·Z complexes took ≈4 hours (laboratory computer with dual Xeon E5-2680v2 CPUs and 256 GB RAM).

It is necessary to mention that the complexation of betaine causes geometric changes to the chromophore anions. For betaine binding sites **1** and **2**, the perturbation is small, while binding at site **3** results in greater distortions because side-on binding causes internal twisting of the allyl bridge. 26Me$^-$·Z(3) and 35Bu$^-$·Z(3), which are the lowest energy geometries for these anion-betaine complexes, are used to illustrate this. The methylene-bridge dihedral angle is distorted from 18° in 26Me$^-$, to 39° in 26Me$^-$·Z(3) (Figure 4.6). For 35Bu$^-$·Z(3), the dihedral angle is 19°. These twists alter the transition energy, compared to the bare anion, by ≈0.04 eV, accounting for much of the betaine-induced spectral shift. Therefore, it is concluded that, for betaine binding site **3**, a significant portion of the betaine-induced shift results from distortion of the chromophore backbone. Note that the present calculations consider only minimum-energy geometries and do not account for gas-phase fluxionality in the experimental data.

4.5 Conclusion and future work

Photodissociation action spectra at $T \approx 300$ K were recorded for bare anions and betaine complexes of six *p*HBDI-based molecules. In each case, betaine complexation leads to a blue-shift of the action spectrum. It is shown that the preferential binding site for betaine changes with functionalisation of the core *p*HBDI unit. Coordination through the phenoxide deprotonation site is dominated by electrostatic forces, although induction and dispersion forces have an important contribution to complex cohesion. On the other hand, steric crowding around the deprotonation site and/or allyl backbone torsion results in a side-on complex geometry (complexes 26Me$^-$·Z and 35Bu$^-$·Z), in which dispersion forces dominate. The anion-betaine spectral shifts are readily reproduced using the STEOM-DLPNO-CCSD method, although with the caveat that comparison with experiment is not always trivial due to fluxionality of the chromophore structures. In reproducing the anion-betaine spectral shifts, point-charge models produce less satisfactory results, compared with full quantum mechanical methods. This is consistent with the fact that induction and dispersion forces are important for complex cohesion, as only electrostatic effects are considered in point-charge models. The methodology assumed in this work could be applied to characterise other anion-betaine complexes and, presumably, also more general ion-zwitterion complexes.

One of the original motivations for development of the betaine tagging strategy was to inform on the charge-transfer character of electronic transitions, provided there is a single and known betaine binding site for asymmetric target molecules. While the $S_1 \leftarrow S_0$ transition for *p*HBDI$^-$ in the gas phase or in GFP is thought to involve some degree of inherent charge-transfer character,[39,80] deployment of a robust theoretical framework to interpret betaine-induced shifts in the chromophores investigated in this work would be a useful direction for future studies.

This work has considered the successful SAPT theory to analyse non-covalent interactions in anion-betaine complexes. As detailed in Section 4.4.3, SAPT is based on tried and tested perturbation theory; however, truncation of perturbation theory terms (*e.g.* to second order) for computational feasibility introduces approximations. Recently, a new framework, termed local energy decomposition (LED), has been reported and benchmarked against SAPT.[81] This method is still fairly new, but is continuing to gain traction; it may prove a more robust energy decomposition strategy than SAPT in the longer term. LED is based on decomposition of DLPNO-CCSD(T) interaction energies into electrostatic, exchange, dispersive, non-dispersive, and repulsive electronic correlation terms. DLPNO-CCSD(T) consistently yields energies within a few kJ mol^{-1} of the corresponding CCSD(T) value,[53–55,81,82] so the total interaction energy should be more accurate than that obtained from SAPT calculations.

Future work will include application of time-resolved strategies, such as femtosecond pump-probe photoelectron imaging, across a similar series of *p*HBDI-based chromophores and complexes. Complexation with various molecules (*e.g.* water, methanol, or betaine) will permit investigation of the effect of the complex on a chromophore's intrinsic photophysical properties, including excited-state lifetimes and photoisomerisation propensity,[4,79] and changes in vibrational autodetachment and internal conversion. The latter changes occur due to the increased electron detachment thresholds in the complexes. In a step towards this goal, time-resolved photoelectron data from *p*HBDI$^-$, 26Me$^-$, 35Me$^-$, and 35Bu$^-$ have been recorded, based on choosing pump wavelengths from the present photodissociation spectra. These data will form the basis of a future study in which the gas-phase data will be compared with solution-phase data and potential energy surface calculations.

References

[1] K. Addison, I. A. Heisler, J. Conyard, T. Dixon, P. C. B. Page and S. R. Meech, *Faraday Discussions*, 2013, **163**, 277–296.

[2] A. Henley and H. H. Fielding, *Int. Rev. Phys. Chem.*, 2019, **38**, 1–34.

[3] R. Y. Tsien, *Annu. Rev. Biochem.*, 1998, **67**, 509–544.

[4] E. Carrascosa, J. N. Bull, M. S. Scholz, N. J. A. Coughlan, S. Olsen, U. Wille and E. J. Bieske, *J. Phys. Chem. Lett.*, 2018, **9**, 2647–2651.

[5] H. M. Berman, J. Westbrook, Z. Feng, G. Gilliland, T. N. Bhat, H. Weissig, I. N. Shindyalov and P. E. Bourne, *Nucleic Acids Res.*, 2000, **28**, 235–242.

[6] A. Shinobu, G. J. Palm, A. J. Schierbeek and N. Agmon, *J. Am. Chem. Soc.*, 2010, **132**, 11093–11102.

[7] D. Sehnal, S. Bittrich, M. Deshpande, R. Svobodová, K. Berka, V. Bazgier, S. Velankar, S. K. Burley, J. Koča and A. S. Rose, *Mol**, 2021.

[8] D. Sehnal, S. Bittrich, M. Deshpande, R. Svobodová, K. Berka, V. Bazgier, S. Velankar, S. K. Burley, J. Koča and A. S. Rose, *Nucleic Acids Res.*, 2021, **49**, W431–W437.

[9] K. Brejc, T. K. Sixma, P. A. Kitts, S. R. Kain, R. Y. Tsien, M. Ormo and S. J. Remington, *Proc. Natl. Acad. Sci.*, 1997, **94**, 2306–2311.

[10] T. Wilhelmsson, *Fluorescent Analogs*, John Wiley & Sons, 2016.

[11] M. Drobizhev, P. R. Callis, R. Nifosì, G. Wicks, C. Stoltzfus, L. Barnett, T. E. Hughes, P. Sullivan and A. Rebane, *Sci. Rep.*, 2015, **5**, 13223.

[12] C.-Y. Lin, M. G. Romei, L. M. Oltrogge, I. I. Mathews and S. G. Boxer, *J. Am. Chem. Soc.*, 2019, **141**, 15250–15265.

[13] C.-Y. Lin and S. G. Boxer, *J. Am. Chem. Soc.*, 2020, **142**, 11032–11041.

[14] M. G. Romei, C.-Y. Lin, I. I. Mathews and S. G. Boxer, *Science*, 2020, **367**, 76–79.

[15] H.-W. Ai, S. G. Olenych, P. Wong, M. W. Davidson and R. E. Campbell, *BMC Biology*, 2008, **6**, 1–13.

[16] C. Filippi, F. Buda, L. Guidoni and A. Sinicropi, *J. Chem. Theor. Comput.*, 2011, **8**, 112–124.

[17] P. Amat and R. Nifosì, *J. Chem. Theor. Comput.*, 2012, **9**, 497–508.

[18] V. R. I. Kaila, R. Send and D. Sundholm, *Phys. Chem. Chem. Phys.*, 2013, **15**, 4491–4495.

[19] N. H. List, J. M. H. Olsen, H. J. A. Jensen, A. H. Steindal and J. Kongsted, *J. Phys. Chem. Lett.*, 2012, **3**, 3513–3521.

[20] J. W. Park and Y. M. Rhee, *J. Am. Chem. Soc.*, 2016, **138**, 13619–13629.

[21] S. B. Nielsen, A. Lapierre, J. U. Andersen, U. V. Pedersen, S. Tomita and L. H. Andersen, *Phys. Rev. Lett.*, 2001, **87**, 228102.

[22] J. Langeland, C. Kjær, L. H. Andersen and S. Brøndsted Nielsen, *ChemPhysChem*, 2018, **19**, 1686–1690.

[23] A. Sirohiwal, F. Neese and D. A. Pantazis, *J. Chem. Theory Comput.*, 2021, **17**, 1858–1873.

[24] F. Segatta, L. Cupellini, M. Garavelli and B. Mennucci, *Chem. Rev.*, 2019, **119**, 9361–9380.

[25] S. Maity, V. Daskalakis, M. Elstner and U. Kleinekathöfer, *Phys. Chem. Chem. Phys.*, 2021, **23**, 7407–7417.

[26] P.-F. Loos, A. Scemama and D. Jacquemin, *J. Phys. Chem. Lett.*, 2020, **11**, 2374–2383.

[27] J. A. Wyer and S. Brøndsted Nielsen, *Angew. Chem. Int. Ed.*, 2012, **51**, 10256–10260.

[28] K. Støchkel, B. F. Milne and S. B. Nielsen, *J. Phys. Chem. A*, 2011, **115**, 2155–2159.

[29] M. S. de Vries and P. Hobza, *Annu. Rev. Phys. Chem.*, 2007, **58**, 585–612.

[30] *Photophysics of Ionic Biochromophores*, ed. S. B. Nielsen and J. A. Wyer, Springer Berlin Heidelberg, 2013.

[31] J. N. Bull, E. Carrascosa, L. Giacomozzi, E. J. Bieske and M. H. Stockett, *Phys. Chem. Chem. Phys.*, 2018, **20**, 19672–19681.

[32] A. B. Wolk, C. M. Leavitt, E. Garand and M. A. Johnson, *Acc. Chem. Res.*, 2013, **47**, 202–210.

[33] M. H. Stockett, M. Boesen, J. Houmøller and S. Brøndsted Nielsen, *Angew. Chem. Int. Ed.*, 2017, **56**, 3490–3495.

[34] J. Rak, P. Skurski and M. Gutowski, *J. Chem. Phys.*, 2001, **114**, 10673–10681.

[35] T. Shikata, *J. Phys. Chem. A*, 2002, **106**, 7664–7670.

[36] K. B. Bravaya, B. L. Grigorenko, A. V. Nemukhin and A. I. Krylov, *Acc. Chem. Res.*, 2011, **45**, 265–275.

[37] J. Conyard, M. Kondo, I. A. Heisler, G. Jones, A. Baldridge, L. M. Tolbert, K. M. Solntsev and S. R. Meech, *J. Phys. Chem. B*, 2011, **115**, 1571–1577.

[38] A. Marini, A. Muñoz-Losa, A. Biancardi and B. Mennucci, *J. Phys. Chem. B*, 2010, **114**, 17128–17135.

[39] S. Olsen, *J. Phys. Chem. B*, 2014, **119**, 2566–2575.

[40] D. J. Tozer, *J. Chem. Phys.*, 2003, **119**, 12697–12699.

[41] A. Dreuw and M. Head-Gordon, *J. Am. Chem. Soc.*, 2004, **126**, 4007–4016.

[42] S. L. Li and D. G. Truhlar, *J. Chem. Theory Comput.*, 2015, **11**, 3123–3130.

[43] N. J. A. Coughlan, M. H. Stockett, C. Kjær, E. K. Ashworth, P. C. B. Page, S. R. Meech, S. B. Nielsen, L. Blancafort, W. S. Hopkins and J. N. Bull, *J. Chem. Phys.*, 2021, **155**, 124304.

[44] M. W. Forbes and R. A. Jockusch, *J. Am. Chem. Soc.*, 2009, **131**, 17038–17039.

[45] A. V. Bochenkova, B. Klaerke, D. B. Rahbek, J. Rajput, Y. Toker and L. H. Andersen, *Angew. Chem. Int. Ed.*, 2014, **53**, 9797–9801.

[46] M. J. Frisch, G. W. Trucks, H. B. Schlegel, G. E. Scuseria, M. A. Robb, J. R. Cheeseman, G. Scalmani, V. Barone, G. A. Petersson, H. Nakatsuji, X. Li, M. Caricato, A. V. Marenich, J. Bloino, B. G. Janesko, R. Gomperts, B. Mennucci, H. P. Hratchian, J. V. Ortiz, A. F. Izmaylov, J. L. Sonnenberg, D. Williams-Young, F. Ding, F. Lipparini, F. Egidi, J. Goings, B. Peng, A. Petrone, T. Henderson,

D. Ranasinghe, V. G. Zakrzewski, J. Gao, N. Rega, G. Zheng, W. Liang, M. Hada, M. Ehara, K. Toyota, R. Fukuda, J. Hasegawa, M. Ishida, T. Nakajima, Y. Honda, O. Kitao, H. Nakai, T. Vreven, K. Throssell, J. A. Montgomery, Jr., J. E. Peralta, F. Ogliaro, M. J. Bearpark, J. J. Heyd, E. N. Brothers, K. N. Kudin, V. N. Staroverov, T. A. Keith, R. Kobayashi, J. Normand, K. Raghavachari, A. P. Rendell, J. C. Burant, S. S. Iyengar, J. Tomasi, M. Cossi, J. M. Millam, M. Klene, C. Adamo, R. Cammi, J. W. Ochterski, R. L. Martin, K. Morokuma, O. Farkas, J. B. Foresman and D. J. Fox, *Gaussian 16 Revision B.01*, 2016, Gaussian Inc. Wallingford CT.

[47] F. Neese, *WIREs Comput. Mol. Sci.*, 2011, **2**, 73–78.

[48] C. Riplinger, P. Pinski, U. Becker, E. F. Valeev and F. Neese, *J. Chem. Phys.*, 2016, **144**, 024109.

[49] R. M. Parrish, L. A. Burns, D. G. A. Smith, A. C. Simmonett, A. E. DePrince, E. G. Hohenstein, U. Bozkaya, A. Y. Sokolov, R. D. Remigio, R. M. Richard, J. F. Gonthier, A. M. James, H. R. McAlexander, A. Kumar, M. Saitow, X. Wang, B. P. Pritchard, P. Verma, H. F. Schaefer, K. Patkowski, R. A. King, E. F. Valeev, F. A. Evangelista, J. M. Turney, T. D. Crawford and C. D. Sherrill, *J. Chem. Theory Comput.*, 2017, **13**, 3185–3197.

[50] T. H. Dunning, *J. Chem. Phys.*, 1989, **90**, 1007–1023.

[51] J.-D. Chai and M. Head-Gordon, *Phys. Chem. Chem. Phys.*, 2008, **10**, 6615–6620.

[52] C. Riplinger and F. Neese, *J. Chem. Phys.*, 2013, **138**, 034106.

[53] D. G. Liakos and F. Neese, *J. Chem. Theory Comput.*, 2015, **11**, 4054–4063.

[54] D. G. Liakos, Y. Guo and F. Neese, *J. Phys. Chem A*, 2019, **124**, 90–100.

[55] I. Sandler, J. Chen, M. Taylor, S. Sharma and J. Ho, *J. Phys. Chem. A*, 2021, **125**, 1553–1563.

[56] S. Boys and F. Bernardi, *Mol. Phys.*, 1970, **19**, 553–566.

[57] T. H. Dunning, *J. Phys. Chem. A*, 2000, **104**, 9062–9080.

[58] F. B. van Duijneveldt, J. G. C. M. van Duijneveldt-van de Rijdt and J. H. van Lenthe, *Chem. Rev.*, 1994, **94**, 1873–1885.

[59] C. D. Sherrill, in *Non-Covalent Interactions in Quantum Chemistry and Physics*, Elsevier, 2017, pp. 137–168.

[60] B. G. Peyton and T. D. Crawford, *J. Phys. Chem. A*, 2019, **123**, 4500–4511.

[61] H. Kruse and S. Grimme, *J. Chem. Phys*, 2012, **136**, 154101.

[62] N. Mehta, T. Fellowes, J. M. White and L. Goerigk, *J. Chem. Theory Comput.*, 2021, **17**, 2783–2806.

[63] A. K. Dutta, M. Saitow, B. Demoulin, F. Neese and R. Izsák, *J. Chem. Phys.*, 2019, **150**, 164123.

[64] J. A. Montgomery, M. J. Frisch, J. W. Ochterski and G. A. Petersson, *J. Chem. Phys.*, 2000, **112**, 6532–6542.

[65] A. E. Reed and F. Weinhold, *J. Chem. Phys.*, 1985, **83**, 1736–1740.

[66] A. V. Marenich, S. V. Jerome, C. J. Cramer and D. G. Truhlar, *J. Chem. Theory Comput.*, 2012, **8**, 527–541.

[67] A. E. Reed and F. Weinhold, *J. Chem. Phys.*, 1983, **78**, 4066–4073.

[68] F. Martin and H. Zipse, *J. Comput. Chem.*, 2004, **26**, 97–105.

[69] B. Jeziorski, R. Moszynski and K. Szalewicz, *Chem. Rev.*, 1994, **94**, 1887–1930.

[70] K. Patkowski, *WIREs Comput. Mol. Sci.*, 2019, **10**, e1452.

[71] E. G. Hohenstein and C. D. Sherrill, *J. Chem. Phys.*, 2010, **132**, 184111.

[72] T. M. Parker, L. A. Burns, R. M. Parrish, A. G. Ryno and C. D. Sherrill, *J. Chem. Phys.*, 2014, **140**, 094106.

[73] E. G. Hohenstein and C. D. Sherrill, *WIRES: Comp. Mol. Sci.*, 2011, **2**, 304–326.

[74] J. N. Bull, M. S. Scholz, E. Carrascosa, G. da Silva and E. J. Bieske, *Phys. Rev. Lett.*, 2018, **120**, 223002.

[75] Y. Toker, J. Langeland, E. Gruber, C. Kjær, S. B. Nielsen, L. H. Andersen, V. A. Borin and I. Schapiro, *Phys. Rev. A*, 2018, **98**, 043428.

[76] D. Zuev, K. B. Bravaya, M. V. Makarova and A. I. Krylov, *J. Chem. Phys.*, 2011, **135**, 194304.

[77] W. Zagorec-Marks, M. M. Foreman, J. R. R. Verlet and J. M. Weber, *J. Phys. Chem. Lett.*, 2020, **11**, 1940–1946.

[78] C. W. West, A. S. Hudson, S. L. Cobb and J. R. R. Verlet, *J. Chem. Phys.*, 2013, **139**, 071104.

[79] C. W. West, J. N. Bull, A. S. Hudson, S. L. Cobb and J. R. R. Verlet, *J. Phys. Chem. B*, 2015, **119**, 3982–3987.

[80] S. Olsen and R. H. McKenzie, *J. Chem. Phys.*, 2012, **137**, 164319.

[81] A. Altun, R. Izsák and G. Bistoni, *Int. J. Quantum Chem.*, 2020, **121**, e26339.

[82] D. G. Liakos, M. Sparta, M. K. Kesharwani, J. M. L. Martin and F. Neese, *J. Chem. Theory Comput.*, 2015, **11**, 1525–1539.

Chapter 5

Photophysics of $p\mathrm{CK}^-$

In this chapter, the properties of the ketone derivative of *E*-4-hydroxycinnamate ($p\mathrm{CK}^-$) are explored using time-resolved fluorescence up-conversion and electronic structure calculations. The UV-B filtering properties of *E*-4-hydroxycinnamate derivatives has permitted the development of commercial sunscreens that contain cinnamate molecules. To facilitate the rational design of improved synthetic alternatives, it is necessary to understand the inherent properties of this class of molecules. In this work, the ultrafast dynamics of $p\mathrm{CK}^-$ in a series of polar protic solvents are explored and shown to have a strong dependence on solvent properties (*i.e.* polarity and viscosity) and temperature. Evidence is presented that supports literature suggestions of solvent mixtures, whose major component is water, preferentially forming a predominantly aqueous local solvation environment around the chromophore. A protocol for modelling solvation of $p\mathrm{CK}^-$ by water is demonstrated to simulate excitation energies with reasonable accuracy. This protocol could be generalised to other solvents. Finally, the solution-phase work is linked with gas-phase experiments previously performed by Dr Bull at the University of Melbourne, Australia and by current collaborators at the University of Waterloo, Canada.

5.1 Introduction

Photoactive yellow protein (PYP) is a water-soluble, blue-light sensing, 14 kDa photoreceptor protein found in the *Halorhodospira halophila* bacterium.[1–3] The absorption spectrum for the protein is defined by the $S_1 \leftarrow S_0$ transition with a maximum at 446 nm.[4] The chromophore unit, a *E*-4-hydroxycinnamate (*para*-hydroxycinnamate), sits inside the hydrophobic protein pocket and is covalently bound to a cysteine residue (Cys69) of the protein *via* a thioester linkage on the keto end (Figure 5.1). The phenoxide end of the chromophore is deprotonated and stabilised by interactions with nearby amino

acid residues.[1,5] In the protein photocycle, the chromophore unit mediates a negative phototactic response of the bacterium to harmful blue light. Upon absorption of blue light, the chromophore undergoes ultrafast $E \rightarrow Z$ photoisomerisation, initiating a complex photocycle and prompting a negative phototactic response in the bacterium.[4,6,7]

Aside from the chromophore in PYP, molecules possessing the *para*-hydroxycinnamate moiety are widespread in nature – *e.g.* sinapoyl malate, and caffeic and ferulic acids, as

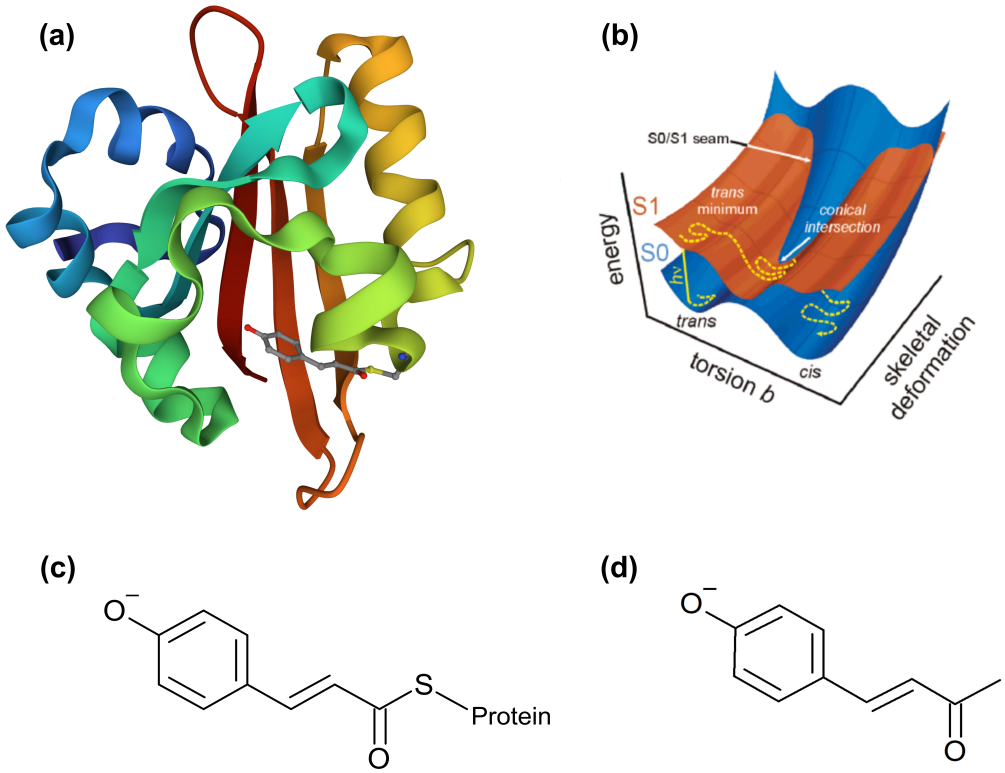


Figure 5.1: **(a)** Structure of photoactive yellow protein (PYP), with the *E*-4-hydroxycinnamate unit and cysteine residue shown (PDB 1UWN). Adapted from the Protein Data Bank[8] and visualised in Mol* Viewer.[9–11] **(b)** The potential energy surface of excited and ground states of the deprotonated chromophore in the protein, for $E \rightarrow Z$ isomerisation, adapted from Groenhof *et al.*[12] Torsion b coordinate corresponds to the $E \rightarrow Z$ isomerisation reaction and the yellow line indicates a typical trajectory along the PES. Structures **(c)** and **(d)** show the chromophore with the thioester bond to the protein, *via* the cysteine residue, and deprotonated *para*-coumaric ketone (pCK$^-$), commonly used as a model for the PYP chromophore, respectively.

UV-B filters in the leaves, stems, and seeds of plants.[13,14] These molecules are found either covalently-bound to cell walls and lignin structures or in their free (unbound) form. Again, the UV-B filtering mechanism efficacy depends on rapid $E \rightarrow Z$ photoisomerisation, occurring *via* passage through a conical intersection seam.[15] These desirable properties have prompted the skincare industry to develop commercial sunscreens containing cinnamate molecules. In an effort to elucidate the ultrafast dynamics of the photoisomerisation mechanism, numerous studies have been performed on hydroxycinnamate-based chromophore derivatives, such as *para*-coumaric acid (pCA$^-$, Figure 5.2(a)) and its ketone (pCK$^-$, Figure 5.1(d)) and ester (pCEs$^-$, Figure 5.2(b)) relatives. While several studies have considered thioester derivatives, they are often unstable in solution and decompose rapidly. Moreover, thioesters are challenging to electrospray in gas-phase studies.

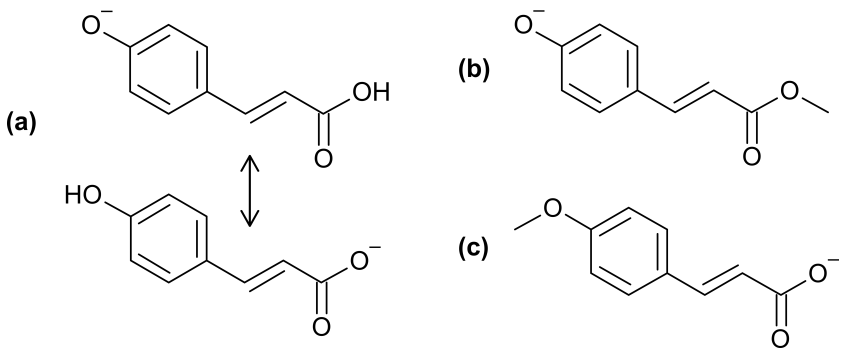


Figure 5.2: Structures of **(a)** *para*-coumaric acid (pCA$^-$), as both its phenoxide (top) and carboxylate (bottom) deprotomers, and its derivatives **(b)** pCEs$^-$ and **(c)** pCEt$^-$.

In the protein, $E \rightarrow Z$ photoisomerisation occurs within a few picoseconds.[16,17] However, in solution the chromophore excited state lifetime is longer. It has been shown that the intrinsic photoisomerisation dynamics of *para*-hydroxycinnamate derivatives depend on a range of variables, including functional group substitution (on the carboxylate tail),[17–22] deprotonation state,[17,19] deprotonation site (*e.g.* for substituted derivatives such as caffeic and ferulic acid, which are also biochromophores in plants),[18,21,22] and solvent environment.[17,19,23,24]

The dynamics of any photochemical reaction in solution are influenced by the solvent molecules within the solvation sphere. When a chromophore is excited, it is promoted from the S_0 ground state, to the S_1 excited state (Figure 5.3). On excitation, the charge distribution within the molecule undergoes an instantaneous change. In response to

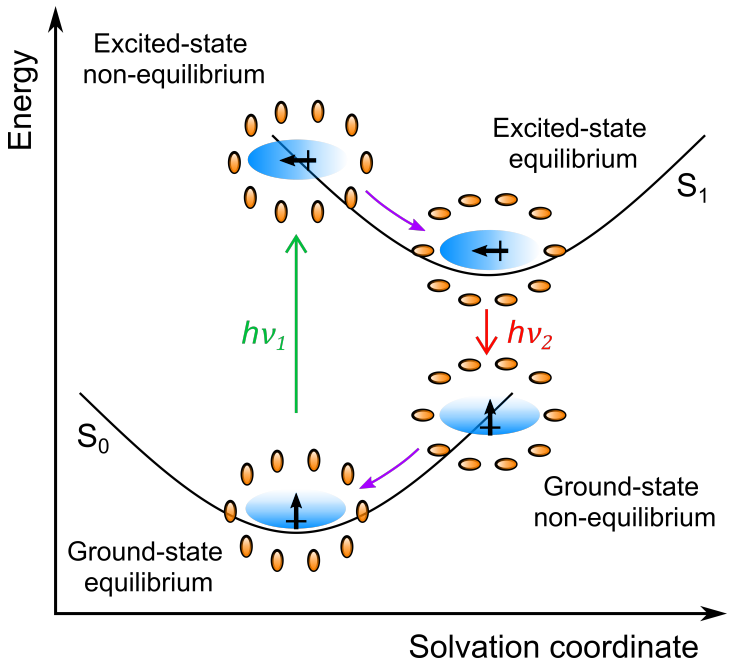


Figure 5.3: Schematic representation of the solvent rearrangement process following excitation of a sample. Note that the change in dipole moment of the chromophore leads to solvent rearrangement, particularly for a polar solvent.

this change, the solvent rearranges on a timescale longer than the molecular charge redistribution, as dictated by the Franck-Condon principle. Thus, immediately after excitation, the excited molecule finds itself in a non-equilibrium geometry with respect to its solvation sphere. Once the solvent molecules rearrange to achieve an equilibrium arrangement (*i.e.* system reaches the S_1 minimum) the whole system becomes more stable. Relaxation to the electronic ground state may be accompanied by emission of light (fluorescence). The red-shift of the peak fluorescence wavelength with respect to the the peak absorption wavelength is termed the *Stokes shift*. The solvent properties will play a part in dictating the fluorescence emission wavelength and the fluorescence lifetime. It is worth noting that gas-phase fluorescence from chromophore molecules usually have extremely low quantum yield (*e.g.* less than 0.1%) for two reasons: (1) internal vibrational energy is not quenched by the solvent, and (2) excited state lifetimes are usually much shorter in the gas phase, compared with solution, due to (1).

It is well-known that solvent rearrangement causes a bimodal response in time-resolved fluorescence measurements,[25] as discussed in Section 3.2. For systems in water, simulations predict a ≈20 fs timescale for the inertial (libration) solvent response,[25] which

can only be resolved with an experiment with sufficiently high time resolution. There is a vast catalogue on previous solution-based studies on *para*-hydroxycinnamates. Here, discussion is focussed on the work by Espagne and co-workers,[17,23] who studied the effect of different solvents on the properties and dynamics of chromophore analogues, including in a selection of alcohols and different solvent mixtures, to explore viscosity and polarity effects. In particular, they explored the dynamics of both neutral and anionic *p*CK and *p*CEs using fluorescence up-conversion with ≈500 fs time resolution. Espagne *et al.* quote fluorescence decays for $p\text{CK}^-$ which are close to or limited by the time-resolution of the experiment. Using fluorescence up-conversion, as described in Section 3.1, this thesis describes efforts to provide improved measurements (≈50 fs time resolution) and ultimately allow comparison with gas-phase data.

Theoretical studies have shown that the condensed-phase environment surrounding the chromophore plays a significant role in determining chromophore properties and dynamics on excitation.[12,26–31] This is because the solvent has a significant impact on the shape of the potential energy surface (PES) of the chromophore. In the protein, the excited state lifetime is much shorter than *in vacuo*. In solution, excited state lifetime is also shorter than in the gas phase, but longer than in the protein. This is because, in the gas phase, there are no interactions, such as with the protein amino acid residues or solvent molecules, to stabilise the excited-state intermediate geometry. The protein interactions lower the energy of the global minimum, bring the conical intersection (CI) closer to said global minimum, and lower the excited state barrier from the Franck-Condon region to the CI region (as shown in Figure 5.1(b)).[12]

The effects of solvation on chromophore electronic structure and vertical excitation energies have been investigated in detail in many theoretical studies, but most notably in Refs. 27 and 29. Despite these works, it is unclear as to the extent that theory needs to treat the solvation sphere in order to correlate the gas-phase dynamics to solution. One of the goals of this thesis is to explore this correspondence using water as the solvent. Although the main focus is on solvation by water, as this is biologically relevant, this work also aims to create a comprehensive bank of data on the properties and dynamics of $p\text{CK}^-$ in a range of solvents:

(i) A comprehensive comparison of different alcohols, from methanol to 1-octanol (except hexanol), which are increasingly less polar and more viscous.

(ii) The impact of solvent viscosity, using different volume ratios of ethylene glycol in mixtures with water.

5.2 Computational methods

This section discusses theoretical methods for modelling solution absorption maxima. Geometry optimisation and vibrational frequency calculations were performed using Gaussian 16.B01[32] at the ωB97X-D/aug-cc-pVDZ level of theory.[33–35] Electronic excited state calculations were performed in Gaussian 16 and MRCC[36,37] using TD-ωB97X-D, and the density-fitted second-order coupled-cluster singles and doubles (df-CC2)[38–41] approach, respectively. Further excited state calculations were performed using STEOM-DLPNO-CCSD/aug-cc-pVDZ in ORCA 5.0.[42]

TD-DFT methods are computationally cheap, but fail to provide an accurate description of charge transfer (CT) transitions.[41] Two cheap coupled-cluster (CC) methods, offering improved physics, are tested – df-CC2 and STEOM-DLPNO-CCSD. Coupled-cluster methods produce more robust descriptions of both locally excited (LE) and CT transitions. The df-CC2 method provides more accurate vertical excitation energies relative to TD-DFT methods, but with comparable computational scaling. The computational cost of the STEOM-DLPNO-CCSD method is also comparable to that of TD-DFT, while its accuracy is comparable to that of EOM-CC.[43]

To explore solvation, vertical excitation energies were computed at the TD-ωB97X-D/aug-cc-pVDZ level of theory, using implicit and explicit solvation methods. Explicit solvation involved stepwise addition of one water molecule to $p\mathrm{CK}^-$, optimising the structure, and calculating the vertical excitation energies. The full process is shown in Figure A1.2. The implicit solvation methods PCM (polarisable continuum model), CPCM (conductor-like polarisable continuum model) and SMD (solvation method based on density) were considered. In CPCM, the solute effectively occupies a cavity surrounded by a polarisable continuum field, representing the solvent.[44] The default cavity description is the van der Waals surface model, built from the van der Waals radii of the solute atoms. In comparison to CPCM, which assumes the solvent behaves as a conductor, the standard PCM method characterises the dielectric permittivity of the specific solvent surrounding the solute cavity.[45] SMD is an alternative (and generally more robust) method that involves separating the solvation free energy into two components: a bulk electrostatic component and a cavity-dispersion–solvent-structure term (interactions between solute and solvent in the first solvation shell).[46]

Selected calculations were performed with the double- and triple-ζ basis sets to explore the influence on excitation energies. The increase in basis set size yielded negligible

changes in excitation energies, thus the double-ζ basis set was deemed adequate.

5.3 Experimental methods

5.3.1 Absorption and fluorescence

Solutions of pCK$^-$, at arbitrary concentrations, were made up in a range of pure solvents: water (Milli-Q), methanol (99 %, Alfa Aesar), ethanol (≥99 % Fisher), 1-propanol (Acros Organics), 2-propanol (≥99.5 %, Sigma Aldrich), 1-butanol (≥99 %, Sigma Aldrich), 1-pentanol (≥99 %, Sigma Aldrich), 1-heptanol (99 %, Lancaster), 1-octanol (≥99 %, Sigma Aldrich), and ethylene glycol (≥99 %, Sigma Aldrich). Further solutions, again at arbitrary concentrations, were made up in a mixture of water and ethylene glycol in different ratios (vol%): 80%, 60%, 40%, 20%. A drop of 1 M sodium hydroxide solution was used to deprotonate the neutral solutions. Ammonia solution was too weakly basic to adequately deprotonate the solutions. The comparison of deprotonation efficacy by sodium hydroxide and the ammonia solution was made by monitoring changes in absorption spectra with addition of base. One drop of 1 M sodium hydroxide was sufficient to change the absorption spectrum fully. UV-vis absorption spectra of the neutral (pCK) and anionic (pCK$^-$) forms were obtained from a Perkin Elmer Lambda XLS spectrometer, scanning a wavelength range of 250–800 nm.

Fluorescence excitation and emission spectra of the pCK$^-$ solutions were recorded on a fluoroSENS bench-top fluorimeter (Gilden photonics). Excitation spectra were measured over 300–700 nm, while emission spectra were measured over the 400–800 nm range. The emission spectra were excited at both 400 nm and selected wavelengths from the blue edge of the excitation spectra for the respective solutions. Excitation-emission maps and time-resolved fluorescence measurements were recorded (at room temperature ($T \approx 300$ K) and $T \approx 77$ K (liquid nitrogen)) using an FS5 spectrofluorometer (Edinburgh Instruments). Time-resolved emission measurements were initiated by pulses from an EPLED-360 (365 nm, 400 ps instrument response (ω)).

5.3.2 Ultrafast fluorescence up-conversion

Ultrafast fluorescence up-conversion enables fluorescence emission to be monitored as a function of time, providing direct insight into excited state lifetimes. As detailed in Section 3.1, the experiment has a time resolution of ≈50 fs. Fluorescence up-conversion

experiments were performed on pCK$^-$ in a range of solvents (see Section 5.3.1) using both static and flow cells. The sample was excited (pumped) at ≈400 nm with an average pump power of 11 mW. While most literature using fluorescence up-conversion on pCK$^-$ in solution make use of a static cell, it is important to make a comparison to the fluorescence lifetimes obtained from the experiment from a flow cell. The flow cell ensures that each 400 nm excitation pulse excites E-isomer molecules, rather than a photostationary state containing both E and Z isomers. Emission was monitored at a wavelength corresponding to that of maximum emission and at several wavelengths either side of the maximum.

5.4 Results and discussion

5.4.1 Merits of computational methods: TD-DFT, CC2, and STEOM

There are many molecules that can undergo CT transitions on excitation, for example pCK$^-$ (Figure 5.4(a)). Excitation of a twisted pCK$^-$ geometry exhibits CT character,

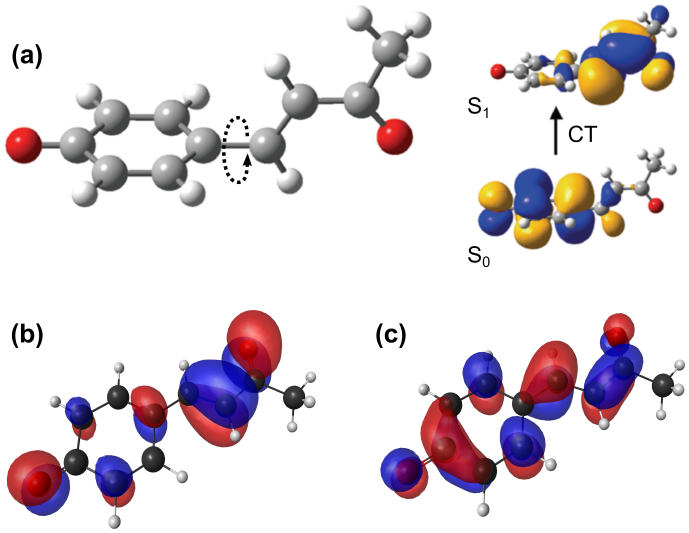


Figure 5.4: Panel **(a)** illustrates the single-bond twisted S_1 structure of pCK$^-$ and the orbitals of the S_0 and S_1 states, illustrating the charge-transfer nature of the $S_1 \leftarrow S_0$ transition. Bond twisting can induce charge-transfer character. Adapted from Boggio-Pasqua *et al.*[31] Also illustrated are the pCK$^-$ **(b)** HOMO and **(c)** LUMO, computed in the Firefly 8.2.0[47] software package at the CASSCF(12,11)/aug-cc-pVDZ level of theory.

while the HOMO and LUMO of planar pCK$^-$ exhibit more local excitation (LE) character. Unsolvated computational data can be compared directly with gas-phase pCK$^-$ data (Section 5.5.3.1, Figure 5.20(d)). The gas-phase data shows photodissociation over the 370–500 nm range, with a maximum at ≈400 nm. These data are compared with computed vertical excitation energies (VEEs) for pCK$^-$ at different levels of theory and data from the literature[48,49] (Table 5.1). The difference between the pCK$^-$ VEEs obtained by TD-ωB97X-D and that from experiment is double that for df-CC2 (0.46 eV and 0.23 eV, respectively). The difference between the CC2 and experimental VEE values for pCA$^-$ (0.15 eV) is comparable to that between df-CC2 and experiment of pCK$^-$. The STEOM-DLPNO-CCSD computed VEE is red-shifted by 0.26 eV relative to the experimental value, compared to the 0.23 eV blue-shifted df-CC2 value. Note that the inherent error of CC2 is typically on the order of 0.2–0.3 eV,[50] and the error in STEOM methods is around 0.1–0.2 eV (for singlet states dominated by a single excitation).[43] As a consequence, it is difficult to comment on the relative accuracies of the excitation energy values obtained by these methods, as both deviate from the experimental value approximately within the inherent error for the respective methods. From these data, it may be concluded that both df-CC2 and STEOM-DLPNO-CCSD yield fairly accurate excitation energies. However, as stated previously, the CC2 approach, like TD-DFT, is a linear response method, known to have limitations when applied to excited state calculations.[45] Therefore, success of df-CC2 in this case may be fortuitous. STEOM, on the other hand, is a hybrid method, combining state-specific and linear-response

Table 5.1: Comparison of vertical excitation energies (VEEs) for pCK$^-$ and pCA$^-$ from computations, at different levels of theory, and from gas-phase experiments. Δ is the relative difference in VEE between the experimental and computed values. [a] indicates calculations were performed using the aug-cc-pVDZ basis set.

Species	**Method**	**VEE / eV**	**Δ / eV**	**Ref.**
pCK$^-$	TD-ωB97X-D[a]	3.28	+0.46	
	df-CC2[a]	3.05	+0.23	
	STEOM-DLPNO-CCSD[a]	2.56	−0.26	
	XMCQDPT2	≈2.90	+0.08	51
	XMCQDPT2[a]	2.66	−0.16	
	Expt.	≈2.82		
pCA$^-$	CC2[a]	3.03	+0.15	48
	Expt.	≈2.88		49

methods, and thus provides accurate results at a lower computational cost than purely state specific methods. The vertical excitation energies of pCK$^-$ computed using the XMCQDPT2 method (≈2.90 eV[51] and 2.66 eV) provide the closest agreement to the experimental value. XMCQDPT2 is a multi-configuration quasi-degenerate perturbation theory method,[52] particularly known for its ability to accurately describe potential energy surfaces and crossing points.[53]

5.4.2 Modelling solvation

Solvation of pCK$^-$ by water was explored using a combination of implicit and explicit solvation models. Following on from the gas-phase calculations, solvation calculations used the TD-DFT (ωB97X-D), CC2 (df-CC2), and STEOM (STEOM-DLPNO-CCSD) methods. As discussed previously, the hybrid approach of STEOM is known to provide more accurate excitation energies than linear response (TD-DFT and CC2) counterparts. This extends to calculations performed using implicit solvation models.[45]

The solvation protocol is described in more detail in Figure A1.2. Briefly, the preliminary single-point energy calculations were performed to identify the more stable solvated structures. Geometries were then reoptimised at the ωB97X-D/aug-cc-pVDZ level of theory and excitation energies calculated using one of the methods outlined above (implicit solvation included). The excitation energies obtained by TD-DFT exhibit an oscillatory behaviour with the addition of explicit water molecules. As shown in Figure 5.5, these oscillations relate to the number of explicit water molecules placed around pCK$^-$, with larger excitation energies for odd numbers of water molecules. The trend line roughly shows convergence with five water molecules. The limited literature on computations of the first solvation sphere of pCK$^-$ (and relatives) uses resolution of identity MP2 (RI-MP2) in geometry optimisations,[27] compared with ωB97X-D used in this thesis. However, in agreement with microsolvated structures of pCA$^-$,[27] water molecules coordinate preferentially with the deprotonation site in pCK$^-$.

For the vertical excitation wavelengths, TD-DFT performs worst, followed by df-CC2, and then STEOM, especially when there is significant charge transfer character, as there is in pCK$^-$, since the electronic transition involves moving charge density from the deprotonation site to the π^* orbital. The plot in Figure 5.5 (b) shows the excitation energies for pCK$^-$ solvated by five explicit water molecules, relative to the experimental value. It is clear that TD-DFT, both with and without implicit solvation, performs poorly.

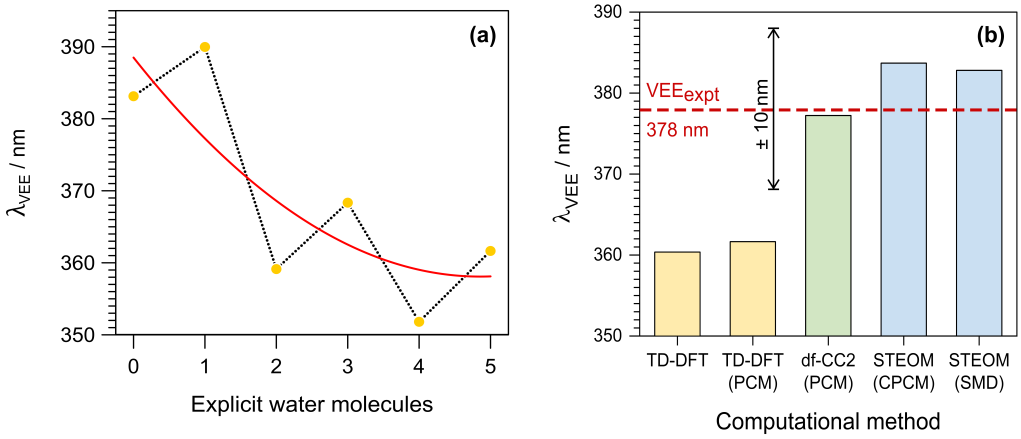


Figure 5.5: Computed vertical excitation wavelengths (λ_{VEE}) of $p\mathrm{CK}^-$ obtained at various levels of theory using different implicit and explicit solvation models. Panel **(a)** shows the oscillating behaviour of the vertical excitation wavelengths obtained at the TD-ωB97X-D/aug-cc-pVDZ level of theory, with PCM, for $p\mathrm{CK}^-$ surrounded by an increasing number of explicit water molecule (0–5). The data is fitted to a polynomial function (red curve). Panel **(b)** depicts calculated vertical excitation wavelengths for $p\mathrm{CK}^-$ surrounded by five explicit water molecules, using different computational methods.

In contrast, df-CC2 performs (fortuitously) well. Two implicit solvation methods were used at the STEOM-DLPNO-CCSD level of theory – SMD and CPCM. The SMD implicit solvation method produces slightly more accurate vertical excitation wavelengths, presumably because of the extra physics included in the model. Overall, these results show that the excitation energies of $p\mathrm{CK}^-$ in water can be simulated accurately using the protocol described in Figure A1.2. This approach should be generalisable to other solvents, such as methanol.

5.4.3 Absorption and fluorescence spectra

The absorption and fluorescence properties of $p\mathrm{CK}^-$ were explored for a series of solvents with differing polarities and viscosities: water, methanol, ethanol, 1-propanol, 2-propanol, 1-butanol, 1-pentanol, 1-heptanol, 1-octanol, ethylene glycol, and water–ethylene-glycol mixtures. Considered are the Stokes shifts between the absorption and emission spectra, the effect of solvent on the spectral maxima, and the effect of solution concentration on the fluorescence spectra. From hereon, solvent names are shortened,

e.g. butanol instead of 1-butanol, with the exception of 1- and 2-propanol.

It is important to note that, regardless of the solvent, neutral and anionic *p*CK exhibit distinct absorption maxima (Figure 5.6). Therefore, even if some neutral *p*CK is present in an anionic sample, it should not interfere with measurements on the anion, particularly when the sample is excited at wavelengths longer than 400 nm.

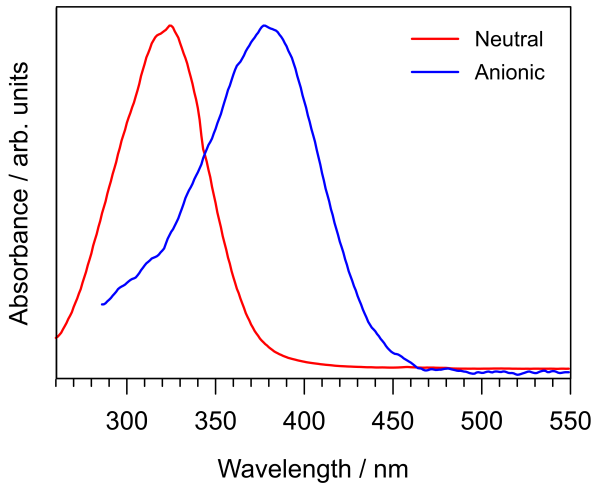


Figure 5.6: Absorption spectra of neutral (red) and anionic (blue) *p*CK in water.

5.4.3.1 Solvatochromism

The absorption and emission spectra of $p\text{CK}^-$ both exhibit a solvatochromic shift, which is dependent upon solvent polarity (Table 5.2). Absorption is less sensitive to solvent polarity than emission because there is no change in the solvent environment between the ground and excited states ($h\nu_1$, Figure 5.3).[54,55] However, a polar solute (in this case a chromophore) in polar solvents should exhibit a shift in absorption maxima with increasing solvent polarity due to solvent stabilisation[56] – namely dipolar solvent-chromophore interactions stabilise the chromophore ground state. If the solute dipole moment increases on excitation, the Franck-Condon excited state is stabilised by the existing solvent cage (partly oriented dipoles), causing red-shift of absorption maxima with increasing polarity. On the other hand, if the chromophore dipole moment decreases on excitation, the dipoles in the existing solvent cage are strained, which destabilises the Franck-Condon excited state. In this case, the absorption maxima are blue-shifted with increasing polarity. Absorption maxima for $p\text{CK}^-$ in water–ethylene-glycol mixtures are blue-shifted with increasing solvent polarity (Figure 5.7). This may suggest preferential solvation of the ground state relative to the excited state, thus increasing the $S_1 \leftarrow S_0$

Table 5.2: Absorption (λ^{A}_{max})and emission (λ^{E}_{max}) maxima with corresponding Stokes shift $\Delta\nu$ and solvent polarity (ε, obtained from Ref. 57). Percentages indicate vol% of water in the water–ethylene-glycol solutions. *Likely an outlier due to water in the sample.

Solvent	$\boldsymbol{\lambda^{A}_{max}}$ **/ nm**	$\boldsymbol{\lambda^{E}_{max}}$ **/ nm**	$\boldsymbol{\Delta\nu}$ **/ cm^{-1}**	$\boldsymbol{\varepsilon}$[57]
H_2O	378	484	5794	80.1
80% H_2O	385	484	5313	77.2
60% H_2O	387	480	5006	73.2
40% H_2O	391	476	4567	67.4
20% H_2O	393	476	4437	58.3
EtGly	388	476	4765	41.4
MeOH	385	480	5141	33
EtOH	392	468	4143	25.3
1-PropOH	405	466	3232	20.8
2-PropOH	409	466	2991	20.18
ButOH*	394	468	4013	17.84
PentOH	400	468	3632	15.13
HeptOH	397	462	3544	11.75
OctOH	394	466	3921	10.3

transition energy. A more likely explanation is because of the induced reaction field formed by the polarisation of the solvent by the chromophore. Given that the chromophore is anionic, it is able to polarise the surrounding solvent, thereby establishing an electric field around itself. The induced reaction field can be treated as an external electric field, because an induced reaction field produces electrochromic spectral shifts in the same way as an electric field.[56]

Interestingly, the absorption maxima of pCK$^-$ in various alcohols follow a peaked trend (as a function of absorption maximum), as the maxima red-shift from methanol to 2-propanol and blue-shift from butanol to octanol (Table 5.2). For methanol to 2-propanol in the series, the trend suggests that the Franck-Condon excited state is destabilised on excitation, while the butanol to octanol trend suggests that the Franck-Condon excited state is stabilised on excitation. Thus, a comparison may be drawn between the first half of the alcohol series and the water–ethylene-glycol mixtures. In both cases, the data suggest that the solvent cage around the Franck-Condon excited state has a destabilising

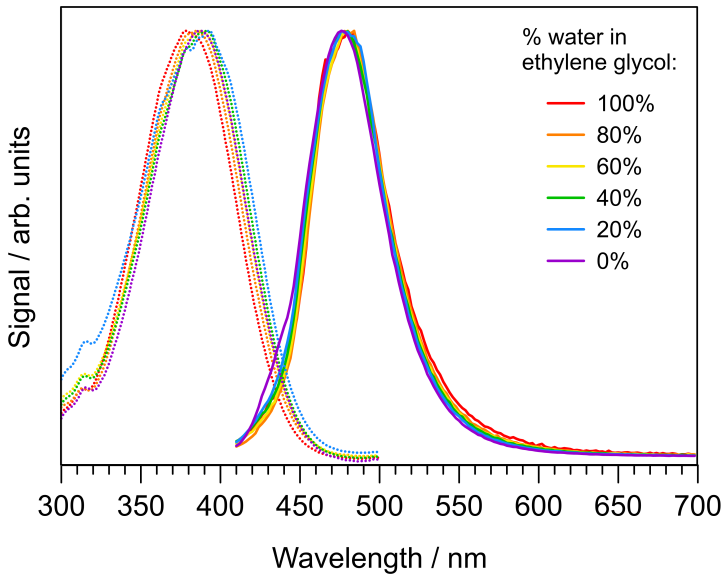


Figure 5.7: Absorption (dotted) and emission (solid) spectra of pCK$^-$ in various mixture of ethylene glycol and water: 0%, 20%, 40%, 60%, 80%, and 100% water.

effect. This may be due to the relatively high polarity of the both the solute and solvents, which results in large solvent-solute interactions. Given that pCK$^-$ possesses a large dipole moment (≈5.6 D), a greater reorientation of the solvent cage is necessary when the dipole moment changes on excitation. Therefore, the Franck-Condon excited state will lie higher in energy because the solvent cage (unchanged from the ground state) will strain the system. In comparison, for pCK$^-$ in pentanol to octanol, the suggested stabilisation of the Franck-Condon excited state likely arises because the solvent-solute interaction is weaker. As a result, the solvent cage requires less reorientation to stabilise the Franck-Condon excited state, so the existing cage already provides some stabilisation to the system. Most fluorophores in solution will display a shift between their absorption and emission maxima, termed the Stokes shift. This is defined as the difference between the peak in excitation energy for the $S_1 \leftarrow S_0$ transition (absorption) and the subsequent fluorescence wavelength (emission). While excitation populates vibrationally excited modes, rapid vibrational energy relaxation to the solvent quenches internal energy. As a result, fluorescence usually occurs from the lowest vibrational level of the S_1 state.

The Stokes shift has two contributions: general and specific solvent effects. General solvent effect theory considers the effect of solvent polarity on Stokes shift. The more polar the fluorophore, the more sensitive it is to solvent polarity and, the more polar

the solvent, the greater the Stokes shift due to greater stabilisation of the S_1 fluorophore dipole moment. pCK$^-$ generally exhibits polarity-dependent shifts (Table 5.2). However, general solvent effects cannot explain the behaviour of fluorophores in different environments fully. For example, the pCK$^-$ Stokes shift in methanol appears anomalously high compared with ethanol, and is comparable to the Stokes shifts of the 60% water solution, even though methanol has a significantly lower polarity. Specific solvent effects consider the interactions between solvent and fluorophore, which also direct the Stokes shift magnitude. Hydrogen-bonding and charge-transfer interactions are particularly relevant to pCK$^-$. Hydrogen bonds are important because pCK$^-$ is polar and contains a negative charge. Charge-transfer interactions are also expected to play a role in the emission red-shifting, since the S_1 state of pCK$^-$ is known to be a charge-transfer state.[31]

To assess the importance of specific solvent interactions, the Stokes shifts in methanol and 60% water–ethylene-glycol are compared. The comparability of the shifts cannot be solely due to polarity (ε = 33 and 73.2,[57] respectively). This suggests specific solvent interactions contribute to the stabilisation of the pCK$^-$ S_1 state in methanol. Since charge-transfer interactions will be important in all the solvents explored, the additional S_1 stabilisation in methanol likely arises due to hydrogen-bonding interactions. On the other hand, the large difference in shift between methanol and ethanol can, at least in part, be ascribed to the difference in hydrogen-bonding ability, given that their polarities are fairly similar (ε = 33 and 25.3,[57] respectively). However, the contributions of general and specific solvent effects are difficult to disentangle. To illustrate this, consider the addition of water to an ethylene glycol solution of pCK$^-$. Table 5.2 shows that greater water content shifts both the absorption and emission maxima only slightly and significantly affects the measured Stokes shift. Only once the water content exceeds the ethylene glycol content, does the emission maximum red-shift slightly. This may be due to the increased hydrogen-bonding interactions with greater water content. However, given that a large change in solvent composition causes a comparatively small emission red-shift, the spectral shift is unlikely to be a result of specific solvent effects.[54]

5.4.3.2 *p*CK$^-$ concentration

It is important to recognise that solution concentration can influence fluorescence spectra. As shown in Figure 5.8, there is a distinct difference in the excitation and emission spectra of pCK$^-$ in water at different concentrations. The excitation spectra of the

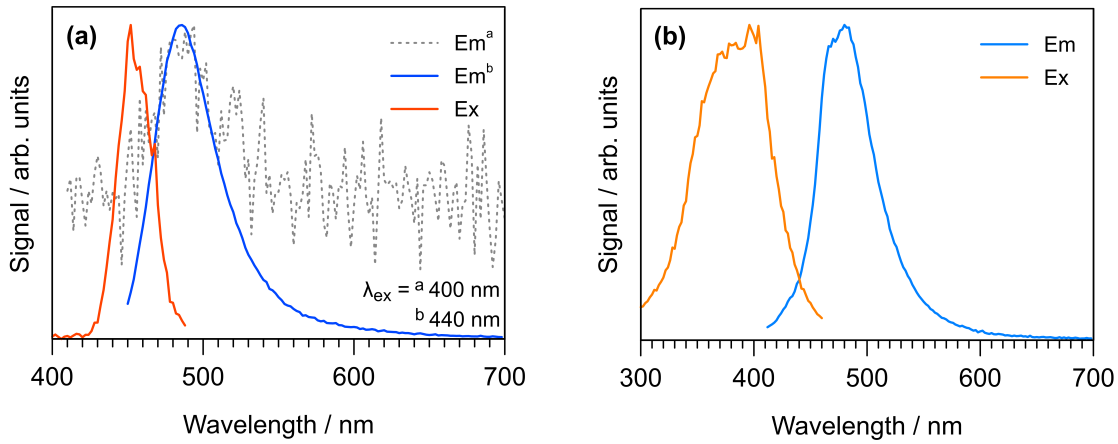


Figure 5.8: Excitation (ex) and emission (em) spectra of **(a)** concentrated and **(b)** dilute solutions of $p\mathrm{CK}^-$ in water (at arbitrary concentrations). Panel **(a)** shows emission spectra from exciting the concentrated sample at 400 nm and 440 nm. The emission spectrum in **(b)** was excited at 400 nm.

concentrated solution (A) is much narrower than that of the dilute solution (B), whose shape is more characteristic of an absorption spectrum. Furthermore, the peak excitation of A lies around 450 nm, while that of solution B lies around 400 nm. From these excitation spectra, it is not surprising that solution A does not emit significantly when excited at 400 nm, instead favouring excitation at 450 nm. Overall, the fluorescence spectra of solution B emulate those expected for $p\mathrm{CK}^-$, where excitation and emission maxima lie around 400 nm and 500 nm, respectively.[17] It is concluded that the difference in fluorescence spectra between the concentrated and dilute solutions is due to inner filter effects. These effects are classed as either *primary* or *secondary*.[54] The *primary* inner-filter effect arises due to the attenuation of the excitation beam as it passes through the sample, resulting in a decrease in emitted fluorescence intensity. The *secondary* inner-filter effect (also called reabsorption) results from emitted fluorescence wavelengths being reabsorbed as they propagate through the sample, causing the emission maximum to be red-shifted.[58] Samples that exhibit reabsorption typically have a high optical density and the effect is most pronounced in moderate/highly concentrated samples whose absorption and emission spectra overlap.[59]

The following outlines the simulation of this narrow excitation band. First, the absorption coefficients ($\varepsilon(\lambda)$) of a dilute solution of $p\mathrm{CK}^-$ in water ($c = 40\,\mu\mathrm{M}$) were calculated from the absorption spectrum, as a function of wavelength, for a 1 cm pathlength (l).

$$A = \frac{I}{I_0} = \varepsilon c l \tag{5.1}$$

Second, the absorbance (A) values of a more concentrated solution of pCK$^-$ in water ($c = 5$ mM) were calculated using Equation 5.1, for a 0.5 cm pathlength. Here, the assumption is made that, when measuring fluorescence, the monochromator detects light from the centre of the sample. Therefore, a pathlength of 0.5 cm is used to mimic the absorption of the concentrated sample at that centre point. The resulting plot, shown in Figure 5.9(a), indicates that, until ≈450 nm, the concentrated solution absorbs all light. Finally, the excitation spectrum of the dilute solution was convoluted with the absorbance values from the second step, producing the simulated excitation spectrum for a 5 mM pCK$^-$ solution (Figure 5.9(b)).

Overall, the simulated excitation spectrum agrees well with the measured excitation spectrum of the concentrated pCK$^-$ solution. This shows that a major contributor to the formation of the narrow excitation band in concentrated solutions is related to the sample absorbing all light in the 250–450 nm range (inner filter effects). As a result, an excitation response is only measured at wavelengths longer than 450 nm, causing the excitation maximum to be red-shifted. Fairly concentrated solutions (arbitrary concentration) of pCK$^-$ were used for time-resolved fluorescence up-conversion measurements,

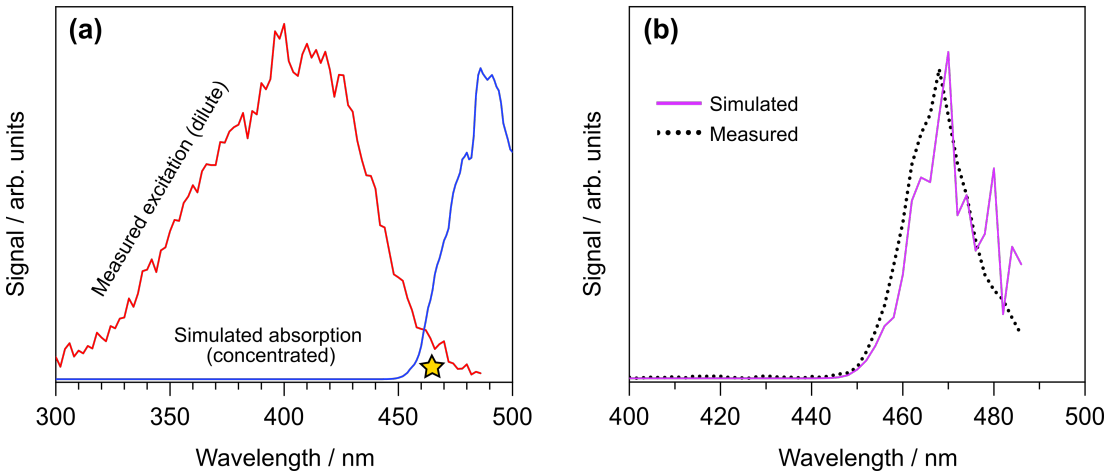


Figure 5.9: Measured and simulated spectra of dilute (40 µM) and concentrated (5 mM) aqueous pCK$^-$ solution. Panel **(a)** depicts the overlap (region marked by the star) of the dilute excitation spectrum (red) with the simulated absorption spectrum of the concentrated solution (blue). Panel **(b)** shows the close agreement of the simulated (line) and measured (dotted) excitation spectra of the 5 mM solution.

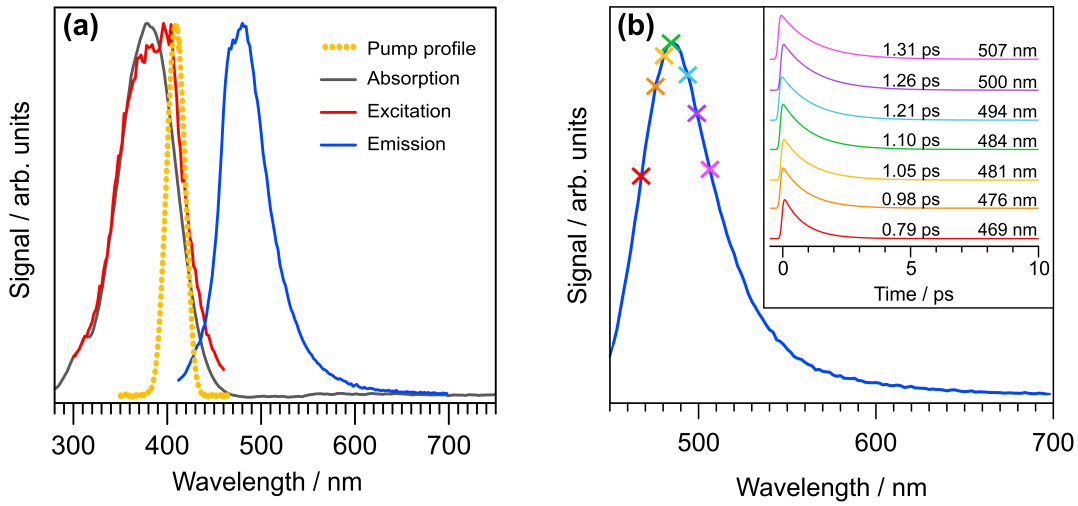


Figure 5.10: Panel **(a)** shows the absorption (grey), excitation (red), and emission (blue) spectra of pCK$^-$ in water, overlaid with the measured profile of the ≈400 nm pump laser pulse (dotted). Panel **(b)** shows the emission wavelengths monitored during fluorescence up-conversion experiments on pCK$^-$ in water (crosses) shown on an emission spectrum of the same system. The fluorescence decays with the corresponding detection wavelength and fluorescence lifetime (without uncertainties) are also depicted (see insert).

to ensure adequate fluorescence signal; however, there was no noticeable interference from inner filter effects.

5.4.4 Time-resolved fluorescence

Fluorescence up-conversion has been widely used to determine the fluorescence lifetime of a variety of fluorophores in different solvents.[5,17,19,60–63] This section focuses on pCK$^-$ in a range of polar protic solvents and solvent mixtures. One aim is to compare the fluorescence lifetime of pCK$^-$ in various solutions to build a picture of how solvent properties affect pCK$^-$ excited state dynamics.

The details of the fluorescence up-conversion experiment have been described in previous sections. Figure 5.10(a) shows the good overlap between the profile of the pump pulse (≈400 nm) overlaid on the excitation and absorption spectra of pCK$^-$ in water. As discussed in Section 5.4.3.1, the absorption spectrum of pCK$^-$ changes with solvent; however, all organic solvents explored in this work result in a red-shifted absorption spectrum relative to pCK$^-$ in water. This leads to optimal overlap between the pump

pulse and the absorption/excitation spectra.

Since the wavelength at which emission is monitored can be tuned, fluorescence decays of pCK$^-$ in water were recorded at a range of emission wavelengths (Figure 5.10(b)). From these data, it is quite clear that the fluorescence lifetime increases the longer the monitored wavelength. This is presumably because the lifetimes (close to 1 ps) are in competition with vibrational energy relaxation processes (vibrational energy quenching timescale typically a few ps). Therefore, the pCK$^-$ fluorescence decays in other solvents were measured by monitoring wavelengths close to the emission maximum. Fluorescence decays were analysed by single- and double-exponential fitting (Section 3.2) and are discussed in Section 5.4.4.1. The changes in fluorescence lifetime with solvent and sample cell properties (flow *versus* static) are discussed in subsequent sections.

5.4.4.1 Single- and double-exponential analysis

Solvent dynamics and rearrangement are an important consideration in solution-phase fluorescence measurements. When a solution is excited, the instantaneous change in solute charge distribution drives a non-instantaneous change in the solvent cage surrounding the solute. As a result, fluorescence decays often exhibit a bimodal response – an initial ultrafast component (τ_1, primarily due to solvent rearrangement/librational solvent motion) and a slower component (τ_2, species fluorescence lifetime) – which depends on solvent properties.[25] It is often not possible to disentangle τ_2 from the fluorescence decay of the molecule.

Table 5.3 lists all fluorescence lifetimes measured, fitted to both the single- (τ_1) and double-exponential (τ_1 and τ_2) convoluted Gaussian functions (Section 3.2). Note that, τ_1 is limited by the cross-correlation of the experiment (55 fs). The suitability of the double-exponential fit depends on solvent properties, with the more viscous, less polar solvents benefitting more from the two-component fit. This can be seen in Figure 5.11, where the fitting residual for octanol decreases when fitted to a double-exponential fit. Both Figure 5.11 and Table 5.3 show that there is a larger solvent rearrangement contribution with a more viscous, less polar solvent, such as octanol. This is particularly noticeable when comparing τ_0 and τ_2 for a series of alcohols. Solutions of methanol and ethanol show very little difference in τ_0 (single-exponential lifetime) and τ_2, suggesting limited contribution of solvent dynamics to fluorescence lifetime. On the other hand, τ_0 and τ_2 diverge much more for heptanol and octanol, indicating that τ_1 is necessary.

Table 5.3: Fluorescence lifetimes of $p\mathrm{CK}^-$ in various solvents and solvent mixtures measured using static (s) and flow (f) fluorescence up-conversion cells, and obtained from single- (τ_0) and double-exponential fitting (τ_1 and τ_2). τ_1 is limited by experiment cross-correlation (55 fs). Percentages indicate vol% of water in the water–ethylene-glycol solutions. ± indicates the fitted uncertainty. EtGly is ethylene glycol.

	Single decay				Double decay							
Solvent	$\boldsymbol{\tau_0^s}$ **/ ps**	**± / ps**	$\boldsymbol{\tau_0^f}$	**± / ps**	$\boldsymbol{\tau_1^s}$ **/ ps**	**± / ps**	$\boldsymbol{\tau_2^s}$ **/ ps**	**± / ps**	$\boldsymbol{\tau_1^f}$ **/ ps**	**± / ps**	$\boldsymbol{\tau_2^f}$ **/ ps**	**± / ps**
MeOH	2.53	0.01	2.44	0.02	0.055	-	2.53	0.01	0.055	-	2.45	0.02
EtOH	3.18	0.02	2.33	0.04	0.055	-	3.25	0.01	0.055	-	2.33	0.04
1-PropOH	3.43	0.07	3.31	0.03	0.055	-	3.55	0.08	0.055	-	3.40	0.07
2-PropOH	5.27	0.05	3.70	0.04	0.055	-	5.40	0.06	0.055	-	3.84	0.04
ButOH	4.31	0.02	5.32	0.05	0.055	-	4.43	0.01	0.055	-	5.47	0.05
PentOH	7.71	0.04	6.96	0.08	0.069	0.002	8.05	0.04	0.055	-	7.11	0.08
HeptOH	7.82	0.06	8.01	0.11	0.080	0.002	8.20	0.06	0.091	0.008	8.44	0.10
OctOH	7.67	0.05	6.19	0.04	0.055	-	8.00	0.05	0.080	0.003	6.57	0.04
H_2O	1.14	0.04	1.18	0.01	0.055	-	1.13	0.00	0.055	-	1.17	0.01
EtGly	6.86	0.04	5.60	0.12	0.080	0.001	6.86	0.04	0.055	-	5.44	0.04
80% H_2O	1.67	0.01	-	-	0.055	-	1.68	0.01	-	-	-	-
60% H_2O	1.95	0.01	-	-	0.055	-	1.95	0.01	-	-	-	-
40% H_2O	2.68	0.02	-	-	0.055	-	2.73	0.02	-	-	-	-
20% H_2O	3.69	0.04	-	-	0.055	-	3.73	0.02	-	-	-	-

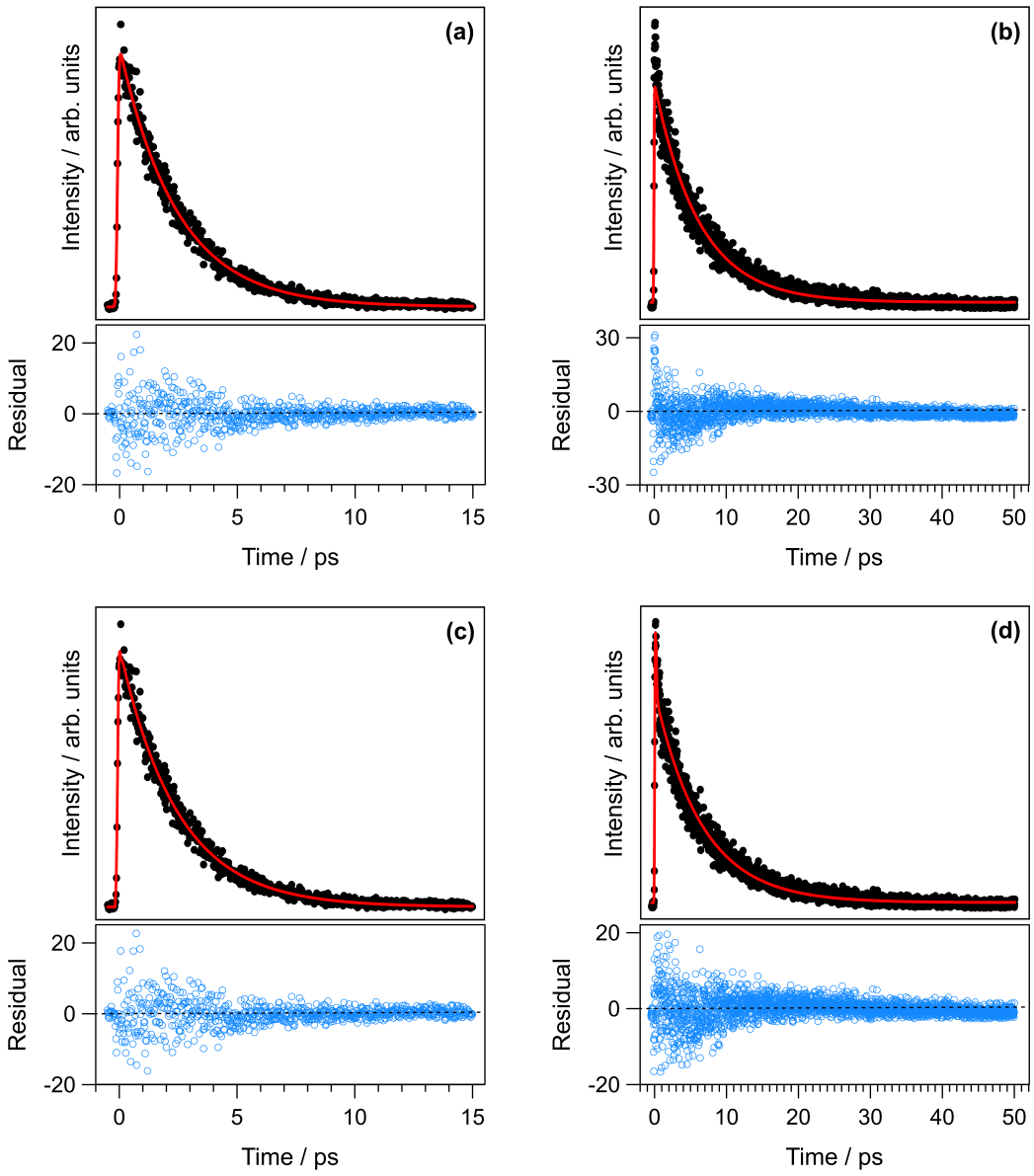


Figure 5.11: Fluorescence decays and fitting residuals for pCK$^-$ in methanol (**(a)** and **(c)**) and octanol (**(b)** and **(d)**. Panels **(a)** and **(b)** show single-exponential fitting, while **(c)** and **(d)** are double-exponential fits.

Previous up-conversion experiments on pCK$^-$ with poorer time resolution ($\approx$500 fs)[17] have shown longer lifetimes in more viscous, less polar solvents; however, the accuracy of double-exponential fitting was limited, due to the time resolution of the experiment. For example, for pCK$^-$ in water, Espagne *et al.* quote 0.5 ps and 1.3 ps for τ_1 and τ_2, respectively. The τ_2 value quoted by Espagne *et al.* compares well with the experimental

data obtained in this thesis (1.14 ps). On the other hand, τ_1 is very different (0.5 ps)[17] and, as the with τ_1 in this thesis, appears limited by the experimental time resolution. In the up-conversion experiments described in this thesis, all the τ_1 values, except for heptanol and octanol, are shorter than the experimental time resolution, which limits the accuracy of these parameters.

5.4.4.2 Comparison of static- and flow-cell up-conversion setups

The majority of reported solution-phase fluorescence up-conversion measurements on pCK$^-$ in the literature were performed using a static cell.[5,17,19,60–63] However, in such a setup, the possibility arises that incoming 400 nm (pump) laser pulses form and sample a mixture of Z- and E-isomers (*i.e.* a photostationary state), rather than just the E-isomer. In this case, the fluorescence lifetime of the sample corresponds to the average of the two species. On the other hand, a flow cell enables continual regeneration of the sample, thus allowing only the E-isomer to be studied. Single-component fitted lifetimes from static and flow cells are shown in Table 5.4. The 0.04 ps difference between the flow and static fluorescence lifetimes of pCK$^-$ in water is quite small, although it is beyond the instrumental uncertainty of the measurements; however, it suggests that changing the experimental setup only has a small effect on the fluorescence lifetime. This suggests either that there is only a trace amount of the Z-isomer, and/or the E- and Z- isomers

Table 5.4: Fluorescence lifetimes of pCK$^-$ (single-component fit) measured in a range of polar protic solvents using static (τ_0^s) and flow (τ_0^f) cells. ± indicates the fitted uncertainty.

Solvent	$\boldsymbol{\tau_0^s}$ **/ ps**	**± / ps**	$\boldsymbol{\tau_0^f}$ **/ ps**	**± / ps**
H_2O	1.14	0.00	1.18	0.01
MeOH	2.53	0.01	2.44	0.02
EtOH	3.18	0.02	2.33	0.04
1-PropOH	3.71	0.07	3.31	0.03
2-PropOH	5.27	0.05	3.69	0.04
1-ButOH	4.31	0.02	5.31	0.05
1-PentOH	7.71	0.04	6.96	0.08
1-HeptOH	7.82	0.06	8.01	0.11
1-OctOH	7.67	0.05	6.19	0.04
EtGly	6.86	0.04	5.60	0.12

have similar excited-state lifetimes.

Double-exponential fitting of the fluorescence decays yields τ_1 and τ_2, the former corresponding to the solvent dynamics but limited by experiment cross-correlation. While τ_1 from the static and flow experiments is mixed, the τ_2 lifetimes obey a similar trend to the single-exponential lifetimes (τ_0), as does the divergence between the static and flow measurements (Figure 5.12).

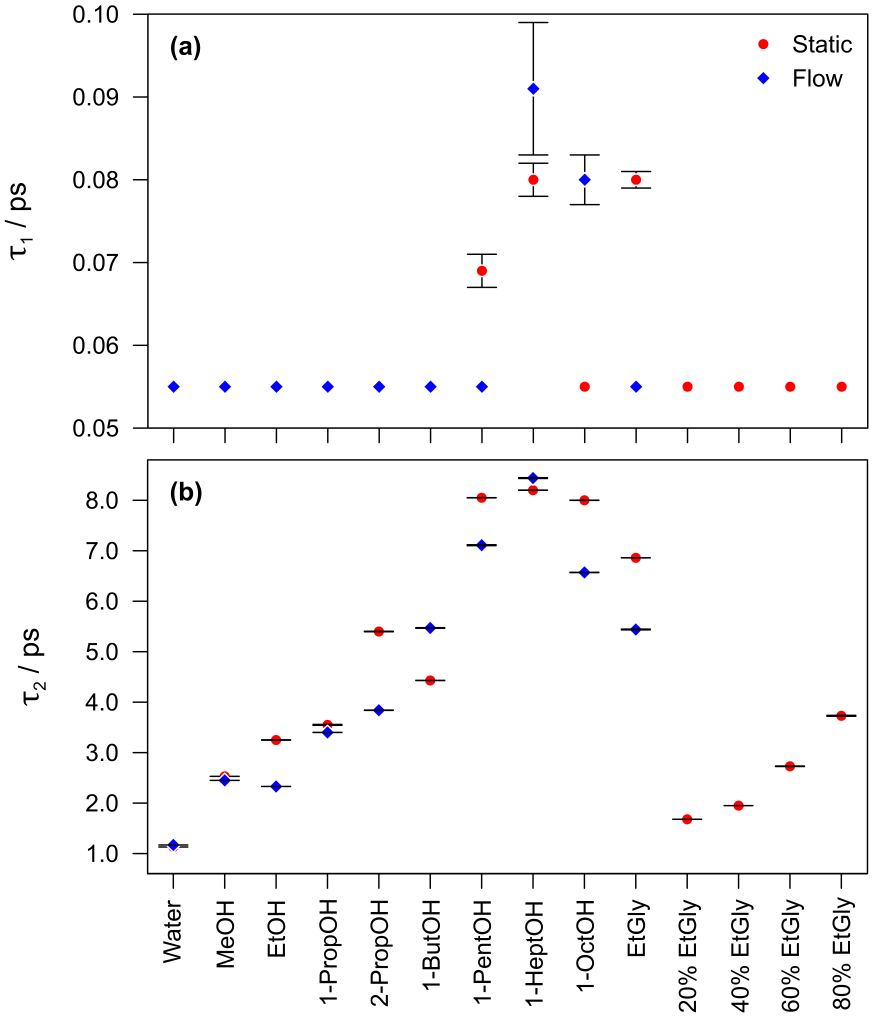


Figure 5.12: Fluorescence lifetimes of pCK$^-$ (from double-exponential fitting) in various solvents/solvent mixtures measured in a static (red) and flow (blue) cell setup – **(a)** τ_1, the fast component (corresponding to solvent rearrangement), and **(b)** τ_2, the slower component (species fluorescence lifetime). Percentages indicate vol% of ethylene glycol in the water–ethylene-glycol solutions.

5.4.4.3 Solvent environment

The fluorescence lifetimes across the solvent series reflect the effect of viscosity and polarity on the excited-state dynamics of pCK$^-$ in solution. The more viscous and less polar the solvent, the longer the fluorescence lifetime. Greater solvent viscosity slows the nuclear relaxation of the chromophore. The greater the polarity, the stronger the interaction between solvent molecules in the coordination spheres and the charged chromophore. However, since solvent polarity and viscosity are inextricably linked, the relative effects are difficult to disentangle. The trend of increasing fluorescence lifetime with decreasing polarity and increasing viscosity, as shown in Figure 5.13 for pCK$^-$ in a range of water–ethylene-glycol solutions, is common to most polar chromophores.

In the solutions with higher water fraction, the fluorescence lifetimes (τ_0) increase gradually, compared with those measured in solutions containing more ethylene glycol (Table 5.5). Espagne *et al.*[17] suggested that in solvent mixtures containing water, the chromophore may preferentially bind with water (*i.e.* the microsolvation sphere around pCK$^-$ will consist of water molecules), in which case limited changes in solute or solvent dynamics would be observed. When water dominates the solution (100–60% water), there is only a gradual increase in τ_0; however, when ethylene glycol dominates the mixture (40–0% water), there is a significant increase in τ_0 (from 3.7 to 6.8 ps). This indicates that pCK$^-$ may bind water preferentially, as the change in lifetime is only seen when water becomes the minority component. Further evidence for this is seen in τ_1

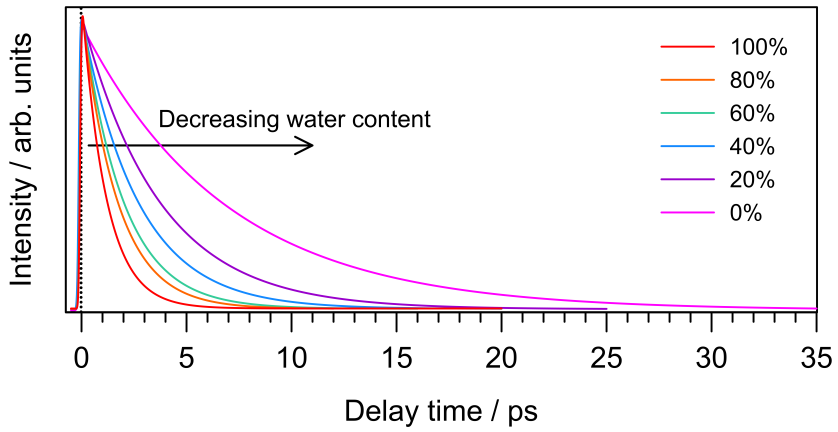


Figure 5.13: Single-exponential fluorescence decay fits for pCK$^-$ in water–ethylene-glycol mixtures, from which fluorescence lifetimes were obtained. The fluorescence decay curves are each normalised to the peak intensity. Percentages indicate vol% of water in the water–ethylene-glycol solutions.

(Table 5.5 and Figure 5.12). Only once ethylene glycol becomes the sole component does τ_1 increase above the experimental time resolution (55 fs). Since flow-cell up-conversion measurements were not performed on the water–ethylene-glycol mixtures, it is difficult to provide further discussion. In summary, it is likely that, in solvent mixtures whose largest component is water, the majority of the local solvation environment (*i.e.* microsolvation) around the solute contains water due to preferential solvation of $p\mathrm{CK}^-$ by water).

Table 5.5: Fluorescence lifetimes of $p\mathrm{CK}^-$ in water–ethylene glycol mixtures (obtained from single- (τ_0) and double-exponential fitting (τ_1 and τ_2)). τ_1 is limited by experiment cross-correlation (55 fs). Percentages indicate the relative volume of water to ethylene glycol in the solutions.

Solvent	$\boldsymbol{\tau_0}$ **/ ps**	$\boldsymbol{\tau_1}$ **/ ps**	$\boldsymbol{\tau_2}$ **/ ps**
100%	1.10±0.01	0.055	1.13±0.00
80%	1.67±0.01	0.055	1.68±0.01
60%	1.95±0.01	0.055	1.95±0.01
40%	2.68±0.02	0.055	2.73±0.02
20%	3.69±0.02	0.055	3.73±0.02
0%	6.86±0.04	0.08±0.00	6.86±0.04

As mentioned in previously, the suitability of the double-exponential fit depends on solvent properties. From Table 5.3, it is clear that the more viscous, less polar solvents exhibit a greater divergence of τ_2 from τ_0, although the overall trend remains the same: fluorescence lifetime increases as solvent polarity decreases and viscosity increases.[17] Under these conditions, solvent rearrangement is slowed, thus resulting in larger τ_2 values (Figure 5.14).

In transition-state theory (TST), a reaction coordinate is described in isolation. At a transition state, the theory assumes that the reaction proceeds to completion. However, TST fails to describe the ability of solvents to drive re-crossing of a barrier, either to the product or back to the reactant. Kramers' theory is commonly used to account for this solvent viscosity-dependent effect,[64] and uses a transmission factor, which depends on solvent viscosity and the PES shape at the transition state.[65]

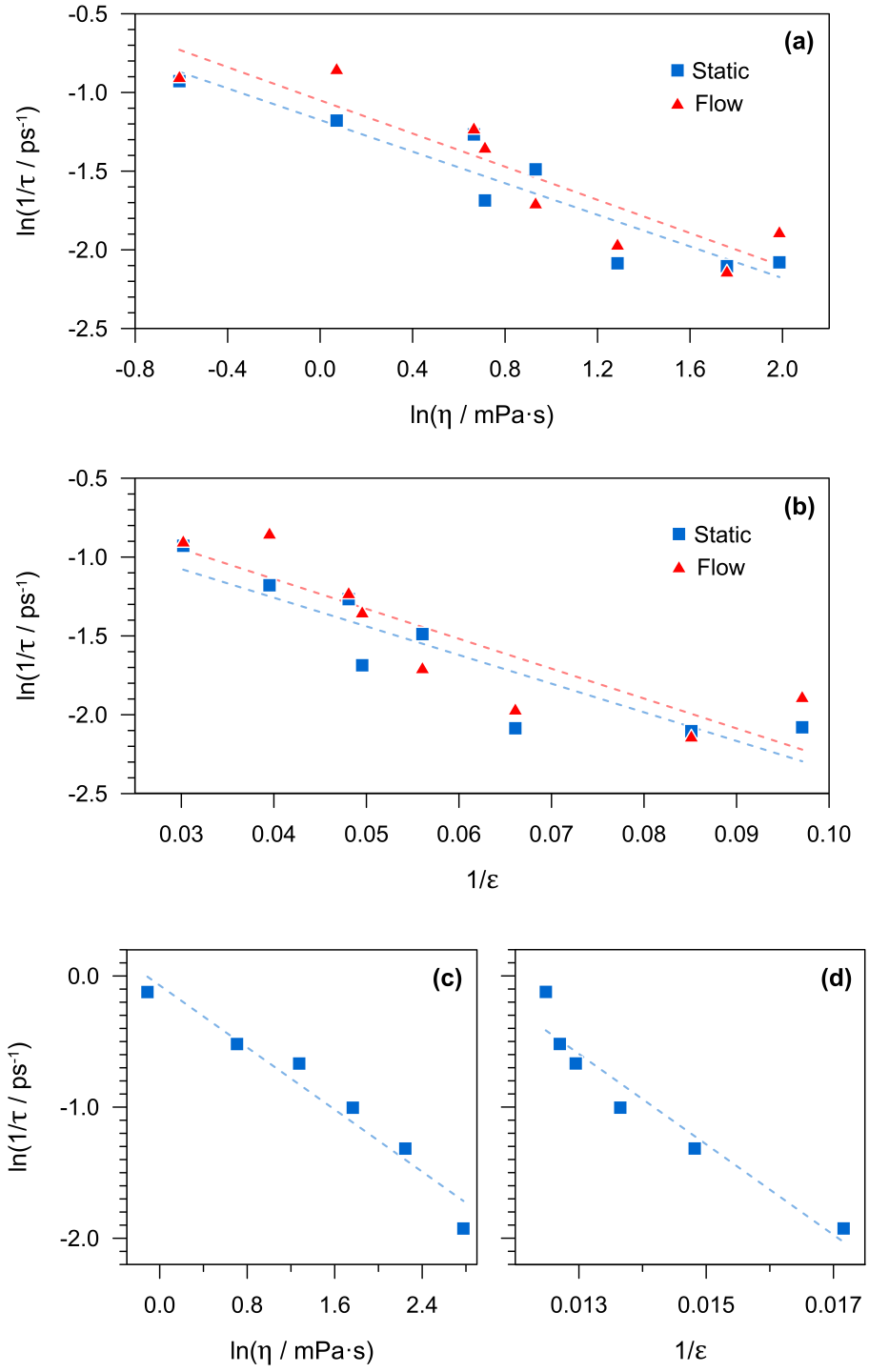


Figure 5.14: Fluorescence lifetimes (τ_2) for pCK$^-$ in (**(a)** and **(b)**) a selection of alcohols and (**(c)** and **(d)**) water–ethylene-glycol mixtures, obtained from double-exponential fitting of decay curves from static (blue) and flow (red) fluorescence up-conversion experiments.

There are systems where Kramers' theory fails to describe the relationship between solvent viscosity and the rate of barrier crossing accurately.[66,67] In these cases, a phenomenological power law (Equation 5.2) can be applied,[68] where k_i is the 'generic' isomerisation rate, C is proportional to $\exp(-E_a/kT)$ (Arrhenius term), and α is a measure of viscosity dependence. Here 'generic' implies both double- and single-bond torsions, which may both quench fluorescence.

$$k_i = C\eta^{-\alpha} \tag{5.2}$$

$$k_i \propto \eta^{-\alpha} \tag{5.3}$$

In high-viscosity solvents, α is predicted as unity; however, this rarely correlates with experimental data.[19,23,64] The experimental data for pCK$^-$ (Figure 5.14) was used to obtain values for α across the series of alcohols and water–ethylene-glycol mixtures. As discussed above, τ_1 reflects solvent rearrangement on excitation; however, since τ_1 values are limited by the experiment cross-correlation (55 fs), it is unphysical to quote $\tau_1 < 0.055$ ps. If τ_1 were not limited by experiment cross-correlation, it should depend on solvent viscosity ($\alpha > 0.8$). Comparatively, τ_2 exhibits a lower viscosity dependence (Table 5.6).

Table 5.6: Parameter α (from power law $k_i \propto \eta^{-\alpha}$) obtained from fitting τ_2 values for a series of alcohols (**A**) and water–ethylene-glycol mixtures (**B**) (See Figure 5.14). Regression coefficient (R^2) in parentheses.

	Sample cell	$\boldsymbol{\alpha_2}$
A	Static	0.50 (0.87)
	Flow	0.53 (0.84)
B	Static	0.59 (0.95)

An important assumption was made in determining α: since the photoisomerisation rate constant k_i was not measured directly, it was approximated as $1/\tau$. This approximation assumes that *E*-*Z* isomerisation is the dominant deactivation pathway and that fluorescence lifetime (τ) is a close approximation of the excited state lifetime. Regardless, the experimental values of α agree well with the literature – $\alpha = 0.54$ and 0.64 for pCK$^-$ and pCEs$^-$ (ester analogue), respectively.[19]

Espagne and co-workers[17,19,23] demonstrated that the viscosity effect on fluorescence

lifetime was particularly significant for pCK$^-$ compared with its neutral form, as the change in lifetime with solvent viscosity was much greater for the former. This is likely due to the greater solvent-solute interactions in the anionic system due to the charged solute. Kramers' theory, and the more sophisticated Grote-Hynes theory,[69] state that the barrier crossing rate of an activated process is controlled by solvent viscosity which, in general, is assumed only to affect low energy barriers on a potential energy surface.[19] This suggests that $E \rightarrow Z$ photoisomerisation in pCK$^-$ should encounter only a small barrier on the S_1 excited state. Other pCK$^-$ derivatives (*e.g.* the ester, pCEs$^-$, and the acid, pCA$^-$) also photoisomerise in solution, so the excited-state barrier must also be fairly small in these systems. The fluorescence lifetime data presented in this chapter show large dependence on solvent viscosity, consistent with the observations of Espagne and co-workers. Modelling of the pCK$^-$ potential energy surfaces across a series of solvents should reveal a change in the excited-state barrier, related to solvent properties.

Fluorescence up-conversion measures the fluorescence decay of a sample, and thus requires samples that fluoresce strongly. On the other hand, a much larger selection of molecules can be studied by transient absorption (TA) spectroscopy. Furthermore, TA monitors excited state lifetime directly and can therefore inform on the excitation and relaxation mechanism of a system.[18–20,23] TA studies of singly-deprotonated analogues of pCK$^-$ in water reveal excited state lifetimes ranging from 2.0 ps to 4.5 ps (≈500 fs time resolution).[19] On the basis of the fluorescence lifetime (τ_2) of pCK$^-$ in water (≈1.1 ps), its excited state lifetime would be expected to be of a similar magnitude.

Compared with the solution-phase environments described above, the PYP environment produces distinct fluorescence dynamics (and also involves a slightly different chromophore - a thioester relative of pCEs$^-$, pCT$^-$). The protein environment surrounding the PYP chromophore is tuned to optimise the $E \rightarrow Z$ photoisomerisation quantum yield of the system. There are minimal contributions from water molecules, because the chromophore is located inside a hydrophobic protein pocket with surrounding amino acid residues preventing water molecules from accessing the chromophore.[70,71] Therefore, the fluorescence dynamics of PYP will depend primarily on chromophore–protein interactions. The general literature consensus is that the time constants (lifetimes) obtained from double-exponential fitting of fluorescence decay profiles of wild-type PYP are approximately 0.7 ps (τ_1) and 4–5 ps (τ_2).[72,73] These timescales are comparable to the lifetimes measured for pCK$^-$ in various viscous polar solutions (*e.g.* 28:72 water-glycerol mixtures[17] and ethylene glycol (Table 5.3)). As a comparison, previous work by Vengris *et al.*[5] estimated the decay time of pCT$^-$ in aqueous alkaline buffer to be 2 ps.

5.4.5 Temperature-dependent fluorescence

Temperature has a significant effect on fluorescence from $p\mathrm{CK}^-$. Lowering sample temperature increases fluorescence intensity (increased fluorescence quantum yield) and blue-shifts the emission maximum wavelength (Figure 5.15). This is because nuclear and solvent motion are frozen at $T = 77\,\mathrm{K}$, so there can be no stabilisation of the excited state through nuclear or solvent rearrangement (unlike at $T = 300\,\mathrm{K}$). Simulated emission transition bands at $T = 77\,\mathrm{K}$ and $T = 300\,\mathrm{K}$ show significantly more hot-bands (and spectral broadening) due to emission from excited vibrational states. In comparison, the excitation spectra change little on cooling (Figure 5.15), with the main difference arising from the spectral band shape (narrower at $T = 77\,\mathrm{K}$ than at $T = 300\,\mathrm{K}$).

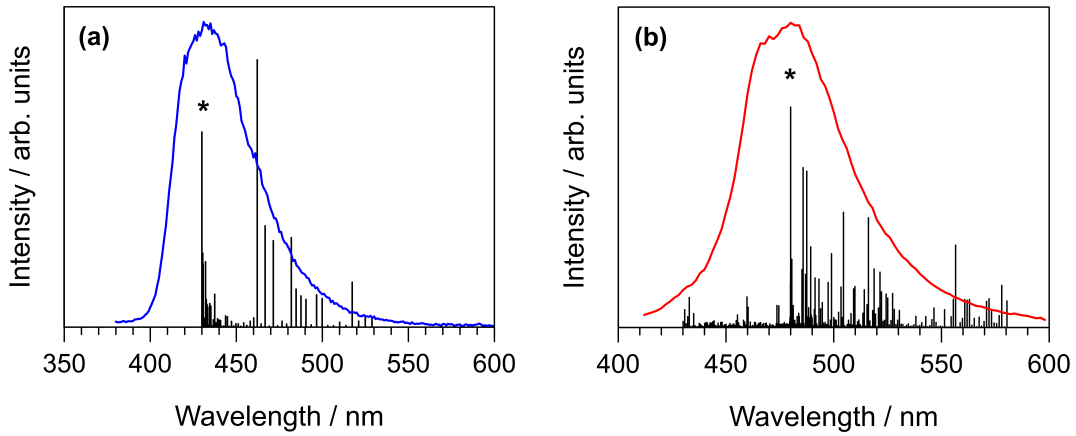


Figure 5.15: Experimental (curves) emission spectra of $p\mathrm{CK}^-$ at **(a)** $T = 77\,\mathrm{K}$ (in ethanol) and **(b)** $T = 300\,\mathrm{K}$ (in water). The FCHT simulated line spectra (lines) were computed, at the ωB97X-D/aug-cc-pVDZ level of theory, for isolated $p\mathrm{CK}^-$. * indicates the 0-0 transition. Vibronic features to shorter wavelengths of the 0-0 transition are hot bands. The simulated emission spectrum does not account for the solvent interactions.

As a comparison to the fluorescence lifetimes obtained by up-conversion experiments at $T \approx 300\,\mathrm{K}$, time-resolved emission spectra of $p\mathrm{CK}^-$ in ethanol were recorded at $T \approx 77\,\mathrm{K}$ (Figure 5.16). Unlike at room temperature, solvent viscosity effects are significantly less important in a glassy matrix. Frozen aqueous solutions are not conducive to fluorescence measurements due to the irregularities and defects that arise on water freezing (and also because of sample tube explosions due to expansion processes on thawing). On the other hand, ethanol has more desirable freezing properties, forming a clear, glassy matrix. Since fluorescence emission at cryogenic temperatures is more

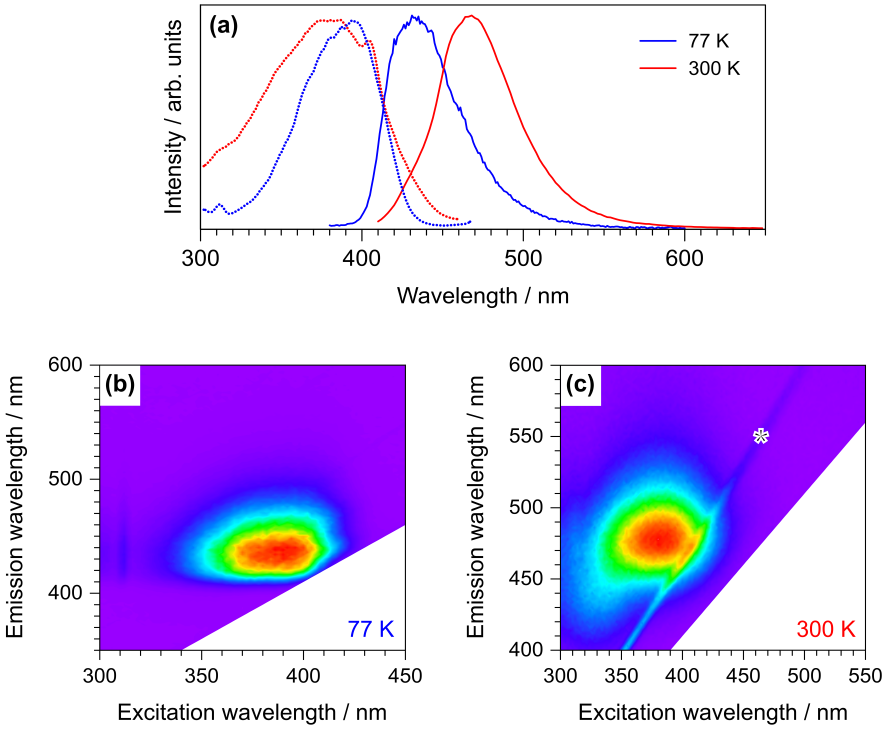


Figure 5.16: The temperature dependence of fluorescence excitation and emission of pCK$^-$: **(a)** excitation (dotted) and emission spectra (solid) at $T \approx 77\,\mathrm{K}$ (blue) and $T \approx 300\,\mathrm{K}$ (red), and **(b)** & **(c)** excitation-emission maps at $T \approx 300\,\mathrm{K}$ and $T \approx 77\,\mathrm{K}$, respectively. Asterisk indicates an artefact from excitation light.

intense and blue-shifted (relative to room temperature, $T \approx 300\,\mathrm{K}$), time-resolved emission on excitation at 365 nm was monitored over 420–460 nm, instead of 470–490 nm ($T \approx 300\,\mathrm{K}$).

The measurements show that lifetime increases by approximately three orders of magnitude – from 3 ps at $T \approx 300\,\mathrm{K}$ to 2 ns at $T \approx 77\,\mathrm{K}$ (Table 5.7). Note that increasing fluorescence lifetime with longer monitoring wavelength is observed at both temperatures, presumably due to the presence of two geometries from which fluorescence can occur. The substantial increase in lifetime on freezing occurs because nuclear motion is hindered significantly, reducing access to the conversion conical intersection.

Table 5.7: Fluorescence lifetimes of pCK$^-$ in different solvents measured at $T \approx 300\,\mathrm{K}$, by fluorescence up-conversion ($\lambda_{ex} \approx 400\,\mathrm{nm}$), and $T \approx 77\,\mathrm{K}$, by time-resolved emission ($\lambda_{ex} \approx 365\,\mathrm{nm}$). λ_m is the emission monitoring wavelength.

Solvent	**T / K**	τ_0 **/ ps**	λ_m **/ nm**
Water	300	1.14±0.00	485
MeOH	300	2.53±0.01	475
EtOH	300	3.18±0.02	470
	77	2040±3	440

5.5 Gas-phase photophysics

Numerous gas-phase experimental studies have focussed on understanding the inherent photochemistry and photosiomerisation behaviour of hydroxycinnamate-based molecules (model PYP chromophores). The appeal of gas-phase studies is the absence of solvent influence. The simplest hydroxycinnamate anion, deprotonated *para*-coumaric acid (pCA$^-$) has been the subject of several studies. The two acidic groups in pCA$^-$ (phenol and carboxylic acid), when deprotonated, give rise to phenoxide and carboxylate deprotomers. The relative deprotomer abundances, when generated through electrospray ionisation, depend on numerous experimental conditions, including solvent, electrospray voltage, and carrier gas.[74,75] Previous studies of anionic hydroxycinnamate-based molecules (e.g. pCA$^-$ and its methylated derivatives (pCEs$^-$ and pCEt$^-$), see Figure 5.2) have employed gas-phase action spectroscopy techniques, including photodetachment and photoelectron spectroscopy,[22,76,77] and ion-storage rings[78–80] (where the formation of the corresponding neutral molecule is monitored as a function of wavelength).

For target ions possessing multiple isomers or deprotomers, there is a need for ion-mobility experiments used in conjunction with photodetachment and photoisomerisation action spectroscopy, allowing the isomers to be probed individually.[81] In the tandem ion-mobility experiments, electrospray ionisation of pCA$^-$ has been shown to create the E-isomeric form of both the phenoxide and carboxylate deprotomers, with only trace amounts of the Z-carboxylate isomer.[82] These deprotomers give rise to easily distinguishable action spectra (350–480 nm and 290–400 nm, respectively)[21] due to distinct electronic structure. For example, it was shown that, upon photoexcitation of the phenoxide deprotomer, there was no evidence of $E \rightarrow Z$ isomerisation, while two photoisomers (keto tautomer and phenoxide deprotomer) were produced upon photoexcitation

of the carboxylate deprotomer. In comparison, the methyl ester (pCEs$^-$) only exists as the phenoxide deprotomer (and also showed no $E \rightarrow Z$ photoisomerisation). These results are consistent with recent time-resolved studies on (E)-pCEs$^-$ demonstrating that electron detachment outcompetes ground state recovery (*e.g.* by $E \rightarrow Z$ photoisomerisation).[22,83] The lack of $E \rightarrow Z$ photoisomerisation was also found for a range of substituted pCA$^-$ derivatives, including sinapinic, ferulic, and caffeic acids.[82] These studies have broadly shown that many *para*-hydroxycinnamates are unlikely to exhibit a wavelength-dependent competition between photodetachment and photodissociation, since the action spectra for these processes are near-identical.

5.5.1 Experimental methods

The photoisomerisation and photodetachment experiments described below were performed by Dr Bull at the University of Melbourne, Australia, and the photodissociation experiments were performed by current collaborators at the University of Waterloo, Canada.

5.5.1.1 Photoisomerisation action spectroscopy

A custom-built tandem ion-mobility spectrometer (IMS), consisting of consecutive ion-mobility spectrometry drift regions terminated by a quadrupole mass filter (IMS-IMS-QMF),[84,85] was used to obtain action spectra of gas-phase pCK$^-$ (Figure 5.17). Briefly, anions were produced by electrospray ionisation (≈ -3 keV) and passed through a heated capillary before being collected by the first ion funnel (IF1). A radio frequency applied to IF1 enabled control of the initial isomer distribution. Ion packets were injected into the first IMS stage (IMS1), *via* pulsing of the first ion gate (IG1), and in which the ions of interest separated according to their collision cross-section with a buffer gas ($\approx$6 Torr). In these experiments, either N_2 or a mixture of N_2 + 1% SF_6 + 1% propan-2-ol were used as the buffer gas. Seeding the buffer gas with a trace amount of SF_6 permits sensitive detection of photo-induced electron detachment, by monitoring $SF_6{}^-$ yield,[86] because SF_6 is an efficient electron scavenger (SF_6 electron affinity $\approx$1 eV).[87,88] Electron-scavenging occurs *via* the following reaction: $SF_6 + e^- \rightarrow SF_6{}^-$. The selected anions traversed the drift region, propelled by an applied electric field (44 V cm^{-1}). Anions of a selected (narrow) range of collision cross-sections were transmitted (40 Hz repetition rate) into the second IMS stage (IMS2) using a Bradbury-Nielsen ion gate (IG2). An optical parametric oscillator (OPO) laser system (EKSPLA NT342B, 20 Hz,

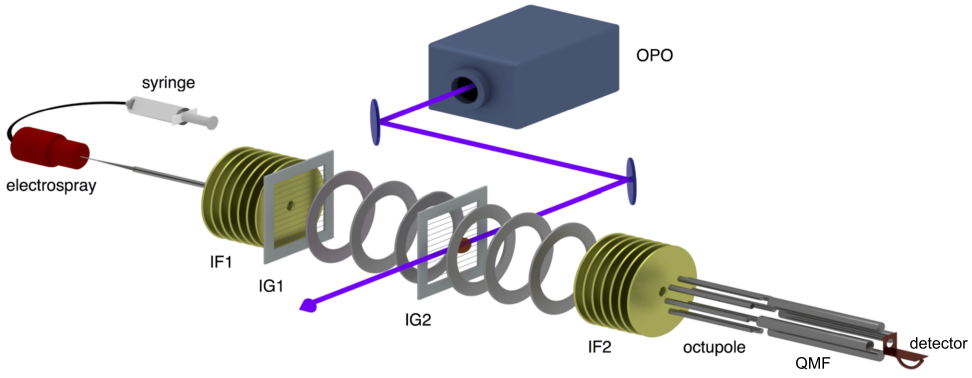


Figure 5.17: Schematic representation of the tandem ion-mobility mass spectrometer used to obtain action spectra of gas-phase $p\mathrm{CK}^-$. Ions produced by electrospray ionisation are collected in the first ion funnel (IF1) and are injected as packets into the first IMS stage (IMS1) by the ion gate (IG1). Ion-mobility selected ion packets are transmitted into the second IMS stage (IMS2) by the second ion gate (IG2). Every second isomer-selected ion packet is irradiated with light from an OPO laser system. Daughter ions are collected in the second ion funnel (IF2) and are then guided into a quadrupole mass filter (QMF) by an octupole ion guide. The QMF mass-selects ions, which are counted by the channeltron detector. Adapted from Scholz *et al.*[85]

$<2\,\mathrm{mJ\,cm^{-2}}$ pulse energy) excited every second ion packet immediately after they entered IMS2. The daughter isomers, created through exposure to light, were separated according to their collision cross-section in IMS2 and radially collected in a second ion funnel (IF2). The ions then were guided through an octupole ion guide and mass selected in a quadrupole mass filter (QMF) operating at $\approx 10^{-6}\,\mathrm{Torr}$, before reaching the channeltron detector connected to a multichannel scalar. The detector system generated an arrival time distribution (ATD) corresponding to ion count as a function of arrival time. The photoinduced signal (action spectrum intensity) was obtained by taking the difference between the 'laser-on' and 'laser-off' ATDs as a function of laser wavelength.

Collision cross-section and arrival time are linked by the ion's mobility. Briefly, the proportionality constant (K) linking the velocity of an ion travelling through a buffer gas (v_d) to the applied electric field (E) is the mobility of said ion, given by

$$v_\mathrm{d} = KE \tag{5.4}$$

The mobility, K, is inversely proportional to the ion's collision integral (cross section) $\Omega^{(1,1)}(T)$[89,90]

$$K = \frac{3ze}{16N}\left(\frac{2\pi}{\mu k_B T}\right)^{1/2}\frac{1}{\Omega^{(1,1)}(T)} \tag{5.5}$$

where z is the electronic ion charge, e is the elementary ion charge, N is the number density of the buffer gas, k_B is the Boltzmann constant, and μ is the reduced mass.

5.5.1.2 Photodissociation action spectroscopy

In addition to the tandem ion-mobility experiments, gas-phase pCK$^-$ was probed by photodissociation action spectroscopy (Figure 5.18) at the University of Waterloo.[91] Although the particular photodissociation action spectrometer used can separate isomers using a derivative of ion-mobility spectrometry (called differential mobility spectrometry, DMS), this is not crucial for pCK$^-$, because electrospray ionisation generates a single isomer.[92,93] Because the DMS capacity was not required in this work, this portion of the experiment is not described in detail. In the experiment, ions were formed

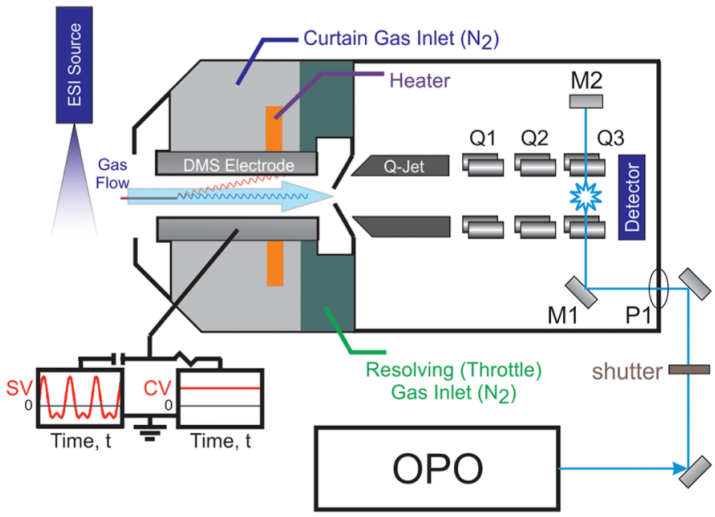


Figure 5.18: Schematic representation of the photodissociation action spectroscopy setup used to obtain action spectra of gas-phase pCK$^-$. Ions, produced by electrospray ionisation (ESI) are carried by the buffer gas between the DMS electrodes. The mobility-selected ions traverse through quadrupole elements Q1–2 until reaching Q3 where they are excited by an optical parametric oscillator (OPO) laser system. The detector monitors and records the intensities of the parent and daughter ions at each OPO output wavelength. Supplied from the Hopkins research group (University of Waterloo).

by electrospray ionisation (ESI) and the anions carried, by N_2 buffer gas (atmospheric pressure), through a heated DMS cell. Two voltages can be applied across the electrodes in the DMS cell: (1) the separation voltage (SV) – an oscillating electric field to modify ion trajectories, and (2) the compensation voltage (CV) – a DC voltage to compensate for off-axis trajectories. In this case, the SV and CV voltages were tuned to broadly transmit the $p\mathrm{CK}^-$ *E*-isomer, although the voltages were not refined, as there was only one isomer present. Mobility-selected ions then traversed through quadrupole elements Q1 and Q2, providing differential pumping and mass-selection. The ions were trapped eventually in Q3, a linear ion trap, where they were excited by an OPO laser system (Continuum Surelite II). Action spectra were obtained by recording the relative intensities of the parent and fragment ions at each OPO output wavelength. The main contributions are anions arising from loss of C_2H_2O (m/z=119) and loss of CH_3/CH_4 (m/z=145/146). There are also small contributions from other minor channels, such as cleavage of the single bond between the phenoxide ring and the double bond. A recent example of use of the FAIMS capacity to separate isomers, allowing for isomer-specific photodissociation spectroscopy, can be found in Coughlan *et al.*,[94] in which three deprotomers/tautomers of the red Kaede fluorescent protein chromophore anion (rKFP^-, relevant to Chapter 4 of this thesis) were studied.

It is important to note that the conditions in the ion mobility experiment and photodissociation experiment are very different. Namely, the ion mobility experiments are performed under ≈6 Torr background conditions, while the photodissociation experiments are performed under 10^{-6} Torr background pressure conditions. In the latter case, dissociation readily occurs since photoactived ions have ample time to undergo internal conversion to the ground electronic state followed by statistical dissociation (usually occurs on microsecond timescale). Conversely, ions in the drift region of the ion mobility experiment are photoactivated in an environment where the collision rate is $\approx 10^9\ \mathrm{s}^{-1}$ at 6 Torr. Rapid excited-state processes occurring on sub-nanosecond timescales, including photoisomerisation by passage through a conical intersection or autodetachment (electron detachment), will tend to take place. On the other hand, slower ground-state processes, such as statistical dissociation or statistical electron ejection (thermionic emission), are suppressed because of collisional deactivation.[21,93] For this reason, photodissociation is quenched in the ion mobility experiment.

5.5.2 Computational methods

Electronic structure calculations were performed using the Gaussian 16.B01[32] and Firefly 8.2.0[47] software packages. Geometry optimisations, vibrational frequencies, and isomerisation transition state searches were performed at the ωB97X-D/aug-cc-pVTZ level of theory.[34,35] The geometries of the S_0 and S_1 states, and the excited-state double-bond twisted intermediate (TS^*_{DB}), were optimised at the CASSCF(10,9)/aug-cc-pVDZ level of theory. The potential energy surface (PES) mapping started from the minimum energy geometry (for S_0 and S_1), from where the allyl dihedral angle was changed in 10° increments and the single-point energies of the unoptimised structures computed at the XMCQDPT2(12,11)/aug-cc-pVDZ level of theory.[52] The choice of active space followed the recommendations of Boggio-Pasqua and Groenhof,[95] achieving a balance between accuracy of the PES and computational expense. The earlier study demonstrated that a (10,9) active space could describe the single- and double-bond torsion pathways of the thio-*p*CEs⁻ (*p*CT⁻) PES to a good degree of accuracy, comparable to a (12,11) active space. Therefore, a (10,9) active space was used for excited state optimisations and the more expensive (12,11) active space used to compute single-point energies.

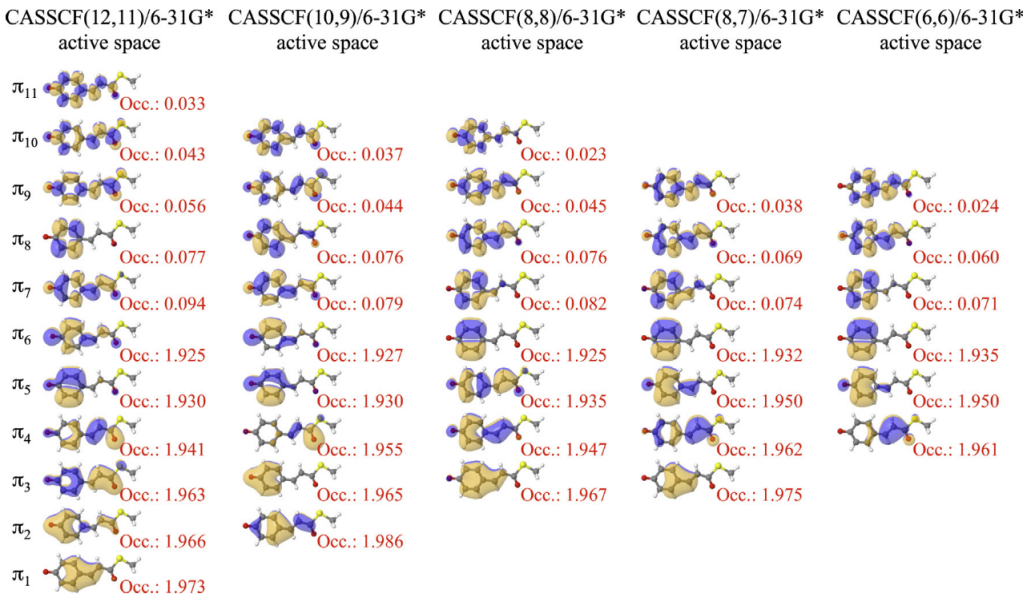


Figure 5.19: Boggio-Pasqua and Groenhof used thio-*p*CT⁻ (thioester of *p*CK⁻ to investigate the effect of reducing active space size on molecular orbital descriptions by visualising the orbitals from CASSCF calculations with active spaces of differing sizes. Adapted from Boggio-Pasqua and Groenhof.[95]

5.5.3 Results and discussion

5.5.3.1 Action spectra

Figure 5.20 shows the arrival time distributions (ATDs) and action spectra for (*E*)-*p*CK$^-$. The black traces in Figure 5.20(a) and (b) are the "light-off" ATDs, with a resolution of $t/\Delta t \approx 70$, which is consistent with the presence of a single isomer based on the mobility resolution and characteristics of the instrument.[96] The generation of a single isomer in electrospray ionisation is expected because of the single deprotonation site in *p*CK$^-$ and because the sample was purchased from Fisher Scientific as the pure *E*-isomer. Furthermore, earlier studies considering a range of *para*-hydroxycinnamates, including *p*CA$^-$ and *p*CEs$^-$, have used experimental data and modelling of collision cross-sections to show that the *E*-isomers are the predominant gas-phase form.[74] The only exception is *p*CA$^-$, where the carboxylate deprotomer was present in trace amounts as the *Z*-isomer.[21] The photoaction ATDs (blue, Figure 5.20(a) and (b)) show the photoappearance of the *Z*-isomer, bleach of the *E*-isomer, and electron detachment to give SF_6^- in (b).

Usually, *E*-isomers have larger collision cross-sections than *Z*-isomers, particularly in "inert" buffer gases, such as N_2 or He, due to the more extended structure of the *E*-isomers. As a result, the *E*-isomer collision cross-section is larger, resulting in a slightly longer arrival time (Figure 5.20(a)). However, in some buffer gases, such as CO_2 or those seeded with organic dopants, the *Z*-isomer has the longer arrival time (Figure 5.20(b)). This is because the collision cross-section (*i.e.* the effective collisional surface area presented by an ion) typically has two components: (1) a small impact parameter (hard-sphere collision), and (2) a large impact parameter (glancing collision). Contribution (1) is important in inert buffer gases, which are best suited for distinguishing isomers with substantially different shapes. On the other hand, buffer gases seeded with organic dopants are more suited to distinguishing isomers based on their long-range intermolecular interactions (including dipole-quadrupole and hydrogen-bonding), which is where contribution (2) gains importance.[97] For *p*CK$^-$ in the N_2 + 1% SF_6 + 1% propan-2-ol buffer gas, it appears that there are isomer-specific interactions which slightly favour the *Z*-isomer, leading to an increase in collision cross-section and arrival time. The main benefit of performing the same experiments under different buffer gas conditions is that the *Z*-isomer is slightly better resolved with the organic dopant (propan-2-ol) seeded into the buffer gas (Figure 5.20(b)). However, an important consideration when choosing a buffer gas is that small increases in collision cross-section can result in a significant increase experimental spectral acquisition times, due to reduced ion through-

put. Finally, it should be noted that photoisomerisation and photodetachment action spectra recorded with N_2 and CO_2 buffer gases (not shown) were near-identical to those in the seeded buffer gas, confirming that gas-phase pCK$^-$ exists as free ions rather than complexes (*e.g.* pCK$^-$·propan-2-ol), as complexes would shift the action spectra (see spectral shifts on complexation of HBDI$^-$ analogues in Chapter 4).

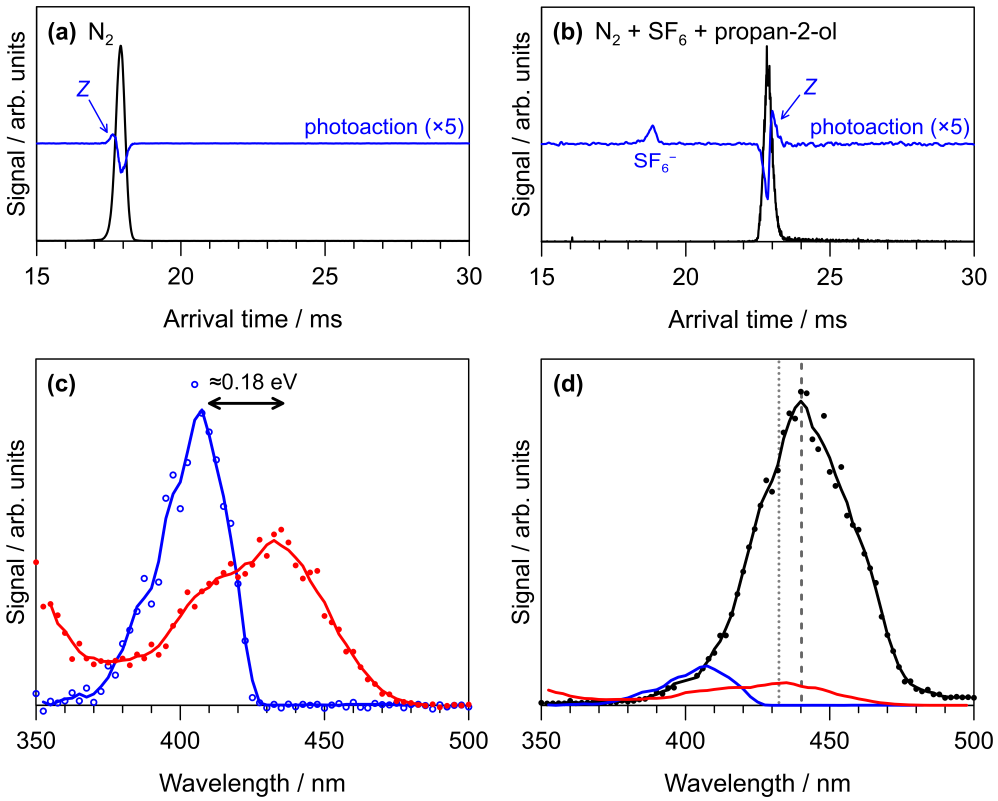


Figure 5.20: Action spectra of (E)-pCK$^-$. Panels **(a)** and **(b)** show "light-off" (black) and "light-on"/photoaction (blue) arrival time distributions at 420 nm excitation in pure N_2 buffer gas and N_2 buffer gas seeded with ≈1% SF_6 and ≈1% propan-2-ol, respectively. The plots in panel **(c)** are the photodetachment (red) and $E \rightarrow Z$ photoisomerisation (blue) spectra, recorded using the Melbourne ion-mobility experiment. Overlaid over the photoisomerisation and photodetachment spectra in panel **(d)** is the photodissociation spectrum (black), recorded over the $S_1 \leftarrow S_0$ absorption band, using the Waterloo experiment. The dashed line shows the maximum photodissociation response (corresponding to vertical excitation wavelength) and the dotted line indicates the electron affinity of pCK, computed by Anstöter *et al.*[51] (see text regarding scaling of spectra in **(d)**.)

The $E \rightarrow Z$ photoisomerisation action spectrum (Figure 5.20(c), blue) spans the 370–430 nm range, with maximum response at 405 nm. In contrast, the photodetachment spectrum (Figure 5.20(c), red) spans a broader range of wavelengths, from 350–480 nm, with maximum response at 435 nm. Lastly, the photodissociation action spectrum (Figure 5.20(d), black) spans the 380–490 nm range, with maximum response at 440 nm. Computed vertical excitation energies discussed in Section 5.4.1 are in good agreement. Note that approximately one third of the photodissociation action spectrum is situated below the computed electron affinity ($\approx$432 nm).[51] While the photodetachment and photoisomerisation action spectra are roughly in proportion to the gas-phase probability for each process, it is difficult to place them on a relative scale compared with photodissociation. In Figure 5.20(d), the photoisomerisation and photodetachment spectra are scaled, such that the blue edges of the isomerisation and dissociation curves are roughly equivalent. However, the intensity of the isomerisation and detachment curves in Figure 5.20(d) are expected to be around 10-fold lower. This is because photodissociation will occur from either the E or Z isomers and isomerisation quantum yields are typically between 1–20%. These action spectra for pCK$^-$ contrast with those for all other *para*-hydroxycinnamates studied to date, such as pCEs$^-$, for two reasons: (1) the photoisomerisation, photodetachment, and photodissociation spectra do not parallel each other, and (2) this is the first *para*-hydroxycinnamate for which $E \rightarrow Z$ photoisomerisation has been observed, albeit only over the blue half of the $S_1 \leftarrow S_0$ absorption band. The disparity between isomerisation and detachment over the S_1 band (the S_2/S_3 bands are in the UV) means that there must be a wavelength-dependent competition between these processes over the 350–500 nm range, implying complex excited-state dynamics.

The differences between the photo-induced action spectra in Figure 5.20(c) and (d) are discussed in terms of the excited-state dynamics that may give rise to these actions. The photodissociation action spectrum is expected to be the closest proxy to the absorption spectrum because dissociation in 'large' molecules occurs almost exclusively through statistical processes. Specifically, the ground electronic state is recovered by internal conversion, after which statistical redistribution of internal energy (intramolecular vibrational redistribution) eventually results in bond scission. Furthermore, this spectrum is in close agreement with the large body of action spectra recorded for PYP chromophore derivatives.[76–80] Statistical dissociation processes can occur in the ultra-high vacuum background conditions of the photodissociation experiment, since energy quenching through collisions is minimised. Conversely, near-complete collisional energy quenching occurs within 100 ns in the drift region of the ion-mobility experiments. Therefore, the 'prompt' isomerisation and electron detachment processes must occur over

timescales of less than a few tens of nanoseconds. No dissociation was observed in the ion mobility experiments. The photoisomerisation action spectrum should thus correspond either to an excited-state process, facilitated by passage through a conical intersection, or to thermal isomerisation, occurring after internal conversion to the ground state. The latter option is unlikely for two reasons: firstly, the *Z*-isomer is less stable than the *E*-isomer, resulting in a very small branching ratio and, secondly, thermal isomerisation is a statistical process that, like dissociation, occurs on much longer timescales than photoisomerisation. The second point also applies to electron detachment; the photodetachment action spectrum will correspond to the excited-state autodetachment process, rather than internal conversion followed by thermionic emission (statistical electron ejection). The autodetachment dynamics in other *para*-hydroxycinnamates have been discussed in detail in Refs. 22 and 83. Finally, it is worth noting that the actual PYP chromophore is a thioester. In the gas-phase, the thioester is expected to exhibit excited-state dynamics similar to its ester derivative (pCEs$^-$), *i.e.* without $E \rightarrow Z$ isomerisation,[22,83] because photoelectron spectroscopy showed no evidence for internal conversion to the ground electronic state (*i.e.* electron detachment dominates).[76]

Two previous studies have investigated the time-resolved dynamics of pCK$^-$ in the gas phase. The first was the pioneering work by Zewail and co-workers[6] which demonstrated, using time-resolved photoelectron spectroscopy, that the excited state formed upon excitation of pCK$^-$ with 400 nm light survives for ≈52 ps, before internally converting to the ground electronic state. While this study could not probe photoisomerisation directly, it was presumed that some fraction of the excited ions would decay to the ground state by passage through an isomerising S_1/S_0 conical intersection, forming a stable *Z* photoisomer. The ≈52 ps excited state lifetime is long compared with typical intramolecular vibrational redistribution timescales (typically several picoseconds),[98] prompting the conclusion that internal conversion is a barrier-controlled process, *i.e.* that a barrier on the excited state hinders motion away from the Franck-Condon geometry/towards the S_1/S_0 conical intersection. This is consistent with high-level molecular dynamics and QM/MM simulations that show a significant barrier to the S_1/S_0 conical intersection on the excited state for the deprotonated chromophore in isolation.[12,31,99,100] On the other hand, more recent measurements on pCK$^-$ excited at 444 nm found the time-resolved photoelectron spectra to be dominated by autodetachment,[51] implying no formation of a stable *Z*-isomer. This latter study compared photoangular distributions, obtained by velocity-map imaging, to theoretical modelling, predicting that the principal excited-state pathway involves single-bond torsion, disagreeing with the earlier work by Zewail and co-workers. However, both studies predict an excited-state potential energy barrier

to reach the $E \rightarrow Z$ isomerising conical intersection, consistent with computational simulations.

The present photoisomerisation data confirm that the two time-resolved experiments detailed above both reached sensible conclusions. At 400 nm, the action spectra in Figure 5.20(c) showed efficient $E \rightarrow Z$ isomerisation while, at 444 nm electron detachment is the dominant relaxation pathway. In many regards, these experimental results are overdue, since the molecular dynamics work by Prof. Robb and collaborators predicted such dynamics in the mid-2000s, yet there are essentially no clear experimental examples of barrier-controlled dynamics in gas-phase data.[12,99]

5.5.3.2 Potential energy surfaces

As mentioned in Section 5.5.2, the choice of active space for potential energy surface (PES) modelling was guided by the 2014 work by Boggio-Pasqua and Groenhof,[95] which demonstrated the extent to which the CASSCF active space could be reduced with only a limited impact on PES and molecular orbital descriptions for thio-pCA$^-$ (Figure 5.19). The (6,6) active space was discarded as it did not describe the correct topological features on the S_1 PES and, along with the (8,7) active space, did not describe the double-bond (β) torsion pathway accurately. The (10,9) active space provided a more accurate description of the single- and double-bond torsion pathways than the (8,8) active space. A reduction in active space from (12,11) to (10,9) provides a significant decrease in computational expense, due to the factorial scaling with system size (the number of electrons and orbitals in the active space), while preserving the accuracy of the (12,11) description. To determine the appropriate active space for the CASSCF/XMCQDPT2 calculations in this work, the orbitals of pCK$^-$ were optimised at the CASSCF(12,11)/aug-cc-pVDZ level of theory (Figure 5.21). The orbitals agree well with those for thio-pCA$^-$. A similar situation was found for the orbitals of the ester derivative of pCK$^-$ (pCEs$^-$, Figure 5.22), which will also be a focus of future work. The differences in orbital appearance and/or ordering are ascribed to the different basis sets and functional groups used in the present orbital optimisation calculations and in the literature, CASSCF(12,11)/aug-cc-pVDZ and CASSCF(12,11)/6-31G*, respectively.

The present investigation of the pCK$^-$ potential energy surface (PES) aims to expand on the work by Anstöter *et al.*,[51] in which the pCK$^-$ photoisomerisation PES was modelled using the XMCQDPT2 method using linear interpolation in internal coordinates.

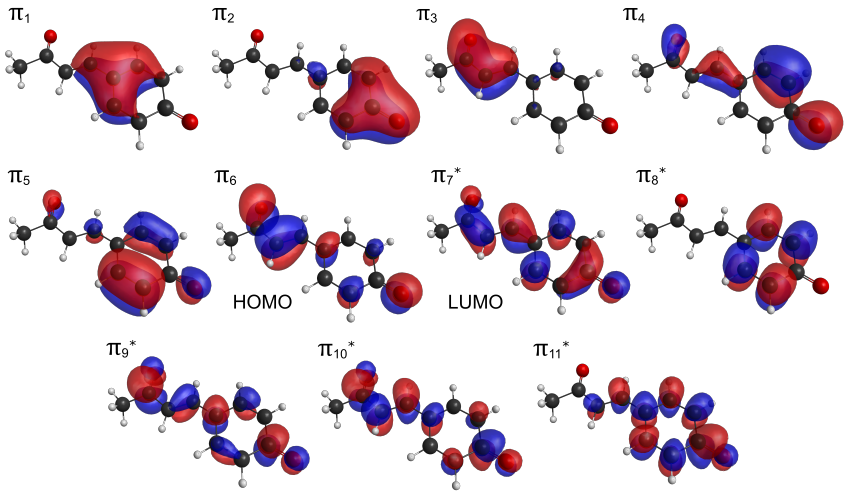


Figure 5.21: Bonding and anti-bonding π-orbitals of pCK$^-$, computed in the Firefly 8.2.0[47] software package at the CASSCF(12,11)/aug-cc-pVDZ level of theory.

The linear interpolation in internal coordinates (LIIC) approach links optimised critical points of a reaction mechanism by the *simplest* path between those geometries. However, because the molecular geometries along the interpolated pathway are not reoptimised, the pathway described is unlikely to be of minimum energy. Instead of using LIIC, this work computes the single-point energies of twisted pCK$^-$ geometries, in 10° increments, at the XMCQDPT2(12,11)/aug-cc-pVDZ level of theory. Note that in the initial scan, the twisted structures are not reoptimised, so the barrier height and conical intersection accuracy is still limited. Vertical excitation energies (VEEs) from the above calculations can be compared with that from experiment (≈2.82 eV, Figure 5.20(d)). Both calculated VEEs are within ±0.2 eV of the experimental value (≈2.90 eV[51] and 2.66 eV), providing better agreement than VEEs calculated by other methods, including STEOM-DLPNO-CCSD (see Table 5.1). In addition to VEEs, the potential energy surfaces provide an indication of the approximate height of the excited-state barrier to double-bond rotation (≈0.25 eV[51] and ≈0.4 eV). The difference between the photodetachment and photoisomerisation action spectra (≈0.18 eV, Figure 5.20(c)) is estimated to be this barrier height, which is slightly smaller than those predicted in calculations. However, both the present calculations and those performed by Anstöter and co-workers did not reoptimise structures along the PES pathway and thus do not correspond to the lowest point over the barrier. Performing a more rigorous transition-state search and optimising structures along the PES pathway would give a more accurate description of the excited-state barrier. Full reoptimisation of the twisted geometries at the CASSF(10,9)/aug-cc-pVDZ

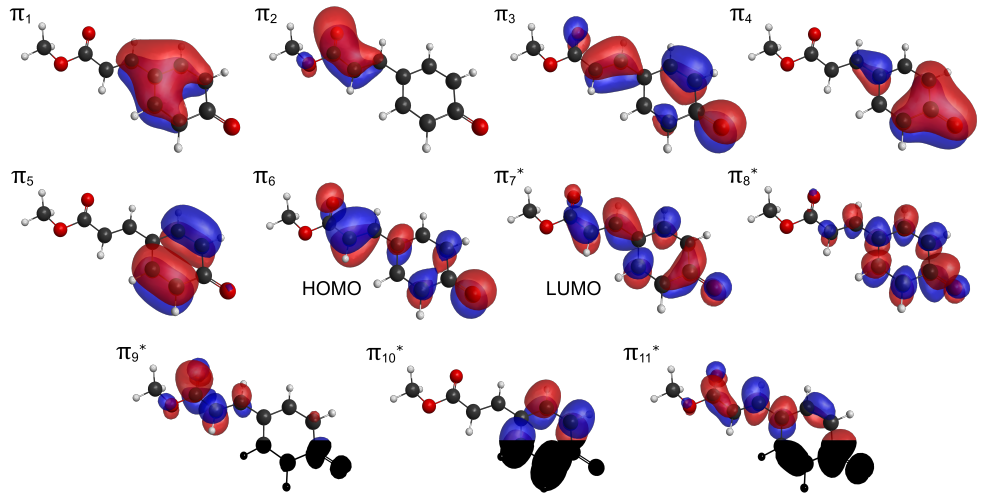


Figure 5.22: Bonding and anti-bonding π-orbitals of *p*CEs$^-$, computed in the Firefly 8.2.0[47] software package at the CASSCF(12,11)/aug-cc-pVDZ level of theory.

level of theory is currently under way. This will also enable optimisation of the conical intersection seam.

The overall PES topologies in Figure 5.23 provide some insight into the reasons behind *p*CK$^-$ dynamics. The ≈2.8 eV ground-state barrier prevents thermal isomerisation because room temperature ($T \approx 300$ K) equates to $E \approx 0.3$ eV of vibrational energy. This drives the need for passage through a conical intersection to achieve isomerisation. Although the S_1/S_0 conical intersection in Figure 5.23 is not optimised, it can be classified as peaked, as indicated by previous modelling studies.[12,51] The S_1 barrier hinders motion of the excited molecule away from the Franck-Condon geometry and towards the conical intersection. When excited, the total internal energy of the molecule is unlikely to surpass the barrier height. Therefore, to achieve motion towards the conical intersection, the system is reliant on intramolecular vibrational redistribution (IVR). The faster the rate of IVR, the sooner energy may be redistributed into favourable vibrational modes, and the sooner the conical intersection is reached, resulting in a shorter fluorescence lifetime. For *p*CK$^-$, Zewail and co-workers[6] measured a lifetime of 52 ps, consistent with a system in which IVR is important, as intramolecular redistribution typically occurs on a 1–10 ps timescale.[101,102]

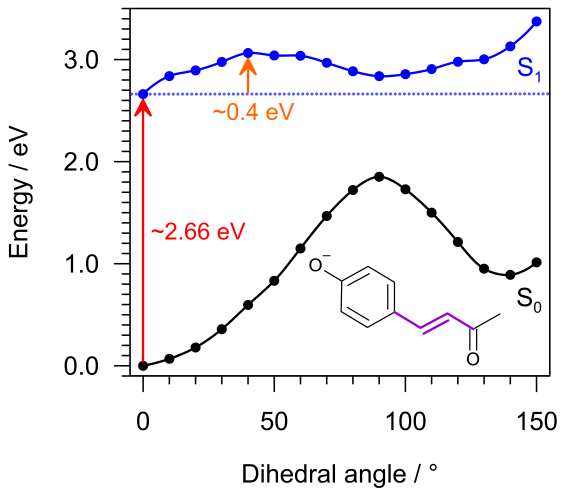


Figure 5.23: S_0 and S_1 potential energy surfaces for double-bond twisting in pCK$^-$, calculated at the XMCQDPT2/aug-cc-pVDZ level of theory. The vertical excitation energy is shown in red (≈2.66 eV) and the S_1 barrier height in orange (≈0.4 eV). The purple bonds in the pCK$^-$ structure indicate the double-bond twist dihedral angle.

5.6 Conclusion and future work

Steady-state and time-resolved measurements of pCK$^-$ were performed in a range of solvents and solvent mixtures and show clear trends in spectral shifts and lifetimes. Computational modelling of the solvation of pCK$^-$ by five water molecules can replicate the experimental absorption maximum to within ±10 nm. Applying the same procedure to the solvation of pCK$^-$ with other solvents, such as methanol, should allow the experimentally-observed shifts in absorption maxima to be replicated. The solvatochromic shifts in the absorption and emission spectra and the resultant Stokes shifts primarily reflect solvent polarity. In analysing the respective Stokes shifts, general and specific solvent effect theory was employed. Two conclusions were drawn from this analysis: (1) that the large difference in Stokes shift between pCK$^-$ in methanol and ethanol cannot merely be due to polarity, but must have a contribution from specific solvent effects (*e.g.* hydrogen bonding), and (2) that the small spectral shifts in emission of pCK$^-$ in mixtures of water and ethylene glycol are unlikely to be due to specific solvent effects. An important outcome from steady-state fluorescence excitation measurements is that solution concentration is significant. Modelling of the narrow excitation band from steady-state spectroscopic data showed considerable absorption of all light (includ-

ing sample fluorescence) over a 200 nm wavelength range. This demonstrated that an excitation maximum red-shift occurs when a solution is too concentrated, due to inner filter effects. However, this has no noticeable effect on the time-resolved fluorescence up-conversion measurements.

Fluorescence up-conversion was performed in both a static and a flow cell to account for potential artificial lengthening of fluorescence lifetime due to excitation of photoisomerised molecules. The discrepancy in lifetime between the static and flowed samples increases in more viscous, less polar solvents, presumably due to slower $Z \rightarrow E$ thermal reversion. Overall, fluorescence lifetime is shortest in water and longest in heptanol/octanol. Although ethylene glycol is highly viscous, its lifetime is more comparable to 2-propanol, attributed to the high polarity of ethylene glycol relative to octanol. Fitting of the up-conversion data to a double-component function allowed analysis of a short timescale component (τ_1), which reflects the solvent rearrangement process on excitation. However, τ_1 was limited by the time resolution of the up-conversion experiment (55 fs). Some viscosity dependence (determined from a phenomenological power law) of τ_2 is observed, indicating that solvent properties and composition are important in dictating fluorescence lifetime. In water–ethylene-glycol mixtures where water is dominant, only a gradual change in τ_2 occurs, although this increases substantially when ethylene glycol dominates. This supports the suggestion by Espagne *et al.*[17] that, in solvent mixtures where water is the major component, there is preferential solvation of the chromophore by water molecules, creating a mostly aqueous local solvation environment around $p\mathrm{CK}^-$. This may apply to other solvent mixtures where the two components have sufficiently different viscosity and/or polarity (and hydrogen-bonding propensity). Further experiments will explore $p\mathrm{CK}^-$ dynamics in a range of solvent solutions by probing photoisomerisation quantum yields.

Gas-phase action spectroscopy has demonstrated two important properties of $p\mathrm{CK}^-$ that set it apart from other *para*-hydroxycinnamates studied to date – firstly, that it undergoes $E \rightarrow Z$ photoisomerisation, and secondly, that there is a wavelength-dependent competition between isomerisation and electron detachment over the 350–500 nm wavelength range. The second point provides validation to two previous studies of $p\mathrm{CK}^-$, one of which had concluded isomerisation to be the dominant process, while the other identified electron detachment as the dominant pathway. This is ascribed to the presence of a small S_1 barrier ($\approx$0.2 eV), whose presence is inferred from the photoisomerisation and photodetachment action spectra and through computational modelling. Given that $p\mathrm{CEs}^-$ exhibits no photoisomerisation in the gas phase, but can photoisomerise in so-

lution, it is concluded that the excited-state barrier in *p*CEs$^-$ is much higher than that of *p*CK$^-$ and that solvent-chromophore interactions stabilise *p*CEs$^-$ to a greater extent than *p*CK$^-$. Future work will focus on fully optimising the excited-state PES to link with experiment and fully define both the S_1 barrier height and the S_1/S_0 conical intersection.

References

[1] M. Baca, G. E. O. Borgstahl, M. Boissinot, P. M. Burke, D. R. Williams, K. A. Slater and E. D. Getzoff, *Biochemistry*, 1994, **33**, 14369–14377.

[2] T. Meyer, *Biochim. Biophys. Acta*, 1985, **806**, 175–183.

[3] T. E. Meyer, E. Yakali, M. A. Cusanovich and G. Tollin, *Biochemistry*, 1987, **26**, 418–423.

[4] W. W. Sprenger, W. D. Hoff, J. P. Armitage and K. J. Hellingwerf, *J. Bacteriol.*, 1993, **175**, 3096–3104.

[5] M. Vengris, M. A. van der Horst, G. Zgrablić, I. H. van Stokkum, S. Haacke, M. Chergui, K. J. Hellingwerf, R. van Grondelle and D. S. Larsen, *Biophys. J.*, 2004, **87**, 1848–1857.

[6] I.-R. Lee, W. Lee and A. H. Zewail, *Proc. Natl. Acad. Sci.*, 2006, **103**, 258–262.

[7] A. Henley and H. H. Fielding, *Int. Rev. Phys. Chem.*, 2019, **38**, 1–34.

[8] H. M. Berman, J. Westbrook, Z. Feng, G. Gilliland, T. N. Bhat, H. Weissig, I. N. Shindyalov and P. E. Bourne, *Nucleic Acids Res.*, 2000, **28**, 235–242.

[9] A. Shinobu, G. J. Palm, A. J. Schierbeek and N. Agmon, *J. Am. Chem. Soc.*, 2010, **132**, 11093–11102.

[10] D. Sehnal, S. Bittrich, M. Deshpande, R. Svobodová, K. Berka, V. Bazgier, S. Velankar, S. K. Burley, J. Koča and A. S. Rose, *Mol**, 2021.

[11] D. Sehnal, S. Bittrich, M. Deshpande, R. Svobodová, K. Berka, V. Bazgier, S. Velankar, S. K. Burley, J. Koča and A. S. Rose, *Nucleic Acids Res.*, 2021, **49**, W431–W437.

[12] G. Groenhof, M. Bouxin-Cademartory, B. Hess, S. P. de Visser, H. J. C. Berendsen, M. Olivucci, A. E. Mark and M. A. Robb, *J. Am. Chem. Soc.*, 2004, **126**, 4228–4233.

[13] J. Ralph, *Phytochem. Rev.*, 2009, **9**, 65–83.

[14] L. A. Baker, M. D. Horbury, S. E. Greenough, F. Allais, P. S. Walsh, S. Habershon and V. G. Stavros, *J. Phys. Chem. Lett.*, 2015, **7**, 56–61.

[15] S. Kinoshita, Y. Harabuchi, Y. Inokuchi, S. Maeda, M. Ehara, K. Yamazaki and T. Ebata, *Phys. Chem. Chem. Phys.*, 2021, **23**, 834–845.

[16] M. L. Groot, L. J. G. W. van Wilderen, D. S. Larsen, M. A. van der Horst, I. H. M. van Stokkum, K. J. Hellingwerf and R. van Grondelle, *Biochemistry*, 2003, **42**, 10054–10059.

[17] A. Espagne, D. H. Paik, P. Changenet-Barret, M. M. Martin and A. H. Zewail, *ChemPhysChem*, 2006, **7**, 1717–1726.

[18] P. Changenet-Barret, A. Espagne, S. Charier, J.-B. Baudin, L. Jullien, P. Plaza, K. J. Hellingwerf and M. M. Martin, *Photochem. Photobiol. Sci.*, 2004, **3**, 823–829.

[19] A. Espagne, D. H. Paik, P. Changenet-Barret, P. Plaza, M. M. Martin and A. H. Zewail, *Photochem. Photobiol. Sci.*, 2007, **6**, 780–787.

[20] P. Changenet-Barret, F. Lacombat and P. Plaza, *J. Photochem. Photobiol. A*, 2012, **234**, 171–180.

[21] J. N. Bull, G. da Silva, M. S. Scholz, E. Carrascosa and E. J. Bieske, *J. Phys. Chem. A*, 2019, **123**, 4419–4430.

[22] J. N. Bull, C. S. Anstöter and J. R. R. Verlet, *J. Phys. Chem. A*, 2020, **124**, 2140–2151.

[23] A. Espagne, P. Changenet-Barret, P. Plaza and M. M. Martin, *J. Phys. Chem. A*, 2006, **110**, 3393–3404.

[24] A. Espagne, P. Changenet-Barret, J.-B. Baudin, P. Plaza and M. M. Martin, in *Femtochemistry VII*, Elsevier, 2006, pp. 204–214.

[25] R. Jimenez, G. R. Fleming, P. V. Kumar and M. Maroncelli, *Nature*, 1994, **369**, 471–473.

[26] E. V. Gromov, I. Burghardt, J. T. Hynes, H. Köppel and L. S. Cederbaum, *J. Photochem. Photobiol. A*, 2007, **190**, 241–257.

[27] D. Zuev, K. B. Bravaya, M. V. Makarova and A. I. Krylov, *J. Chem. Phys.*, 2011, **135**, 194304.

[28] D. Zuev, K. B. Bravaya, T. D. Crawford, R. Lindh and A. I. Krylov, *J. Chem. Phys.*, 2011, **134**, 034310.

[29] S. Frutos-Puerto, A. Muñoz-Losa, M. E. Martín and M. A. Aguilar, *Comput. Theor. Chem.*, 2014, **1040-1041**, 287–294.

[30] F. F. García-Prieto, A. Muñoz-Losa, M. L. Sánchez, M. E. Martín and M. A. Aguilar, *Phys. Chem. Chem. Phys.*, 2016, **18**, 27476–27485.

[31] M. Boggio-Pasqua and G. Groenhof, *J. Phys. Chem. B*, 2011, **115**, 7021–7028.

[32] M. J. Frisch, G. W. Trucks, H. B. Schlegel, G. E. Scuseria, M. A. Robb, J. R. Cheeseman, G. Scalmani, V. Barone, G. A. Petersson, H. Nakatsuji, X. Li, M. Caricato, A. V. Marenich, J. Bloino, B. G. Janesko, R. Gomperts, B. Mennucci, H. P. Hratchian, J. V. Ortiz, A. F. Izmaylov, J. L. Sonnenberg, D. Williams-Young, F. Ding, F. Lipparini, F. Egidi, J. Goings, B. Peng, A. Petrone, T. Henderson, D. Ranasinghe, V. G. Zakrzewski, J. Gao, N. Rega, G. Zheng, W. Liang, M. Hada, M. Ehara, K. Toyota, R. Fukuda, J. Hasegawa, M. Ishida, T. Nakajima, Y. Honda, O. Kitao, H. Nakai, T. Vreven, K. Throssell, J. A. Montgomery, Jr., J. E. Peralta, F. Ogliaro, M. J. Bearpark, J. J. Heyd, E. N. Brothers, K. N. Kudin, V. N. Staroverov, T. A. Keith, R. Kobayashi, J. Normand, K. Raghavachari, A. P. Rendell, J. C. Burant, S. S. Iyengar, J. Tomasi, M. Cossi, J. M. Millam, M. Klene, C. Adamo, R. Cammi, J. W. Ochterski, R. L. Martin, K. Morokuma, O. Farkas, J. B. Foresman and D. J. Fox, *Gaussian 16 Revision B.01*, 2016, Gaussian Inc. Wallingford CT.

[33] J.-D. Chai and M. Head-Gordon, *Phys. Chem. Chem. Phys.*, 2008, **10**, 6615–6620.

[34] J.-D. Chai and M. Head-Gordon, *J. Chem. Phys.*, 2008, **128**, 084106.

[35] T. H. Dunning, *J. Chem. Phys.*, 1989, **90**, 1007–1023.

[36] M. Kállay, P. R. Nagy, D. Mester, Z. Rolik, G. Samu, J. Csontos, J. Csóka, P. B. Szabó, L. Gyevi-Nagy, B. Hégely, I. Ladjánszki, L. Szegedy, B. Ladóczki, K. Petrov, M. Farkas, P. D. Mezei and Á. Ganyecz, *MRCC, a quantum chemical program suite*, See www.mrcc.hu.

[37] M. Kállay, P. R. Nagy, D. Mester, Z. Rolik, G. Samu, J. Csontos, J. Csóka, P. B. Szabó, L. Gyevi-Nagy, B. Hégely, I. Ladjánszki, L. Szegedy, B. Ladóczki, K. Petrov, M. Farkas, P. D. Mezei and Á. Ganyecz, *J. Chem. Phys.*, 2020, **152**, 074107.

[38] D. Mester, P. R. Nagy and M. Kállay, *J. Chem. Theory Comput.*, 2019, **15**, 6111–6126.

[39] D. Mester and M. Kállay, *J. Chem. Theory Comput.*, 2019, **15**, 4440–4453.

[40] D. Mester, P. R. Nagy and M. Kállay, *J. Chem. Phys.*, 2018, **148**, 094111.

[41] D. Mester, P. R. Nagy and M. Kállay, *J. Chem. Phys.*, 2017, **146**, 194102.

[42] F. Neese, *WIREs Comput. Mol. Sci.*, 2011, **2**, 73–78.

[43] R. Berraud-Pache, F. Neese, G. Bistoni and R. Izsák, *J. Chem. Theory Comput.*, 2019, **16**, 564–575.

[44] V. Barone and M. Cossi, *J. Phys. Chem. A*, 1998, **102**, 1995–2001.

[45] G. Scalmani, M. J. Frisch, B. Mennucci, J. Tomasi, R. Cammi and V. Barone, *J. Chem. Phys.*, 2006, **124**, 094107.

[46] A. V. Marenich, C. J. Cramer and D. G. Truhlar, *J. Phys. Chem. B*, 2009, **113**, 6378–6396.

[47] A. A. Grandovsky, *Firefly version 8.2.0*, http://classic.chem.msu.su/gran/firefly/index.html.

[48] M. Uppsten and B. Durbeej, *J. Comput. Chem.*, 2012, **33**, 1892–1901.

[49] T. Rocha-Rinza, O. Christiansen, J. Rajput, A. Gopalan, D. B. Rahbek, L. H. Andersen, A. V. Bochenkova, A. A. Granovsky, K. B. Bravaya, A. V. Nemukhin, K. L. Christiansen and M. B. Nielsen, *J. Phys. Chem. A*, 2009, **113**, 9442–9449.

[50] C. Hättig and F. Weigend, *J. Chem. Phys.*, 2000, **113**, 5154–5161.

[51] C. S. Anstöter, B. F. E. Curchod and J. R. R. Verlet, *Nat. Commun.*, 2020, **11**, 2827.

[52] A. A. Granovsky, *J. Chem. Phys.*, 2011, **134**, 214113.

[53] J. W. Park, *J. Chem. Theory Comput.*, 2021, **17**, 6122–6133.

[54] J. R. Lakowicz, *Principles of Fluorescence Spectroscopy*, Springer, 2007.

[55] M. Sauer, J. Hofkens and J. Enderlein, in *Handbook of Fluorescence Spectroscopy and Imaging*, Wiley-VCH Verlag GmbH & Co. KGaA, 2011, pp. 1–30.

[56] C. Reichardt, *Solvents and Solvent Effects in Organic Chemistry*, VCH, Weinheim, Federal Republic of Germany New York, NY, USA, 1988.

[57] *CRC Handbook of Chemistry and Physics*, ed. W. M. Haynes, CRC Press, Boca Raton, Florida, 97th edn., 2017.

[58] J. Kimball, J. Chavez, L. Ceresa, E. Kitchner, Z. Nurekeyev, H. Doan, M. Szabelski, J. Borejdo, I. Gryczynski and Z. Gryczynski, *Methods Appl. Fluoresc.*, 2020, **8**, 033002.

[59] L. Ceresa, J. Kimball, J. Chavez, E. Kitchner, Z. Nurekeyev, H. Doan, J. Borejdo, I. Gryczynski and Z. Gryczynski, *Methods Appl. Fluoresc.*, 2021, **9**, 035005.

[60] D. C. Todd, J. M. Jean, S. J. Rosenthal, A. J. Ruggiero, D. Yang and G. R. Fleming, *J. Chem. Phys.*, 1990, **93**, 8658–8668.

[61] S. Takeuchi and T. Tahara, *J. Phys. Chem. A*, 1997, **101**, 3052–3060.

[62] K. Addison, I. A. Heisler, J. Conyard, T. Dixon, P. C. B. Page and S. R. Meech, *Faraday Discussions*, 2013, **163**, 277–296.

[63] H. Chosrowjan, S. Taniguchi and F. Tanaka, *FEBS J.*, 2015, **282**, 3003–3015.

[64] J. M. Anna and K. J. Kubarych, *J. Chem. Phys.*, 2010, **133**, 174506.

[65] F. Y. H. Niels E. Henriksen, *Theories of Molecular Reaction Dynamics: The Microscopic Foundation of Chemical Kinetics*, Oxford University Press, 2012.

[66] S. P. Velsko, D. H. Waldeck and G. R. Fleming, *J. Chem. Phys.*, 1983, **78**, 249–258.

[67] D. H. Waldeck, *Chem. Rev.*, 1991, **91**, 415–436.

[68] B. Bagchi and D. W. Oxtoby, *J. Chem. Phys.*, 1983, **78**, 2735–2741.

[69] R. F. Grote and J. T. Hynes, *J. Chem. Phys.*, 1980, **73**, 2715–2732.

[70] G. E. O. Borgstahl, D. R. Williams and E. D. Getzoff, *Biochemistry*, 1995, **34**, 6278–6287.

[71] S. Yamaguchi, H. Kamikubo, K. Kurihara, R. Kuroki, N. Niimura, N. Shimizu, Y. Yamazaki and M. Kataoka, *Proc. Natl. Acad. Sci.*, 2009, **106**, 440–444.

[72] P. Changenet, H. Zhang, M. van der Meer, K. Hellingwerf and M. Glasbeek, *Chem. Phys. Lett.*, 1998, **282**, 276–282.

[73] H. Hanada, Y. Kanematsu, S. Kinoshita, M. Kumauchi, J. Sasaki and F. Tokunaga, *J. Lumin.*, 2001, **94-95**, 593–596.

[74] M. Almasian, J. Grzetic, J. van Maurik, J. D. Steill, G. Berden, S. Ingemann, W. J. Buma and J. Oomens, *J. Phys. Chem. Lett.*, 2012, **3**, 2259–2263.

[75] H. Xia and A. B. Attygalle, *Anal. Chem.*, 2016, **88**, 6035–6043.

[76] M. A. Parkes, C. Phillips, M. J. Porter and H. H. Fielding, *Phys. Chem. Chem. Phys.*, 2016, **18**, 10329–10336.

[77] A. Henley, A. M. Patel, M. A. Parkes, J. C. Anderson and H. H. Fielding, *J. Phys. Chem. A*, 2018, **122**, 8222–8228.

[78] I. Nielsen, S. Boyé-Péronne, M. E. Ghazaly, M. Kristensen, S. B. Nielsen and L. Andersen, *Biophys. J.*, 2005, **89**, 2597–2604.

[79] T. Rocha-Rinza, O. Christiansen, D. B. Rahbek, B. Klærke, L. H. Andersen, K. Lincke and M. Brøndsted Nielsen, *Chem. Eur. J.*, 2010, **16**, 11977–11984.

[80] L. H. Andersen, A. V. Bochenkova, J. Houmøller, H. V. Kiefer, E. Lattouf and M. H. Stockett, *Phys. Chem. Chem. Phys.*, 2016, **18**, 9909–9913.

[81] H. Zettergren, A. Domaracka, T. Schlathölter, P. Bolognesi, S. Díaz-Tendero, M. Łabuda, S. Tosic, S. Maclot, P. Johnsson, A. Steber, D. Tikhonov, M. C. Castrovilli, L. Avaldi, S. Bari, A. R. Milosavljević, A. Palacios, S. Faraji, D. G. Piekarski, P. Rousseau, D. Ascenzi, C. Romanzin, E. Erdmann, M. Alcamí, J. Kopyra, P. Limão-Vieira, J. Kočišek, J. Fedor, S. Albertini, M. Gatchell, H. Cederquist, H. T. Schmidt, E. Gruber, L. H. Andersen, O. Heber, Y. Toker, K. Hansen, J. A. Noble, C. Jouvet, C. Kjær, S. B. Nielsen, E. Carrascosa, J. Bull, A. Candian and A. Petrignani, *Eur. Phys. J. D*, 2021, **75**, 152.

[82] J. N. Bull, J. T. Buntine, E. Carrascosa, M. H. Stockett and E. J. Bieske, *Eur. Phys. J. D*, 2021, **75**, 67.

[83] J. N. Bull, C. S. Anstöter and J. R. R. Verlet, *Nat. Commun.*, 2019, **10**, 5820.

[84] J. N. Bull, E. Carrascosa, L. Giacomozzi, E. J. Bieske and M. H. Stockett, *Phys. Chem. Chem. Phys.*, 2018, **20**, 19672–19681.

[85] M. S. Scholz, J. N. Bull, N. J. A. Coughlan, E. Carrascosa, B. D. Adamson and E. J. Bieske, *J. Phys. Chem. A*, 2017, **121**, 6413–6419.

[86] J. N. Bull, J. T. Buntine, M. S. Scholz, E. Carrascosa, L. Giacomozzi, M. H. Stockett and E. J. Bieske, *Faraday Discuss.*, 2019, **217**, 34–46.

[87] J. Troe, T. M. Miller and A. A. Viggiano, *J. Chem. Phys.*, 2012, **136**, 121102.

[88] S. Menk, S. Das, K. Blaum, M. W. Froese, M. Lange, M. Mukherjee, R. Repnow, D. Schwalm, R. von Hahn and A. Wolf, *Phys. Rev. A*, 2014, **89**, 022502.

[89] H. E. Revercomb and E. A. Mason, *Anal. Chem.*, 1975, **47**, 970–983.

[90] B. D. Adamson, N. J. A. Coughlan, R. E. Continetti and E. J. Bieske, *Phys. Chem. Chem. Phys.*, 2013, **15**, 9540–9548.

[91] F. V. Heldmaier, N. J. A. Coughlan, A. Haack, R. Huard, M. Guna, B. B. Schneider, J. C. Y. L. Blanc, J. L. Campbell, M. Nooijen and W. S. Hopkins, *Phys. Chem. Chem. Phys.*, 2021, **23**, 19892–19900.

[92] E. Carrascosa, J. N. Bull, M. S. Scholz, N. J. A. Coughlan, S. Olsen, U. Wille and E. J. Bieske, *J. Phys. Chem. Lett.*, 2018, **9**, 2647–2651.

[93] J. N. Bull, M. S. Scholz, E. Carrascosa, G. da Silva and E. J. Bieske, *Phys. Rev. Lett.*, 2018, **120**, 223002.

[94] N. J. A. Coughlan, M. H. Stockett, C. Kjær, E. K. Ashworth, P. C. B. Page, S. R. Meech, S. B. Nielsen, L. Blancafort, W. S. Hopkins and J. N. Bull, *J. Chem. Phys.*, 2021, **155**, 124304.

[95] M. Boggio-Pasqua and G. Groenhof, *Comput. Theor. Chem.*, 2014, **1040-1041**, 6–13.

[96] B. D. Adamson, N. J. A. Coughlan, P. B. Markworth, R. E. Continetti and E. J. Bieske, *Rev. Sci. Instrum.*, 2014, **85**, 123109.

[97] J. N. Bull, N. J. A. Coughlan and E. J. Bieske, *J. Phys. Chem. A*, 2017, **121**, 6021–6027.

[98] D. J. Nesbitt and R. W. Field, *J. Phys. Chem.*, 1996, **100**, 12735–12756.

[99] M. Boggio-Pasqua, M. A. Robb and G. Groenhof, *J. Am. Chem. Soc.*, 2009, **131**, 13580–13581.

[100] M. Boggio-Pasqua, C. F. Burmeister, M. A. Robb and G. Groenhof, *Phys. Chem. Chem. Phys.*, 2012, **14**, 7912–7928.

[101] M. Quack, in *Energy Storage and Redistribution in Molecules*, ed. J. Hinze, Springer, 1983, pp. 493–511.

[102] T. Uzer and W. Miller, *Phys. Rep.*, 1991, **199**, 73–146.

Chapter 6

Characterisation of DTEs

This chapter describes the characterisation of selected photophysical properties of dithienylethene (DTE) molecules in solution using experimental and computational methods. The DTE molecules were synthesised by Dr George Vamvounis (James Cook University, Australia) with the ultimate goal of incorporating these molecules into technological applications, including optically-controlled thin-film electronics, *e.g.* logic gates for transistors. The rational design of DTE molecules for such applications requires understanding of their photophysical properties as both the monomeric and polymeric species – selected monomeric species are the focus of this chapter. Solvation of the DTE species is explored using electronic structure methods, showing that solvation first occurs *via* fluorine-methanol and methanol-methanol electrostatic interactions. Explicit solvation with three methanol molecules is adequate to describe microsolvation at the TD-ωB97X-D/cc-pVDZ level of theory. Spectroscopic fluorescence techniques, including time-resolved and temperature-dependent methods, reveal preliminary data on DTE dynamics, including by-product formation and temperature-dependent fluorescence time constants. These data will guide future experiments focussed on photoisomerisation quantum yields and detailed excited state dynamics.

6.1 Introduction

Two families of thermally irreversible photoswitch candidates, both derivatives of stilbene, were identified over 30 years ago – diarylethenes (DAEs)[1,2] (Figure 1.2(c)) and heterocyclic fulgides[3] (Figure 1.2(d)). Unlike stilbene, which undergoes $E \rightarrow Z$ photoisomerisation, DAEs and heterocyclic fulgide derivatives photocyclise. Because the photocyclisation is reversible between thermally stable forms, they are classed as P-type (photochemically reversible) photoswitches. Such photoswitches are uncommon; DAEs and heterocyclic fulgides are two of only a few families identified as exhibiting this prop-

erty.[4] These families, including DAEs and the more recent donor-acceptor Stenhouse adducts,[5,6] offer ample opportunity for synthetic development. Initially, DAEs were simply stilbenes in which the phenyl groups had been replaced with heterocyclic rings. Further developments found that substitution of a perfluorocyclopentene ring on the isomerising C=C double bond significantly improved fatigue resistance on repeat photoswitching cycles and effected changes in switching dynamics.[7,8]

There is an extensive library of literature on DAEs and their photoswitching properties, developed since the late-1980s. A vast selection of DAE structures and substitutions have been explored;[8–11] however, the isomers containing thiophene or furan as the aryl groups are favoured over those containing phenyl or pyrrolyl rings.[2,8] This is because thiophene and furan groups allow the formation of stable closed-ring isomers that don't thermally revert at room temperature,[2] attributed to a smaller difference between the open- and closed-ring isomer ground-state energies. This aromatic stabilisation energy dictates the reaction energy barrier to cycloreversion which, in turn, controls the thermal stability of the closed-ring isomer. The term "diarylethene" is used as an umbrella term for this class of photoswitch molecules, while dithienylethene (DTE) refers to specific DAEs in which the heterocyclic ring is a thiophene unit.

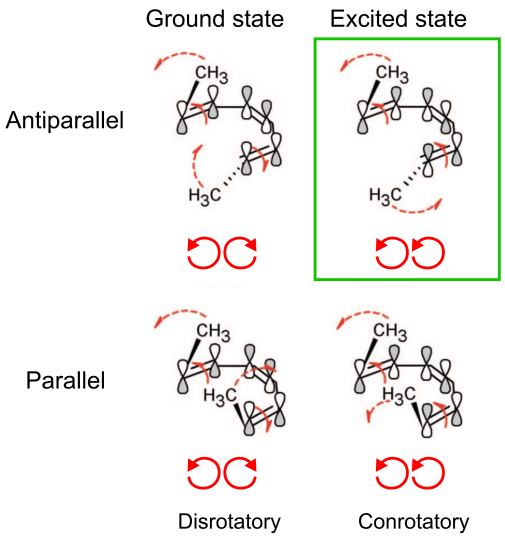


Figure 6.1: Dis- and conrotatory motion of the antiparallel and parallel forms of the mechanistically important DAE hexatriene unit. The favoured state, motion, and conformer for cyclisation is highlighted in green. Adapted from Staykov *et al.*[12]

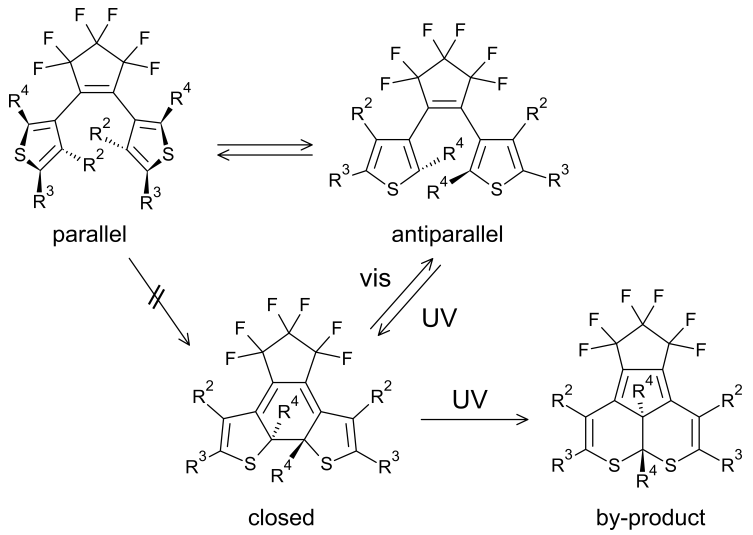


Figure 6.2: Reaction pathway of a generic DTE. The parallel and antiparallel conformers thermally interconvert, but only the antiparallel conformer can cyclise on UV irradiation. The open isomer is recovered on irradiation at visible wavelengths. Further UV irradiation of the closed isomer forms a by-product, from which other forms cannot be recovered.

The photocyclisation of DTEs is a 6π-electrocyclic reaction based on the Woodward-Hoffman rules, dictating that the cyclisation occurs by conrotatory motion (Figure 6.1). This motion ensures optimal orbital overlap to allow the creation of the connective carbon-carbon single bond to form the central six-membered ring. As open isomers, DTEs have flexibility in the hexatriene unit, which undergoes isomerisation, resulting in parallel and antiparallel conformers (Figure 6.2). According to the Woodward-Hoffmann rules, electrocyclic reactions of antiparallel DTEs favour dis- and conrotatory motion on the ground- and excited-states, respectively. Typically, DTEs have a methyl group at position R^4, which introduces steric hinderance, creating a barrier to thermal disrotatory motion. On the other hand, the barrier to conrotatory motion on the excited state is low, allowing photocyclisation. For parallel DTEs, the ground state disrotatory motion does not experience steric hinderance; however, the ground-state barrier prevents thermal cyclisation of the parallel isomer. Additionally, there is a large barrier to the conrotatory mode on the excited state, due to steric hinderance. Thus, the antiparallel form is photoactive and photocyclisation can only take place from this geometry.[12] Once cyclised, the closed-ring isomer can either revert back to the open isomer or form a by-product. The propensity for by-product formation determines the fatigue resistance of DAEs – the lower the rate of by-product formation, the more fatigue resistant the

photoswitch. The literature describes various approaches to increase fatigue resistance of DAEs, primarily through functional group adaptations, where a clear link between substituent properties and fatigue behaviour have been demonstrated.[13,14] This thesis details some preliminary investigation of the fatigue properties of some substituted DAEs.

E-Z photoswitches, such as azobenzene or stilbene, are routinely incorporated into larger photoswitchable molecules because their dynamics have been studied extensively; these data provide a foundation for more sophisticated photoswitch design.[15] However, azobenzenes and stilbenes offer limited capacity for photo-controllable conductivity, restricting their suitability for optoelectronic applications. In contrast, other photocyclising photoswitches have greater capacity for photo-controllable conductivity, and are separated into three categories: (1) DAEs/DTEs, (2) spiropyran-merocyanines,[16,17] and (3) donor-acceptor Stenhouse adducts.[5,6] This thesis focusses on the DTEs, since the synthetic routes are well-established and scalable. Synthesis of photoswitches (1)-(3) is fairly simple, although functionalisation of DTEs is simpler than for the photoswitches in categories (2) and (3), making DTEs more available for grafting into various applications. At the start of this section, the potential application of DTEs in thin-film electronics was introduced. In this application, the conduction properties of polymers containing dithienylethene molecules can be modulated through irradiation with visible/UV light or mechanical strain. For these molecules to be incorporated into polymeric films, suitable functional group substitutions (*e.g.* carboxylic acids and aldehydes) need to be introduced to allow for conjugated linking groups. Selected monomeric DTE molecules are the focus of this chapter, aiming to characterise the photophysical properties of the compounds in solution and using computational approaches. The other isomers and forms of those eight compounds are shown in Figures A2.1 and A2.2.

Of the eight DTE compounds shown in Figure 6.3, five were identified as having been investigated or characterised previously in the literature – B2287, NS2-22, NS2-24, CG1-107, and CG1-108. The former three are particularly popular because of their relative simplicity.[13,18–27] Typically, they form the basis on which other, more complex, DTEs are designed and built, so understanding their properties can help direct work on more sophisticated derivatives. On the other hand, the derivatives with functional group substitutions (aldehydes and acids) are important, as these groups are required for incorporation into technological applications, *e.g.* to form polymers in thin-film optoelectronics.

Diarylethenes undergo 6π-photocyclisation which, by definition, takes place on an ex-

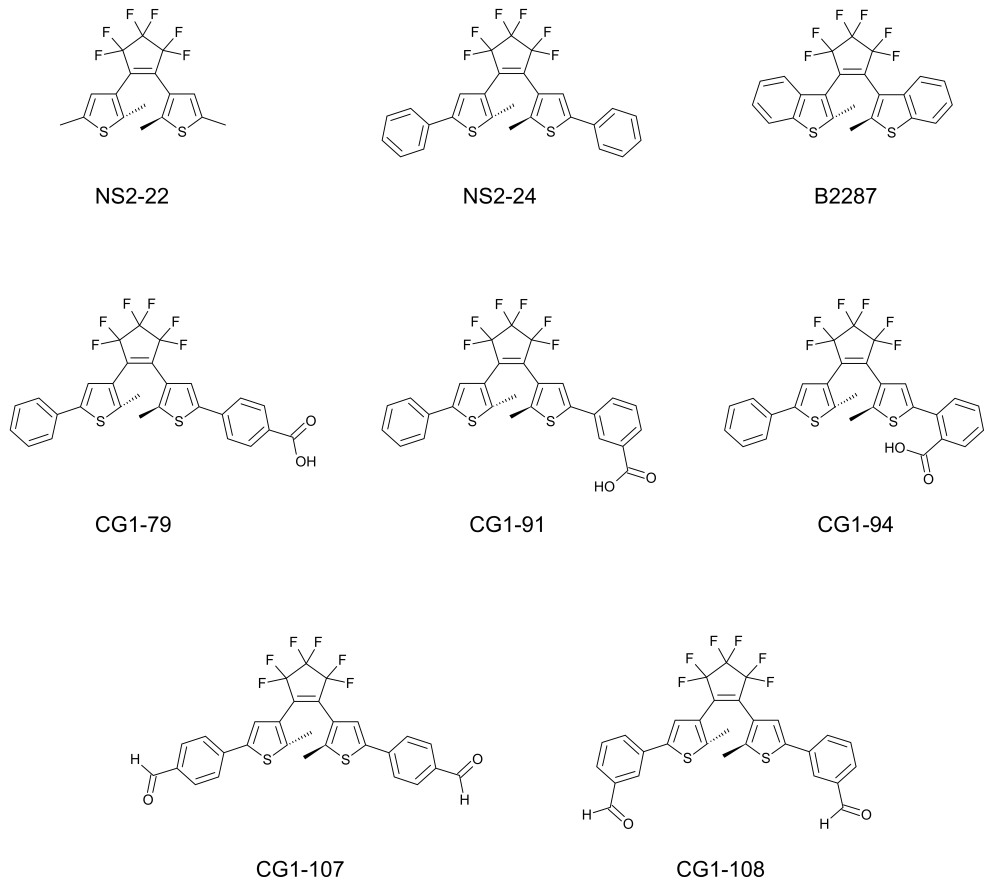


Figure 6.3: Chemical structures and abbreviations of eight dithienylethenes investigated in this thesis. Naming convention follows organic synthesis reaction scheme by the synthetic group at James Cook University, Australia.

cited state. It is therefore desirable to identify the important excited states, those with large oscillator strengths, and their vertical excitation energies (VEEs). Since the initial development of DTEs in the 1980s, much theoretical work probing the reaction dynamics and potential energy surfaces of dithienylethenes has been performed.[2,12,28–31] One of the most commonly used methods is the B3LYP hybrid functional,[12,23,28–30] but it is now near-obsolete and superseded by other functionals, such as ωB97X-D. In this chapter, the time-dependent ωB97X-D method is used to explore the effect of solvation on the vertical excitation energies of the simplest DTE (NS2-22, Figure 6.3) and the results compared with those obtained by density-fitted CC2.

A fundamental characteristic of photoswitches is that the two isomers have distinct absorption profiles. For dithienylethenes, the antiparallel (AP) isomer only absorbs at

ultraviolet (UV) wavelengths, while the closed isomer has absorption bands in both the UV and visible regions (Figure 6.4). This difference arises due to the difference in π-conjugation between the two isomers. In the AP isomer, the π-conjugation is localised on the thiophene unit; however, it is delocalised over the entire molecular backbone in the closed isomer. Therefore, the HOMO-LUMO gap is smaller, shifting the absorption band to a longer wavelength, in this case into the visible region. Generally, the more extended the π-conjugation in the closed isomer, the longer the visible absorption wavelength.[8]

There exists a large array of previous studies on DAE/DTEs seeking to explore how cyclisation and cycloreversion processes change with solvent.[19,22,29] Spectroscopic pump-probe methods, such as transient absorption and time-resolved fluorescence, are widely used for this purpose. For ring-closing, the time constants reported in non-polar solvents consistently fall in the 1–3 ps range.[7,18,23,27,29] On the other hand, the reported ring-opening time constants show a much larger range of values, for example from 6.5 ps[27] to 325 ps.[32] B2287 (Figure 6.3) has separately been shown to cyclise within 1 ps[23,29] and undergo cycloreversion within approximately 50 ps.[18,33] The closed-ring excited lifetimes for various DTEs have been determined to be of timescales ranging from sub-picosecond to tens of picoseconds, typically in non-polar solvents, such as *n*-hexane.[21]

Temporal evolution of absorbance for the closed and the open isomers facilitate measurement of cyclisation and cycloreversion quantum yields, respectively. Quantum yield depends on the functionalisation of the DTE, resulting in cycloreversion quantum yields anywhere from 10^{-5} to 0.6,[21] with the addition electron-withdrawing substituents increasing cycloreversion quantum yield.[34] The calculated yields for a given species typically encompass a range of values, because the outcome depends on solvent properties[29] and irradiation wavelength.[22] By way of illustration, NS2-22 in hexane exhibits cyclisation and cycloreversion quantum yields of 0.40 and 0.12, respectively.[25] Conversely, cyclisation of NS2-24 in hexane has a quantum yield of ≈0.6–0.68,[35–37] (0.56 in acetonitrile)[37] while the cycloreversion quantum yield is significantly smaller (0.013 in hexane).[35]

There is no direct comparison available for a series of structurally similar DTE molecules (as opposed to DAE molecules) probed at the same excitation wavelengths in the same solvent. One of the aims of this project was to investigate the properties of eight differently-substituted DTEs in methanol. Future work will be performed investigating these same DTEs in other more non-polar solvents, where the relative stability of

ring-open and ring-closed forms change, and will also involve exploring polymeric DTE molecules, including some with fluorescent tags.

6.2 Computational methods

Geometry optimisation and vibrational frequency calculations were performed using Gaussian 16.B01[38] at the ωB97X-D/cc-pVDZ level of theory.[39–41] Electronic excited state calculations were performed with the cc-pVDZ and cc-pVTZ basis sets in Gaussian 16 and MRCC,[42,43] using time-dependent DFT (TD-DFT) and the density-fitted second-order coupled-cluster singles and doubles (df-CC2)[44–47] approach, respectively. The structures of the parallel, antiparallel, closed, and by-product forms were first optimised at the ωB97X-D/cc-pVDZ level of theory, then TD-ωB97X-D was used to obtain vertical excitation energies and oscillator strengths of the first eight excited states. There is a significant difference in the number of basis sets required for the cc-pVDZ and cc-pVTZ basis sets. To illustrate the point, for NS2-22, cc-pVDZ contains 196 basis functions, while cc-pVTZ contains 338. This is an ≈70% increase in the number of basis functions, representing a substantial increase in computational expense. However, there was little change in vertical excitation energies between the double- and triple-ζ basis sets, using both the ωB97X-D and df-CC2 methods. Therefore, the double-ζ was deemed adequate for purpose, lowering the computational cost of subsequent calculations.

The effect of solvent on the vertical excitation energies of the antiparallel and closed isomers of compound NS2-22 was investigated, at the TD-ωB97X-D/cc-pVDZ level of theory, using implicit (PCM, methanol) and explicit solvation methods. Explicit solvation involved systematic addition of methanol molecules to the DTE, optimising the structure, and then calculating the excitation energies. The workflow is summarised in Figure A2.3.

6.3 Experimental methods

Absorption spectra (250–800 nm) for solutions of the eight DTEs in methanol (99 %, Alfa Aesar) were obtained using a Perkin Elmer Lambda XLS spectrometer. To inform on spectra of the coloured closed-isomer forms, the DTE solutions were irradiated at 275 nm (Thorlabs M275L4 LED), creating a photostationary state. Cycloreversion to

the open isomer was achieved using 590 nm light (Thorlabs M590L4 LED).

Fluorescence excitation and emission spectra for the DTEs in methanol (fluoroSENS fluorimeter, Gilden photonics) were measured over 300–800 nm and 400–800 nm, respectively. Excitation-emission maps and time-resolved fluorescence measurements (at room temperature ($T \approx 300$ K) and $T \approx 77$ K (liquid nitrogen)) were recorded using an FS5 spectrofluorometer (Edinburgh Instruments). Pulses of light from EPLED-360 (365 nm), ELP-485 (478 nm), EPLED-570 (575 nm) sources were used to excite the samples, with instrument responses (ω) defined as 400 ps, 150 ps, and 700 ps, respectively. These light sources supply pulses with durations down to 400 ps (EPLED) and 50 ps (EPL).

Ultrafast fluorescence up-conversion (Section 3.1) was used to obtain preliminary data on the fluorescence lifetime of a DTE by-product. The sample was excited (pumped) at ≈400 nm with an average pump power of 11 mW. Analysis methods are discussed in Section 3.2.

6.4 Results and discussion

6.4.1 Comparison of computational methods

Electronic excited states of DAEs and DTEs have been commonly calculated using the somewhat obsolete TD-B3LYP method.[12,23,28–30] Comparison of the performance of B3LYP to that of ωB97X-D indicated that, for the calculation of excited states of solvated and unsolvated DTEs, the latter is more suitable. Briefly, TD-B3LYP (2.2–2.3 eV) has been shown to provide closer agreement with the experimentally-obtained $S_1 \leftarrow S_0$ transition energy (2.40 eV, in *n*-hexane), compared with TD-ωB97X-D (2.7–2.8 eV).[33] However, ωB97X-D treats non-covalent interactions more effectively than B3LYP, making the former more suited to solvation calculations. Excitation energies computed at the TD-ωB97X-D/cc-pVDZ and cc-pVTZ levels of theory differ by ≤20 nm for both the antiparallel-open and closed isomers (Tables A2.1 and A2.2), suggesting that the smaller basis set provides a reasonable description.

Comparison of the computed vertical excitation wavelengths, for the antiparallel (AP) and closed (CL) isomers of NS2-22 (Table 6.1), with the absorption spectra (Figure 6.4) shows that the calculated excitation wavelengths are in good agreement with the absorption bands. There is some discrepancy in oscillator strengths between the computed

Table 6.1: Bright excited states from df-CC2/cc-pVDZ and TD-ωB97X-D/cc-pVDZ calculations on the antiparallel (AP) and closed (CL) isomers of NS2-22. Oscillator strengths are given in parentheses.

AP	λ_{exc} / **nm**		**CL**	λ_{exc} / **nm**	
Exc. state	**df-CC2**	**ωB97X-D**	Exc. state	**df-CC2**	**ωB97X-D**
3	247 (0.9)	238 (0.2)	**1**	466 (0.3)	452 (0.2)
6	208 (0.2)	217 (0.4)	**5**	251 (0.3)	246 (0.2)

excited states, particularly for the NS2-22 AP isomer. While df-CC2 assigns the largest oscillator strength to excited state 3, TD-ωB97X-D predicts that excited state 6 is brighter. The df-CC2 result is in closest agreement with the AP absorption spectrum, as a peak is observed around 250 nm. For the CL isomer, both TD-ωB97X-D and df-CC2 predict the first and fifth excited states to be bright. The vertical excitation wavelengths of excited states 1 and 5 are consisted with the absorption spectra of closed NS2-22. Note that, unlike TD-DFT, df-CC2 uses the more accurate CIS oscillator strengths. For the remaining DTEs (Tables A2.3 and A2.4), there is a difference between the bright excited states predicted by TD-ωB97X-D and df-CC2, with those obtained by df-CC2 generally in better accord with experimental wavelengths.

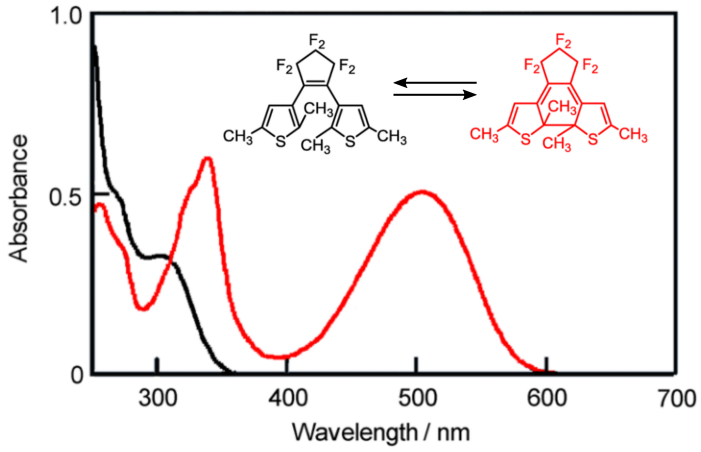


Figure 6.4: Absorption spectra of the antiparallel (black) and closed (red) isomers of NS2-22, adapted from Irie *et al.*[8]

6.4.2 Modelling solvation

The effect of solvent on the electronic excitation energies of NS2-22 was investigated at the TD-ωB97X-D/cc-pVDZ level of theory, with implicit (PCM) and explicit solvation. The compound NS2-22 was used for this purpose because it is the simplest of the eight DTEs and the others are based on the same core structure. Preliminary calculations comparing basis sets again found only ≈15 nm difference in excitation wavelength between the double- and triple-ζ basis sets (Table A2.5).

Explicit solvation calculations were performed to determine the number of methanol molecules needed to describe DTE microsolvation (Table 6.2). The difference in unsolvated and PCM vertical excitation wavelengths is smaller for df-CC2 (several nanometres) than for TD-ωB97X-D (≈10 nm). The red-shift in excitation wavelength with solvation arises due to stabilisation by non-covalent interactions between NS2-22 and methanol, shifting the computed excitation energies closer to the experimental value. Because PCM only contributes an electrostatic potential, explicit solvent molecules were included in solvation calculations to investigate the effect of the additional electrostatic potential (+PCM). These calculations show a red-shift with inclusion of solvation (Table 6.2). The difference is more noticeable in the visible wavelength region for the closed isomer, where the shift is up to ≈10 nm. Compared with the unsolvated vertical ex-

Table 6.2: Summary of the vertical excitation wavelengths of the unsolvated, and lowest energy singly- (sol1.x) and doubly-solvated (sol2.x) geometries of the antiparallel (AP) and closed (CL) isomers of NS2-22. The wavelengths correspond to those of the first and third excited states of the CL and AP isomers, respectively. Data were obtained from df-CC2 and TD-ωB97X-D calculations with the cc-pVDZ basis set. '+ PCM' indicates the addition of PCM implicit solvation to the calculation.

		λ_{exc} / nm		λ_{exc} / nm	
	sol.	**df-CC2**	**+ PCM**	**ωB97X-D**	**+ PCM**
CL	-	466	467	452	460
	1.0	-	-	258	464
	2.1	469	-	460	466
AP	-	247	247	238	241
	1.0	-	-	240	242
	2.2	247	-	242	244

citation wavelengths, explicit solvation with PCM causes a red-shift of up to ≈20 nm. Although this is a significant difference in terms of calculations, it is still classed as a relatively small solvent-induced shift (*e.g.* compared with pCK$^-$, see Chapter 5).

Stabilisation of the system on addition of explicit solvents causes the excitation wavelength red-shift (Figure 6.5). Additionally, Figure 6.5 shows that the difference in vertical excitation wavelengths begins to plateau around 466–467 nm with the number of explicit solvent molecules. The trend approximately follows an exponential function with the form: $y = a - bc^x$. This suggests that the excitation wavelengths will change only slightly with further methanol molecules and it is unlikely that the computed excitation wavelengths would replicate the experimental absorption maximum (≈520 nm). As a

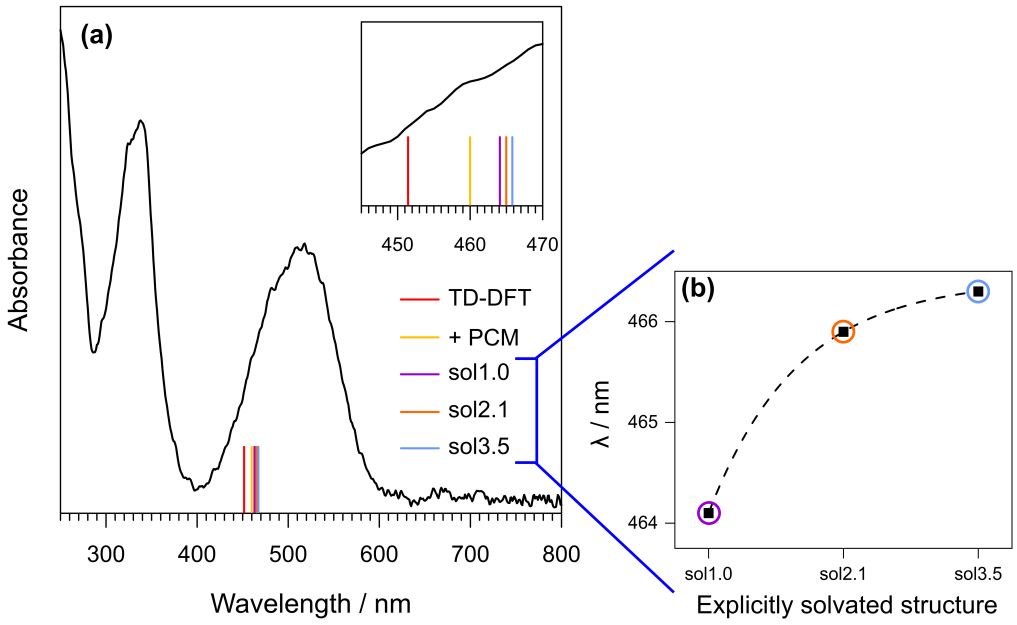


Figure 6.5: The calculated vertical excitation wavelengths of closed NS2-22 are shown by **(a)** coloured lines on the absorption spectrum of closed NS2-22 in methanol (region expanded in insert). The explicit solvated excitation wavelengths are **(b)** plotted as a function solvated structure, fitted to an asymptotic exponential function ($y = a - bc^x$) to demonstrate the tendency towards a plateau. TD-DFT indicates a calculation at the TD-ωB97X-D level of theory, while '+ PCM' includes implicit solvation. The abbreviations sol1.0, sol2.1, and sol3.5 are the lowest energy structures for the singly, doubly, and triply explicitly solvated NS2-22, respectively, computed at the TD-ωB97X-D level of theory with PCM.

result, it is assumed that explicit solvation with three methanol molecules is adequate to describe the microsolvation of NS2-22 at the TD-ωB97X-D/cc-pVDZ level of theory, while accepting that the experimental value will not be obtained with this method. The experimental value may be better replicated by including implicit solvation in df-CC2 or STEOM-CCSD calculations, however the latter would be too expensive.

The lowest energy doubly-solvated structures for the anti-parallel (AP) and closed (CL) isomers both show a preference for hydrogen bonding the first methanol with a fluorine atom of the perfluorocyclopentene ring, while the second methanol interacts with the oxygen atom of the first (Figure 6.6). The lower stability solvated geometries were generally those involving sulfur-methanol hydrogen bonds, or those for which the second methanol was not in the vicinity of the first (Figures A2.4 and A2.5). This suggests that

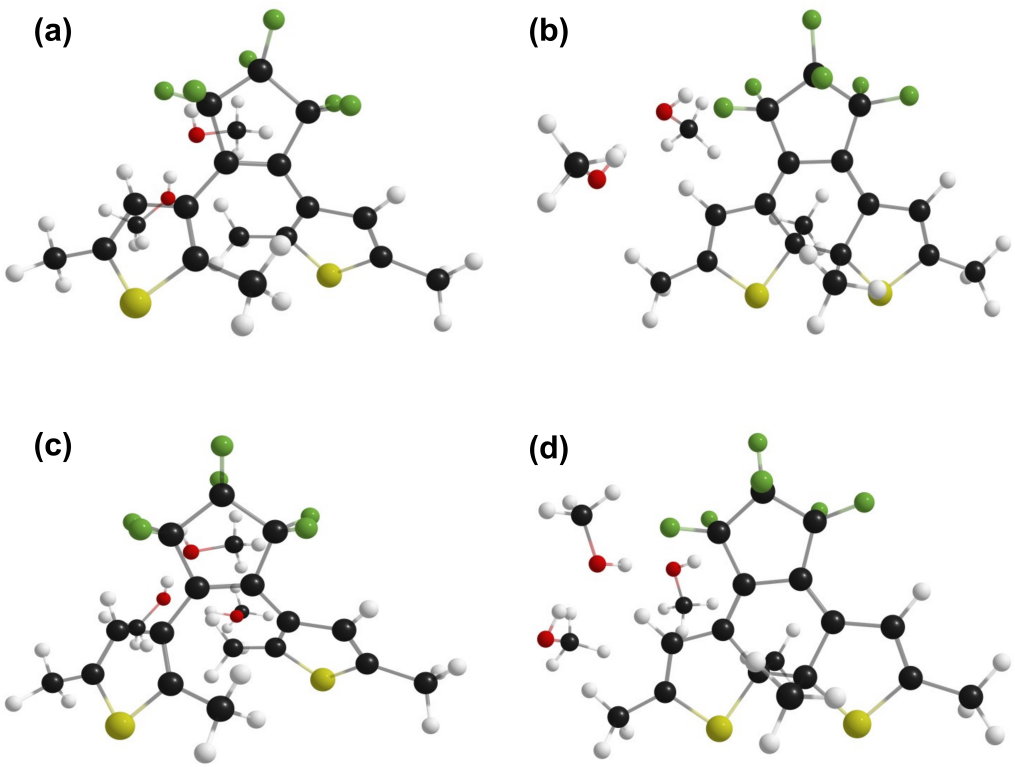


Figure 6.6: Lowest energy doubly- (**(a)** and **(b)**) and triply-solvated (**c** and **d**) structures of antiparallel (left) and closed (right) NS2-22. The first methanol hydrogen bonds to a fluorine atom, while subsequent methanol molecules hydrogen-bond with the preceding methanol.

any further solvation should form fluorine-methanol or methanol-methanol electrostatic interactions.

6.4.3 Absorption and fluorescence spectra

There is a clear distinction between the absorption spectra of the open and closed (CL) isomers of DTEs (Figure 6.4). The open form absorbs in the UV region, typically between 275 nm and 300 nm. Conversely, the spectrum of the photostationary state (formed on UV irradiation of the antiparallel (AP) isomer with 275 nm light and where both AP and CL isomers are present) exhibits bands in both the UV and visible regions. Absorption of visible wavelengths arises because, on ring-closing, π-conjugation is delocalised over the whole molecule. The absorption spectra of the eight DTE compounds of interest (Figure 6.7) show slightly red-shifted visible absorption with more extended π-conjugation. Those compounds forming blue solutions on irradiation display absorption bands peaking at $\approx$600 nm, while the absorption bands of the red solutions lie closer to 500 nm. Comparing the structures of two such compounds, for example CG1-108 (Figure 6.7(h)) and NS2-22 (Figure 6.7(b)), shows the former has greater π-conjugation when in the ring-closed isomer than the latter.

The placement of functional groups plays an important role in the absorption properties of DTE compounds. Consider the related structures NS2-24, CG1-79, CG1-91, and CG1-94. NS2-24 does not have the additional carboxylic acid group and has shorter π-conjugation, resulting in an absorption maximum at a shorter wavelength. The absorption maximum of CG1-79 (carboxylic acid group in the *para* position on the phenyl) is red-shifted by $\approx$10 nm relative to NS2-24. On the other hand, when the carboxylic acid group is at the *meta* position (CG1-91), the π-electrons cannot be conjugated over the carboxylic acid group, yielding a similar absorption maximum in CG1-91 compared with NS2-24. CG1-94 is anomalous as its carboxylic acid group is *ortho* on the phenyl group, supporting delocalisation, but its absorption maximum is comparable to NS2-24. This suggests the presence of a destabilising influence on the system (possibly intramolecular steric effects), thereby increasing the HOMO-LUMO gap.

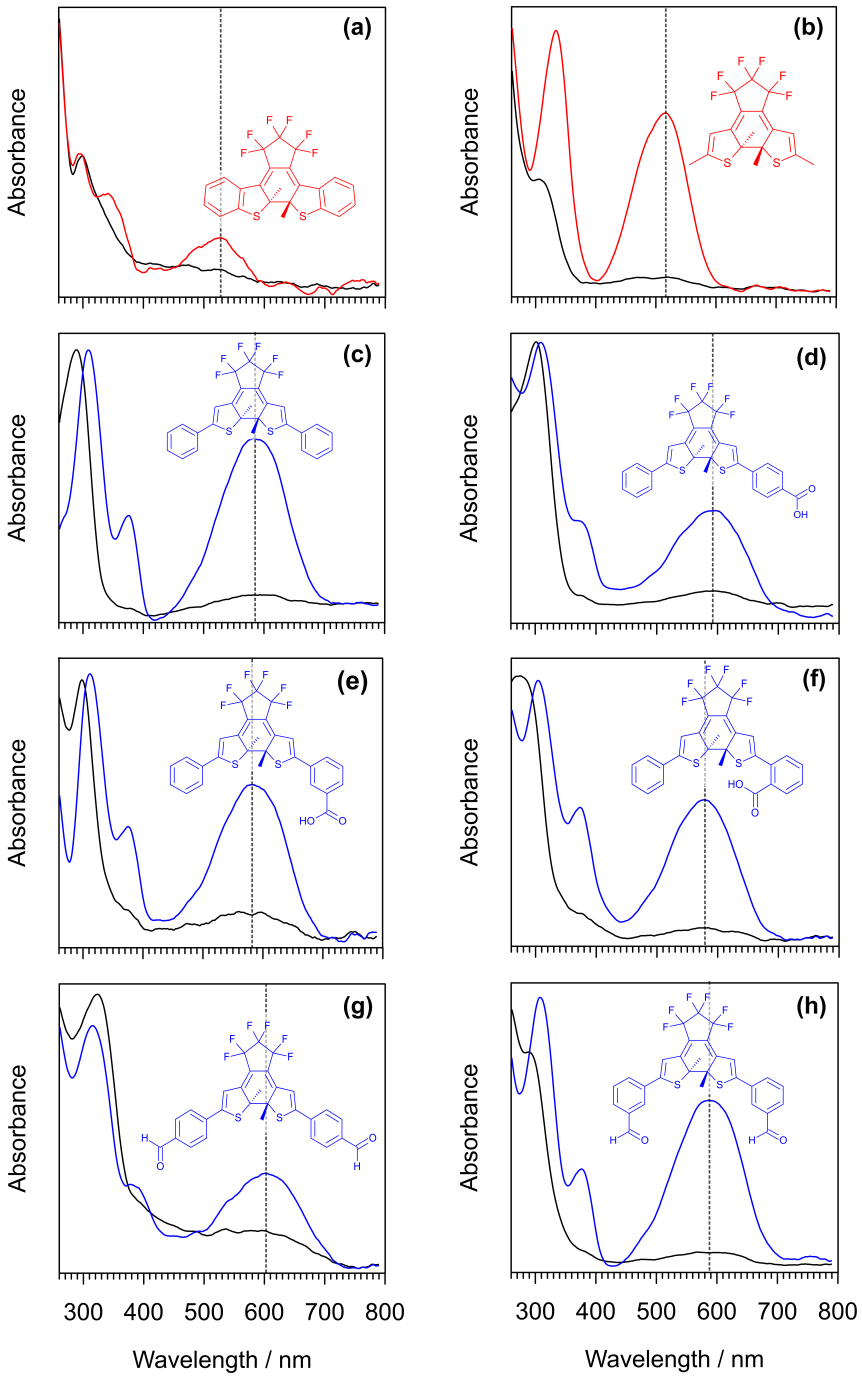
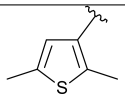
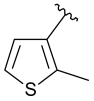
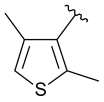
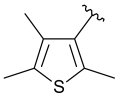
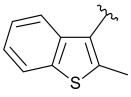
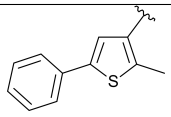
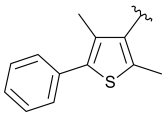
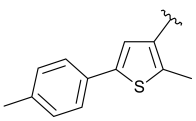


Figure 6.7: Absorption spectra of the open (black) and closed (coloured) forms of **(a)** B2287, **(b)** NS2-22, **(c)** NS2-24, **(d)** CG1-79, **(e)** CG1-91, **(f)** CG1-94, **(g)** CG1-107, and **(h)** CG1-108, recorded in methanol. The colours of the spectra indicate the colour of the irradiated DTE solutions (at arbitrary concentrations). Bands in the range of 380–400 nm **(c)**–**(h)** likely arise due to by-product formation.

Compared with NS2-24, both CG1-107 and CG1-108 have greater π-conjugation and are more polar, due to the *two* aldehyde groups, one on each phenyl ring. While the *meta* aldehyde groups of CG1-108 add no further conjugation to the system, the addition of the two aldehyde groups red-shift the absorption maximum by ≈10 nm relative to NS2-24. As such, the absorption maximum of CG1-108 is comparable to that for CG1-79. CG1-107, on the other hand, has more extensive π-conjugation due to its *para*

Table 6.3: Absorption maxima (λ_{max}) of DTE compounds of the same and comparable structures to NS2-22, B2287, and NS2-24 from this work (expt.) and literature.

Thiophene functionalisation	**Solvent**	$\boldsymbol{\lambda}_{max}$ **/ nm**	**Ref.**
NS2-22 	methanol	520	expt.
	hexane	503	25
	hexane	509	25
	hexane	562	24
	hexane	525	25
B2287 	methanol	520	expt.
		517	21
	n-hexane	515	22
NS2-24 	methanol	520	expt.
		575	26
	hexane	534	24
		562	22
	acetonitrile	588	13

aldehyde groups. Thus, CG1-107 has the most red-shifted absorption maximum relative to NS2-24.

The absorption maxima from the recorded UV-vis spectra are consistent with those of the same/comparable structures obtained from the literature (Table 6.3). As mentioned in the previous chapter, absorption spectra are less sensitive to solvent polarity than fluorescence emission spectra. Polar compounds are expected to exhibit slightly longer absorption wavelengths in more polar solvents, such as methanol ($\varepsilon = 33$),[48] compared with a non-polar solvent, such as hexane ($\varepsilon = 1.89$).[48] The red-shifted absorption maximum for NS2-22 in methanol (520 nm), relative to hexane (503 nm)[25] indicates stabilisation by the polar solvent. Comparatively, the difference in B2287 absorption maxima in methanol and hexane is much smaller, suggesting B2287 is less sensitive to solvent polarity than NS2-22. In comparison, compounds such as CG1-91 or CG1-107 would be expected to exhibit a greater change in absorption maximum, depending on solvent polarity, since they have additional polar functional groups.

6.4.3.1 Temperature-dependent fluorescence

Excitation-emission (XM) maps of the closed forms of the eight DTEs (Figures 6.8 and 6.9) recorded at room temperature ($T \approx 300$ K) show a clear difference in excitation/emission properties across the series of compounds. Given that irradiating the open-isomer DTEs forms a photostationary state between the open and closed isomers, the emission signal on 300–350 nm excitation will contain contributions from both the AP and CL forms. This work is thus focussed on absorption by the CL isomer with visible light.

The absorption spectra of the CL isomers (Figure 6.7) exhibit three absorption bands: **(1)** in the UV, **(2)** around 400 nm, and **(3)** between 500 nm and 600 nm (responsible for the solution colour). Region **1** is ignored due to the overlap with absorption of the AP form. The dominant feature in most of the XM maps is centred around an excitation wavelength of 400 nm, suggesting that excitation of the functionality/molecule responsible for absorption band **2** is the source of the majority of the fluorescence of these DTEs at $T \approx 300$ K. This is likely the by-product. Compounds B2287 (Figure 6.8(e)), CG1-79 (Figure 6.8(f)), and CG1-108 (Figure 6.9(e)) are exceptions to this, likely due to the particularly intense signal in the 300–350 nm excitation region which may be masking some of the intensity of the signal around 400 nm. The inserts in Figures 6.8(f)

and 6.9(e) show that CG1-79 and CG1-108 fluoresce in the 400 nm region. On the other hand, the Figure 6.8(e) insert shows fluorescence emission from 500-550 nm excitation of B2287 is greater than that from 400 nm excitation. Weak contours also appear in the ≈500–550 nm excitation region in several of the XM maps, corresponding to absorption

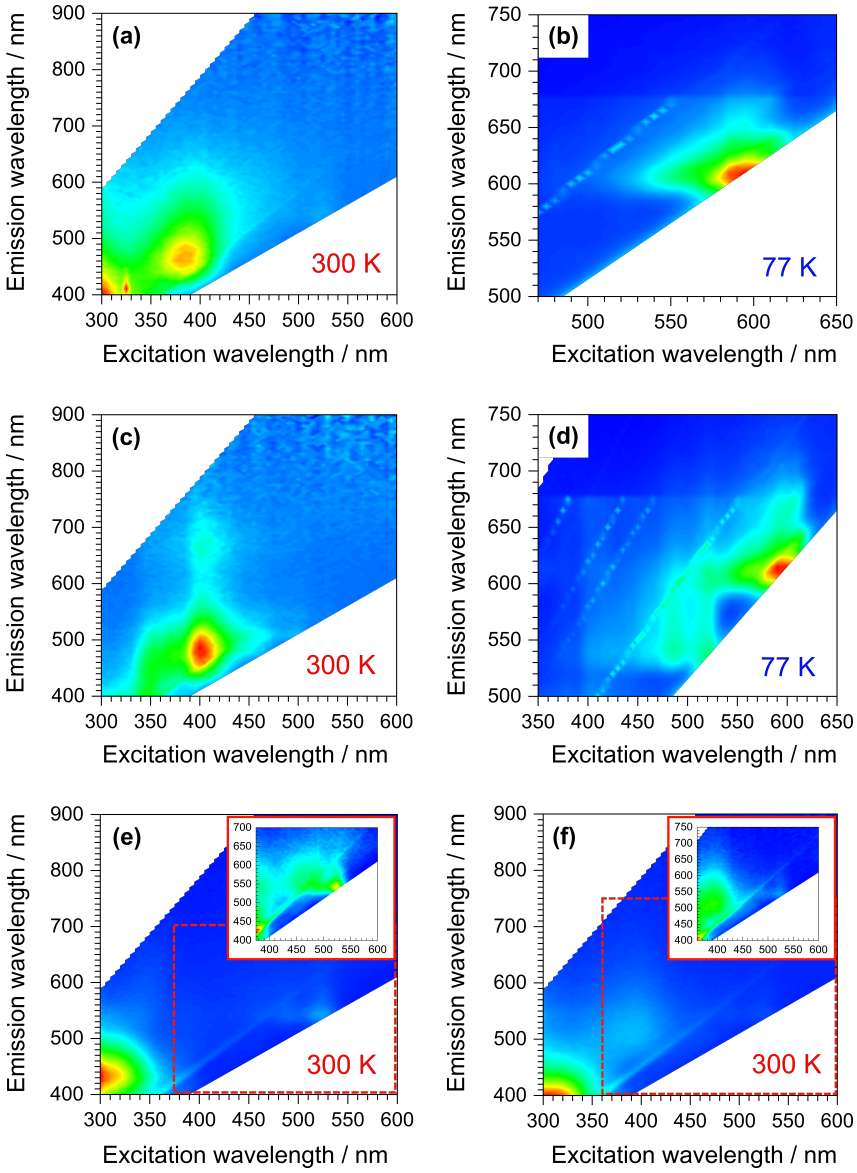


Figure 6.8: Excitation-emission (XM) maps of the closed-isomer forms of **(a)** NS2-22, **(c)** NS2-24, **(e)** B2287, and **(f)** CG1-79, recorded at $T \approx 300$ K in methanol. Panels **(b)** and **(d)** show the XM maps, recorded at $T \approx 77$ K in methanol, of NS2-22 and NS2-24, respectively. Inserts are XM maps of areas of weak fluorescence signal. Diagonal lines are an artefact from scattering of the excitation light.

by band **3**, suggesting the presence of some minor fluorescence resulting from the band **3** functionality (the closed isomer). This suggests that fluorescence may be dominated by the by-product at $T \approx 300\,\mathrm{K}$, even when present in relatively small proportions. In contrast, XM maps recorded at $T \approx 77\,\mathrm{K}$ only present signal in the ≈600 nm excitation

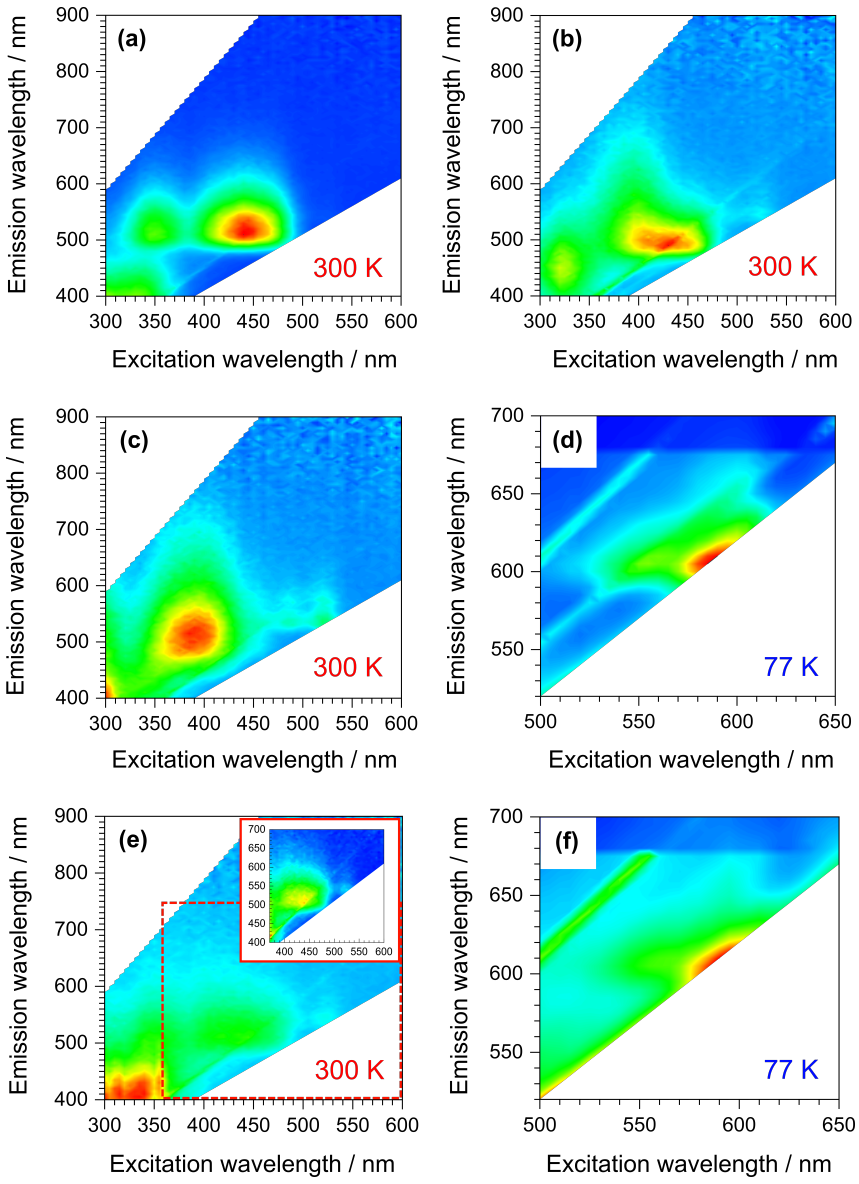


Figure 6.9: Excitation-emission (XM) maps of the closed-isomer forms of **(a)** CG1-91, **(b)** CG1-94, **(c)** CG1-107, and **(e)** CG1-108, recorded at $T \approx 300\,\mathrm{K}$ in methanol. Panels **(d)** and **(f)** show the XM maps, recorded at $T \approx 77\,\mathrm{K}$ in methanol, of CG1-107 and CG1-108, respectively. The insert is an excitation-emission map of an area of weak fluorescence signal. Diagonal lines are an artefact from scattering of the excitation light.

wavelength range, and the intense signals around excitation wavelengths of 350 nm and 400 nm seen in the $T \approx 300$ K maps are not visible at $T \approx 77$ K. It is likely that the 350 nm and 400 nm excitation peaks are masked by the much brighter 500–550 nm signal. Furthermore, comparing the weak contours in the ≈500–550 nm excitation region at $T \approx 300$ K with the XM maps at $T \approx 77$ K, there is a clear red-shift from ≈520 nm to ≈600 nm.

Fluorescence excitation and emission spectra of the closed-isomers at $T \approx 77$ K (Figures 6.10 and 6.11) reveal excitation maxima around 580–600 nm and emission maxima around 600–630 nm. The excitation spectra are broader and the emission spectra are

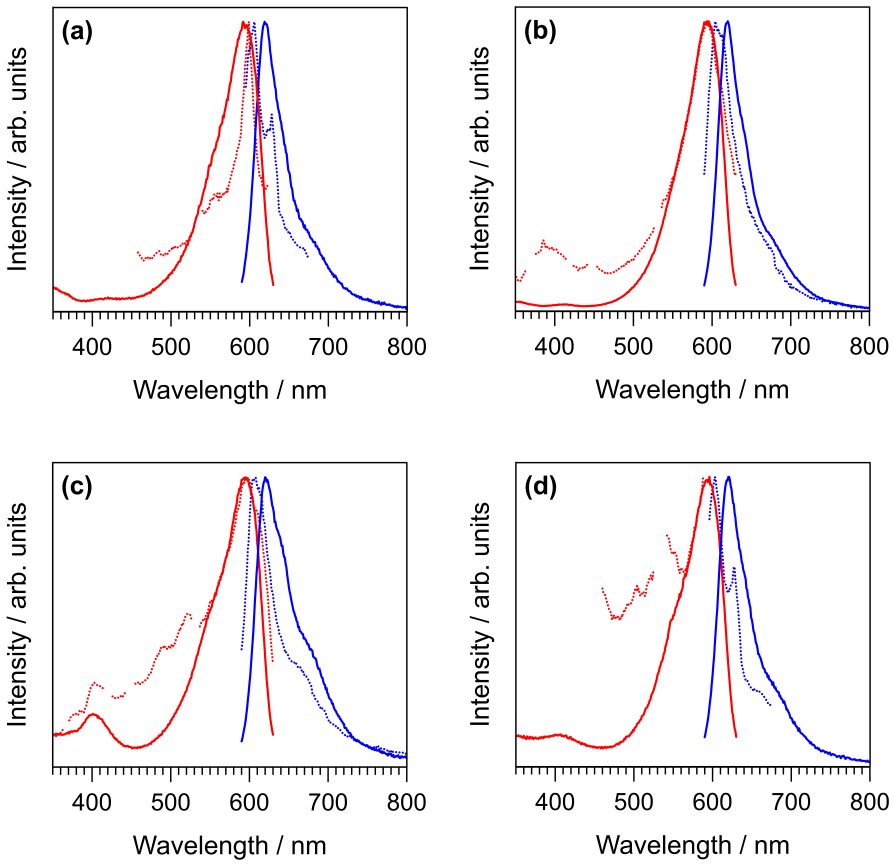


Figure 6.10: Excitation (red) and emission (blue) spectra of **(a)** B2287, **(b)** NS2-22, **(c)** NS2-24, and **(d)** CG1-79, recorded at $T \approx 300$ K (solid lines) and $T \approx 77$ K (dotted lines) in methanol. Gaps in the $T \approx 77$ K excitation spectra are present due to removal of signal that arose from internal reflections in the spectrofluorometer setup. These are the disregarded diagonal lines in the XM maps.

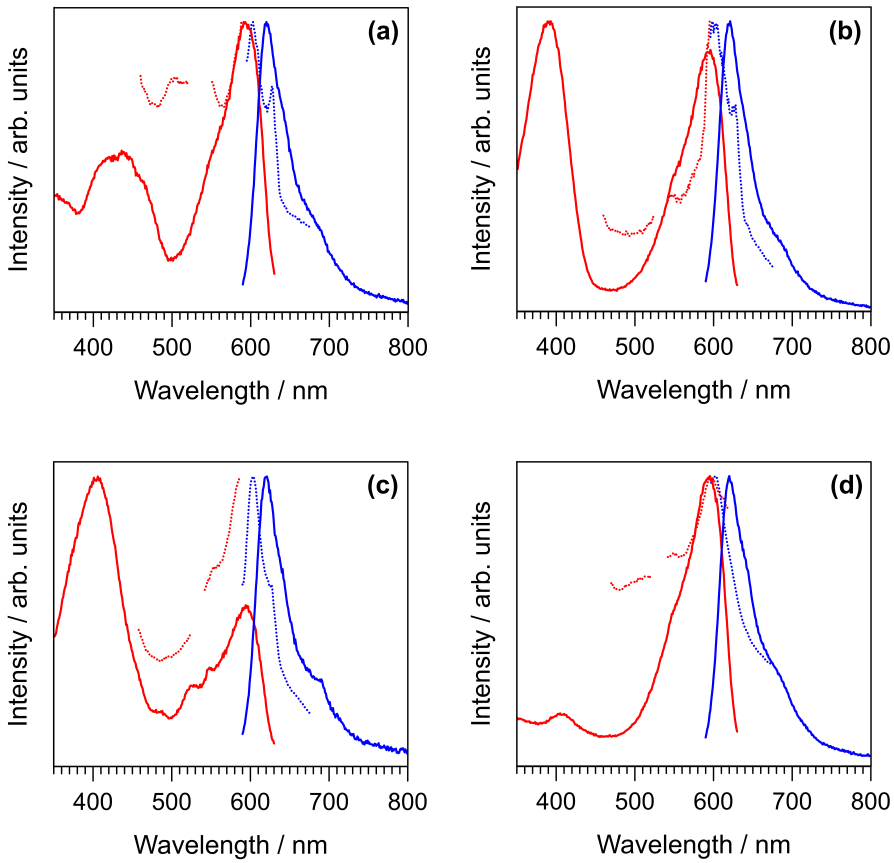


Figure 6.11: Excitation (red) and emission (blue) spectra of **(a)** CG1-91, **(b)** CG1-94, **(c)** CG1-107, and **(d)** CG1-108, recorded at $T \approx 300\,\mathrm{K}$ (solid lines) and $T \approx 77\,\mathrm{K}$ (dotted lines) in methanol. Gaps in the $T \approx 77\,\mathrm{K}$ excitation spectra are present due to removal of signal that arose from internal reflections in the spectrofluorometer setup.

blue-shifted (relative to $T \approx 300\,\mathrm{K}$). This is presumably due to freezing out of conformations at $T \approx 77\,\mathrm{K}$. The differing apparent Stokes shift at the two temperatures may be because different competitive deactivation pathways are probed, or because fluorescence at $T \approx 300\,\mathrm{K}$ is dominated by the by-product (absorbing around 400 nm). DTE potential energy surfaces are discussed further in Sections 6.4.4 and 6.4.7. The scattering artefacts present in the fluorescence emission spectra and XM maps at $T \approx 77\,\mathrm{K}$ arose because fluorescence measurements were performed in methanol which, at low temperatures, crystallises rather than forming a clear glass (*e.g.* ethylene glycol). Methanol was used because of poor DTE solubility in ethylene glycol and other polar solvents.

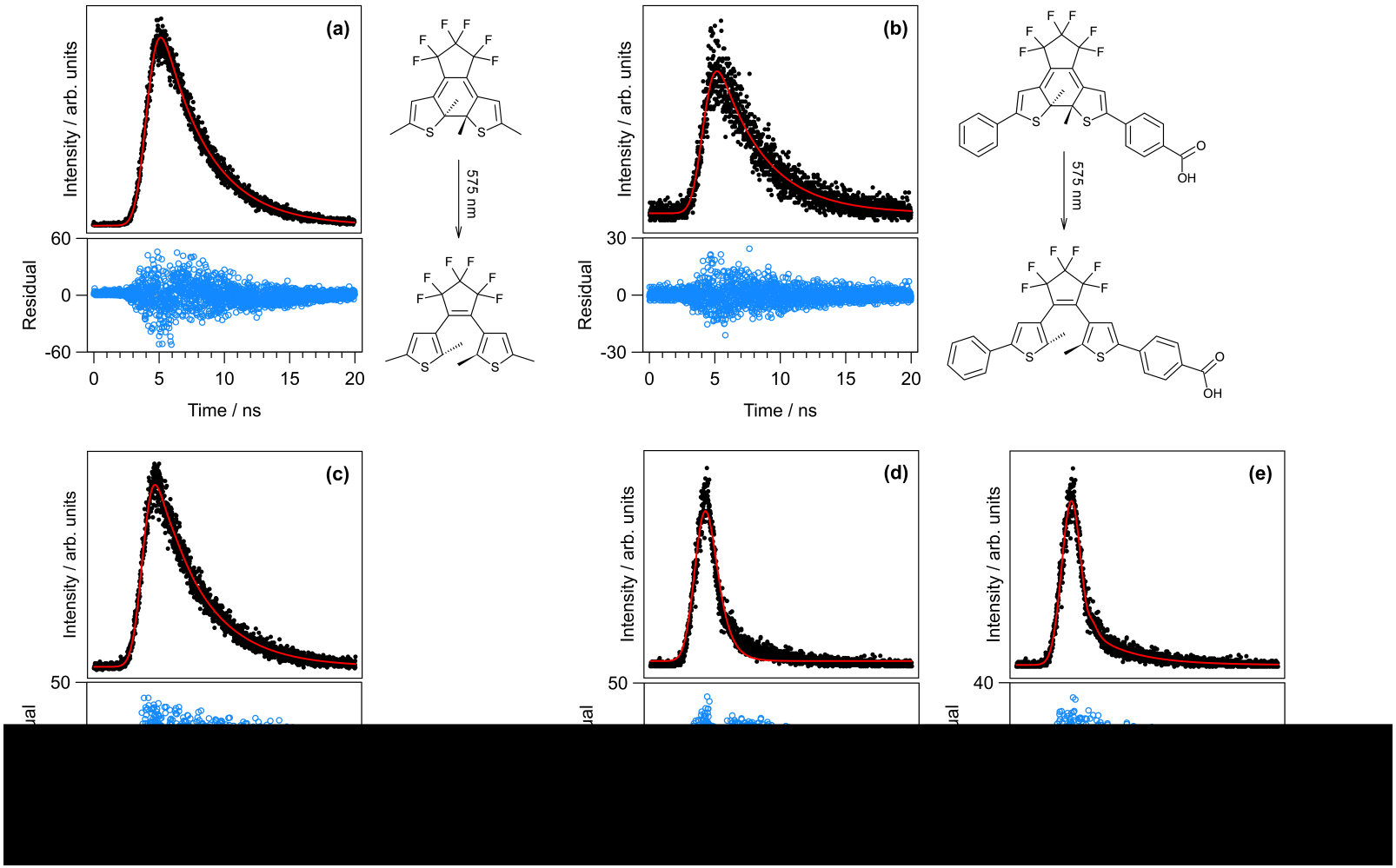


Figure 6.12: Time-resolved emission for DTEs **(a)** NS2-22 and **(b)** CG1-79 in methanol at **(a)**–**(b)** $T \approx 300\,\mathrm{K}$ and **(c)**–**(e)** at $T \approx 77\,\mathrm{K}$. A double-exponential fit is shown to be more suited for **(e)** CG1-79 at $T \approx 77\,\mathrm{K}$. The other decay curves are suited to single-component fits.

6.4.4 Time-resolved fluorescence

There have been numerous time-resolved (transient absorption and fluorescence) studies of DAE and DTE molecules over the last 20 years.[18–20,23,27,29] In many regards, the literature is difficult to approach and concisely summarise because the dynamics (excited-state lifetimes and quantum yield) depend strongly on functional group substitution and solvent, with reported values often of differing orders magnitude depending on these variables. Broadly speaking, the electrocyclisation (ring-closing) reaction, induced by UV absorption, has been studied more thoroughly,[19,20,23,29] although many involve photostationary states, for which the closed isomer also absorbs in the UV. While transient absorption has successfully probed the dynamics associated with the emergence of the ring-closed (visible) absorption band, transient fluorescence has shown complex results, due to differing dynamics associated with dual emission, arising from the parallel and antiparallel conformations, and distinct excited-state lifetimes associated with each (sub-200 ps and <10 ps, respectively).[19,20,23] Although the cycloreversion (ring-opening) reaction has received much less attention, it has been established that the dynamics (lifetimes and quantum yield) are more complicated, since the reaction coordinate follows internal conversion and traversal of an excited-state barrier before reaching the key ring-opening conical intersection.[22,27] The scheme is summarised in Figure 6.13, with further details in Figure 6.14(a).

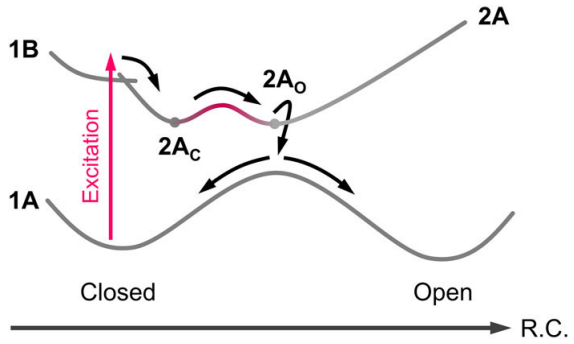


Figure 6.13: Diarylethene cycloreversion reaction scheme. 1A and 2A are the ground- and excited-states, respectively. $2A_C$ is a local closed-isomer minimum and $2A_O$ is the geometry at the 2A/1A conical intersection. Adapted from Sotome *et al.*[27]

Attempts to study the open- or closed-isomer DTEs using femtosecond fluorescence up-conversion at $T \approx 300$ K were unsuccessful because there is insufficient absorption at 400 nm. Time-resolved emission measurements were feasible due to the availability of excitation light sources of various wavelengths. Time-resolved emission spectra in

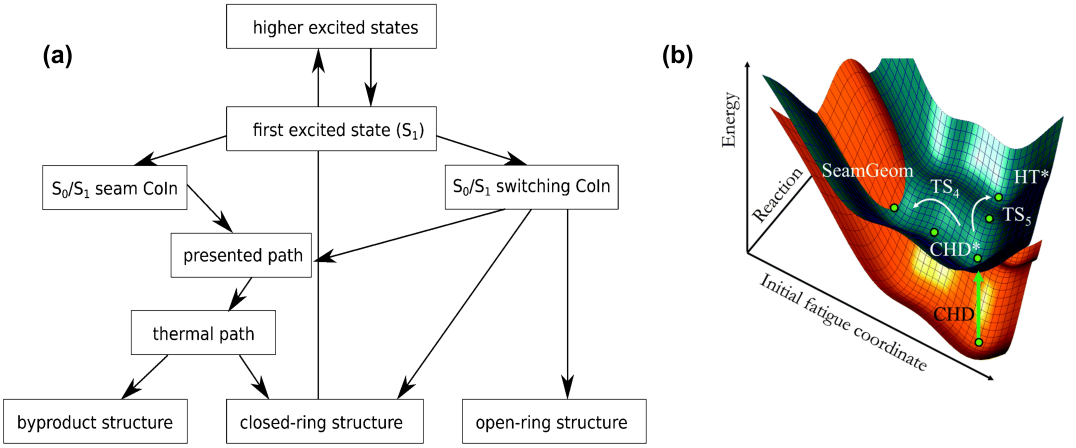


Figure 6.14: Panel **(a)** is a schematic of multiple possible relaxation pathways for a closed-isomer thiophenylethene (a type of DTE) upon excitation. Adapted from Matis *et al.*[49] Panel **(b)** shows a representation of a thiophenylethene's potential energy surfaces (S_0, orange; S_1, green) for the initial fatigue coordinate. CHD and HT represent the closed and open isomers, respectively. SeamGeom is an S_1/S_0 conical intersection, ultimately leading to by-product formation (not shown). Adapted from Mendive-Tapia *et al.*[50]

methanol reveal that 575 nm excitation at $T \approx 300$ K produces very little signal (over an acquisition time of ≈3 minutes) from which no decay constant could be extracted accurately. This was remedied by increasing signal acquisition time (≥20 minutes). Over the same ≈3-minute acquisition period at $T \approx 77$ K, excitation at 575 nm produced clear decay curves, with decay constants around 3–4 ns. Excitation at 365 nm and 478 nm produced more intense signal than 575 nm at $T \approx 300$ K; however, these wavelengths do not probe the regions of interest – namely the 500–600 nm range in which only the ring-closed isomers absorb. The $T \approx 300$ K time-resolved data is unlikely to correspond to excitation of the by-product, since it does not absorb at the 575 nm pump wavelength (see Section 6.4.6).

The time-resolved data are interpreted in terms of the cycloreversion model described earlier. At $T \approx 300$ K, the experimental data fits to a single lifetime component with a ≈3.5 ns decay constant (Table 6.4). At $T \approx 77$ K, most DTEs require a two-component fit, with the first component (τ_1) having a sub-nanosecond lifetime and the second component (τ_2) having a longer lifetime, similar to the $T \approx 300$ K data. The shortest pump pulse duration is 400 ps, and thus limits some of the τ_1 values. For the $T \approx 77$ K data,

Table 6.4: Fluorescence lifetimes of DTEs in methanol measured at $T \approx 300\,\mathrm{K}$ and $T \approx 77\,\mathrm{K}$, by time-resolved emission ($\lambda_{ex} = 575\,\mathrm{nm}$). Emission was monitored at 620 nm at $T \approx 300\,\mathrm{K}$ and 630 nm at $T \approx 77\,\mathrm{K}$. Lifetimes denoted by * are limited by the pump pulse duration (≈400 ps).

	77 K			**300 K**
DTE	τ_0 / **ns**	τ_1 / **ns**	τ_2 / **ns**	τ_0 / **ns**
B2287	-	0.14±0.00*	2.86±0.10	3.55±0.05
NS2-22	3.50±0.03	-	-	3.53±0.02
NS2-24	3.64±0.02	-	-	3.45±0.08
CG1-79	-	0.33±0.02*	3.25±0.16	3.51±0.05
CG1-91	-	0.27±0.03*	3.28±0.15	3.40±0.04
CG1-94	-	0.39±0.02*	3.39±0.18	3.53±0.06
CG1-107	-	0.45±0.03	3.72±0.11	3.45±0.05
CG1-108	-	0.47±0.09	3.17±0.12	3.49±0.05

τ_1 and τ_2 are interpreted as the initial 1B→2A internal conversion and the traversal of the $2A_C \rightarrow 2A_O$ barrier (Figure 6.13), respectively, with the latter requiring extensive nuclear motion. The two most intriguing results are: (1) the presently-measured lifetimes in methanol are substantially longer than those recorded in non-polar solvents for similar DTEs, *e.g.* <100 ps in *n*-hexane,[18] and (2) fluorescence lifetimes are similar at $T \approx 300\,\mathrm{K}$ and $T \approx 77\,\mathrm{K}$. Point (1) suggests that methanol solvation perturbs (increases) the excited-state barrier to ring-opening significantly. Future experiments should systematically vary solvent polarity to explore this effect. The similarity in fluorescence lifetimes at the two temperatures (point (2)) suggests that the temperature-dependent experiments likely probe different fractions of at least two competitive pathways, given that there are multiple deactivation pathways on the potential energy surface (Figure 6.14). In contrast to the DTEs, $p\mathrm{CK}^-$ dynamics change significantly on cooling (Section 5.4.5), because single-/double-bond torsion is hindered in the glassy matrix. It should be noted that there is no existing literature for time-resolved emission of DTEs at $T \approx 77\,\mathrm{K}$.

As outlined above, dual component fluorescence is a known characteristic of the ring-closing reaction in DTEs, with signals arising due to parallel-isomer fluorescence and antiparallel-isomer ring-closure. It is reasonable to assume similar dynamics for the cycloreversion reaction, especially considering the complex potential energy surface along

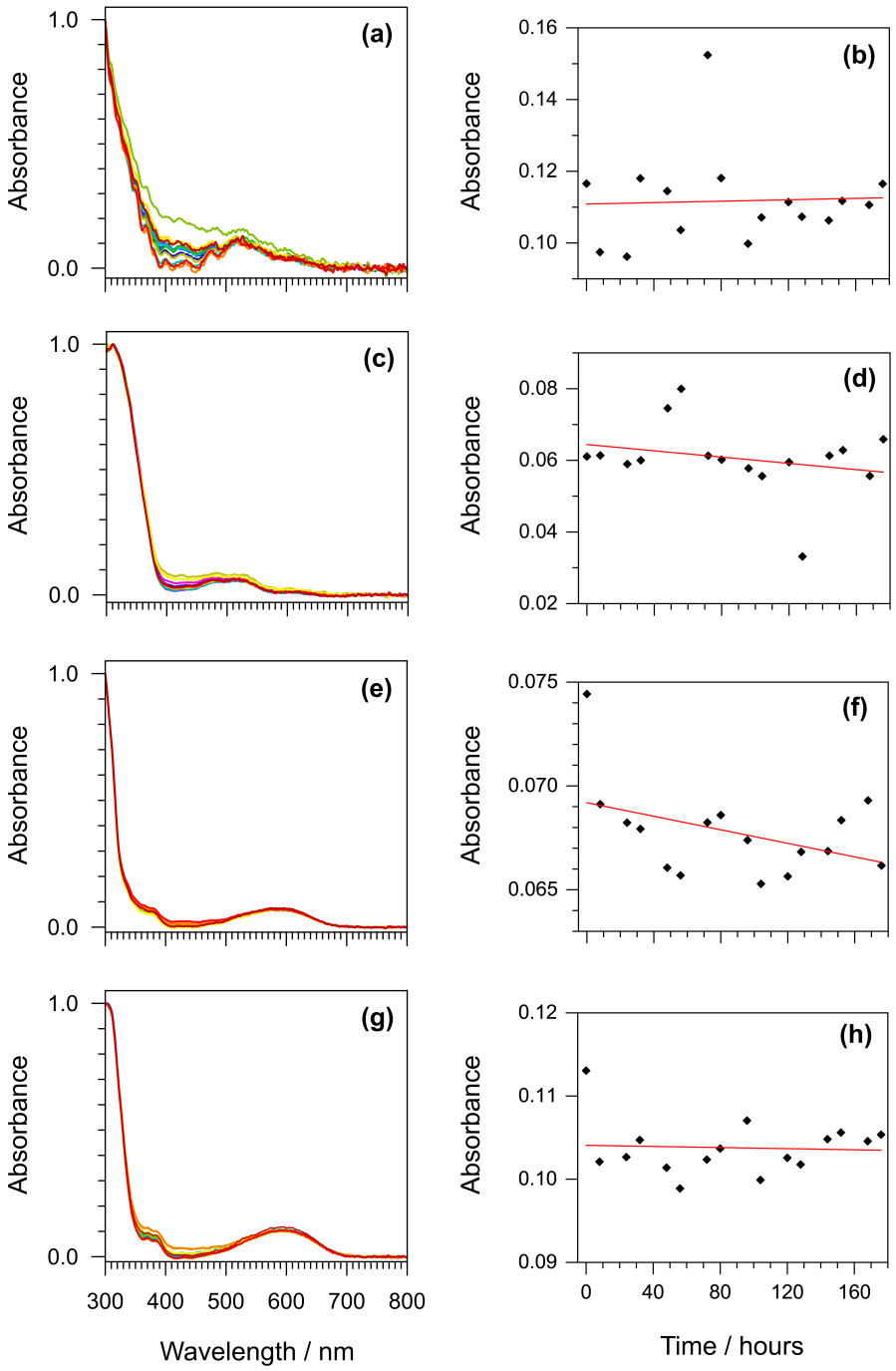


Figure 6.15: Time-series absorption spectra of irradiated **(a)** B2287, **(c)** NS2-22, **(e)** NS2-24, and **(g)** CG1-79, in methanol. The peak absorbance of the 500–600 nm band from each spectrum are plotted on the right, **(b, d, f, h)**. Absorbance is normalised to the maximum signal.

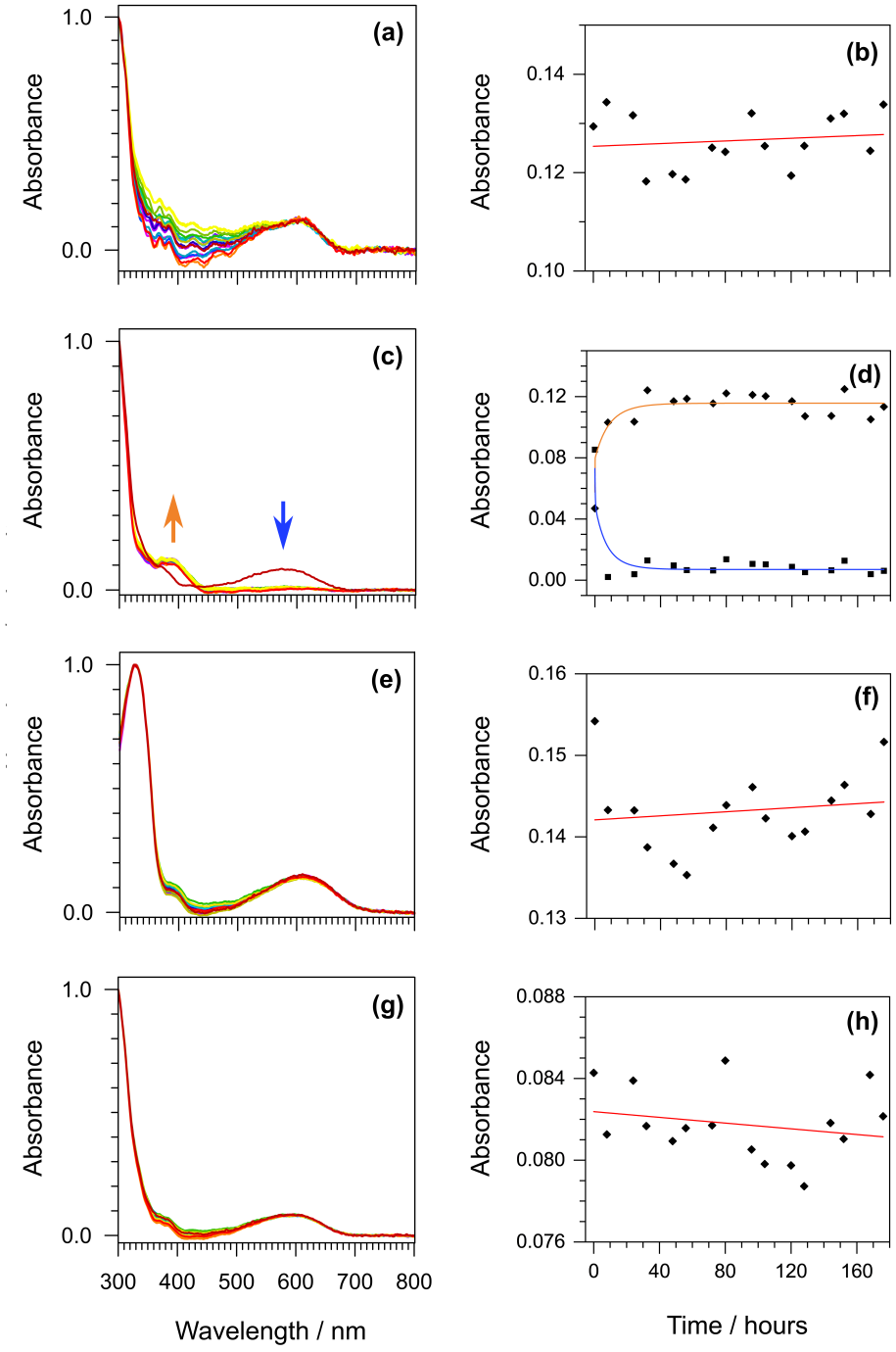


Figure 6.16: Time-series absorption spectra of irradiated **(a)** CG1-91, **(c)** CG1-94, **(e)** CG1-107, and **(g)** CG1-108, in methanol. The peak absorbance of the 500–600 nm band of each spectrum are plotted on the right, **(b, d, f, h)**. On plots **(c)** and **(d)**, blue represents the disappearing band, arising from the closed isomer, while orange represents the new band, attributed to the by-product. CG1-94 decomposes rapidly. Absorbance is normalised to the maximum signal.

the reaction coordinate (Figures 6.13 and 6.14). Future studies may benefit from systematic temperature-dependent experiments to inform on correlations between excited-state lifetimes and isomerisation quantum yields of the two fluorescence components. Unfortunately, the Edinburgh Instruments time-resolved instrument used in this work could only perform $T \approx 77\,\mathrm{K}$ (liquid nitrogen bath), $T \approx 300\,\mathrm{K}$ (room temperature cell), or $T > 300\,\mathrm{K}$ (heated flow cell). Additionally, because fluorescence is weak at $T \approx 300\,\mathrm{K}$, experiments at higher temperatures are of limited use.

6.4.5 Change in absorption spectra over time

One of the fundamental requirements of a functional DTE photoswitch is the formation of a stable closed isomer on irradiation. The solutions of DTE in methanol were irradiated at 275 nm for five minutes (15 minutes for B2287) and absorption spectra measured at regular intervals over 180 hours. When not being used, the solutions were stored in the dark and their exposure to extraneous light minimised.

The spectra in Figures 6.15 and 6.16 show that there is little change in the appearance of the absorption spectra over 180 hours in all but one of the solutions. This is exemplified by the plots of maximum absorbance for the visible-wavelength bands as a function of time (adjacent to the spectra). Only CG1-94 exhibited a noticeable change in its absorption spectrum, occurring within the first eight hours. The closed-isomer band (≈575 nm) disappears, while a new band (≈380 nm) appears (Figures 6.16(c) and (d)). It is clear, by comparing the subsequent spectrum to that of the open isomer of CG1-94 (Figure 6.7(f)), that the change in the absorption spectra is not due to conversion from the closed to the open isomer. From this, it is speculated that the culprit is the by-product, as this is a feasible alternative reaction pathway for DTEs (Figure 6.2). The condensed-ring by-product is a known issue for many DTEs, but has not been studied in detail due to difficulties in quantifying isomers involved in each switching cycle (NMR and IR spectra are congested).

6.4.6 The strange case of the yellow CG1-94 solution

In the previous section, the change in the CG1-94 absorption spectrum within eight hours of irradiation is attributed to the by-product. The change in absorption was accompanied by a change in solution colour – from blue to yellow. By comparing the absorption spectra of the colourless (open-isomer), blue (closed-isomer), and yellow so-

lutions (Figure 6.17) of CG1-94, it is clear that the latter contains a new band around 380 nm, which is not present in the spectra of either the open- or closed-isomers, including CG1-79 and CG1-91 (the same functional groups as CG1-94, but in different positions). The yellow solution has a large Stokes shift (6077 cm^{-1}).

A solution of a closed-isomer DTE, when irradiated at 590 nm, would eventually revert back from blue to colourless. However, after irradiation of the yellow solution at 590 nm for approximately one hour, there was no noticeable difference in the absorption spectrum (Figure 6.17(b)). Furthermore, the absorption spectrum showed no noteworthy

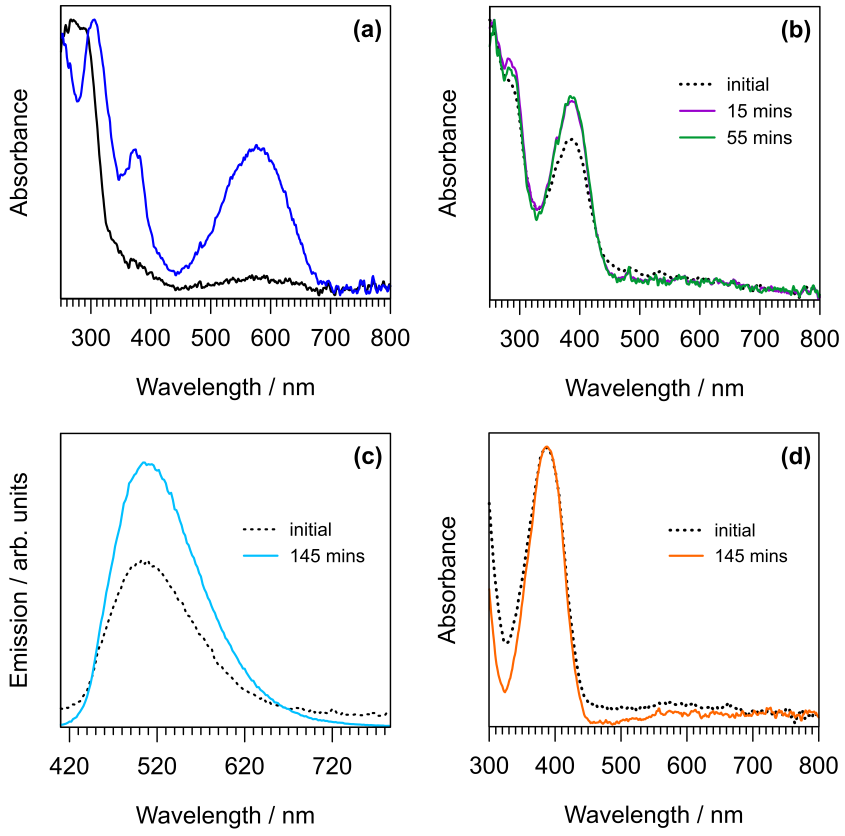


Figure 6.17: Absorption spectra in methanol of **(a)** the open (black) and closed (blue) isomers of CG1-94, and **(b)** the initial yellow solution of CG1-94, followed by irradiation at 590 nm for 15 and 55 minutes. **(c)** Fluorescence emission spectra of the initial yellow solution, followed by irradiation at 275 nm for 145 minutes, show that the fluorescence intensity increased while the absorption spectrum **(d)** did not change. Absorbance is normalised to the maximum signal.

change when irradiated with 275 nm light for a total of 145 minutes (Figure 6.17(c)); however, the emission intensity increased (Figure 6.17(d)). These data suggest two important points. Firstly, the absence of change in the absorption spectrum indicates the compound is not photoswitchable using either 275 nm or 590 nm radiation. Secondly, the increase in fluorescence emission implies that not all of the molecules in the solution had previously converted to this yellow form and that irradiation at 275 nm drives further conversion. From this, it is inferred that the yellow compound is formed through UV irradiation and cannot be reversed photochemically. The reaction scheme in Figure 6.2 shows the possible formation of a non-photoswitchable by-product on further irradiation of the closed isomer with UV light. This matches the properties of the yellow solution,

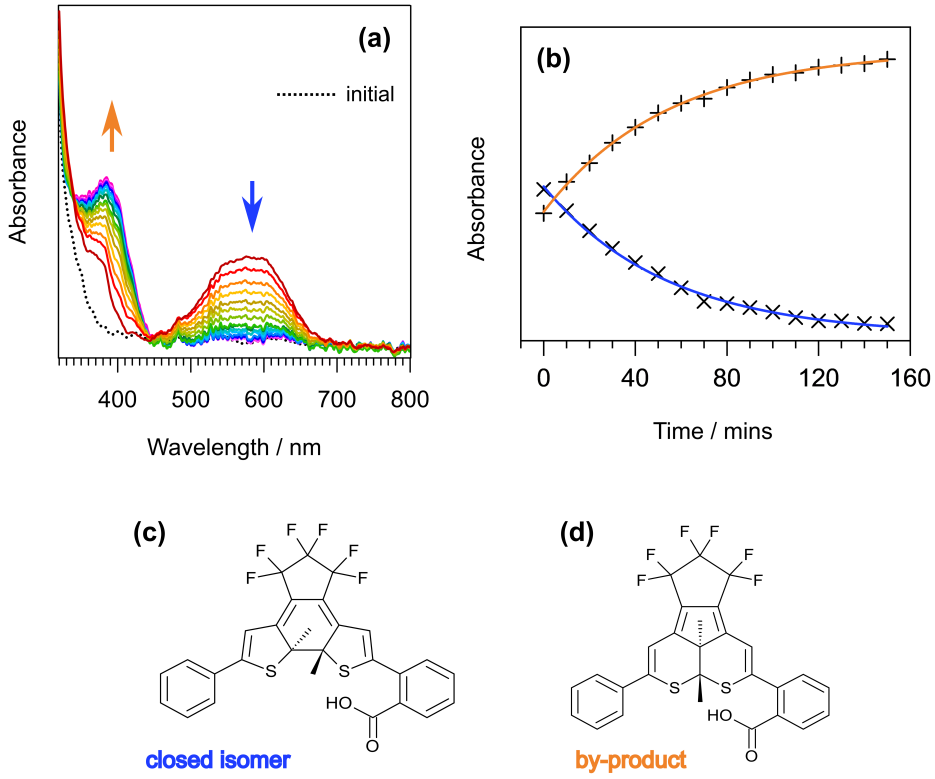


Figure 6.18: A methanol solution of open-antiparallel CG1-94 (initial) was irradiated at 275 nm for 10 minutes and **(a)** absorption spectra recorded at 10 minute intervals. **(b)** The change in absorbance of the 380 nm (yellow) and 575 nm (blue) bands were plotted as a function of time, fitted to exponential growth ($y = A_1 e^{(x/t_1)} + y_0$) and decay ($y = A_1 e^{(-x/t_1)} + y_0$) curves, respectively. Also shown are the structures of the **(c)** closed isomer ($\lambda_{max} = 575$ nm) and **(d)** by-product ($\lambda_{max} = 380$ nm).

supporting the conclusion that the compound responsible is the CG1-94 by-product (Figure 6.18(d)).

Section 6.4.5 discussed the change in absorption spectra of the closed-isomer DTEs as a function of time. Of the compounds, only CG1-94 showed a significant change in its absorption spectrum, which occurred within the first eight hours after irradiation. This was probed further to explore timescale of conversion to the by-product. A solution of CG1-94 in methanol was irradiated for 10 minutes with 275 nm UV light and absorption spectra recorded at 10 minute intervals (Figure 6.18(a)). The absorption band centred around 380 nm grows with time, while that at 575 nm decreases. Figure 6.18(b) shows the change in absorbance as a function of time for the 380 nm (orange) and 575 nm (blue) bands. The trends correspond to exponential growth and decay, respectively. Two isosbestic points (wavelengths where the total absorbance of a sample undergoing a physical change does not change) are present in Figure 6.18(a) at 340 nm and 450 nm. This indicates that no secondary reactions are taking place. Thus, it is reasonable to assume that by-product formation, driving growth of the 380 nm band, occurs by degradation of the closed isomer (Figure 6.18(c)). This is in agreement with the previously discussed evidence and the well-established reaction pathway for DTE photoswitches that shows the formation of a by-product on further UV irradiation of the closed isomer.[13,35] The reaction coordinate to the by-product is complex and likely influenced by both thermal and photochemical decomposition.

The formation of the by-product can be monitored by fluorescence excitation-emission (XM) maps recorded at regular intervals after irradiation of a solution of open CG1-94 at 275 nm (Figure 6.19). The region of intense fluorescence is seen to shift in the spectra recorded at 5 minutes to 55 minutes after irradiation, with the latter beginning to correlate well with the XM map of the yellow solution. Comparison of the XM maps of the by-product at $T \approx 300\,\mathrm{K}$ and $T \approx 77\,\mathrm{K}$ reveals a slight broadening and red-shift in the maximum excitation wavelength range. Moreover, some weak vibronic structure can be discerned over excitation wavelengths of 400–450 nm and corresponding to emission at approximately 495 nm and 520 nm.

Emission spectra of the yellow solution excited at 575 nm are similar to those of closed CG1-94 (Figure 6.11(b)), which is further evidence that the yellow solution arises from CG1-94. Excitation of the by-product at 478 nm produces quite distinct emission spectra (Figure 6.19(f)). At $T \approx 300\,\mathrm{K}$ the emission band is very broad (500–800 nm) while, at $T \approx 77\,\mathrm{K}$, the band is noticeably narrower (520–700 nm) with a much more defined

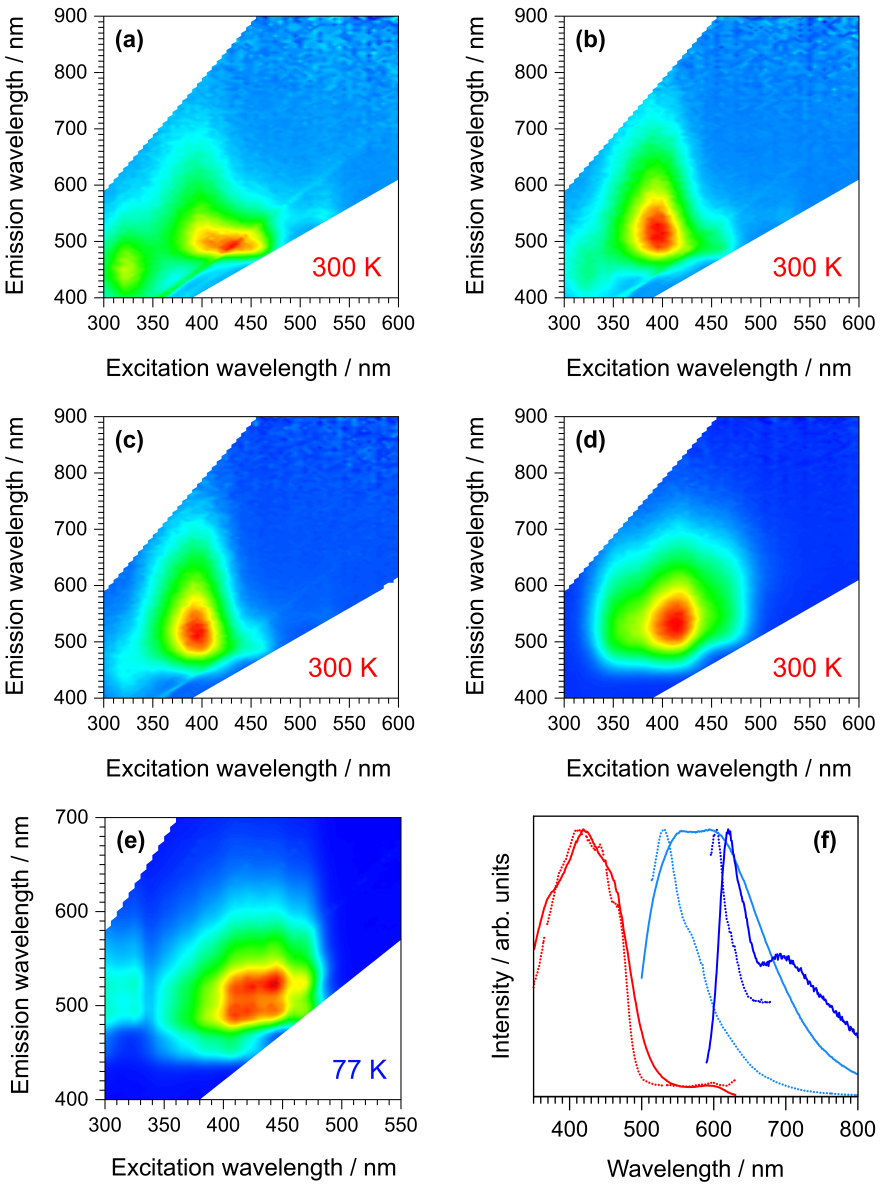


Figure 6.19: Excitation-emission (XM) maps of CG1-94 in methanol irradiated at 275 nm and recorded at regular time intervals. Panels **(a)**–**(c)** correspond to time after irradiation: **(a)** 5 minutes, **(b)** 30 minutes, and **(c)** 55 minutes. Panels **(d)** and **(e)** show the XM maps of the CG1-94 by-product at $T \approx 300\,\mathrm{K}$ and $T \approx 77\,\mathrm{K}$, respectively. As a comparison, **(f)** gives the excitation (red) and emission (blue) spectra of the CG1-94 by-product at $T \approx 300\,\mathrm{K}$ (solid lines) and $T \approx 77\,\mathrm{K}$ (dotted lines). The emission spectra were excited at 575 nm (dark blue) and 478 nm (light blue), respectively. Gaps in the $T \approx 77\,\mathrm{K}$ excitation spectra are present due to removal of signal that arose from internal reflections in the spectrofluorometer setup.

peak. The flat peak of the emission band at $T \approx 300\,\mathrm{K}$ may be due to detector saturation.

In summary, the mysterious yellow solution is assigned to the CG1-94 by-product (Figure 6.18(d)). Preliminary fluorescence up-conversion measurements ($\lambda_{ex} \approx 400\,\mathrm{nm}$) indicate this by-product has a decay constant exceeding 100 ps. This is supported by time-resolved emission measurements ($\lambda_{ex} = 478\,\mathrm{nm}$), which yield decay constants of $\approx$0.5 ns at $T \approx 300\,\mathrm{K}$ and $\approx$5 ns at $T \approx 77\,\mathrm{K}$. On 478 nm excitation at $T \approx 77\,\mathrm{K}$, the by-product decay constant, is approximately double that of the closed isomer excited at 575 nm. The ease with which this by-product forms, compared with the other DTE solutions, suggests that CG1-94 is very sensitive to UV irradiation and is hence expected to exhibit low fatigue resistance to photoswitching.

6.4.7 Fatigue

A key property of ideal photoswitches is fatigue resistance. The fatigue coordinate (formation of the by-product shown in Figure 6.2) of compounds CG1-107 and CG1-94 were probed over a number of cyclisation and cycloreversion cycles. The solution was first irradiated at 275 nm for 5 minutes (cyclisation) and, immediately following this, an absorption spectrum of the resulting blue solution recorded. The blue solution was then irradiated at 590 nm for 35 minutes (cycloreversion) and a further absorption spectrum measured. This process was repeated multiple times. Irradiation of the open-isomer solutions at 275 nm for five minutes produced an obvious colour change, indicating cyclisation had taken place. Achieving cycloreversion required a much longer irradiation time. After 35 minutes of irradiation at 590 nm, the solution appeared colourless to the naked eye, although there was still a small band associated with the closed isomer (500–600 nm) in the absorption spectrum. The irradiation time needed to achieve full cycloreversion to the open isomer would have likely been so long that multiple switching cycles would have been impracticable. Therefore, irradiation at 590 nm for 35 minutes was deemed sufficient.

The measured absorption spectra of the CG1-107 open- and closed-isomer (Figure 6.20) showed no obvious changes over the eleven switching cycles. This is to be expected, as DTEs with comparable structures have been shown to withstand more than 850 switching cycles.[13] The absorbance of the band centred about 600 nm fluctuated over the switching cycles; however there was no clear trend to the changes (Figure 6.20(c)).

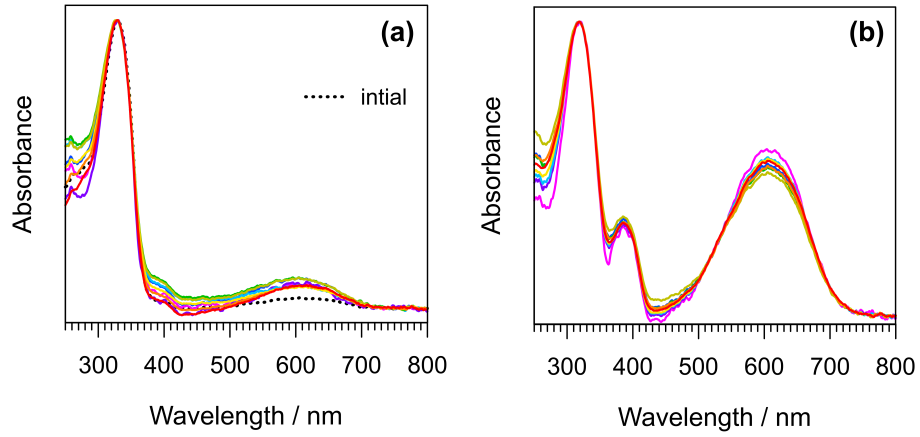


Figure 6.20: A solution of open-antiparallel CG1-107 (initial) was alternately irradiated at **(b)** 275 nm (5 mins) and **(a)** 590 nm (35 mins), and absorption spectra recorded after each irradiation.

This suggests that, for CG1-107, many more switching cycles would be required to show a noticeable change in absorption spectrum. For a functional photoswitch, high fatigue resistance means that the switching cycle can be repeated many thousands of times without significantly impacting the switching performance.[8] Eleven switching cycles is far from the many thousands a functional photoswitch should be able to withstand. However, this is a promising result as it indicates that CG1-107 has some level of fatigue resistance.

Compared with CG1-107, CG1-94 degrades much faster (Section 6.4.6), suggesting that it has a very low fatigue resistance. In the open-isomer absorption spectrum, a peak around 380 nm clearly develops linearly within the first few complete switching cycles (Figure 6.21(c)). The 380 nm and 575 nm bands of the closed-isomer absorption spectrum also follow linear growth and decay trends, respectively (Figure 6.21(d)). This indicates that the formation of the 380 nm band occurs at the detriment to the blue 575 nm band. This further supports the assignment that the yellow solution contains the CG1-94 by-product. As seen in Figure 6.18(b), the by-product forms after a single exposure of the sample to UV radiation and the resulting decay of the closed form is dominated by thermal decomposition. On the other hand, repeated switching between the closed- and open-isomers (Figure 6.21) drives photochemical decomposition. However, although it is clear that the closed-isomer of CG1-94 is decomposing, it is difficult to disentangle the thermal and photochemical contributions, to either 'resting' or

switching decomposition. This is because by-product formation is complex and involves multiple photochemical and thermal pathways, as shown by previous computational studies (Figure 6.14).[49–51] Potential energy surfaces for these processes (one example shown in Figure 6.14(b)) indicate numerous transition states and conical intersection seams, which are altered with functional group substitution and solvation (*e.g.* polar *versus* non-polar).[13] This high degree of complexity requires systematic experiments to

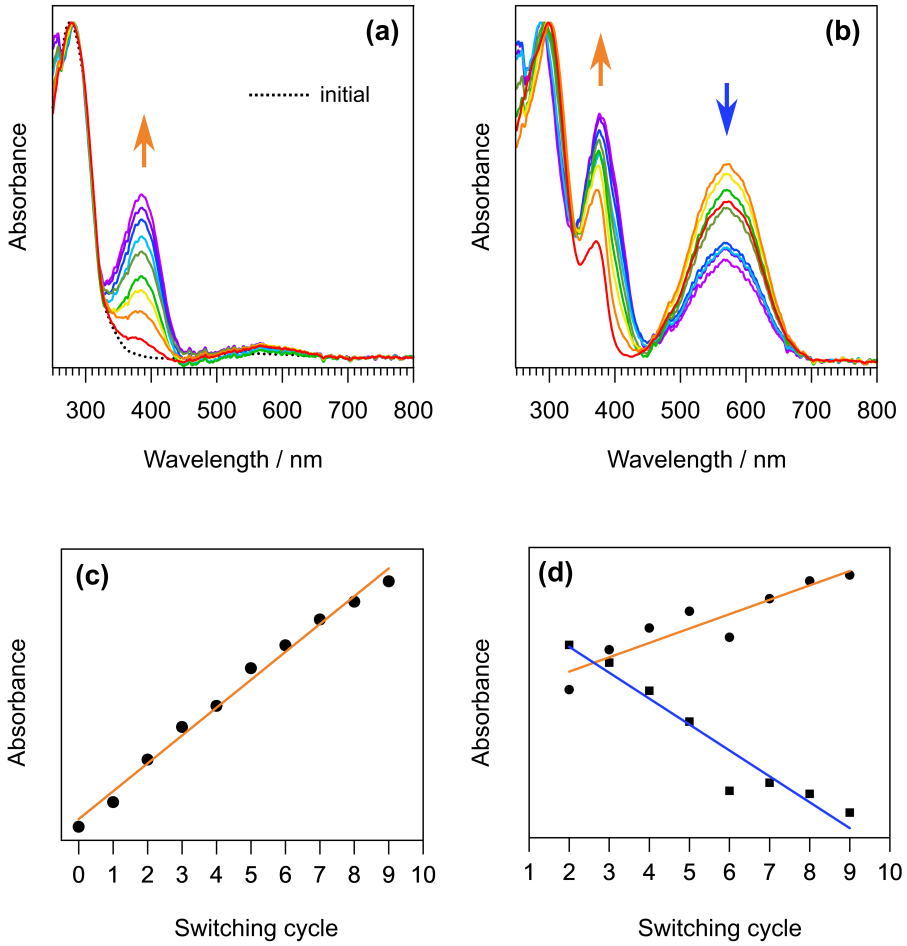


Figure 6.21: A solution of open-antiparallel CG1-94 (initial) was alternately irradiated at **(b)** 275 nm (5 mins) and **(a)** 590 nm (35 mins) and absorption spectra recorded after each irradiation. The change in absorbance of **(c)** the 380 nm (yellow) band from the 590 nm spectrum, plotted as a function of switching cycle, showed an increasing linear trend. The change in absorbance of **(d)** the 380 nm (yellow) and 575 nm (blue) bands from the 275 nm spectrum, plotted as a function of switching cycle, also follow linear trends (increasing and decreasing, respectively).

establish trends in by-product formation and "rules of thumb" for desirable synthetic strategies and photoswitch frameworks.

In addition to fatigue by repeated photoswitching (some DTEs can undergo more than 10000 switching cycles with minimal degradation), a previous study by Irie and co-workers[35] showed that structures comparable to NS2-24 decay in less than 500 cycles, due to oxidised product formation in the presence of oxygen. Therefore, the eight DTEs of interest may degrade both by oxidation and photoswitching, although the relative contributions of these effects would depend on the compound's structure. This is because there is a clear correlation between DTE substituents/functionalisation and the fatigue resistance of the compound.[13,35] To understand the formation of the CG1-94 by-product more fully, system behaviour should be monitored over a long timescale and over many hundreds of switching cycles.

6.5 Conclusion and future work

The computational and experimental data detailed in this chapter are preliminary results which will be used to inform and direct future work. Geometry optimisation calculations show initial solvation of NS2-22 preferentially occurring through fluorine-methanol electrostatic interactions, with subsequent methanol molecules forming an electrostatic network with the preceding molecules. TD-DFT calculations, using implicit and explicit descriptions of methanol, yield a computed vertical excitation wavelength of ≈466 nm (three explicit methanol molecules), compared with an experimental value of $\lambda_{max} \approx 520$ nm. It is concluded that three explicit methanol molecules are adequate to describe the microsolvation of NS2-22 at the TD-ωB97X-D/cc-pVDZ level of theory, whilst accepting that the experimental vertical excitation wavelength will not be replicated using this method.

As shown in previous studies,[8,25,26] the functionalisation of the core DTE unit dictates the absorption and fluorescent properties of the compound, with greater conjugation producing a red-shifted absorption maximum. Of the eight compounds investigated, CG1-94 presented the lowest fatigue resistance, as both absorption spectra and excitation-emission maps of the closed isomer showed rapid by-product formation. Time-resolved fluorescence emission measurements revealed decay constants on the order of nanoseconds. The 3–4 ns cycloreversion time constants in methanol are an order of magnitude larger than those in the literature (measured in hexane), ascribed to the greater

solvent polarity changing (increasing) the S_1 barrier to ring opening. The similarity in lifetimes at $T \approx 300\,\mathrm{K}$ and $\approx 77\,\mathrm{K}$ suggest these experiments probe different fractions of the multiple competitive deactivation pathways. Further studies of the cycloreversion dynamics would benefit from temperature-dependent studies probing the correlation between excited-state lifetimes and isomerisation quantum yields.

Future work will include more rigorous investigation of the DTE fatigue coordinates, in addition to measuring photoswitching quantum yields (and fatigue efficiency) in various solvents. For example, on-line ion-mobility mass-spectrometry on irradiated and photoswitched solutions would permit monitoring of by-product formation (fatigue). Ion-mobility spectrometry separates ionic isomers (formed by electrospray ionisation) by shape (through collisions with a buffer gas), thus permitting individual isomers to be studied.[52] Absolute yields can be measured by conventional methods, but ion-mobility spectrometry can be used to measure relative quantum yields (including of the by-product) in a high-throughput manner. Other techniques, such as NMR or IR spectroscopy, are difficult to use due to multiple isomers and congested spectral signatures. Furthermore, NMR is difficult to deploy as on-line techniques and IR lacks spectral resolution.

References

[1] M. Irie and M. Mohri, *J. Org. Chem.*, 1988, **53**, 803–808.

[2] S. Nakamura and M. Irie, *J. Org. Chem.*, 1988, **53**, 6136–6138.

[3] H. G. Heller and J. R. Langan, *J. Chem. Soc., Perkin Trans. 2*, 1981, 341–343.

[4] M. Irie and M. Morimoto, in *Photochemistry*, Royal Society of Chemistry, 2019, pp. 457–497.

[5] S. Helmy, F. A. Leibfarth, S. Oh, J. E. Poelma, C. J. Hawker and J. R. de Alaniz, *J. Am. Chem. Soc.*, 2014, **136**, 8169–8172.

[6] S. Helmy, S. Oh, F. A. Leibfarth, C. J. Hawker and J. R. de Alaniz, *J. Org. Chem.*, 2014, **79**, 11316–11329.

[7] P. R. Hania, A. Pugzlys, L. N. Lucas, J. J. D. de Jong, B. L. Feringa, J. H. van Esch, H. T. Jonkman and K. Duppen, *J. Phys. Chem. A*, 2005, **109**, 9437–9442.

[8] M. Irie, T. Fukaminato, K. Matsuda and S. Kobatake, *Chem. Rev.*, 2014, **114**, 12174–12277.

[9] P. R. Hania, R. Telesca, L. N. Lucas, A. Pugzlys, J. van Esch, B. L. Feringa, J. G. Snijders and K. Duppen, *J. Phys. Chem. A*, 2002, **106**, 8498–8507.

[10] H. Miyasaka, S. Araki, A. Tabata, T. Nobuto, N. Malaga and M. Irie, *Chem. Phys. Lett.*, 1994, **230**, 249–254.

[11] Y. Nakayama, K. Hayashi and M. Irie, *J. Org. Chem.*, 1990, **55**, 2592–2596.

[12] A. Staykov and K. Yoshizawa, *J. Phys. Chem. C*, 2009, **113**, 3826–3834.

[13] M. Herder, B. M. Schmidt, L. Grubert, M. Pätzel, J. Schwarz and S. Hecht, *J. Am. Chem. Soc.*, 2015, **137**, 2738–2747.

[14] S. Fredrich, R. Göstl, M. Herder, L. Grubert and S. Hecht, *Angew. Chem. - Int. Ed.*, 2015, **55**, 1208–1212.

[15] A. A. Beharry and G. A. Woolley, *Chem. Soc. Rev.*, 2011, **40**, 4422–4437.

[16] P. Vandewyer, J. Hoefnagels and G. Smets, *Tetrahedron*, 1969, **25**, 3251–3266.

[17] M. Gagliardi, F. Pignatelli and V. Mattoli, *Sens. Actuators Phys.*, 2020, **302**, 111804.

[18] S. Shim, T. Joo, S. C. Bae, K. S. Kim and E. Kim, *J. Phys. Chem. A*, 2003, **107**, 8106–8110.

[19] S. Shim, I. Eom, T. Joo, E. Kim and K. S. Kim, *J. Phys. Chem. A*, 2007, **111**, 8910–8917.

[20] Y. Ishibashi, M. Fujiwara, T. Umesato, H. Saito, S. Kobatake, M. Irie and H. Miyasaka, *J. Phys. Chem. C*, 2011, **115**, 4265–4272.

[21] Y. Ishibashi, T. Umesato, S. Kobatake, M. Irie and H. Miyasaka, *J. Phys. Chem. C*, 2012, **116**, 4862–4869.

[22] T. Sumi, Y. Takagi, A. Yagi, M. Morimoto and M. Irie, *Chem. Commun.*, 2014, **50**, 3928–3930.

[23] K. Seo, I. Eom, S. Shim, C. H. Kim and T. Joo, *Bull. Korean Chem. Soc.*, 2019, **40**, 352–358.

[24] M. Irie, K. Sakemura, M. Okinaka and K. Uchida, *J. Org. Chem.*, 1995, **60**, 8305–8309.

[25] K. Higashiguchi, K. Matsuda, Y. Asano, A. Murakami, S. Nakamura and M. Irie, *Eur. J. Org. Chem.*, 2005, **2005**, 91–97.

[26] T. Yamaguchi and M. Irie, *J. Mater. Chem*, 2006, **16**, 4690–4694.

[27] H. Sotome, K. Une, T. Nagasaka, S. Kobatake, M. Irie and H. Miyasaka, *J. Chem. Phys.*, 2020, **152**, 034301.

[28] D. Guillaumont, T. Kobayashi, K. Kanda, H. Miyasaka, K. Uchida, S. Kobatake, K. Shibata, S. Nakamura and M. Irie, *J. Phys. Chem. A*, 2002, **106**, 7222–7227.

[29] Y. Ishibashi, T. Umesato, M. Fujiwara, K. Une, Y. Yoneda, H. Sotome, T. Katayama, S. Kobatake, T. Asahi, M. Irie and H. Miyasaka, *J. Phys. Chem. C*, 2016, **120**, 1170–1177.

[30] M. Boggio-Pasqua, M. Ravaglia, M. J. Bearpark, M. Garavelli and M. A. Robb, *J. Phys. Chem. A*, 2003, **107**, 11139–11152.

[31] S. Nakamura, K. Uchida and M. Hatakeyama, *Molecules*, 2013, **18**, 5091–5103.

[32] J. Ern, A. Bens, H.-D. Martin, S. Mukamel, D. Schmid, S. Tretiak, E. Tsiper and C. Kryschi, *Chem. Phys.*, 1999, **246**, 115–125.

[33] H. Sotome, H. Okajima, T. Nagasaka, Y. Tachii, A. Sakamoto, S. Kobatake, M. Irie and H. Miyasaka, *ChemPhysChem*, 2020, **21**, 1485–1485.

[34] R. Iwai, M. Morimoto and M. Irie, *Photoch. Photobio. Sci.*, 2020, **19**, 783–789.

[35] M. Irie, T. Lifka, K. Uchida, S. Kobatake and Y. Shindo, *Chem. Commun.*, 1999, 747–750.

[36] J. J. D. de Jong, L. N. Lucas, R. Hania, A. Pugzlys, R. M. Kellogg, B. L. Feringa, K. Duppen and J. H. van Esch, *Eur. J. Org. Chem.*, 2003, **2003**, 1887–1893.

[37] S. Kobatake, Y. Terakawa and H. Imagawa, *Tetrahedron*, 2009, **65**, 6104–6108.

[38] M. J. Frisch, G. W. Trucks, H. B. Schlegel, G. E. Scuseria, M. A. Robb, J. R. Cheeseman, G. Scalmani, V. Barone, G. A. Petersson, H. Nakatsuji, X. Li, M. Caricato, A. V. Marenich, J. Bloino, B. G. Janesko, R. Gomperts, B. Mennucci, H. P. Hratchian, J. V. Ortiz, A. F. Izmaylov, J. L. Sonnenberg, D. Williams-Young, F. Ding, F. Lipparini, F. Egidi, J. Goings, B. Peng, A. Petrone, T. Henderson, D. Ranasinghe, V. G. Zakrzewski, J. Gao, N. Rega, G. Zheng, W. Liang, M. Hada, M. Ehara, K. Toyota, R. Fukuda, J. Hasegawa, M. Ishida, T. Nakajima, Y. Honda, O. Kitao, H. Nakai, T. Vreven, K. Throssell, J. A. Montgomery, Jr., J. E. Peralta, F. Ogliaro, M. J. Bearpark, J. J. Heyd, E. N. Brothers, K. N. Kudin, V. N. Staroverov, T. A. Keith, R. Kobayashi, J. Normand, K. Raghavachari, A. P. Rendell, J. C. Burant, S. S. Iyengar, J. Tomasi, M. Cossi, J. M. Millam, M. Klene, C. Adamo, R. Cammi, J. W. Ochterski, R. L. Martin, K. Morokuma, O. Farkas, J. B. Foresman and D. J. Fox, *Gaussian 16 Revision B.01*, 2016, Gaussian Inc. Wallingford CT.

[39] J.-D. Chai and M. Head-Gordon, *Phys. Chem. Chem. Phys.*, 2008, **10**, 6615–6620.

[40] J.-D. Chai and M. Head-Gordon, *J. Chem. Phys.*, 2008, **128**, 084106.

[41] T. H. Dunning, *J. Chem. Phys.*, 1989, **90**, 1007–1023.

[42] M. Kállay, P. R. Nagy, D. Mester, Z. Rolik, G. Samu, J. Csontos, J. Csóka, P. B. Szabó, L. Gyevi-Nagy, B. Hégely, I. Ladjánszki, L. Szegedy, B. Ladóczki, K. Petrov, M. Farkas, P. D. Mezei and Á. Ganyecz, *MRCC, a quantum chemical program suite*, See www.mrcc.hu.

[43] M. Kállay, P. R. Nagy, D. Mester, Z. Rolik, G. Samu, J. Csontos, J. Csóka, P. B. Szabó, L. Gyevi-Nagy, B. Hégely, I. Ladjánszki, L. Szegedy, B. Ladóczki, K. Petrov, M. Farkas, P. D. Mezei and Á. Ganyecz, *J. Chem. Phys.*, 2020, **152**, 074107.

[44] D. Mester, P. R. Nagy and M. Kállay, *J. Chem. Theory Comput.*, 2019, **15**, 6111–6126.

[45] D. Mester and M. Kállay, *J. Chem. Theory Comput.*, 2019, **15**, 4440–4453.

[46] D. Mester, P. R. Nagy and M. Kállay, *J. Chem. Phys.*, 2018, **148**, 094111.

[47] D. Mester, P. R. Nagy and M. Kállay, *J. Chem. Phys.*, 2017, **146**, 194102.

[48] *CRC Handbook of Chemistry and Physics*, ed. W. M. Haynes, CRC Press, Boca Raton, Florida, 97th edn., 2017.

[49] J. R. Matis, J. B. Schönborn and P. Saalfrank, *Phys. Chem. Chem. Phys.*, 2015, **17**, 14088–14095.

[50] D. Mendive-Tapia, A. Perrier, M. J. Bearpark, M. A. Robb, B. Lasorne and D. Jacquemin, *Phys. Chem. Chem. Phys.*, 2014, **16**, 18463–18471.

[51] P. D. Patel, I. A. Mikhailov, K. D. Belfield and A. E. Masunov, *Int. J. Quantum Chem.*, 2009, **109**, 3711–3722.

[52] J. N. Bull, E. Carrascosa, M. S. Scholz, N. J. A. Coughlan and E. J. Bieske, *The Analyst*, 2017, **142**, 2100–2103.

Chapter 7

Summary

The photophysics of selected natural and synthetic photoswitches (pCK$^-$, derivatives of pHBDI$^-$, and functionalised DTEs) have been investigated using computational methods alongside solution- and gas-phase spectroscopic techniques. The overarching goals were to ascertain environmental impacts on the intrinsic absorption profiles and ensuing excited state dynamics.

Chapter 4 discusses the application of the betaine binding strategy (emulating some protein properties) to several pHBDI$^-$ derivatives, exploring the electrochromic betaine-induced shifts using photodissociation action spectroscopy. Computational SAPT analysis was used to determine the dominant binding interactions in the pHBDI$^-$-betaine complexes, showing that, while the predominant contribution is from electrostatic forces, induction and dispersion forces also play a role. The ability of a full quantum mechanical (coupled cluster) and various point-charge methods to replicate the action spectra maxima were compared, proving that point-charge modelling of betaine is inadequate in this system. The established computational protocol can be applied to other anion-betaine, or presumably anion-solvent, complexes.

Chapter 5 explores the solution- and gas-phase dynamics of pCK$^-$, probed by several state-of-the-art spectroscopic techniques and computational measurements to explore the effect of solvation on the excited-state potential energy surface leading to $E \rightarrow Z$ isomerisation. A strong viscosity dependence in excited-state lifetime was observed, with chromophore microsolvation being the critical factor in dictating lifetime for mixed solvents. Computational methods for replicating solvated vertical excitation energies and for mapping the potential energy surface were assessed, indicating the need for both implicit and explicit solvation, and showing the presence of an excited-state barrier, respectively. Future work aims to fully optimise the excited-state potential energy surface, conical intersection, and barrier height, the latter of which can be compared with gas-phase spectroscopic data.

Chapter 6 describes some of the photoswitch properties (such as excited-state lifetime) of synthetic dithyenylethene (DTE) molecules, probed by spectroscopic techniques in solution and by computational methods to replicate solvated vertical excitation energies. These preliminary data on DTE photophysical properties will be expanded on in the future by further solution-phase measurements (such as photoisomerisation quantum yield) and gas-phase measurements, for which the solution-phase data is required for comparison. Furthermore, the photophysics of the more technologically applicable polymeric forms of the DTEs studied in this thesis will be explored in solution, requiring reference data on the monomeric forms.

Chapters 4 and 5 investigate the photophysics of models for naturally occurring chromophores that undergo *E*-*Z* photoisomerisation in solution and the gas-phase. Both chapters consider the level of theory required to replicate experimental data. For these anionic compounds with considerable charge-transfer character in the $S_1 \leftarrow S_0$ transition, it is clear that "solvent" molecules (*i.e.* betaine in Ch.4 and water in Ch.5) must be described fully to account for the specific solvent-solute interactions. Comparatively, greater approximations for solvation can be made for the synthetic DTE photoswitches, attributed to the absence of a charge site and differing charge-transfer character.

Appendix

A1 Photophysics of pCK$^-$

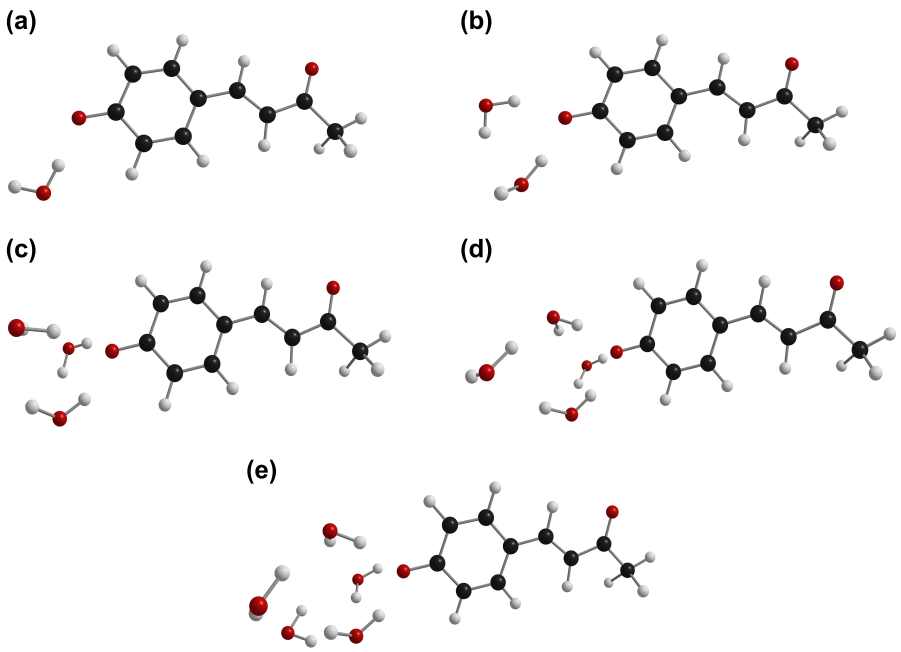


Figure A1.1: Lowest energy structures of anionic *para*-coumaric ketone (pCK$^-$) solvated with **(a)**–**(e)** 1–5 water molecules, at the ωB97X-D/aug-cc-pVDZ level of theory, in Gaussian 16B.01.

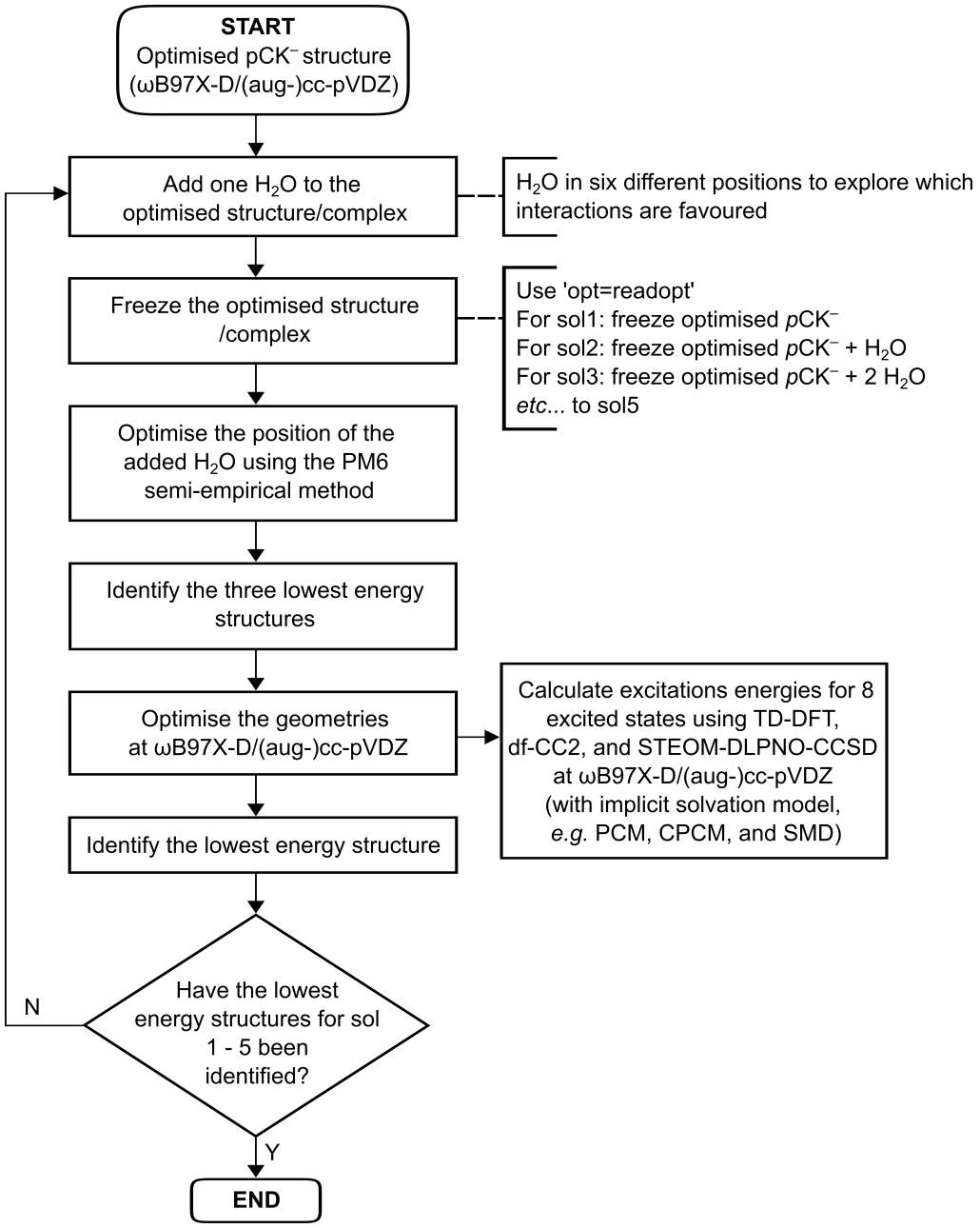


Figure A1.2: Computational process by which the effect of explicit solvation of pCK$^-$ was explored. All calculations were performed in Gaussian 16B.01.

Table A1.1: Energies of the various geometries of pCK$^-$ solvated with 1–5 water molecules, obtained from calculations at the PM6/aug-cc-pVDZ and ωB97X-D/aug-cc-pVDZ levels of theory, in Gaussian 16B.01. ΔE(DFT) is the difference in energy of the solvated forms relative to the most stable form. The darker shading indicates the most stable geometries for the respective solvations.

1 H_2O	**sol1.0**	**sol1.1**	**sol1.2**	**sol1.3**
E(PM6) / au	-0.26038	-0.25640	-0.26034	0.25530
E(DFT) / au	-613.3081	-613.3048	-613.3076	-
ΔE(DFT) / kJ mol^{-1} (eV)	0.00	8.73 (0.09)	1.20 (0.01)	-
2 H_2O	**sol2.0**	**sol2.1**	**sol2.2**	**sol2.3**
E(PM6) / au	-0.36660	-0.36660	-0.36144	-0.36660
E(DFT) / au	-689.7491	-689.7491	-	-689.7491
ΔE(DFT) / kJ mol^{-1} (eV)	0.00	0.00	0.00	
3 H_2O	**sol3.0**	**sol3.1**	**sol3.2**	**sol3.3**
E(PM6) / au	-0.47304	-0.46935	-0.46722	-0.47304
E(DFT) / au	-	-766.1858	-766.1858	-766.1914
ΔE(DFT) / kJ mol^{-1} (eV)	-	14.72 (0.15)	14.63 (0.15)	0.00
4 H_2O	**sol4.0**	**sol4.1**	**sol4.2**	**sol4.3**
E(PM6) / au	-0.57452	-0.57404	-0.57410	-0.57300
E(DFT) / au	-842.6309	-842.6276	-842.6278	-842.6273
ΔE(DFT) / kJ mol^{-1} (eV)	0.00	8.51 (0.09)	8.01 (0.08)	9.21(0.10)
5 H_2O	**sol5.0**	**sol5.1**	**sol5.2**	**sol5.3**
E(PM6) / au	-0.67597	-0.67436	-0.67459	-0.67459
E(DFT) / au	-919.0669	-	-919.0668	-919.0668
ΔE(DFT) / kJ mol^{-1} (eV)	0.00	-	0.4 (0.004)	0.4 (0.004)

Table A1.2: Excitation energies of the first eight excited states of pCK$^-$ obtained from MRCC calculations, at the df-CC2/aug-cc-pVDZ and df-CC2/aug-cc-pVTZ levels of theory, and TD-DFT calculations (in Gaussian 16B.01), at the ωB97X-D/aug-cc-pVDZ and ωB97X-D/aug-cc-pVTZ levels of theory. The oscillator strengths (f) are highlighted by their relative magnitudes, where green indicates a large value.

Exc state	**Method**	**E$_{exc}$ / nm**	***f***	**Method**	**E$_{exc}$ / nm**	***f***
1	TD-DFT	377	0.94	MRCC	420	0.00
2	*aug-cc-pVDZ*	328	0.00	*aug-cc-pVDZ*	405	1.22
3		307	0.00		370	0.00
4		306	0.00		356	0.00
5		304	0.00		326	0.00
6		294	0.00		319	0.00
7		272	0.00		316	0.00
8		267	0.00		316	0.00
1	TD-DFT	378	0.94	MRCC	421	0.00
2	*aug-cc-pVTZ*	339	0.00	*aug-cc-pVTZ*	397	0.00
3		320	0.00		365	1.19
4		308	0.00		360	0.00
5		306	0.00		354	0.00
6		304	0.00		324	0.17
7		289	0.07		321	0.00
8		285	0.00		319	0.00

Table A1.3: Excitation energies of the first eight excited states of pCK$^-$, with PCM (water), obtained from MRCC calculations, at the df-CC2/aug-cc-pVDZ and df-CC2/aug-cc-pVTZ levels of theory, and TD-DFT calculations (in Gaussian 16B.01), at the ωB97X-D/aug-cc-pVDZ and ωB97X-D/aug-cc-pVTZ levels of theory. The oscillator strengths (f) are highlighted by their relative magnitudes, where green indicates a large value.

Exc state	**Method**	**E$_{exc}$ / nm**	***f***	**Method**	**E$_{exc}$ / nm**	***f***
1	TD-DFT	383	1.06	MRCC	396	1.21
2	*aug-cc-pVDZ*	308	0.00	*aug-cc-pVDZ*	319	0.01
3		283	0.08		307	0.10
4		278	0.00		297	0.00
5		267	0.00		293	0.00
6		240	0.00		266	0.00
7		239	0.00		265	0.03
8		237	0.09		245	0.00
1	TD-DFT	383	1.06	MRCC	398	1.20
2	*aug-cc-pVTZ*	308	0.00	*aug-cc-pVTZ*	319	0.01
3		283	0.08		308	0.10
4		278	0.00		293	0.00
5		270	0.00		289	0.00
6		243	0.00		260	0.21
7		242	0.00		259	0.00
8		237	0.08		248	0.00

Table A1.4: Excitation energies of the first eight excited states of the three lowest energy structures of pCK$^-$ solvated by one explicit water molecule. Of the three, sol1.0 is the most stable. Along with the explicit solvation, PCM was included for the second row results. Obtained from TD-DFT calculations at the ωB97X-D/aug-cc-pVDZ level of theory, in Gaussian 16B.01. The oscillator strengths (f) are highlighted by their relative magnitudes, where green indicates a large value.

Exc state	**Structure**	**E_{exc} / nm**	***f***	**Structure**	**E_{exc} / nm**	***f***	**Structure**	**E_{exc} / nm**	***f***
1	**sol1.0**	365	0.92	**sol1.1**	380	1.01	**sol1.2**	372	0.94
2	*no PCM*	307	0.00		313	0.01		310	0.00
3		301	0.00		311	0.00		309	0.01
4		293	0.00		295	0.00		282	0.07
5		283	0.07		285	0.00		282	0.00
6		275	0.00		283	0.07		278	0.00
7		272	0.00		279	0.00		277	0.00
8		262	0.00		263	0.00		257	0.00
1	**sol1.0**	366	1.03	**sol1.1**	390	1.13	**sol1.2**	374	1.05
2	*with PCM*	304	0.00		291	0.00		312	0.00
3		281	0.08		284	0.00		280	0.07
4		260	0.01		280	0.07		258	0.07
5		255	0.00		262	0.01		258	0.00
6		234	0.00		241	0.08		236	0.11
7		234	0.11		236	0.00		232	0.00
8		232	0.00		235	0.00		231	0.00

Table A1.5: Excitation energies of the first eight excited states of the three lowest energy structures of pCK$^-$ solvated by two explicit water molecules. Of the three, sol2.3 is the most stable. Along with the explicit solvation, PCM was included for the second row results. Obtained from TD-DFT calculations at the ωB97X-D/aug-cc-pVDZ level of theory, in Gaussian 16B.01. The oscillator strengths (f) are highlighted by their relative magnitudes, where green indicates a large value.

Exc state	**Structure**	**E_{exc} / nm**	***f***	**Structure**	**E_{exc} / nm**	***f***	**Structure**	**E_{exc} / nm**	***f***
1	**sol2.0**	359	0.93	**sol2.1**	359	0.93	**sol2.3**	359	0.93
2	*no PCM*	305	0.00		305	0.00		305	0.00
3		292	0.00		292	0.00		292	0.00
4		280	0.06		280	0.06		280	0.06
5		274	0.00		273	0.00		273	0.00
6		261	0.00		262	0.00		261	0.00
7		260	0.00		260	0.00		260	0.00
8		251	0.01		251	0.01		251	0.01
1	**sol2.0**	359	1.04	**sol2.1**	359	1.04	**sol2.3**	359	1.04
2	*with PCM*	306	0.00		306	0.00		306	0.00
3		278	0.07		278	0.07		278	0.07
4		254	0.01		254	0.01		254	0.01
5		245	0.00		244	0.00		245	0.00
6		233	0.12		233	0.12		233	0.12
7		289	0.00		289	0.00		289	0.00
8		227	0.00		227	0.00		227	0.00

Table A1.6: Excitation energies of the first eight excited states of the three lowest energy structures of pCK$^-$ solvated by three explicit water molecules. Of the three, sol3.3 is the most stable. Along with the explicit solvation, PCM was included for the second row results. Obtained from TD-DFT calculations at the ωB97X-D/aug-cc-pVDZ level of theory, in Gaussian 16B.01. The oscillator strengths (f) are highlighted by their relative magnitudes, where green indicates a large value.

Exc state	**Structure**	**E_{exc} / nm**	***f***	**Structure**	**E_{exc} / nm**	***f***	**Structure**	**E_{exc} / nm**	***f***
1	**sol3.1**	356	0.93	**sol3.2**	366	1.01	**sol3.3**	353	0.94
2	*no PCM*	306	0.00		287	0.00		307	0.00
3		285	0.01		284	0.01		278	0.00
4		279	0.06		278	0.05		276	0.05
5		269	0.00		267	0.00		260	0.00
6		269	0.00		266	0.00		260	0.00
7		254	0.00		252	0.00		248	0.00
8		246	0.01		245	0.03		242	0.02
1	**sol3.1**	356	1.03	**sol3.2**	368	1.11	**sol3.3**	353	1.05
2	*with PCM*	306	0.00		291	0.00		307	0.00
3		277	0.07		277	0.06		275	0.06
4		252	0.01		251	0.01		249	0.01
5		241	0.00		250	0.00		241	0.00
6		241	0.13		237	0.12		232	0.14
7		227	0.00		227	0.00		224	0.00
8		226	0.00		226	0.00		224	0.00

Table A1.7: Excitation energies of the first eight excited states of the three lowest energy structures of pCK$^-$ solvated by four explicit water molecules. Of the three, sol4.0 is the most stable. Along with the explicit solvation, PCM was included for the second row results. Obtained from TD-DFT calculations at the ωB97X-D/aug-cc-pVDZ level of theory, in Gaussian 16B.01. The oscillator strengths (f) are highlighted by their relative magnitudes, where green indicates a large value.

Exc state	**Structure**	**E_{exc} / nm**	***f***	**Structure**	**E_{exc} / nm**	***f***	**Structure**	**E_{exc} / nm**	***f***
1	**sol4.0**	352	0.95	**sol4.1**	347	0.92	**sol4.2**	347	0.91
2	*no PCM*	307	0.00		309	0.00		309	0.00
3		276	0.04		276	0.06		276	0.05
4		276	0.01		270	0.00		266	0.00
5		259	0.00		247	0.00		252	0.00
6		250	0.00		247	0.00		247	0.00
7		246	0.00		241	0.01		237	0.02
8		241	0.02		237	0.05		236	0.02
1	**sol4.0**	352	1.05	**sol4.1**	347	1.03	**sol4.2**	347	1.01
2	*with PCM*	307	0.00		308	0.00		308	0.00
3		275	0.06		275	0.07		275	0.06
4		248	0.01		245	0.01		245	0.01
5		238	0.00		237	0.00		236	0.00
6		232	0.14		230	0.15		230	0.15
7		225	0.00		224	0.01		224	0.01
8		223	0.00		220	0.00		220	0.00

Table A1.8: Excitation energies of the first eight excited states of the three lowest energy structures of pCK$^-$ solvated by five explicit water molecules. Of the three, sol5.0 is the most stable. Along with the explicit solvation, PCM was included for the second row results. Obtained from TD-DFT calculations at the ωB97X-D/aug-cc-pVDZ level of theory, in Gaussian 16B.01. The oscillator strengths (f) are highlighted by their relative magnitudes, where green indicates a large value.

Exc state	**Structure**	**E_{exc} / nm**	***f***	**Structure**	**E_{exc} / nm**	***f***	**Structure**	**E_{exc} / nm**	***f***
1	**sol5.0**	349	0.95	**sol5.2**	360	1.03	**sol5.3**	360	1.03
2	*no PCM*	308	0.00		291	0.00		291	0.00
3		276	0.05		275	0.04		275	0.04
4		273	0.00		270	0.00		270	0.00
5		256	0.00		256	0.00		256	0.00
6		245	0.00		254	0.00		254	0.00
7		244	0.00		242	0.09		242	0.08
8		283	0.04		240	0.01		240	0.01
1	**sol5.0**	351	1.05	**sol5.2**	351	1.05	**sol5.3**	262	1.12
2	*no PCM*	307	0.00		307	0.00		293	0.00
3		275	0.06		275	0.06		274	0.05
4		248	0.01		248	0.01		246	0.01
5		236	0.00		236	0.00		244	0.00
6		232	0.14		232	0.14		234	0.13
7		225	0.00		225	0.00		255	0.00
8		223	0.00		223	0.00		222	0.00

Table A1.9: Excitation energies of the first eight excited states of the lowest energy solvated geometries (1,3, and 5 water molecules) of pCK$^-$. Obtained from MRCC calculations at the df-CC2/aug-cc-pVDZ level of theory, with PCM (water). The oscillator strengths (f) are highlighted by their relative magnitudes, where green indicates a large value.

Exc state	**Structure**	**E_{exc} / nm**	***f***	**Structure**	**E_{exc} / nm**	***f***	**Structure**	**E_{exc} / nm**	***f***
1	**sol1.0**	377	1.13	**sol3.3**	365	1.11	**-**	-	-
2		311	0.01		311	0.01		-	-
3		292	0.10		288	0.09		-	-
4		290	0.00		282	0.00		-	-
5		283	0.00		273	0.00		-	-
6		260	0.00		252	0.00		-	-
7		257	0.04		250	0.05		-	-
8		242	0.00		242	0.00		-	-
1	**sol5.0**	377	1.19	**sol5.2**	277	1.19	**sol5.3**	377	1.19
2		302	0.01		302	0.01		302	0.01
3		288	0.08		288	0.08		288	0.08
4		280	0.00		280	0.00		280	0.00
5		278	0.00		278	0.00		278	0.00
6		251	0.00		251	0.00		251	0.00
7		249	0.04		249	0.04		249	0.04
8		243	0.00		243	0.01		243	0.00

A2 Characterisation of DTEs

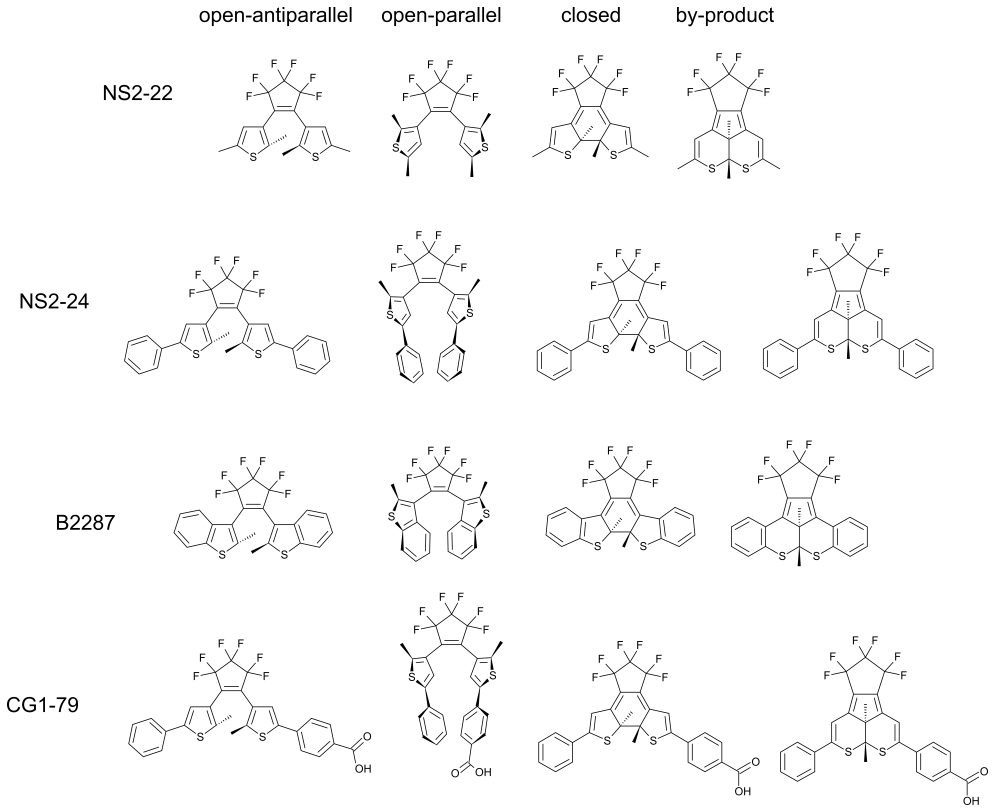


Figure A2.1: All the forms of four out of the eight dithienylethenes under investigation. Reactants (open-antiparallel, open-parallel) and products (closed, and by-product).

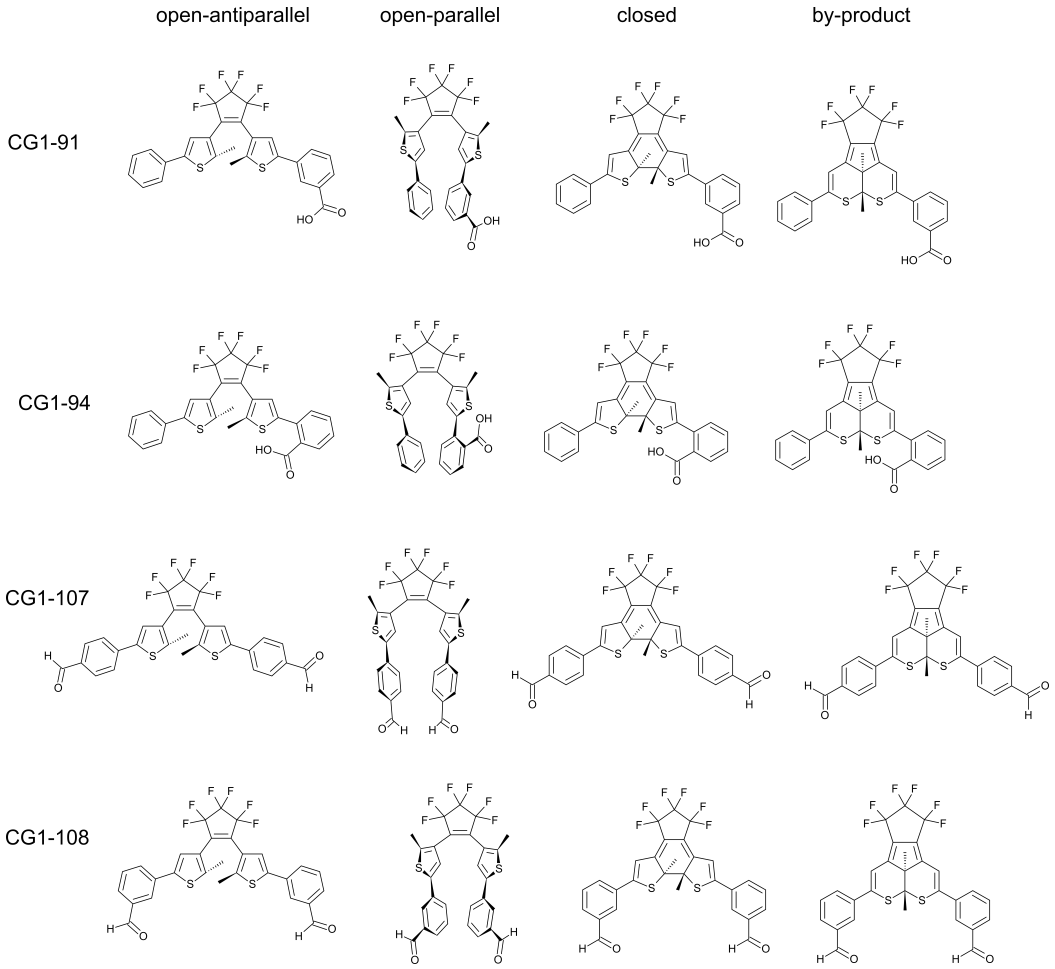


Figure A2.2: All the forms of four out of the eight dithienylethenes under investigation. Reactants (open-antiparallel, open-parallel) and products (closed, and by-product).

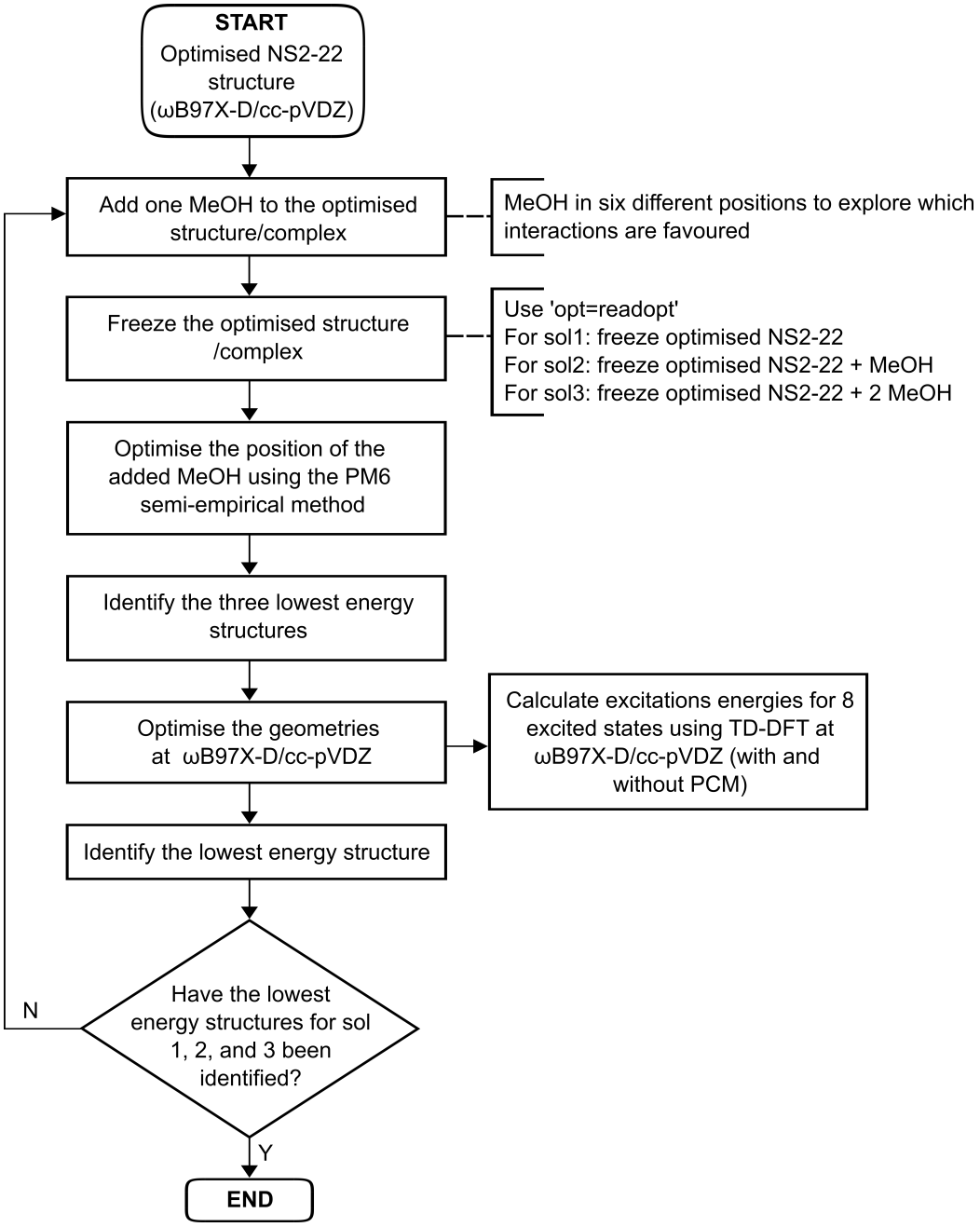


Figure A2.3: Computational process by which the effect of explicit solvation of dithienylethene NS2-22 was explored. All calculations were performed in Gaussian 16B.01.

Table A2.1: Energies of the various geometries of the singly-, doubly-, and triply-solvated antiparallel NS2-22, obtained from calculations at the PM6/cc-pVDZ and ωB97X-D/cc-pVDZ levels of theory, in Gaussian 16B.01. ΔE(DFT) is the difference in energy of the solvated forms relative to the most stable form. The darker shading indicates the most stable geometries for the respective solvations.

1 MeOH	**o-sol1.0**	**o-sol1.1**	**o-sol1.2**	**o-sol1.3**	**o-sol1.4**	**o-sol1.5**
E(PM6) / au	-0.4971	-0.4960	-0.4964	-0.4971	-0.4956	-0.4956
E(DFT) / au	-2167.080	-	-2167.074	-2167.075	-	-
ΔE(DFT) / kJ mol^{-1} (eV)	0.00	-	18.06 (0.19)	15.48 (0.16)	-	-
2 MeOH	**o-sol2.0**	**o-sol2.1**	**o-sol2.2**	**o-sol2.3**	**o-sol2.4**	**o-sol2.5**
E(PM6) / au	-0.5709	-0.5700	-0.5731	-0.5731	-0.5705	-0.5707
E(DFT) / au	-2282.782	-	-2282.786	-	-	-2282.780
ΔE(DFT) / kJ mol^{-1} (eV)	12.04 (0.13)	-	0.00	-	-	16.02 (0.17)
3 MeOH	**o-sol3.0**	**o-sol3.1**	**o-sol3.2**	**o-sol3.3**	**o-sol3.4**	**o-sol3.5**
E(PM6) / au	-0.6519	-0.6546	-0.6525	-0.6553	-0.6529	-0.6586
E(DFT) / au	-	-2398.498	-	-2398.493	-	-2398.498
ΔE(DFT) / kJ mol^{-1} (eV)	-	1.22 (0.01)	-	13.11 (0.14)	-	0.00

Table A2.2: Energies of the various geometries of the singly-, doubly-, and triply-solvated closed NS2-22, obtained from calculations at the PM6/cc-pVDZ and ωB97X-D/cc-pVDZ levels of theory, in Gaussian 16B.01. ΔE(DFT) is the difference in energy of the solvated forms relative to the most stable form. The darker shading indicates the most stable geometries for the respective solvations.

1 MeOH	**c-sol1.0**	**c-sol1.1**	**c-sol1.2**	**c-sol1.3**	**c-sol1.4**	**c-sol1.5**
E(PM6) / au	-0.5709	-0.5700	-0.5731	-0.5731	-0.5705	-0.5707
E(DFT) / au	-2167.061	-2167.056	-	-	-	-2167.058
ΔE(DFT) / kJ mol^{-1} (eV)	0.00	1.33 (0.01)	-	-	-	5.90 (0.06)
2 MeOH	**c-sol2.0**	**c-sol2.1**	**c-sol2.2**	**c-sol2.3**	**c-sol2.4**	**c-sol2.5**
E(PM6) / au	-0.5841	-0.5839	-0.5831	-0.5827	-0.5821	-0.5807
E(DFT) / au	-2282.761	-2282.771	-2282.768	-	-	-
ΔE(DFT) / kJ mol^{-1} (eV)	26.67 (0.28)	0.00	8.88 (0.09)	-	-	-
3 MeOH	**c-sol3.0**	**c-sol3.1**	**c-sol3.2**	**c-sol3.3**	**c-sol3.4**	**c-sol3.5**
E(PM6) / au	-0.6644	-0.6646	-0.6638	-0.6669	-0.6619	-0.6682
E(DFT) / au	-	-2398.472	-	-2398.475	-	-2398.478
ΔE(DFT) / kJ mol^{-1} (eV)	-	16.47 (0.17)	-	9.79 (0.10)	-	0.00

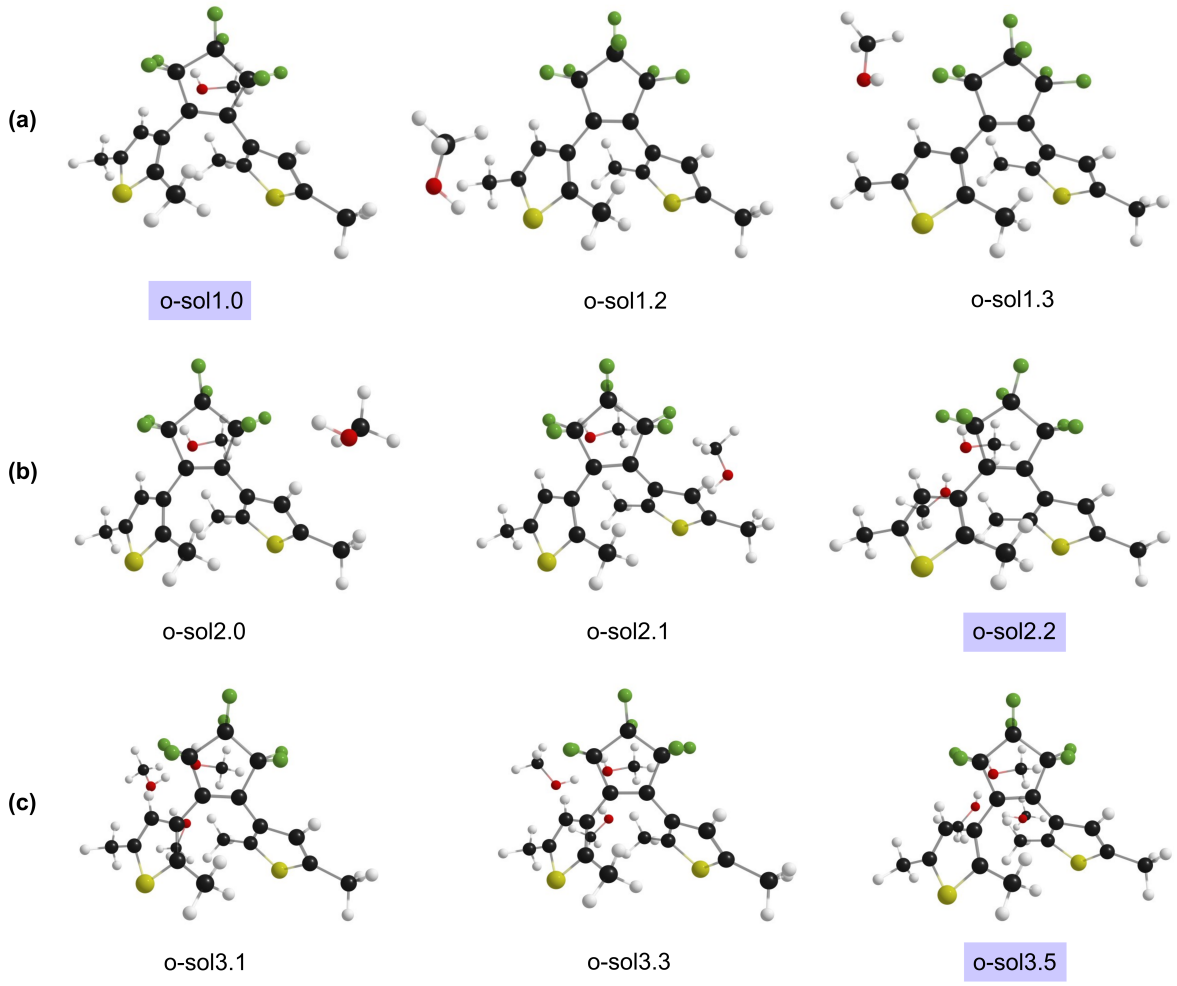


Figure A2.4: Open NS2-22 structures, optimised under explicit solvation, with **(a)** one, **(b)** two, and **(c)** three methanol molecules, at the ωB97X-D/cc-pVDZ level of theory, in Gaussian 16B.01.

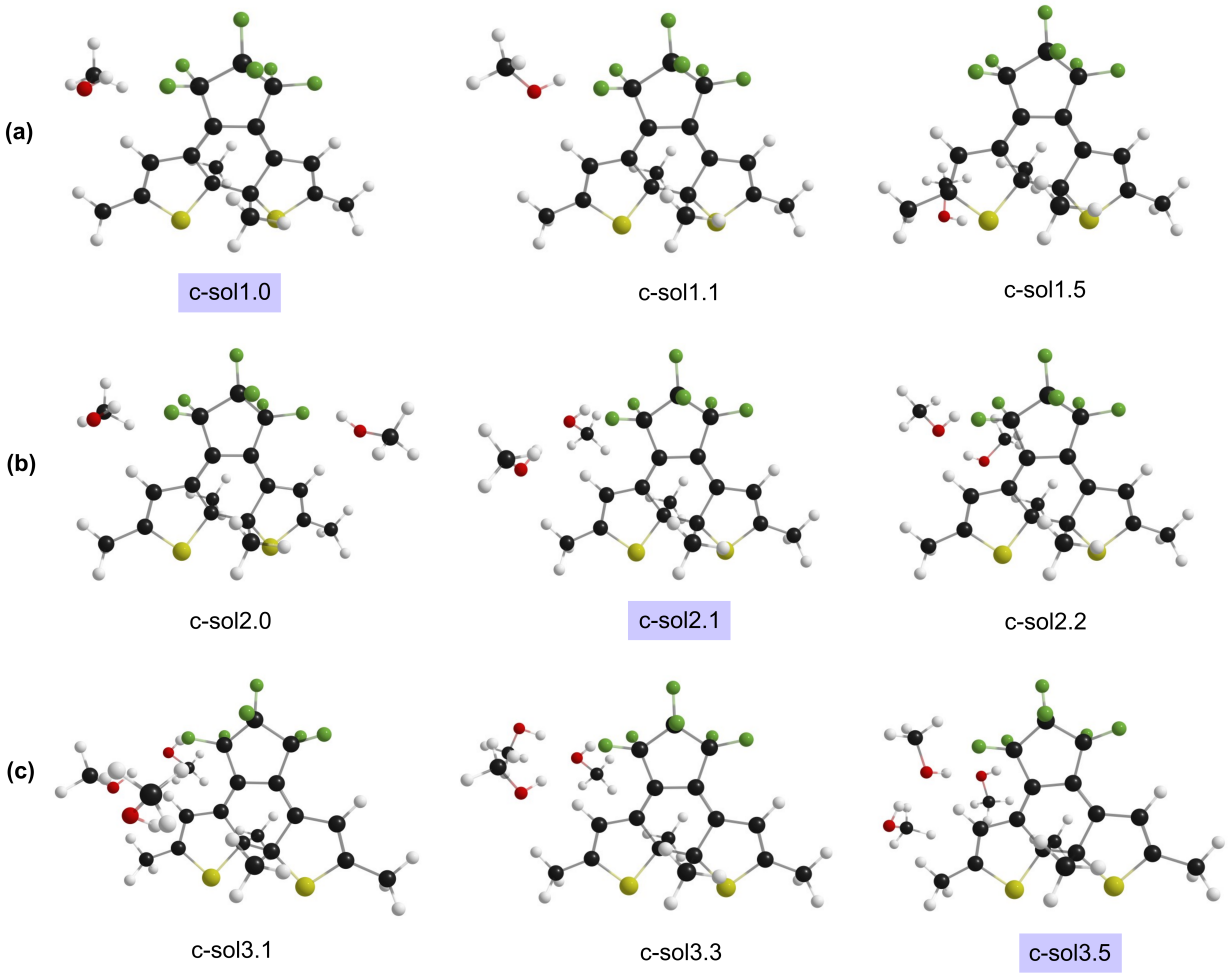


Figure A2.5: Closed NS2-22 structures, optimised under explicit solvation, with **(a)** one, **(b)** two, and **(c)** three methanol molecules, at the ωB97X-D/cc-pVDZ level of theory, in Gaussian 16B.01.

Table A2.3: Excitation energies of the first eight excited states of antiparallel (AP), parallel (PA), closed (CL), and by-product (BP) NS2-22 obtained from TD-DFT calculations at the ωB97X-D/cc-pVDZ and ωB97X-D/cc-pVTZ levels of theory, in Gaussian 16B.01. The oscillator strengths (f) are highlighted by their relative magnitudes, where green indicates a large value.

Exc state	**Species**	**E_{exc} / nm**	***f***	**Species**	**E_{exc} / nm**	***f***	**Species**	**E_{exc} / nm**	***f***
1	**AP**	286	0.17	**AP**	290	0.10	**PA**	275	0.16
2	*cc-pVDZ*	256	0.02	*cc-pVTZ*	259	0.02	*cc-pVDZ*	264	0.03
3		238	0.17		241	0.17		236	0.14
4		226	0.05		230	0.03		225	0.10
5		223	0.06		226	0.09		220	0.19
6		217	0.45		221	0.41		219	0.18
7		203	0.01		209	0.00		206	0.02
8		202	0.01		208	0.00		202	0.00
1	**CL**	452	0.16	**CL**	457	0.16	**BP**	444	0.09
2	*cc-pVDZ*	305	0.13	*cc-pVTZ*	309	0.13	*cc-pVDZ*	295	0.12
3		272	0.00		282	0.00		249	0.22
4		246	0.00		254	0.00		246	0.00
5		246	0.18		248	0.18		236	0.07
6		237	0.11		239	0.11		222	0.00
7		213	0.00		217	0.00		220	0.03
8		211	0.00		213	0.01		213	0.01

Table A2.4: Excitation energies of the first eight excited states of antiparallel (AP), parallel (PA), closed (CL), and by-product (BP) NS2-22 obtained from MRCC calculations at the df-CC2/cc-pVDZ and df-CC2/cc-pVTZ levels of theory. The oscillator strengths (f) are highlighted by their relative magnitudes, where green indicates a large value.

Exc state	**Species**	**E_{exc} / nm**	***f***	**Species**	**E_{exc} / nm**	***f***	**Species**	**E_{exc} / nm**	***f***
1	**AP**	282	0.15	**AP**	291	0.13	**PA**	273	0.17
2	*cc-pVDZ*	259	0.02	*cc-pVTZ*	267	0.01	*cc-pVDZ*	268	0.19
3		247	0.88		254	0.83		244	0.65
4		231	0.01		237	0.01		231	0.07
5		214	0.06		222	0.05		213	0.05
6		208	0.18		215	0.10		207	0.15
7		203	0.04		210	0.06		207	0.05
8		200	0.09		210	0.13		201	0.08
1	**CL**	466	0.30	**CL**	478	0.29	**BP**	446	0.15
2	*cc-pVDZ*	342	0.18	*cc-pVTZ*	349	0.03	*cc-pVDZ*	331	0.17
3		276	0.33		295	0.50		262	0.00
4		261	0.00		268	0.00		254	0.18
5		251	0.29		259	0.25		247	0.23
6		241	0.09		251	0.09		228	0.04
7		219	0.03		230	0.01		222	0.01
8		217	0.11		210	0.03		222	0.10

Table A2.5: Excitation energies of the first eight excited states of antiparallel (AP) and closed (CL) NS2-22, with added PCM to include solvation effects of methanol. Obtained from TD-DFT calculations at the ωB97X-D/cc-pVDZ and ωB97X-D/cc-pVTZ levels of theory, in Gaussian 16B.01. The oscillator strengths (f) are highlighted by their relative magnitudes, where green indicates a large value.

Exc state	**Species**	**E_{exc} / nm**	***f***	**Species**	**E_{exc} / nm**	***f***
1	**AP**	292	0.13	**AP**	296	0.13
2	*cc-pVDZ*	261	0.03	*cc-pVTZ*	264	0.03
3		241	0.23		244	0.23
4		227	0.08		231	0.06
5		225	0.06		228	0.10
6		219	0.50		223	0.46
7		202	0.05		207	0.01
8		201	0.00		207	0.01
1	**CL**	460	0.20	**CL**	466	0.20
2	*cc-pVDZ*	308	0.17	*cc-pVTZ*	311	0.19
3		270	0.01		279	0.01
4		246	0.23		252	0.00
5		245	0.01		249	0.24
6		237	0.13		239	0.13
7		211	0.02		217	0.00
8		211	0.00		212	0.02

Table A2.6: Excitation energies of the first eight excited states of antiparallel (AP) and closed (CL) NS2-22, with added PCM to include solvation effects of methanol. Obtained from MRCC calculations at the df-CC2/cc-pVDZ and df-CC2/cc-pVTZ levels of theory. The oscillator strengths (f) are highlighted by their relative magnitudes, where green indicates a large value.

Exc state	**Species**	**E_{exc} / nm**	f	**Species**	**E_{exc} / nm**	f
1	**AP**	285	1.21	**AP**	295	0.14
2	*cc-pVDZ*	262	0.12	*cc-pVTZ*	271	0.02
3		247	5.84		254	0.86
4		231	0.06		237	0.01
5		214	0.20		222	0.03
6		207	1.27		215	0.16
7		203	0.19		209	0.04
8		200	0.34		208	0.11
1	**CL**	467	0.30	**CL**	479	0.29
2	*cc-pVDZ*	341	0.33	*cc-pVTZ*	348	0.08
3		271	0.18		289	0.46
4		259	0.00		267	0.00
5		249	0.31		256	0.27
6		238	0.08		248	0.08
7		218	0.03		228	0.02
8		214	0.11		214	0.01

Table A2.7: Excitation energies of the first eight excited states of the three lowest energy singly-solvated geometries of antiparallel NS2-22. Of the three, o-sol1.0 is the most stable. Along with the explicit solvation (addition of one methanol molecule), PCM was included for those on the second row. Obtained from TD-DFT calculations at the ωB97X-D/cc-pVDZ level of theory, in Gaussian 16B.01. The oscillator strengths (f) are highlighted by their relative magnitudes, where green indicates a large value.

Exc state	**Structure**	**E_{exc} / nm**	***f***	**Structure**	**E_{exc} / nm**	***f***	**Structure**	**E_{exc} / nm**	***f***
1	**o-sol1.0**	291	0.10	**o-sol1.2**	286	0.11	**o-sol1.3**	292	0.13
2	*no PCM*	261	0.02		257	0.02		263	0.02
3		240	0.16		238	0.19		243	0.18
4		228	0.09		226	0.04		227	0.08
5		225	0.02		223	0.07		224	0.03
6		218	0.44		218	0.42		217	0.44
7		204	0.05		205	0.01		204	0.02
8		203	0.01		202	0.02		203	0.01
1	**o-sol1.0**	295	0.13	**o-sol1.2**	291	0.14	**o-sol1.3**	295	0.15
2	*with PCM*	264	0.03		261	0.03		265	0.03
3		242	0.22		241	0.25		244	0.24
4		228	0.11		227	0.05		228	0.11
5		226	0.03		225	0.07		225	0.04
6		219	0.49		220	0.48		219	0.50
7		204	0.07		203	0.02		203	0.05
8		201	0.01		202	0.03		202	0.01

Table A2.8: Excitation energies of the first eight excited states of the three lowest energy doubly-solvated geometries of antiparallel NS2-22. Of the three, o-sol2.2 is the most stable. Along with the explicit solvation (addition of two methanol molecules), PCM was included for the second row results. Obtained from TD-DFT calculations at the ωB97X-D/cc-pVDZ level of theory, in Gaussian 16B.01. The oscillator strengths (f) are highlighted by their relative magnitudes, where green indicates a large value.

Exc state	**Structure**	**E_{exc} / nm**	***f***	**Structure**	**E_{exc} / nm**	***f***	**Structure**	**E_{exc} / nm**	***f***
1	**o-sol2.0**	297	0.11	**o-sol2.2**	293	0.11	**o-sol2.5**	292	0.11
2	*no PCM*	266	0.02		264	0.02		263	0.02
3		245	0.17		242	0.16		241	0.18
4		230	0.09		228	0.09		228	0.08
5		225	0.01		225	0.02		225	0.02
6		218	0.43		218	0.45		219	0.43
7		205	0.05		204	0.04		205	0.01
8		204	0.01		201	0.01		204	0.03
1	**o-sol2.0**	299	0.13	**o-sol2.2**	297	0.13	**o-sol2.5**	295	0.14
2	*with PCM*	268	0.03		266	0.03		265	0.03
3		246	0.22		244	0.21		243	0.23
4		230	0.12		229	0.11		229	0.10
5		226	0.02		226	0.03		226	0.03
6		220	0.49		220	0.51		221	0.48
7		204	0.07		204	0.06		204	0.06
8		202	0.01		201	0.01		203	0.01

Table A2.9: Excitation energies of the first eight excited states of the three lowest energy singly-solvated geometries of closed NS2-22. Of the three, c-sol1.0 is the most stable. Along with the explicit solvation (addition of one methanol molecule), PCM was included for the second row results. Obtained from TD-DFT calculations at the ωB97X-D/cc-pVDZ level of theory, in Gaussian 16B.01. The oscillator strengths (f) are highlighted by their relative magnitudes, where green indicates a large value.

Exc state	**Structure**	**E_{exc} / nm**	***f***	**Structure**	**E_{exc} / nm**	***f***	**Structure**	**E_{exc} / nm**	***f***
1	**c-sol1.0**	458	0.16	**c-sol1.1**	456	0.16	**c-sol1.5**	447	0.17
2	*no PCM*	310	0.13		310	0.13		303	0.13
3		272	0.01		272	0.01		272	0.01
4		247	0.16		248	0.14		246	0.00
5		246	0.03		246	0.05		244	0.17
6		238	0.11		238	0.11		236	0.10
7		213	0.01		212	0.01		213	0.01
8		212	0.00		211	0.00		211	0.00
1	**c-sol1.0**	464	0.20	**c-sol1.1**	462	0.20	**c-sol1.5**	456	0.21
2	*with PCM*	310	0.17		311	0.17		306	0.18
3		267	0.01		270	0.01		270	0.01
4		248	0.23		248	0.23		245	0.22
5		245	0.01		244	0.02		244	0.02
6		238	0.13		238	0.13		236	0.12
7		211	0.00		211	0.00		211	0.01
8		211	0.02		210	0.01		210	0.00

Table A2.10: Excitation energies of the first eight excited states of the three lowest energy doubly-solvated geometries of closed NS2-22. Of the three, c-sol2.1 is the most stable. Along with the explicit solvation (addition of two methanol molecules), PCM was included for the second row results. Obtained from TD-DFT calculations at the ωB97X-D/cc-pVDZ level of theory, in Gaussian 16B.01. The oscillator strengths (f) are highlighted by their relative magnitudes, where green indicates a large value.

Exc state	**Structure**	**E_{exc} / nm**	***f***	**Structure**	**E_{exc} / nm**	***f***	**Structure**	**E_{exc} / nm**	***f***
1	**c-sol2.0**	466	0.16	**c-sol2.1**	460	0.16	**c-sol2.2**	459	0.15
2	*no PCM*	313	0.13		311	0.13		312	0.13
3		272	0.01		271	0.01		271	0.01
4		248	0.19		248	0.17		250	0.17
5		246	0.01		245	0.02		246	0.02
6		239	0.11		238	0.12		241	0.06
7		213	0.01		216	0.00		236	0.05
8		212	0.00		212	0.00		212	0.00
1	**c-sol2.0**	471	0.20	**c-sol2.1**	466	0.20	**c-sol2.2**	464	0.19
2	*with PCM*	312	0.17		311	0.17		312	0.17
3		271	0.01		269	0.01		269	0.01
4		249	0.24		249	0.23		249	0.22
5		244	0.01		244	0.01		244	0.02
6		239	0.12		238	0.13		239	0.12
7		212	0.00		212	0.00		228	0.01
8		212	0.02		212	0.02		211	0.01

Table A2.11: Excitation energies of the first eight excited states of the lowest energy doubly-solvated geometries of antiparallel and closed NS2-22. Obtained from MRCC calculations at the df-CC2/cc-pVDZ level of theory with PCM. The oscillator strengths (f) are highlighted by their relative magnitudes, where green indicates a large value.

Exc state	**Structure**	**E_{exc} / nm**	***f***	**Structure**	**E_{exc} / nm**	***f***
1	**o-sol2.2**	283	0.15	**c-sol2.1**	469	0.30
2		260	0.02		343	0.22
3		247	0.80		277	0.29
4		232	0.07		262	0.00
5		214	0.09		251	0.30
6		208	0.18		241	0.09
7		204	0.04		219	0.03
8		199	0.09		217	0.12

Table A2.12: Excitation energies of the first eight excited states of the lowest energy triply-solvated geometries of antiparallel and closed NS2-22. Along with the explicit solvation (addition of three methanol molecules), PCM was included for the second column results. Obtained from TD-DFT calculations at the ωB97X-D/cc-pVDZ level of theory, in Gaussian 16B.01. The oscillator strengths (f) are highlighted by their relative magnitudes, where green indicates a large value.

Exc state	**Structure**	**E_{exc} / nm**	***f***	**Structure**	**E_{exc} / nm**	***f***
1	**o-sol3.5**	295	0.12	**o-sol3.5**	298	0.14
2	*no PCM*	264	0.02	*with PCM*	267	0.03
3		243	0.15		244	0.21
4		228	0.08		229	0.11
5		225	0.03		226	0.03
6		218	0.45		220	0.51
7		204	0.04		204	0.06
8		202	0.00		201	0.01
1	**c-sol3.5**	460	0.17	**c-sol3.5**	466	0.20
2	*no PCM*	311	0.12	*with PCM*	311	0.17
3		271	0.01		269	0.01
4		248	0.16		249	0.22
5		244	0.02		243	0.01
6		238	0.12		238	0.14
7		214	0.00		211	0.00
8		212	0.01		211	0.01

Abbreviations

1-ButOH	1-butanol
1-HeptOH	1-heptanol
1-OctOH	1-octanol
1-PentOH	1-pentanol
1-PropOH	1-propanol
2-PropOH	2-propanol
26Me	2,6-methylated derivative of *para*-hydroxybenzylideneimidazolinone
35Bu	3,5-butylated derivative of *para*-hydroxybenzylideneimidazolinone
35Me	3,5-methylated derivative of *para*-hydroxybenzylideneimidazolinone
AP	antiparallel
ATD	arrival time distribution
BBO	β-barium borate
BP	by-product
BSSE	basis set superposition error
CASSCF	complete active space self-consistent field
CBE	cluster binding energy
CC	coupled-cluster
CCSD	coupled-cluster singles and doubles
CCSD(T)	coupled-cluster singles and doubles, with perturbative triples
CI	configuration interaction
CI	conical intersection
CIS	configuration interaction singles
CISD	configuration interaction singles and dougles
CL	closed
CM5	Hirshfeld-CM5 populations
CPCM	conducter-like polarisation continuum model
CT	charge transfer
CW	continuous wave

DAE	diarylethene
df-CC2	density-fitted CC2
DFT	density functional theory
DLPNO	domain-based local pair natural orbitals
DMS	differential mobility spectrometry
DTE	dithienylethene
EOM-CC	equation-of-motion coupled-cluster
EPL	picosecond pulsed diode laser
EPLED	picosecond pulsed light emitting diode
ESI	electrospray ionisation
EtGly	ethylene glycol
EtOH	ethanol
FCHT	Franck-Condon Herzberg-Teller
FCI	full configuration interaction
FWHM	full-width half-maximum
GDD	group delay dispersion
GFP	green fluorescent protein
GVD	group velocity dispersion
HF	Hartree-Fock
HOMO	highest-occupied molecular orbital
IF1	first ion funnel
IF2	second ion funnel
IG1	first ion gate
IG2	second ion gate
IMS	ion-mobility spectrometry/spectrometer
IMS1	first ion-mobility spectrometry stage
IMS2	second-ion mobility spectrometry stage
IR	infrared
IRF	instrument response function
IVER	intermolecular vibrational energy redistribution/relaxation
IVR	intramolecular vibrational redistribution
LE	local excitation
LED	light-emitting diode
LIIC	linear interpolation in internal coordinates
LR	linear response
LUMO	lowest-unoccupied molecular orbital
m/z	mass-to-charge ratio

MBS	minimum basis set Mulliken populations
MCSCF	multiconfigurational self-consistent field
MeOH	methanol
MQ	Milli-Q water
MR	multi-reference
MRCC	multi-reference configuration interaction coupled-cluster
MRCI	multi-reference configuration interaction
NBO	natural bond order populations
Nd:YVO_4	neodymium yttrium vanadate
NMR	nuclear magnetic resonance
OPO	optical parametric oscillator
P	parallel
*p*CA	*para*-coumaric acid
*p*CEs	*para*-coumaric ester (methylated at carboxylate end)
*p*CEt	*para*-coumaric ester (methylated at phenoxide end)
*p*CK	*para*-coumaric ketone
*p*CT	*para*-coumaric thioester
PCM	polarisable continuum model
PCM	polarisable continuum model
PES	potential energy surface
*p*HBDI	*para*-hydroxybenzylideneimidazolinone
Phe	phenylated derivative of *para*-hydroxybenzylideneimidazolinone
PM6	parameterised model 6
PYP	photoactive yellow protein
QM	quantum mechanical
QM/MM	quantum mechanics/molecular mechanics
QMF	quadrupole mass filter
rKFP	red Kaede fluorescent protein
SAPT	symmetry-adapted perturbation theory
SAPT	symmetry-adapted perturbation theory
SAPT0	truncated symmetry-adapted perturbation theory
SCF	self-consistent field
SFG	sum frequency generation
SHG	sum harmonic generation
SMD	solvation model density
SS	state specific
STEOM	similarity-transformed equation of motion

TD	time-dependent
TD-DFT	time-dependent DFT
thio-pCA	*para*-coumaric tioester
Ti:S	Titanium-Sapphire
TST	transition state theory
UV	ultraviolet
VDE	vertical detachment energy
VEE	vertical excitation energy
XM	excitation-emission
XMCQDPT2	extended multi-configuration quasi-degenerate perturbation theory